

**Design and Implementation of
Analytical Mathematics for
SIFT-MS Medical
Applications**

Katherine Tracey Moorhead

A thesis presented for the degree of
Doctor of Philosophy
in
Bioengineering
at the
University of Canterbury,
Christchurch, New Zealand.

16 September 2009

Acknowledgements

I would like to thank my research supervisors, Prof. J. Geoffrey Chase, Prof. Zoltan Endre, Dr. Dominic Lee, and Dr. Geoff Shaw for their support and guidance over the last three years. Also thanks to Dr. Jenny Scotter and Dr. Randall Allardyce, my project mentors from Syft Technologies, and to Dr. Chris Hann from the Mechanical Engineering Department.

Special thanks to Dr. Jonathan Hill from the Christchurch Kidney Research Group at the Department of Medicine, University of Otago - Christchurch, for his help with the animal experiments. Also thanks to Dr. John Pickering, Dr. Helen Milne, Don Ponnampereuma, and Maryam Nejat from the Christchurch Kidney Research Group, and Jenn Bothwell and Anne Morrison from the CARA group.

In the Syft laboratory in the Department of Surgery at the Christchurch Hospital, thanks to Dr. Malina Storer and Dr. Sunny Hu. Lastly, thanks to those patients and animals who participated in the clinical trials.



“If at first, the idea is not absurd, then there is no hope for it”

–Albert Einstein

Contents

Acknowledgements	iii
Abstract	xxxi
1 Introduction	1
1.1 Selected Ion Flow Tube-Mass Spectrometry	2
1.1.1 Principles of SIFT-MS	2
1.1.2 Precursor Reactions	3
1.1.3 Mode of Operation	5
1.1.4 Applications	6
1.2 Breath Sampling	7
1.2.1 Breath Metabolites	7
1.2.2 Respiratory Physiology	8
1.2.3 Sample Collection	10
1.3 Summary	11
2 Cross-sectional Classification Models	13
2.1 Experimental Design	13
2.1.1 Validation Study: Nitrogen (N_2) in Tedlar Bags	14
2.1.2 Case Study: Dialysis	15
2.2 Pre-processing	16
2.3 Statistical Classification Analysis	19
2.3.1 Classification	19
2.3.2 Bootstrap Method for Estimating Prediction Error	21
2.3.3 Reliability	23
2.3.4 Biomarkers	24
2.4 Results and Discussion	25
2.4.1 Validation Study: Nitrogen in Tedlar Bags	25
2.4.1.1 Probability Density Profiles	26
2.4.1.2 Biomarkers	27
2.4.1.3 Reliability	28
2.4.2 Dialysis Proof-Of-Concept Study	30

2.4.2.1	Probability Density Profiles	30
2.4.2.2	Biomarkers	31
2.4.2.3	Reliability	32
2.5	Experimental Discussion and Conclusions	34
2.6	Classification User Interface	36
3	Longitudinal Classification Models and Dialysis Study I	39
3.1	Paired Classification Model	40
3.1.1	Normalisation	40
3.1.2	Visualisation of Results	42
3.2	Introduction to Dialysis	44
3.3	Dialysis Clinical Study Design	47
3.3.1	Dialysis Study I Methodology	49
3.4	Dialysis Study I Results	50
3.4.1	SIM Scans	50
3.4.2	Mass Scans	53
3.4.2.1	H_3O^+	54
3.4.2.2	NO^+	57
3.4.2.3	O_2^+	59
3.5	Summary	63
4	Dialysis Study II	65
4.0.1	Dialysis Study II Methodology	65
4.1	Dialysis Study II Results	66
4.1.1	SIM Scans	66
4.1.2	Mass Scans	69
4.1.2.1	H_3O^+	69
4.1.2.2	NO^+	76
4.1.2.3	O_2^+	81
4.2	Summary and Future Work	87
5	Acute Renal Failure in Rats - Animal Study Design	89
5.1	Kidney Anatomy and Physiology	89
5.1.1	Kidney Structure and Function	89
5.1.2	Ammonia Excretion	92
5.1.3	Glomerular Filtration Rate	93
5.1.4	Renal Histology	95
5.1.5	Acute Renal Failure	97
5.2	Study Design	100
5.3	Induction of Acute Renal Failure	101
5.4	Inulin Clearance Tests for Determining GFR	106
5.4.1	Clearance Techniques	106

5.4.2	Serial Blood Sampling and Cannulation	113
5.4.3	Final Inulin Clearance method	120
5.5	Creatinine Clearance for GFR Determination	120
5.6	Breath Collection for Determination of GFR	122
5.7	Summary	127
6	ARF in Rats - Mathematical Methods	129
6.1	Inulin Clearance Modelling for GFR Determination	129
6.2	Creatinine Estimates of GFR	137
6.3	Breath collection for GFR estimation	137
6.3.1	SIM Scans	137
6.3.2	Interpreting SIM Scan raw data	143
6.3.3	Mass Scans	145
6.4	Summary	146
7	ARF in Rats - Results and Discussion	149
7.1	Correlation of gold standard renal markers with breath ammonia .	150
7.1.1	Grace - Rat 1	150
7.1.1.1	Inulin Clearance	150
7.1.1.2	Creatinine	151
7.1.1.3	Ammonia SIM Scans	152
7.1.2	Heidi - Rat 2	153
7.1.2.1	Inulin Clearance	153
7.1.2.2	Creatinine	154
7.1.2.3	Ammonia SIM Scans	155
7.1.3	Isis - Rat 3	156
7.1.3.1	Inulin Clearance	156
7.1.3.2	Creatinine	157
7.1.3.3	Ammonia SIM Scans	158
7.1.4	Maya - Rat 4	160
7.1.4.1	Inulin Clearance	160
7.1.4.2	Creatinine	161
7.1.4.3	Ammonia SIM Scans	162
7.1.5	Nell - Rat 5	163
7.1.5.1	Inulin Clearance	163
7.1.5.2	Creatinine	164
7.1.5.3	Ammonia SIM Scans	165
7.1.6	Olive - Rat 6	166
7.1.6.1	Inulin Clearance	166
7.1.6.2	Creatinine	167
7.1.6.3	Ammonia SIM Scans	168
7.1.7	Paige - Rat 7	169

7.1.7.1	Inulin Clearance	169
7.1.7.2	Creatinine	170
7.1.7.3	Ammonia SIM Scans	171
7.1.8	Quin - Rat 8	173
7.1.8.1	Inulin Clearance	173
7.1.8.2	Creatinine	173
7.1.8.3	Ammonia SIM Scans	174
7.1.9	Sophie - Rat 9	176
7.1.9.1	Inulin Clearance	176
7.1.9.2	Creatinine	177
7.1.9.3	Ammonia SIM Scans	177
7.1.10	Tosca - Rat 10	179
7.1.10.1	Inulin Clearance	179
7.1.10.2	Creatinine	180
7.1.10.3	Ammonia SIM Scans	181
7.1.11	Ula - Rat 11	182
7.1.11.1	Inulin Clearance	182
7.1.11.2	Creatinine	182
7.1.11.3	Ammonia SIM Scans	183
7.1.12	Summary	185
7.2	SIM Scan - Isoprene	185
7.3	Renal Histology	189
7.4	Identification of Biomarkers of ARF	191
7.4.1	H_3O^+ Precursor	192
7.4.1.1	Normal verses ARF	192
7.4.1.2	Cannulation Surgery verses ARF Surgery	196
7.4.2	O_2^+ Precursor	201
7.5	Summary	208
8	Conclusions and Future Work	211
8.1	Conclusions	211
8.2	Future Work	214

List of Figures

1.1	Schematic of analyte quantification via SIFT-MS, Smith and Spanel [2005]	3
1.2	Typical SIM scan output	6
1.3	Typical mass scan output	6
1.4	Gas exchange in the alveolus, Purves et al. [1995]	9
1.5	Lung anatomy with detail of pleural cavity, Randall et al. [2002]	9
2.1	Typical mass scan over 10-100 amu	16
2.2	Typical mass scan focused on 17-22amu	17
2.3	Typical mass scan peak at 19 amu	17
2.4	Noise in the raw data at 18, 20 and 21 amu	18
2.5	Fitting Probability density profiles to raw data	20
2.6	Probability densities for a given mass	20
2.7	Reliability curve showing the reliability of a given classification based on its log-odds value	24
2.8	Piecewise classification, showing the log-odds ratios obtained at each mass that combine to form the final log-odds ratio used for classification	25

2.9	Biomarkers schematic with Log-odds ratio	25
2.10	Selected probability density profiles using H_3O^+ precursor	26
2.11	Log-odds density profiles for biomarker selection in validation study	28
2.12	Reliability curve for validation study classification model	29
2.13	ROC curve for validation study classification model	29
2.14	Probability density profiles obtained using H_3O^+ precursor on dialysis concentration data	31
2.15	Log-odds density profiles for biomarker selection in the dialysis study	33
2.16	Reliability Curve for Dialysis Study Classification Model	34
2.17	ROC Curve for Dialysis Study Classification Model	34
2.18	Cross-sectional Classification User Interface	36
3.1	Normalisation Illustration: Left-no normalisation; Centre-Relative normalisation, Equation (3.1); Right-Absolute normalisation, Equation (3.2)	42
3.2	Typical image plot highlighting top biomarker masses by probability density profiles created from the mean to standard deviation ratio of subsequent bootstrap datasets.	43
3.3	Dialysis circuit diagram illustrating external filtering of wastes from the blood in patients with renal failure Martini [2006]	45
3.4	DS101 SIM Scan	50
3.5	DS102 SIM Scan	50
3.6	DS111 SIM Scan	51

3.7	DS113 SIM Scan	51
3.8	DS114 SIM Scan	51
3.9	DS115 SIM Scan	52
3.10	Classification on <i>raw</i> data over all masses with the H_3O^+ precursor, as determined by Equation (2.3)	55
3.11	Classification on <i>normalised</i> data over all masses (Equation (3.1) with the H_3O^+ precursor, as determined by Equation (2.3)	55
3.12	Biomarker identification in Dialysis Study I with the H_3O^+ precursor	56
3.13	Probability density profiles for Mass 18 obtained via raw and normalised, pre and post dialysis datasets. Log-odds probability density profile for identification of biomarkers is shown, <i>right</i> with Area of Overlap (AOL) indicating the degree of overlap of the density profiles.	56
3.14	Probability density profiles for Mass 36 obtained from raw and normalised, pre and post dialysis datasets.	57
3.15	Probability density profiles for Mass 54 obtained from raw and normalised, pre and post dialysis datasets.	57
3.16	Classification on <i>raw</i> data over all masses with the NO^+ precursor, as determined by Equation (2.3)	58
3.17	Classification on <i>normalised</i> data over all masses (Equation (3.1) with the NO^+ precursor, as determined by Equation (2.3)	58
3.18	Biomarker identification in Dialysis Study I with the NO^+ precursor	59
3.19	Classification on <i>raw</i> data over all masses with the O_2^+ precursor, as determined by Equation (2.3)	60

3.20	Classification on <i>normalised</i> data over all masses (Equation (3.1) with the O_2^+ precursor, as determined by Equation (2.3)	60
3.21	Biomarker identification in Dialysis Study I with the O_2^+ precursor	61
3.22	Probability density profiles for Mass 17 obtained from raw and normalised, pre and post dialysis datasets using the O_2^+ precursor.	61
3.23	Probability density profiles for Mass 18 obtained from raw and normalised, pre and post dialysis datasets using the O_2^+ precursor.	61
3.24	Probability density profiles for Mass 35 obtained from raw and normalised, pre and post dialysis datasets using the O_2^+ precursor.	62
3.25	Mass Probability density profiles for Mass 36 obtained from raw and normalised, pre and post dialysis datasets using the O_2^+ precursor.	62
3.26	Mass Probability density profiles for Mass 53 obtained from raw and normalised, pre and post dialysis datasets using the O_2^+ precursor.	62
3.27	Mass Probability density profiles for Mass 54 obtained from raw and normalised, pre and post dialysis datasets using the O_2^+ precursor.	63
4.1	DS201 SIM Scan	66
4.2	DS202 SIM Scan	67
4.3	DS203 SIM Scan	67
4.4	DS204 SIM Scan	67
4.5	DS205 SIM Scan	68
4.6	Classification from <i>raw</i> data over all masses using the H_3O^+ precursor	70

4.7	Classification from <i>normalised</i> data over all masses using the H_3O^+ precursor	70
4.8	Biomarker identification using the H_3O^+ precursor	70
4.9	Probability density profiles for Mass 43 obtained via raw and normalised, pre and post dialysis datasets with the H_3O^+ precursor. Log-odds probability density profile for identification of biomarkers is shown, <i>right</i>	72
4.10	Probability density profiles for Mass 44 obtained via raw and normalised, pre and post dialysis datasets with the H_3O^+ precursor.	72
4.11	Probability density profiles for Mass 58 obtained via raw and normalised, pre and post dialysis datasets with the H_3O^+ precursor.	73
4.12	Probability density profiles for Mass 61 obtained via raw and normalised, pre and post dialysis datasets with the H_3O^+ precursor.	73
4.13	Probability density profiles for Mass 62 obtained via raw and normalised, pre and post dialysis datasets with the H_3O^+ precursor.	73
4.14	Probability density profiles for Mass 78 obtained via raw and normalised, pre and post dialysis datasets with the H_3O^+ precursor.	74
4.15	Probability density profiles for Mass 79 obtained via raw and normalised, pre and post dialysis datasets with the H_3O^+ precursor.	74
4.16	Probability density profiles for Mass 80 obtained via raw and normalised, pre and post dialysis datasets with the H_3O^+ precursor.	74
4.17	Probability density profiles for Mass 97 obtained via raw and normalised, pre and post dialysis datasets with the H_3O^+ precursor.	75
4.18	Probability density profiles for Mass 118 obtained via raw and normalised, pre and post dialysis datasets with the H_3O^+ precursor.	75

- 4.19 Probability density profiles for Mass 121 obtained via raw and normalised, pre and post dialysis datasets with the H_3O^+ precursor. 75
- 4.20 Classification on *raw* data over all masses with the NO^+ precursor, as determined by Equation (2.3) 76
- 4.21 Classification on *normalised* data over all masses (Equation (3.1)) with the NO^+ precursor, as determined by Equation (2.3) 77
- 4.22 Biomarker identification in Dialysis Study II with the NO^+ precursor 77
- 4.23 Probability density profiles for Mass 59 obtained from raw and normalised, pre and post dialysis datasets using the NO^+ precursor. 78
- 4.24 Probability density profiles for Mass 60 obtained from raw and normalised, pre and post dialysis datasets using the NO^+ precursor. 78
- 4.25 Probability density profiles for Mass 61 obtained from raw and normalised, pre and post dialysis datasets using the NO^+ precursor. 79
- 4.26 Probability density profiles for Mass 72 obtained from raw and normalised, pre and post dialysis datasets using the NO^+ precursor. 79
- 4.27 Probability density profiles for Mass 77 obtained from raw and normalised, pre and post dialysis datasets using the NO^+ precursor. 79
- 4.28 Probability density profiles for Mass 78 obtained from raw and normalised, pre and post dialysis datasets using the NO^+ precursor. 80
- 4.29 Probability density profiles for Mass 79 obtained from raw and normalised, pre and post dialysis datasets using the NO^+ precursor. 80
- 4.30 Probability density profiles for Mass 88 obtained from raw and normalised, pre and post dialysis datasets using the NO^+ precursor. 80
- 4.31 Probability density profiles for Mass 89 obtained from raw and normalised, pre and post dialysis datasets using the NO^+ precursor. 81

- 4.32 Probability density profiles for Mass 152 obtained from raw and normalised, pre and post dialysis datasets using the NO^+ precursor. 81
- 4.33 Classification on *raw* data over all masses with the O_2^+ precursor, as determined by Equation (2.3) 82
- 4.34 Classification on *normalised* data over all masses (Equation (3.1) with the O_2^+ precursor, as determined by Equation (2.3) 82
- 4.35 Biomarker identification in Dialysis Study II with the O_2^+ precursor 82
- 4.36 Probability density profiles for Mass 43 obtained from raw and normalised, pre and post dialysis datasets using the O_2^+ precursor. 83
- 4.37 Probability density profiles for Mass 44 obtained from raw and normalised, pre and post dialysis datasets using the O_2^+ precursor. 84
- 4.38 Probability density profiles for Mass 58 obtained from raw and normalised, pre and post dialysis datasets using the O_2^+ precursor. 84
- 4.39 Probability density profiles for Mass 60 obtained from raw and normalised, pre and post dialysis datasets using the O_2^+ precursor. 84
- 4.40 Probability density profiles for Mass 61 obtained from raw and normalised, pre and post dialysis datasets using the O_2^+ precursor. 85
- 4.41 Probability density profiles for Mass 62 obtained from raw and normalised, pre and post dialysis datasets using the O_2^+ precursor. 85
- 4.42 Probability density profiles for Mass 79 obtained from raw and normalised, pre and post dialysis datasets using the O_2^+ precursor. 85
- 4.43 Probability density profiles for Mass 80 obtained from raw and normalised, pre and post dialysis datasets using the O_2^+ precursor. 86
- 4.44 Probability density profiles for Mass 81 obtained from raw and normalised, pre and post dialysis datasets using the O_2^+ precursor. 86

4.45	Probability density profiles for Mass 103 obtained from raw and normalised, pre and post dialysis datasets using the O_2^+ precursor.	86
4.46	Probability density profiles for Mass 151 obtained from raw and normalised, pre and post dialysis datasets using the O_2^+ precursor.	87
5.1	Kidney Anatomy, Merriam-Webster [2006]	89
5.2	Structure of a nephron, Randall et al. [2002]	90
5.3	PCT Epithelial Cell, Randall et al. [2002]	91
5.4	Tubular Excretion of Ammonia (Gln-Glutamine; GA-Glutaminase; Glu-Glutamate; GDH-Glutamate Dehydrogenase, Weiner and Hamm [2007]	93
5.5	Juxtaglomerular Complex for monitoring renal blood flow, Randall et al. [2002]	94
5.6	Normal Tubular Histology: <i>p</i> - Proximal Convolved Tubule; <i>d</i> - Distal Convolved Tubule, King [2007]	96
5.7	Normal Tubular Histology: <i>cd</i> - Collecting Duct; <i>ts</i> - Thin Segment of Loop of Henle; <i>d</i> - Distal Convolved Tubule, King [2007]	96
5.8	Normal Tubular Histology: Longitudinal Section of Collecting Duct and Thick Segment of Loop of Henle, King [2007]	96
5.9	Renal circulation, highlighting position of the renal vein, University of Debrecen [2009]	103
5.10	ARF Surgical Technique: Top left, mid-ventral incision; top right, locating kidney; bottom left, clamping renal artery; bottom right, suturing each tissue layer with a running stitch.	105
5.11	CIM for Pilot Rat 1	111
5.12	CIM for Pilot Rat 2	111

5.13	CIM for Pilot Rat 5	111
5.14	Subsequent bolus clearances for Pilot Rat 6 - Model fitted to raw data	112
5.15	Subsequent bolus clearances for Pilot Rat 7	113
5.16	Subsequent bolus clearances for Pilot Rat 8	113
5.17	Double blunt needle assembly Bakar and Niazi [1982]	114
5.18	Double blunt needle cannulation technique Bakar and Niazi [1982]	114
5.19	Position of the jugular vein	115
5.20	Rat coat to prevent rat accessing the indwelling cannula	116
5.21	Cannulation Surgery: Top left, rat positioned for surgery; top right, isolating the jugular vein; bottom left, inserting the cannula; bottom right, obtaining blood from cannula.	116
5.22	Cannulation Surgery: Top left, tying cannula in place; top right, gavage needle to thread the cannula sub-cutaneously to the back of neck; bottom left, positioning cannula at the back of neck; bottom right, wrapped in cannula-protecting coat.	117
5.23	Pilot Animal Inulin Clearance Curve	118
5.24	Pilot Animal Day 2 Inulin Clearance	119
5.25	Relationship between creatinine clearance and GFR in humans	121
5.26	Rat restraining device	124
5.27	Breath collection apparatus	124
5.28	Increase in acetone as measured with H_3O^+ precursor over duration of anaesthesia	125

5.29	Increase in acetone as measured with NO^+ precursor over duration of anaesthesia	126
5.30	Increase in acetone as measured with O_2^+ precursor over duration of anaesthesia	126
5.31	Decrease in isoprene in Rat 1 over duration of anaesthesia	127
5.32	Decrease in isoprene in Rat 2 over duration of anaesthesia	127
6.1	Two-Compartment Model of Kidney Function	129
6.2	Rat 1 Raw inulin concentration data to enable modelling of volume of distribution	133
6.3	Rat 2 Raw inulin concentration data to enable modelling of volume of distribution	134
6.4	Rat 1 Model fit to raw inulin concentration data for volume of distribution determination. The non-zero slope indicates $GFR \neq 0$	135
6.5	Rat 2 Model fit to raw inulin concentration data. The non-zero slope indicates $GFR \neq 0$	135
6.6	Relationship between plasma creatinine and GFR in all rats	137
6.7	Relationship between background and breath ammonia in healthy rats	138
6.8	Rat Breathing Circuit	140
6.9	Relationship between breath ammonia and GFR, where the a=2.19 slope is a population estimate for Equation (6.21)	141
6.10	Relationship between background and breath isoprene in healthy rats	142

6.11	Typical SIM scan, showing oscillation in reported concentration at equilibrium	143
6.12	Density profile of typical SIM scan for determining <i>true</i> analyte concentration	144
6.13	Endogenously generated analyte transport into alveolar breath . .	145
6.14	Analyte transport out of background air	146
7.1	Grace: Modelling of inulin concentration in the plasma and interstitial compartments over a 70 minute clearance test conducted on 4 separate occasions. 1: Two days post cannulation surgery; 2-4: Six hours, 30 hours, and two days post ARF induction, respectively	150
7.2	Grace: Plasma creatinine concentration and correlation with GFR via inulin clearance	151
7.3	Grace: SIM scan analysis of ammonia in breath and background air	152
7.4	Grace: A comparison of GFR estimates via bolus inulin clearance, plasma creatinine concentration, and breath ammonia concentration, following cannulation surgery at 0 hours, and surgery for ARF induction at 120 hours	153
7.5	Heidi: Inulin clearance summary. 1: Two days post cannulation surgery; 2-4: One, 24 and 48 hours post ARF induction, respectively	154
7.6	Heidi: Plasma creatinine concentration and correlation with GFR via inulin clearance	155
7.7	Heidi: SIM scan ammonia in breath and background air	155
7.8	Heidi: GFR estimation via bolus inulin clearance, plasma creatinine, and breath ammonia	156

7.9	Isis: Inulin clearance summary, 1: Two days post cannulation surgery; 2-6: Six hours, 20 hours, 30 hours, 2 days and 4 days post ARF induction	157
7.10	Isis: Plasma creatinine concentration and correlation with GFR via inulin clearance	158
7.11	Isis: SIM scan ammonia concentration in rat breath and background air	159
7.12	Isis: GFR estimation via bolus inulin clearance, plasma creatinine, and breath ammonia	159
7.13	Maya: Inulin clearance summary, 1-2: Six hours and 2 days post cannulation surgery, respectively; 3-6: Six hours, 30 hours, 2 days and 4 days post ARF induction, respectively.	160
7.14	Maya: Plasma creatinine concentration and correlation with GFR via inulin clearance	161
7.15	Maya: SIM scan ammonia concentration in rat breath and background air	162
7.16	Maya: GFR estimation via bolus inulin clearance, plasma creatinine, and breath ammonia	162
7.17	Nell: Inulin clearance summary. 1-2: Six hours and 2 days post cannulation surgery, respectively; 3-6: Six hours, 30 hours, 2 days, and 4 days post ARF induction, respectively.	163
7.18	Nell: Plasma creatinine concentration and correlation with GFR via inulin clearance	164
7.19	Nell: SIM scan ammonia concentration in breath and background air	165
7.20	Nell: GFR estimation via bolus inulin clearance, plasma creatinine, and breath ammonia	166

7.21 Olive: Inulin clearance summary. 1-2: Six hours and 2 days post cannulation surgery; 2-7: Six hours, 30 hours, 2 days, 4 days, and 6 days post ARF induction, respectively	167
7.22 Olive: Plasma creatinine concentration and correlation with GFR via inulin clearance	168
7.23 Olive: SIM scan ammonia in breath and background air	168
7.24 Olive: GFR estimation via bolus inulin clearance, plasma creatinine, and breath ammonia	169
7.25 Paige: Inulin clearance summary. 1-2: Six hours and 2 days post cannulation surgery; 3-6: Six hours, 30 hours, 2 days, and 4 days post ARF induction, respectively.	170
7.26 Paige: Plasma creatinine concentration and correlation with GFR via inulin clearance	171
7.27 Paige: SIM scan ammonia in breath and background air	172
7.28 Paige: GFR estimation via bolus inulin clearance, plasma creatinine, and breath ammonia	172
7.29 Quin: Inulin clearance summary. 1-2: Six hours and 2 days post cannulation surgery; 3-4: Six hours and 30 hours post ARF induction.	173
7.30 Quin: Plasma creatinine concentration and correlation with GFR via inulin clearance	174
7.31 Quin: SIM scan ammonia in breath and background air	175
7.32 Quin: GFR estimation via bolus inulin clearance, plasma creatinine, and breath ammonia	175
7.33 Sophie: Inulin clearance summary. 1-2: Six hours and 2 days post cannulation surgery, respectively.	176

7.34 Sophie: Plasma creatinine concentration and correlation with GFR via inulin clearance	177
7.35 Sophie: SIM scan ammonia in breath and background air	178
7.36 Sophie: GFR estimation via bolus inulin clearance, plasma creati- nine, and breath ammonia	178
7.37 Tosca: Inulin clearance summary. 1-2: Six hours and 2 days post cannulation surgery; 3-5: Six hours, 30 hours and 2 days post ARF induction, respectively.	179
7.38 Tosca: Plasma creatinine concentration and correlation with GFR via inulin clearance	180
7.39 Tosca: SIM scan ammonia in rat breath and background air	181
7.40 Tosca: GFR estimation via bolus inulin clearance, plasma creati- nine, and breath ammonia	181
7.41 Ula: Inulin clearance summary.1-2: Six hours and 2 days post cannulation surgery; 3: Six hours post ARF induction.	182
7.42 Ula: Plasma creatinine concentration and correlation with GFR via inulin clearance	183
7.43 Ula: SIM scan ammonia in breath and background air	184
7.44 Ula: GFR estimation via bolus inulin clearance, plasma creatinine, and breath ammonia	184
7.45 Grace, rat #1: Breath Isoprene over ARF Trial	185
7.46 Heidi, rat #2: Breath Isoprene over ARF Trial	186
7.47 Isis, rat #3: Breath Isoprene over ARF Trial	186
7.48 Maya, rat #4: Breath Isoprene over ARF Trial	186

7.49	Nell, rat #5: Breath Isoprene over ARF Trial	187
7.50	Olive, rat #6: Breath Isoprene over ARF Trial	187
7.51	Paige, rat #7: Breath Isoprene over ARF Trial	187
7.52	Quin, rat #8: Breath Isoprene over ARF Trial	188
7.53	Sophie, rat #9: Breath Isoprene over ARF Trial	188
7.54	Tosca, rat #10: Breath Isoprene over ARF Trial	188
7.55	Ula, rat #11: Breath Isoprene over ARF Trial	189
7.56	Rat kidney (Nell) 7 days after a 60 minute ischaemia-reperfusion injury. The dilated collecting ducts contain cell debris, sloughed apoptotic and necrotic cells.	190
7.57	Rat kidney (Nell) 7 days after a 60 minute ischaemia-reperfusion injury. Dilated collecting ducts show both necrotic and viable epithelial cells. A dense pink stained tubular cast is seen.	190
7.58	Rat kidney (Maya) 7 days after a 60 minute ischaemia-reperfusion injury. Cortical proximal tubules with largely intact brush borders (pink stain).	191
7.59	Classification between <i>normal</i> and <i>ARF</i> over all masses using the H_3O^+ precursor	193
7.60	Biomarker identification in the <i>normal</i> and <i>ARF</i> states using the H_3O^+ precursor	193
7.61	<i>Left</i> : Probability density profile for Mass 38 obtained via normal and ARF datasets with the H_3O^+ precursor. <i>Right</i> : Log-odds probability density profile for identification of biomarkers is shown, right.	194

- 7.62 *Left*: Probability density profile for Mass 59 obtained via normal and ARF datasets with the H_3O^+ precursor. *Right*: Log-odds probability density profile for identification of biomarkers is shown, right. 194
- 7.63 *Left*: Probability density profile for Mass 77 obtained via normal and ARF datasets with the H_3O^+ precursor. *Right*: Log-odds probability density profile for identification of biomarkers is shown, right. 194
- 7.64 *Left*: Probability density profile for Mass 60 obtained via normal and ARF datasets with the H_3O^+ precursor. *Right*: Log-odds probability density profile for identification of biomarkers is shown, right. 195
- 7.65 *Left*: Probability density profile for Mass 78 obtained via normal and ARF datasets with the H_3O^+ precursor. *Right*: Log-odds probability density profile for identification of biomarkers is shown, right. 195
- 7.66 *Left*: Probability density profile for Mass 63 obtained via normal and ARF datasets with the H_3O^+ precursor. *Right*: Log-odds probability density profile for identification of biomarkers is shown, right. 195
- 7.67 *Left*: Probability density profile for Mass 79 obtained via normal and ARF datasets with the H_3O^+ precursor. *Right*: Log-odds probability density profile for identification of biomarkers is shown, right. 196
- 7.68 Classification between *post-cannulation* and *post-ARF* over all masses using the H_3O^+ precursor 197
- 7.69 Biomarker identification in the *post-cannulation* and *post-ARF* states using the H_3O^+ precursor 197

- 7.70 Time profiles for all rats with at 59 (acetone) and 77 (acetone with water cluster), using the H_3O^+ precursor. Odd numbered rats are in the left column, and even numbered rats are in the right column. 198
- 7.71 Time profiles for all rats at masses 58, 60 and 78, corresponding to TMA, using the H_3O^+ precursor. Odd numbered rats are in the left column, and even numbered rats are in the right column. . . . 199
- 7.72 Time profiles for all rats at mass 79, using the H_3O^+ precursor. *Red*: samples used in ARF classification; *Magenta*: samples used in Cannulation classification; *Green*: samples used in Normal classification. Odd numbered rats are in the left column, and even numbered rats are in the right column. 200
- 7.73 Classification between *normal* and *ARF* over all masses using the O_2^+ precursor 201
- 7.74 Biomarker identification in the *normal* and *ARF* states using the O_2^+ precursor 201
- 7.75 *Left*: Probability density profile for Mass 43 obtained via normal and ARF datasets with the O_2^+ precursor. *Right*: Log-odds probability density profile for identification of biomarkers is shown, right. 202
- 7.76 *Left*: Probability density profile for Mass 58 obtained via normal and ARF datasets with the O_2^+ precursor. *Right*: Log-odds probability density profile for identification of biomarkers is shown, right. 202
- 7.77 *Left*: Probability density profile for Mass 59 obtained via normal and ARF datasets with the O_2^+ precursor. 203
- 7.78 *Left*: Probability density profile for Mass 77 obtained via normal and ARF datasets with the O_2^+ precursor. 203
- 7.79 Classification between *post-cannulation* and *post-ARF* over all masses using the O_2^+ precursor 203

- 7.80 Biomarker identification between *post-cannulation* and *post-ARF* over all masses using the O_2^+ precursor 204
- 7.81 Time profiles for all rats at mass 43, using the O_2^+ precursor. Odd numbered rats are in the left column, and even numbered rats are in the right column. 205
- 7.82 Time profiles for all rats at mass 58, using the O_2^+ precursor. Odd numbered rats are in the left column, and even numbered rats are in the right column. 206
- 7.83 Time profiles for all rats at mass 59, using the O_2^+ precursor. Odd numbered rats are in the left column, and even numbered rats are in the right column. 207
- 7.84 Time profiles for all rats at mass 77, using the O_2^+ precursor. . . 208

List of Tables

2.1	VOCs detected by SPME in samples of N_2 stored in Tedlar bags for 24 hours (modified from Parker et al. [2003])	15
2.2	Biomarkers for H_3O^+ classification in validation study	27
2.3	Biomarkers for classification in Dialysis study	32
3.1	Artificially generated longitudinal concentration data for an individual mass, over repeat dialysis sessions in 3 patients	41
3.2	Dialysis Study I Sample Population	49
3.3	Dialysis Study I Correlation	53
3.4	Dialysis Study I Top Biomarkers	54
4.1	Dialysis Study II Sample Population	66
4.2	Dialysis Study II Correlation of breath ammonia, TMA and acetone with gold standard BUN and Creatine values	68
4.3	Dialysis Study II Top Biomarkers with H_3O^+ precursor	71
4.4	Dialysis Study II Top Biomarkers with NO^+ precursor	78
4.5	Dialysis Study II Top Biomarkers with O_2^+ precursor	83
5.1	GFR Monitoring Schedule	101

5.2	Rat Anaesthetic and Analgesic Drug Regime	102
5.3	Pilot Studies on ARF	104
5.4	Clearance Experiments	109
5.5	Bolus Experiments	112
6.1	Parameters for Volume of Distribution Determination	134
7.1	Grace: Inulin clearance parameters	151
7.2	Heidi: Inulin clearance parameters	154
7.3	Isis: Inulin clearance parameters	158
7.4	Maya: Inulin clearance parameters	161
7.5	Nell: Inulin clearance parameters	164
7.6	Olive: Inulin clearance Parameters	166
7.7	Paige: Inulin clearance parameters	171
7.8	Quin: Inulin clearance parameters	174
7.9	Sophie: Inulin clearance parameters	176
7.10	Tosca: Inulin clearance parameters	180
7.11	Ula: Inulin clearance parameters	183
7.12	Top Biomarkers of ARF with the H_3O^+ precursor.	192
7.13	Top Biomarkers of ARF with the O_2^+ precursor	202

Nomenclature

SIFT-MS	Selected Ion Flow Tube - Mass Spectrometry
VOC	Volatile Organic Compound
SIM	Selected Ion Monitoring
SPME	Solid Phase Micro-extraction
PTFE	Polytetrafluoroethylene
ROC	Receiver Operating Characteristic
GUI	Graphical User Interface
URR	Urea Reduction Ratio
BUN	Blood Urea Nitrogen
GC-MS	Gas Chromatography Mass Spectrometry
TMA	Trimethylamine
TMNO	Trimethylamine-N-oxide
AOL	Area of OverLap
ARR	Ammonia Reduction Ratio
PCT	Proximal Convolutud Tubule
DCT	Distal Convolutud Tubule
GFR	Glomerular Filtration Rate
ADH	Antidiuretic hormone
ARF	Acute Renal Failure
AKI	Acute Kidney Injury
CKD	Chronic Kidney Disease
CRF	Chronic Renal Failure
Na^+	Sodium ion
Cl^-	Chloride ion
K^+	Potassium ion
H^+	Hydrogen ion
NH_3	Ammonia
NH_4^+	Ammonium ion
AUC	Area Under Curve
SC	Subcutaneous
IV	Intravenous
IP	Intraperitoneal
TER	Tubular Extraction Rate
CIM	Constant Infusion Method
PAH	p-aminohippuric acid

Abstract

Selected Ion Flow Tube-Mass Spectrometry (SIFT-MS) is an analytical measurement technology for the real-time quantification of volatile organic compounds in gaseous samples. This technology has current and potential applications in a wide variety of industries, although the focus of this research is in medical science. In this field, SIFT-MS has potential as a diagnostic device, capable of determining the presence of a particular disease or condition. In addition, SIFT-MS can be used to monitor the progression of a disease state, or predict deviations from expected behaviour. Lastly, SIFT-MS can be used for the identification of biomarkers of a particular disease state. All these possibilities are available non-invasively and in real-time, by analysing breath samples.

SIFT-MS produces an extensive amount of data, requiring specific mathematical methods to identify *biomarker* masses that differ significantly between populations or time-points. Two classification methods are presented for the analysis of SIFT-MS mass scan data. The first method is a cross-sectional classification model, intended to differentiate between the diseased and non-diseased state. This model was validated in a simple test case. The second method is a longitudinal classification model, intended to identify key *biomarkers* that change over time, or in response to treatment.

Both of these classification models were validated in 2 clinical trials, investigating renal function in humans and rats. The first clinical trial monitored changes in breath ammonia, TMA and acetone concentrations over the course of dialysis treatment. Correlations with the current gold standard plasma creatinine, and blood urea nitrogen were reported. Finally, biomarkers of renal function were identified that change predictably over the course of treatment.

The second trial induced acute renal failure in rats, and monitored the change

in renal function observed during recovery. For comparison and validation of the result, a 2-compartment model was developed for estimating renal function via a bolus injection of a radio-labelled inulin tracer, and was compared with the current gold standard plasma creatinine measurement, modified using the Cockcroft-Gault equation for rats. These two methods were compared with SIFT-MS monitoring of breath analytes, to examine the potential for non-invasive biomarkers of kidney function. Results show good promise for the non-invasive, real-time monitoring of breath analytes for diagnosis and monitoring of kidney function, and, potentially, other disease states.

Chapter 1

Introduction

Selected Ion Flow Tube - Mass Spectrometry (SIFT-MS) is a relatively new analytical technique for the real-time quantification of volatile organic compounds (VOCs) [Smith and Spanel, 1996]; [Freeman and McEwan, 2002]. It relies on chemical ionisation of trace gas molecules in air or breath samples introduced into a helium carrier using H_3O^+ , NO^+ and/or $O_2^{+\bullet}$ precursor ions. Hence, the identity of a sample VOC can be found by comparison of the mass of the product ions with an existing database. The sensitivity of the instrument is currently around 100 parts per trillion in real time [Milligan et al., 2007].

The SIFT-MS system can offer unique capability in the early and rapid detection of a wide variety of diseases, infectious bacteria and patient conditions. This outcome can be achieved by creating disease and normal mass scan datasets using SIFT-MS, and developing classification methods to identify an unknown patient as normal or diseased. By identifying which masses (and therefore VOCs) contribute most strongly towards a successful classification, biomarkers for a particular disease state can be discovered. Longitudinal studies can also be carried out in which the concentration of a particular analyte can be monitored over time to potentially infer the progression of the disease state.

1.1 Selected Ion Flow Tube-Mass Spectrometry

1.1.1 Principles of SIFT-MS

SIFT-MS is a quantitative mass spectrometric method that exploits the chemical ionisation of positively charged precursor ions that react with the VOCs in an air or breath sample. In particular, H_3O^+ , NO^+ and $O_2^{+\bullet}$ precursor ions are typically used, since they do not react with the main compounds found in air or breath (N_2 , O_2 , CO_2 and Ar). The process steps are summarised below, and illustrated in Figure 1.1.

1. Precursor ions are generated by passing water vapour through a microwave discharge;
2. A quadrupole mass filter is used to select the required precursor ion based on its mass/charge ratio;
3. The precursor ion is injected into a fast-flowing inert carrier gas (helium), which carries the precursor ion along the flow tube;
4. The sample for analysis is introduced into the flow tube via a calibrated capillary;
5. The precursor ion reacts with the VOCs from the sample to form product ions;
6. A representative proportion of the product ions then pass through a small orifice at the downstream end of the flow tube, and into a differentially pumped quadrupole mass spectrometer that filters ions according to mass;
7. The selected product ions pass to the channeltron particle multiplier/detector where they are counted;
8. Knowledge of the concentration of the product ion and the rate of the reaction allows identification and quantification of the reactant compound.

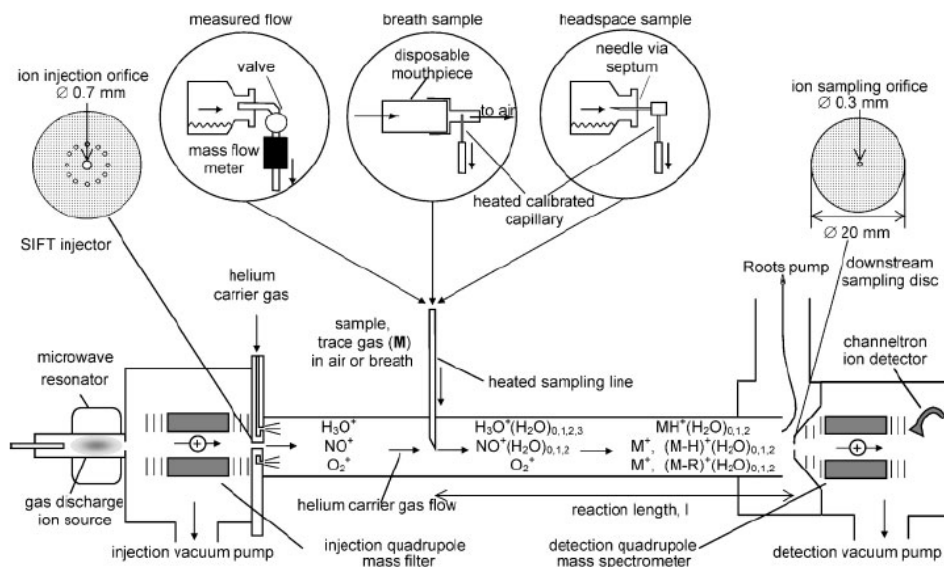


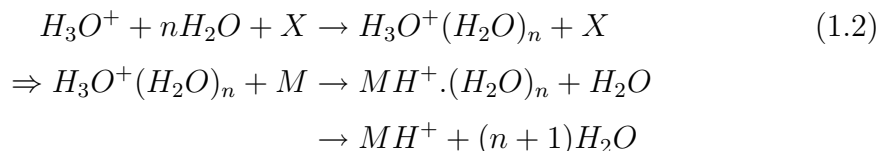
Figure 1.1 Schematic of analyte quantification via SIFT-MS, Smith and Spanel [2005]

1.1.2 Precursor Reactions

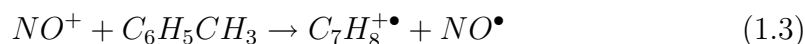
Most organic ions, M , react with the H_3O^+ precursor via simple proton transfer, in which usually only 1 or 2 product ions are formed.



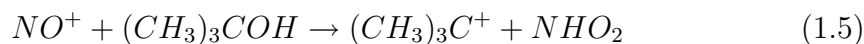
When ions are introduced into humid air, such as in breath, clustering of the water molecules occurs. The reaction thus takes place as described by Equation (1.2), where X is a third body such as a helium atom that stabilises the cluster ion against unimolecular dissociation, [Smith and Spanel, 2005]. When the hydrated precursor ion encounters a reactant trace gas molecule such as ammonia, the reaction proceeds via *ligand switching*, as seen in the second part of Equation (1.2). If this reaction is sufficiently exothermic, the water molecule can be released, leaving the protonated reactant ion, as seen in the third part of Equation (1.2).



Reactions with the NO^+ precursor also produce only 1 or 2 product ions. However, they can proceed via charge transfer, ion transfer, or ion-molecule association. Aromatic hydrocarbons react with the NO^+ precursor via charge transfer, as seen in Equation (1.3) for toluene, to produce radical cations.



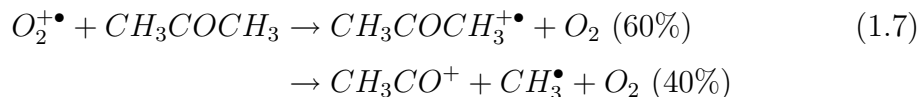
Hydride ion transfer occurs when saturated aldehydes, ethers and primary or secondary alcohols react with the NO^+ precursor, as seen in Equation (1.4) for acetaldehyde. Hydroxide ion transfer occurs in reactions of NO^+ with tertiary alcohols, as shown for 2-methyl-2-propanol in Equation (1.5).



Ion-molecule association is very common in reactions between NO^+ and polar organic molecules such as carboxylic acids, esters, and ketones [Smith and Spanel, 2005]. The reaction proceeds as shown in Equation 1.6 for acetone, where helium acts as a stabilising body.



Most reactions with the $O_2^{+\bullet}$ precursor proceed via non-dissociative charge transfer to produce the radical cation $M^{+\bullet}$, or by dissociative charge transfer to produce 2 or more product ions, as seen in Equation (1.7) for acetone.



Analysis of trace gas molecules by all three precursors described above helps ensure the correct identification and quantification of the reactant. If the reactant reacts with 2 or more precursors, then it should appear in each mass spectra in the same concentration. From these analyses and a (correct) identification, analysis for biomarkers and/or clinical diagnosis can begin.

1.1.3 Mode of Operation

SIFT-MS can operate in 2 different modes:

1. Selected Ion Monitoring Mode (SIM)
2. Mass Scan Mode

SIM scans are performed to determine the concentration of a specific analyte(s) with known product masses, using one or more of the 3 precursor ions described. In this mode, only the precursor ion masses and product ions masses are counted with the channeltron particle multiplier/detector. Each of these masses is counted for 25-50ms before counting the next mass. A typical SIM scan output is shown in Figure 1.2.

In mass scan mode, all masses, or more accurately, mass-to-charge ratios, m/z , over the instrument detection range are sampled and counted with a chosen precursor. In the experiments described in this thesis, all 3 precursor ions were utilised in the reactions, and masses 10-180m/z were monitored. Results are given in counts per second, a concentration obtained from the counts recorded by the channeltron multiplier over a specified sampling interval.

Identification of the product peaks in the mass spectra are then related back to the reactant sample. Mass scan mode is useful when the identity of the VOCs

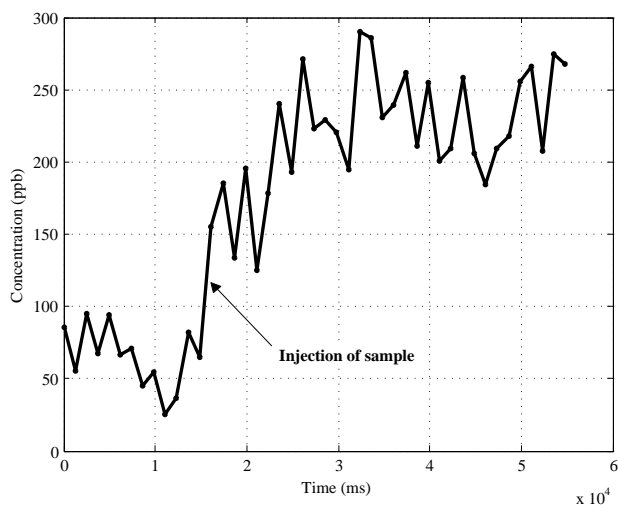


Figure 1.2 Typical SIM scan output

in a sample are unknown, for example, when investigating new biomarkers of a particular disease state. A typical mass scan output is shown in Figure 1.3.

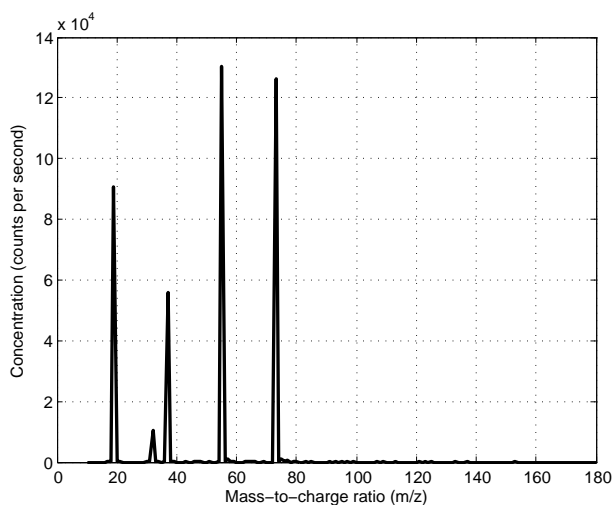


Figure 1.3 Typical mass scan output

1.1.4 Applications

SIFT-MS has current and potential applications in many different industries, such as environmental, agriculture and food sciences, homeland security, and medical science. Specific applications include:

- Monitoring VOC exposure in the home or workplace, such as polluted town air, cigarette smoke, industry solvents, etc.

- VOC identification in exhaust gases
- VOC identification in soil samples for the farming industry
- Monitoring food freshness and preparation
- Detection of illicit substances such as drugs, tobacco or explosives for Homeland Security
- Medical applications such as detection of diseases, infectious bacteria, cancers, and other patient conditions
- Monitoring medical conditions such as the progression of a disease state, or the onset of renal failure

This research focuses on the use of SIFT-MS as a tool for identifying and monitoring disease states by analysis of breath analytes. Such an application requires knowledge of the physiology and biochemistry of respiration in the mammalian lung, which is discussed further in the next section.

1.2 Breath Sampling

1.2.1 Breath Metabolites

Human breath consists mostly of nitrogen, oxygen, carbon dioxide, water and inert gases, as well as numerous trace components, such as ammonia, acetone, isoprene and ethanol. Volatile substances in breath can be absorbed from the environment, or generated endogenously from the body as a product of metabolism. Hence, in a healthy subject, concentrations of these trace elements in breath are dependent on environmental conditions, and can vary with circadian rhythms, exercise, and food consumption.

For example, acetone, produced by lipid peroxidation, is increased during fasting. Another example is isoprene, produced during cholesterol synthesis, which is at a maximum level around 6am, and at a minimum at 6pm [Miekisch et al., 2004]. Finally, levels of ammonia are increased after a high-protein red meat meal. These examples briefly show the potential range of possibilities for

disease diagnosis and monitoring, as well as the potential for confounding variation.

Certain disease states can interfere with the biochemical balance in the body, resulting in measurable changes in blood chemistry. Gas exchange between the blood, lung epithelia and alveolar gas means that analytes measured in breath contain readily accessible information about a subjects physiological state. For example, ammonia levels increase significantly during hepatic or renal impairment, when removal of ammonia from the blood via conversion to urea or via excretion is limited. However, as noted, such levels may be skewed due to diet or other factors, presenting a difficult classification and diagnosis problem.

1.2.2 Respiratory Physiology

Air enters the lungs through the oral cavity or nasal passages, which join in the pharynx. The pharynx gives rise to the trachea, which is supported by cartilage rings to prevent collapse as the pressure changes during the breathing cycle. The trachea subdivides to form bronchi and bronchioles, which branch repeatedly, leading eventually to terminal and respiratory bronchioles that are directly connected to alveoli. Alveoli are surrounded by a dense capillary network, providing a site for gas exchange. Substances diffusing into the blood, must cross an aqueous film, or *surfactant*, the alveolar epithelial cells, an interstitial space, and the endothelial cells of the blood capillaries. The structure of the gas exchange surface is shown in Figure 1.4 [Purves et al., 1995].

Three types of cell make up the lung epithelium:

- Type I cells are squamous epithelial cells with a thin, plate-like structure;
- Type II cells have a laminated body within the cell and surface villi for producing surfactants;
- Type III cells are rich in mitochondria and have numerous microvilli for active transport from the lung fluid.

Ventilation occurs by contraction of the diaphragm, which increases the volume of the thoracic and pleural cavities, creating a negative pressure which causes

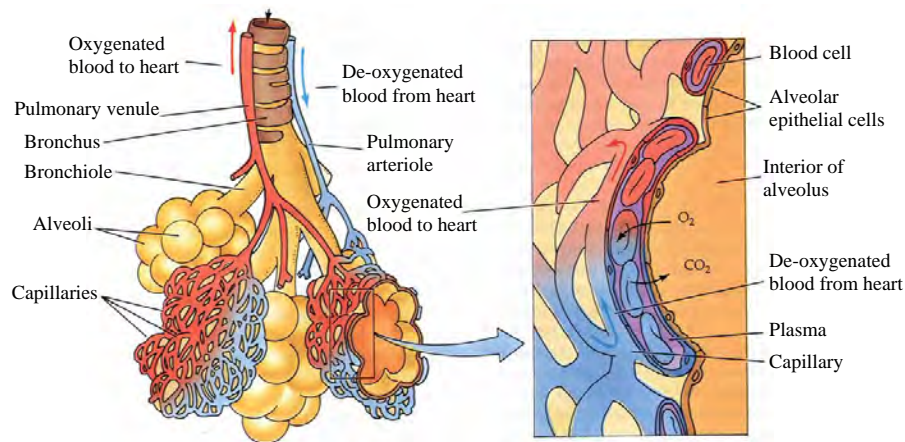


Figure 1.4 Gas exchange in the alveolus, Purves et al. [1995]

the lungs to expand as air is drawn in. When the diaphragm stops contracting, the lungs recoil forcing the air back out. Hence, inhalation is an active process, with muscle contraction, and exhalation is usually passive [Randall et al., 2002]. Details of the anatomy are shown in Figure 1.5.

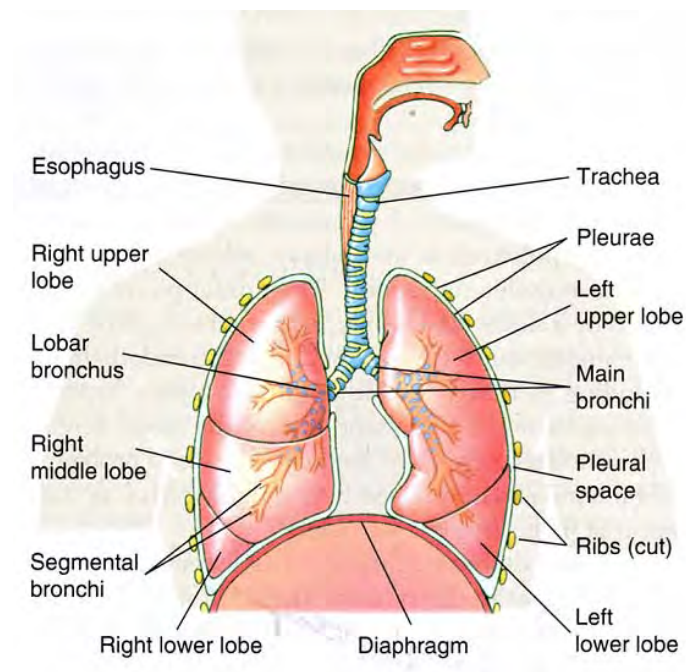


Figure 1.5 Lung anatomy with detail of pleural cavity, Randall et al. [2002]

The amount of air moved into and out of the lungs at each breath is referred to as the *tidal volume*. To reach the gas exchange surface in the alveoli, air must

first pass through the upper airways not involved in gas transfer. At the end of inhalation, the air in these tubes will be filled with ambient air, and will be the first to be exhaled with the next breath. This volume of air not involved in gas transfer is called the *anatomic deadspace*. In addition, some air may be supplied to non-functional alveoli, or alveoli perfused at too high a rate, thus increasing the volume of air not involved in gas exchange. This latter volume is referred to as the *physiological deadspace*, and it includes the anatomic deadspace.

The rate of blood perfusion of the respiratory surface depends on the requirements of the tissues for gas transfer and the gas-transport capacity of the blood. To ensure sufficient oxygen delivery to the respiratory surface to saturate the blood with oxygen, the rate of ventilation, \dot{V}_A , is optimised to the rate of perfusion, \dot{Q} . Any changes in the oxygen content of the inspired air or in the oxygen requirements of the tissues, requires a corresponding change in ventilation. Hence, oxygen is provided to the respiratory surface at such a rate as the blood is capable of carrying it away, thus promoting diffusion across the surface at the highest possible rate.

As well as carrying oxygen to the tissues, blood must also carry away metabolic wastes such as carbon dioxide and other VOCs. Such wastes can be excreted by the kidneys in the urine, through the skin by sweating, via the digestive system in the faeces, or by exhalation in the breath. Excretion and uptake of VOCs in the breath depends on the ventilation/perfusion ratio in the lung, and the concentration gradients of the substances across the respiratory surface. Therefore, a subject breathing in an environment with a low VOC concentration will measure different alveolar VOC concentrations to the same subject breathing in a high VOC environment because of the different concentration gradient for diffusion. Similarly, when the external VOC concentration becomes higher than the endogenous concentration, the VOC will diffuse into blood instead of appearing in the exhaled breath.

1.2.3 Sample Collection

Breath can be sampled either directly into the SIFT-MS instrument, or collected remotely in Tedlar bags and brought to the machine. Remote collection has its difficulties, particularly when measuring water-soluble compounds like ammonia

which readily adsorb onto the bag surface. This effect can be moderated by keeping the bag warm [Neilson, 2006], however, direct breath remains the preferred method of breath sampling when possible.

The 2 other main variations in breath sampling relate to the fraction of breath that is collected. Most studies use mixed expiratory sampling, which includes deadspace air and hence artificially dilutes (for endogenous substances), or concentrates (for external contaminants) the measured analyte. However, if background air is also sampled, and the deadspace volume can be accounted for, the alveolar fraction of the breath can be extracted. The other main approach is alveolar sampling, in which the first (deadspace) portion of the breath is discarded, and only the alveolar air exchanged from the blood, is sampled [Lad, 2006].

To determine endogenous concentrations of analytes, correction for background inspiratory air must be performed. Several different approaches have been adopted to account for this problem, however the validity of subtraction methods is questionable [Schubert et al., 2005]. Such approaches include:

- Assuming a constant background analyte concentration, and performing a relative, rather than an absolute, analysis;
- Subtracting inspired air from expired air concentrations to determine *alveolar gradients* [Phillips, 1997];
- Eliminating ambient concentrations by having the subject breath pure air prior to measurement [Risby and Sehnert, 1999].

1.3 Summary

SIFT-MS is a quantitative mass spectrometric method that exploits the chemical ionisation of positively charged precursor ions that react with the VOCs in gaseous samples. Certain disease states can interfere with the biochemical balance in the body, resulting in measurable changes in blood chemistry, which can be measured in the breath using SIFT-MS. Hence, the SIFT-MS system can offer unique capability in the early and rapid detection of a wide variety of diseases,

infectious bacteria and patient conditions, as well as the ability to monitor the progression of a disease state, non-invasively, and in real-time.

Chapter 2

Cross-sectional Classification Models

This chapter presents new classification methods and tests for the classification of cross-sectional sets of mass scan data. This process is broken into four steps:

1. Pre-processing to remove noise from the raw mass scan data;
2. Creating probability distributions for each of the 2 test classification groups;
3. Obtaining a classification and a reliability measure for that classification;
4. Identifying useful biomarkers.

Two cases are presented. The first case is a simple direct validation study that aimed to differentiate *dry* nitrogen samples from *wet* nitrogen samples to clearly test and prove the methods developed. The second case study used the classification model in a clinical setting to determine the differences between dialysis patients before and after treatment, thus examining kidney function, which has direct application in critical care and drug dosing, among other arenas. The classification model is also able to determine which masses are most useful in this classification and therefore those compounds that act as biomarkers for kidney function.

2.1 Experimental Design

The study methodology is divided into three sections:

1. Experimental design for the validation study and dialysis case study;
2. Pre-processing of mass scan raw data;
3. Statistical analysis, including classification, prediction error estimation, reliability, and sensitivity/specificity analysis.

They are presented in this order to construct the algorithms and methods in the context of these case studies. This approach can better highlight specific processing issues that arise.

2.1.1 Validation Study: Nitrogen (N_2) in Tedlar Bags

A simple test study was conducted to validate the statistical classification model developed. Samples of gas collected remotely from the SIFT-MS device were collected in a Tedlar bag composed of polyvinyl fluoride, which the manufacturers claim to be chemically inert [Dupont, 1995]. Before using the tedlar bags, the manufacturers recommend flushing the bags with purified air or nitrogen.

However, other studies have shown using Solid Phase Micro-extraction (SPME) that the Tedlar bags emit 15 different VOCs into samples stored in the bags for 24 hours, as detailed in Table 2.1 [Parker et al., 2003]. Phenol, acetone and acetic acid are persistently present even after purging the bags with purified nitrogen [Parker et al., 2003]. Hence, one outcome of this study is determining the ability to detect and account for these effects in this common form of breath sample collection.

In this study, multiple samples of N_2 in Tedlar bags were tested by performing mass scans over a range of 10-150 atomic mass units (amu) using the precursors H_3O^+ , NO^+ and O_2^+ . The bags were new and all flushed at least three times prior to testing directly from the bag.

N_2 in Tedlar bags was also vented to sterile glass bottles filled with water using a sterile stainless steel needle, and a polytetrafluoroethylene (PTFE) permeable septum. The gas in the bottles was then tested by performing mass scans. 25 *Dry Nitrogen* samples (Nitrogen in a tedlar bag) and 25 *Wet Nitrogen* samples (Nitrogen in tedlar bag vented to bottle) were tested.

Table 2.1 VOCs detected by SPME in samples of N_2 stored in Tedlar bags for 24 hours (modified from Parker et al. [2003])

VOC	No Purge	Purge Bag
Acetone	+	+
Acetaldehyde	+	-
Decane	+	-
Octane	+	-
Toluene	+	-
2,3-Butadione	+	-
Ethyl Benzene	+	-
Nonane	+	-
Isoprene	+	-
Tridecane	+	-
Dodecane	+	-
Tetradecane	+	-
Acetic Acid	+	+
Pentadecane	+	-
Phenol	+	+

The specific objectives of this first study were as follows:

1. Determine what VOCs are added when venting to a Tedlar bag containing purified nitrogen;
2. Determine which VOCs or their water clusters increase or diminish when passed through sterile glass bottles filled with water;
3. Differentiate between the 2 test groups;
4. Validate the classifier using this presumably *clean* system.

2.1.2 Case Study: Dialysis

One patient with impaired kidney function underwent dialysis treatment on seven separate occasions, with breath mass scans performed one hour into the treatment and after 4 hours of treatment. These mass scans were taken over a range of 10-150 amu using the precursors H_3O^+ , NO^+ and O_2^+ . The specific aims of this study were:

- To develop probability density profiles for the pre- and post-dialysis groups;
- To determine if it is possible to reliably differentiate between the 2 sample groups;
- To identify possible new biomarkers for kidney function.

The study was based on the fact that dialysis takes a patient from a state of kidney failure to functional status, *artificially*. Hence, dialysis provides a built in comparison for analysing kidney function and investigating potential biomarkers. Ethics approval was granted as part of a larger separate trial for the collection and use of this data by the Upper South B Regional Ethics Committee (URB/05/12/178).

2.2 Pre-processing

In this study, SIFT-MS mass scans measured the concentration of products at each 0.2 of a mass unit to obtain results. However, there was a significant amount of machine and precursor noise, as shown in Figures 2.1 and 2.2. The data contained noise, anomalous electronic signals produced by the SIFT-MS instrument, which had to be filtered before analysis.

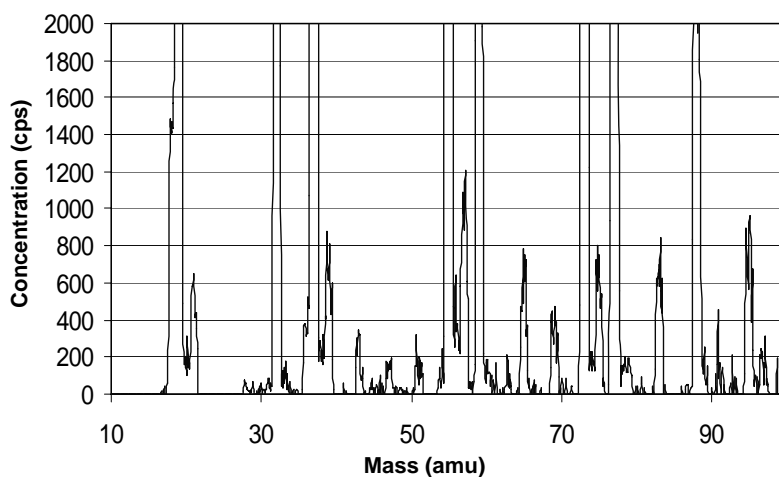


Figure 2.1 Typical mass scan over 10-100 amu

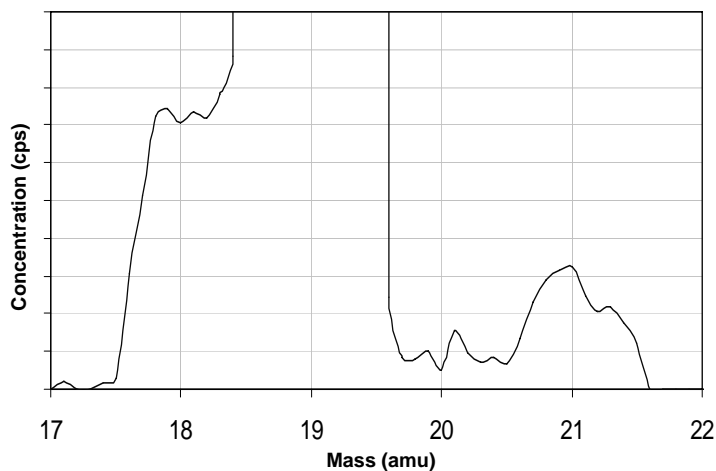


Figure 2.2 Typical mass scan focused on 17-22amu

Any filtering process must result in an accurate reading of concentration at each whole number mass unit. A normal peak from a mass scan is usually centred around a whole mass unit. At half its height, it is usually 0.8 mass units wide, as shown in Figure 2.3. However, as seen in Figure 2.4, this definition of a standard peak is not always seen in practice, except at masses with large concentrations. The actual peaks in Figure 2.4 are considered to be at the positions indicated by crosses.

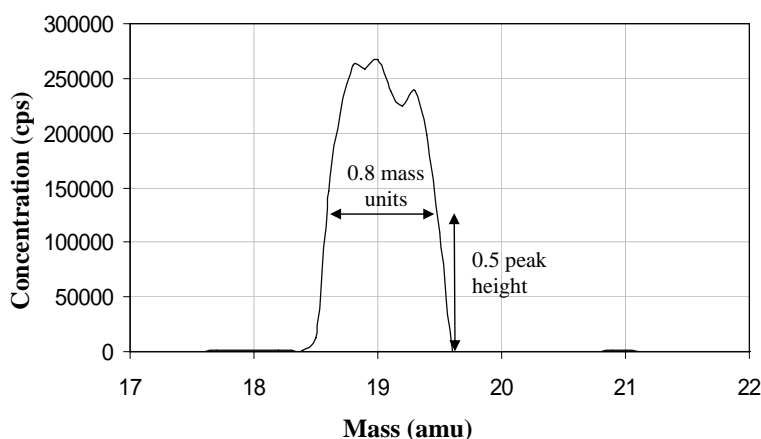


Figure 2.3 Typical mass scan peak at 19 amu

Figure 2.4 was obtained using the H_3O^+ precursor. The H_3O^+ precursor has mass 19, thus accounting for the off-the-scale peak seen at this mass. The H_3O^+ precursor will also generate peaks at masses 37, 55 and 73, due to H_3O^+ forming clusters with H_2O in humid samples. A large concentration of precursor ion is used in SIFT-MS, to ensure complete reaction of the VOCs in the sample.

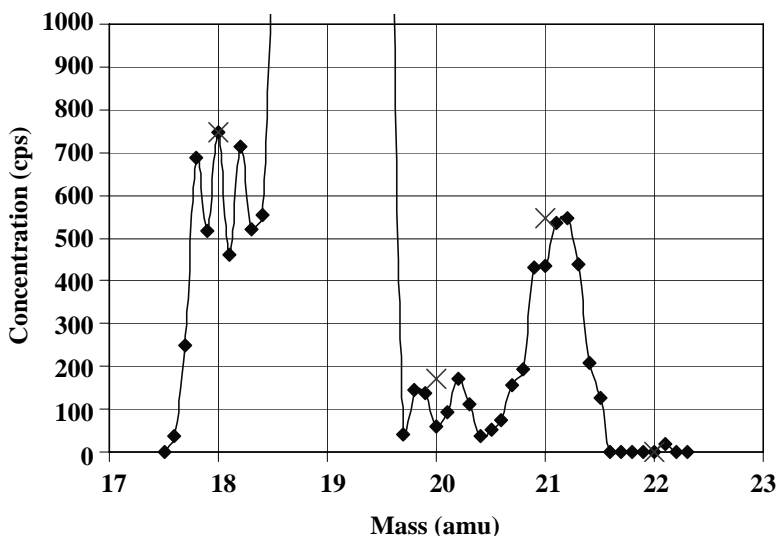


Figure 2.4 Noise in the raw data at 18, 20 and 21 amu

Thus, the mass scan should always show maximum peaks at the precursor-related masses. A non-precursor related peak that is greater than the maximum precursor peak indicates an erroneous result because the particular VOC present in the sample would have swamped the precursor signal. Because a different amount of precursor ion is used for each reaction, mass scans were normalised to the sum of the product precursor peaks. For example, for the H_3O^+ precursor, this normalising factor is the sum of the peaks at masses 19, 37, 55 and 73.

Pre-processing steps for mass scan data therefore involve:

- Normalising each data point to the sum of the precursor ion peaks, allowing comparisons to be drawn between samples that receive a different amount of reactant precursor ion;
- Removing large erroneous peaks greater than the precursor peaks, and data points that cause a peak to rise too sharply. This process eliminates machine errors, and samples with high concentrations of compounds that swamp the precursor signal;
- Finding the tip of the peak, by looking at concentrations before and after the whole mass unit, and determining if a suspected peak exists in reality by considering the number of non-zero readings within 1 mass unit;
- Reducing the concentration matrix to include only whole mass values for analysis.

2.3 Statistical Classification Analysis

The goal of classification is to compare the concentrations obtained at each mass in the mass scan of an unknown sample with a previously established database. The end result is a classification of the unknown sample into one of the database groups. As well as the classification, an estimate of the prediction error and a reliability measure are required. Biomarkers can be obtained by determining which masses in the mass scan were most useful in classifying the unknown sample.

2.3.1 Classification

Kernel density estimates are used for the classification of mass scan data [Hastie and Friedman, 2001]. Test datasets of known classification are used to develop probability density profiles for each of the two datasets: Groups j and k . An unknown sample is then tested against the datasets, with the result being a classification into either Group j or Group k . In a diagnostic analysis, j and k would be the non-disease and diseased states.

After pre-processing the raw mass scan data, each sample is left with a vector of concentration values at each whole mass unit. With mass scans performed over a range of 10-150 amu, the resulting vector has length 141. For each mass, a mixed distribution made up of a kernel density and a Dirac delta function is used to develop a density profile from each group using each sample's concentration value at that mass. Stronger, generally smoother density profiles are obtained with greater numbers of different mass scan samples. Typical density profiles fitted to two datasets are shown in Figure 2.5.

When a mass scan from an unknown sample is obtained, pre-processing is used to create a vector of concentration values at each of the 141 masses. For each mass, the probability densities for groups j and k at the concentration of the unknown sample are compared. Let x_0 denote the concentration of the unknown sample at the given mass, and $f_j(x_0)$ and $f_k(x_0)$ denote the probability densities of groups j and k respectively at the concentration of the unknown sample. This situation is illustrated in Figure 2.6, where the plot shown would be useful for classification as given by the minimal overlap of distributions.

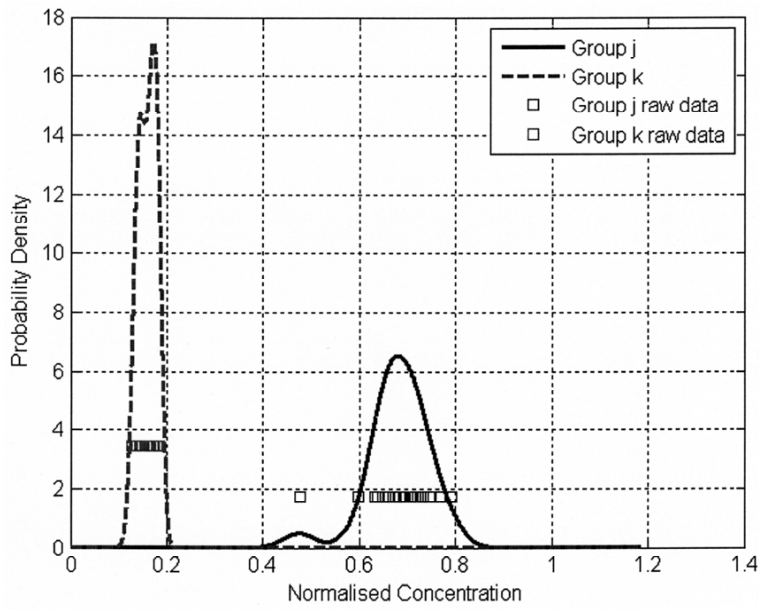


Figure 2.5 Fitting Probability density profiles to raw data

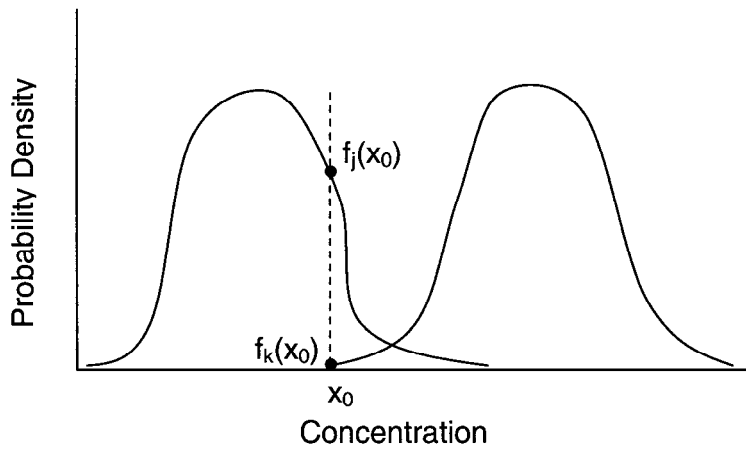


Figure 2.6 Probability densities for a given mass

For each mass, Equation (2.1) gives the probability of the given sample being from Group j , given the concentration value obtained at that mass is x_0 .

$$\hat{Pr}(j|x_0) = \frac{\hat{\pi}_j \hat{f}_j(x_0)}{\hat{\pi}_k \hat{f}_k(x_0) + \hat{\pi}_j \hat{f}_j(x_0)} \quad (2.1)$$

where $\hat{\pi}$ is the prior probability (prior) of the sample being in that group. When no information is known about the data, the priors ($\hat{\pi}_j, \hat{\pi}_k$) are set to 0.5. If the ratio in Equation (2.1) is greater than a specified threshold, q , then the sample is classified as being in the numerator group (Group j), otherwise it is classified as being in Group k .

The log-odds ratio is defined as the natural log of the probability of a group j classification divided a group k classification, Equation (2.2).

$$\text{Log - odds Ratio} = \ln \frac{\hat{P}r(j|x_0)}{\hat{P}r(k|x_0)} \quad (2.2)$$

Equation (2.2) can be broken down into Equation (2.3), where the log-odds ratios are effectively summed over all masses to result in a final log-odds ratio over all masses.

$$\ln \frac{\hat{P}r(j|x_0)}{\hat{P}r(k|x_0)} = \ln \frac{\hat{\pi}_j}{\hat{\pi}_k} + \sum_{m=1}^m \ln \frac{\hat{f}_j(x_{0\cdot}, m)}{\hat{f}_k(x_{0\cdot}, m)} \quad (2.3)$$

A final log-odds ratio greater than $\ln[q/(1-q)]$, where q is the threshold described above, and indicates the sample is in the numerator group (Group j). Otherwise, it is in the denominator group (Group k).

2.3.2 Bootstrap Method for Estimating Prediction Error

Once density profiles have been created for the two datasets, the stratified bootstrap method is used to estimate the prediction error of the classification model. Bootstrap samples are created by choosing with replacement from the original sample until a bootstrap sample is created that is the same size as the original sample [Hastie and Friedman, 2001]. For example, if Group j contained 20 sets of mass scans, and Group k contained 25 sets of mass scans, each bootstrap sample would contain 20 Group j scans and 25 Group k scans, with some scans included more than once, and some completely left out as the sampling was done with replacement. This process is repeated B times, producing B bootstrap datasets,

where B is sufficiently large to ensure that all patients (of 45 in the example above) are left out of at least 1 bootstrap dataset.

The bootstrap estimate of the classification error is defined in Equation (2.4),

$$\hat{E}^{(1)} = \frac{1}{N} \sum_{i=1}^N \frac{1}{|C^{-i}|} \sum_{b \in |C^{-i}|} I(\hat{y}^b(x_i) \neq y_i) \quad (2.4)$$

where N is the total number of samples, $|C^{-i}|$ is the number of bootstrap samples that do not contain sample i , \hat{y}^b is the classifier trained on bootstrap sample b , $I(\hat{y}^b(x_i) \neq y_i)$ equals 1 if sample i is classified incorrectly and 0 otherwise.

The kernel classifier is trained with bootstrap datasets that do not contain sample i as the training set, and then use sample i as the test set. This process is repeated for all bootstrap samples that do not contain sample i . The total of incorrect classifications is summed and divided by the number of bootstrap samples that did not contain sample i . This overall process is repeated for each sample. It concludes by averaging the number of incorrect classifications over all samples, giving $\hat{E}^{(1)}$.

The bootstrap estimate is biased upward as an estimate of the true classification error, suffering from training-set-size bias. This limitation is alleviated using the 0.632 estimator [Hastie and Friedman, 2001], as defined in Equation (2.5),

$$\hat{E}^{(0.632)} = 0.368\bar{e} + 0.632\hat{E}^{(1)} \quad (2.5)$$

where \bar{e} is the biased error, calculated using all the data as the training set, and testing each sample against this set. The biased error, \bar{e} , is biased downward of the true error because the test data is also found in the training set. Hence, Equation (2.5) is combination of the upwards biased $\hat{E}^{(1)}$ and the downwards biased \bar{e} .

The overall prediction error should be compared with random classification,

for which the overall error rate, P^* , is given by Equation (2.6).

$$P^* = p_j(1 - \hat{\pi}_j) + (1 - p_j)\hat{\pi}_j \quad (2.6)$$

With a prior probability set at 0.5, the overall error rate for a random classifier is 50%, regardless of group proportions (p_j and p_k) in the sample.

2.3.3 Reliability

Density profiles of the log-odds ratio obtained from the bootstrap method can be plotted for each group, and a reliability curve can be generated, as shown in Equation (2.7) and Figure 2.7,

$$\hat{Pr}(S = j|\lambda) = \frac{\hat{f}(\lambda|S = j)\hat{Pr}(S = j)}{\hat{f}(\lambda|S = j)\hat{Pr}(S = j) + \hat{f}(\lambda|S = k)\hat{Pr}(S = k)} \quad (2.7)$$

where $\hat{Pr}(S = j|\lambda)$ is the probability of the sample, S , being in Group j given the log-odds ratio, λ ; $\hat{f}(\lambda|S = j)$ is the probability of the log-odds ratio for Group j ; $\hat{Pr}(S = j)$ is the probability that the sample is in group j .

This situation is illustrated in Figure 2.7. A good dataset will have minimal overlap between the two density profiles because where a significant difference is detected between sample groups, a large log-odds ratio should always be obtained. As shown in Figure 2.7, if an unknown sample is classified with a log-odds ratio, λ , of +200, one can be approximately 100% certain that classification is correct. This result occurs because at a log-odds ratio of +200, the probability that the sample is in group k is approximately 0. Therefore, by Equation 2.7, the reliability reduces to unity, represented here as 100% on the Reliability scale. However, the log-odds ratio obtained where group j and k profiles overlap (at approximately -5 in Figure 2.7), has a reliability of 50%, indicating an equally likely probability of correct as incorrect classification.

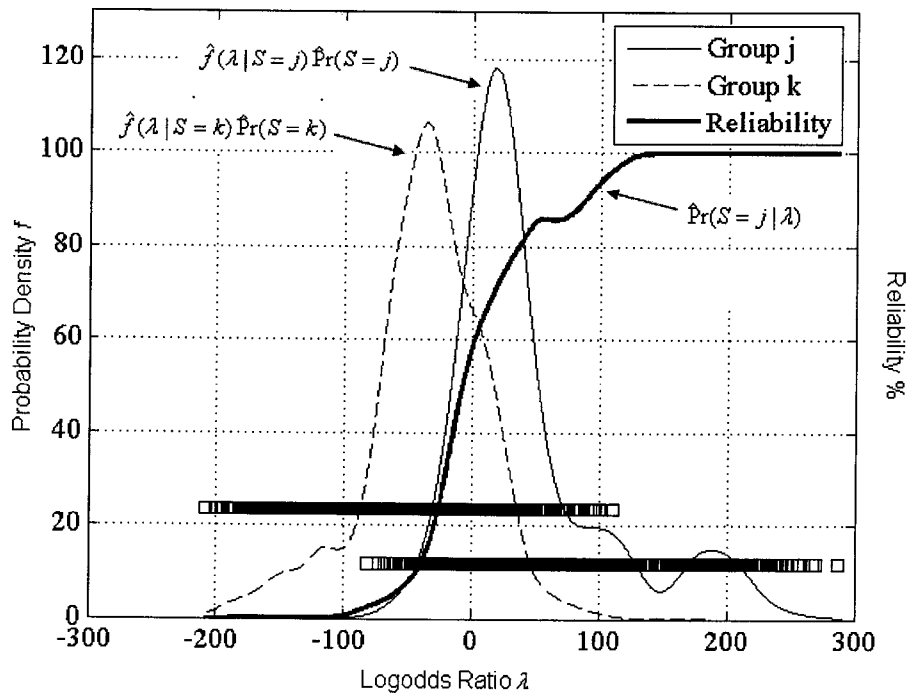


Figure 2.7 Reliability curve showing the reliability of a given classification based on its log-odds value

2.3.4 Biomarkers

Any sample to be classified, is done so by summing the log-odds ratios at each mass, to give an overall log-odds ratio. With a classification threshold of 0 for Equation (2.3), a positive log-odds ratio indicates the sample is in Group j , and a negative log-odds ratio indicates that the sample is in Group k . The two examples shown in Figure 2.8 display relatively large log-odds ratios, with each mass's ratio generally consistently displaying the same sign (positive or negative). Therefore, one can be confident of the final classification. Those masses that contribute large log-odds ratios towards the final classification may be considered as useful biomarkers.

Biomarkers are found by determining which masses have log-odds density profiles with minimal overlap. Density profiles are created, as described previously, for each individual mass. The area of overlap is shaded in the schematic of Figure 2.9 and is calculated using the Trapezoid Rule. The masses with the smallest areas of overlap are the best biomarkers.

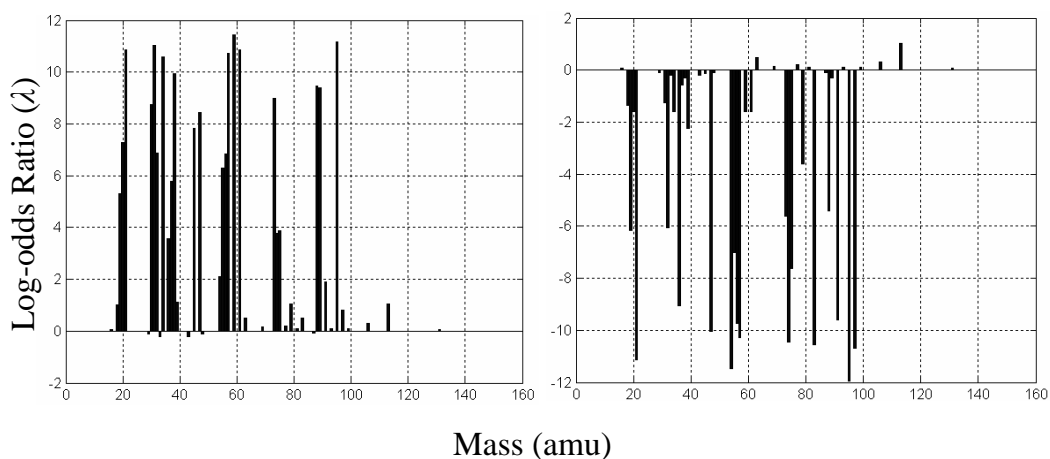


Figure 2.8 Piecewise classification, showing the log-odds ratios obtained at each mass that combine to form the final log-odds ratio used for classification

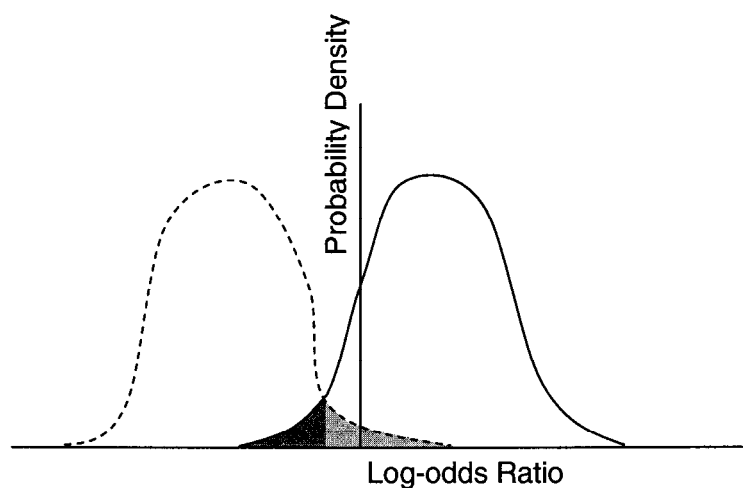


Figure 2.9 Biomarkers schematic with Log-odds ratio

2.4 Results and Discussion

2.4.1 Validation Study: Nitrogen in Tedlar Bags

Using the 0.632 bootstrap estimator method to estimate prediction error, with $B = 500$ bootstrap samples, there was 0% classification error over all precursors, indicating excellent differentiation between sample groups. All results for this validation study are shown for the H_3O^+ precursor only. In addition, concentrations shown were normalised to the sum of the precursor value, as described in Section 2.2.

2.4.1.1 Probability Density Profiles

Density profiles including log-odds ratios are shown in Figure 2.10 for a selection of the biomarkers noted in the next section. Excellent separation was evident between density profiles for the two groups. Note that the squares indicate the concentrations of the raw data, and the corresponding curves are the probability density profiles fitted to that raw data. It is clear in the figure that the raw data is well separated between the two groups being compared.

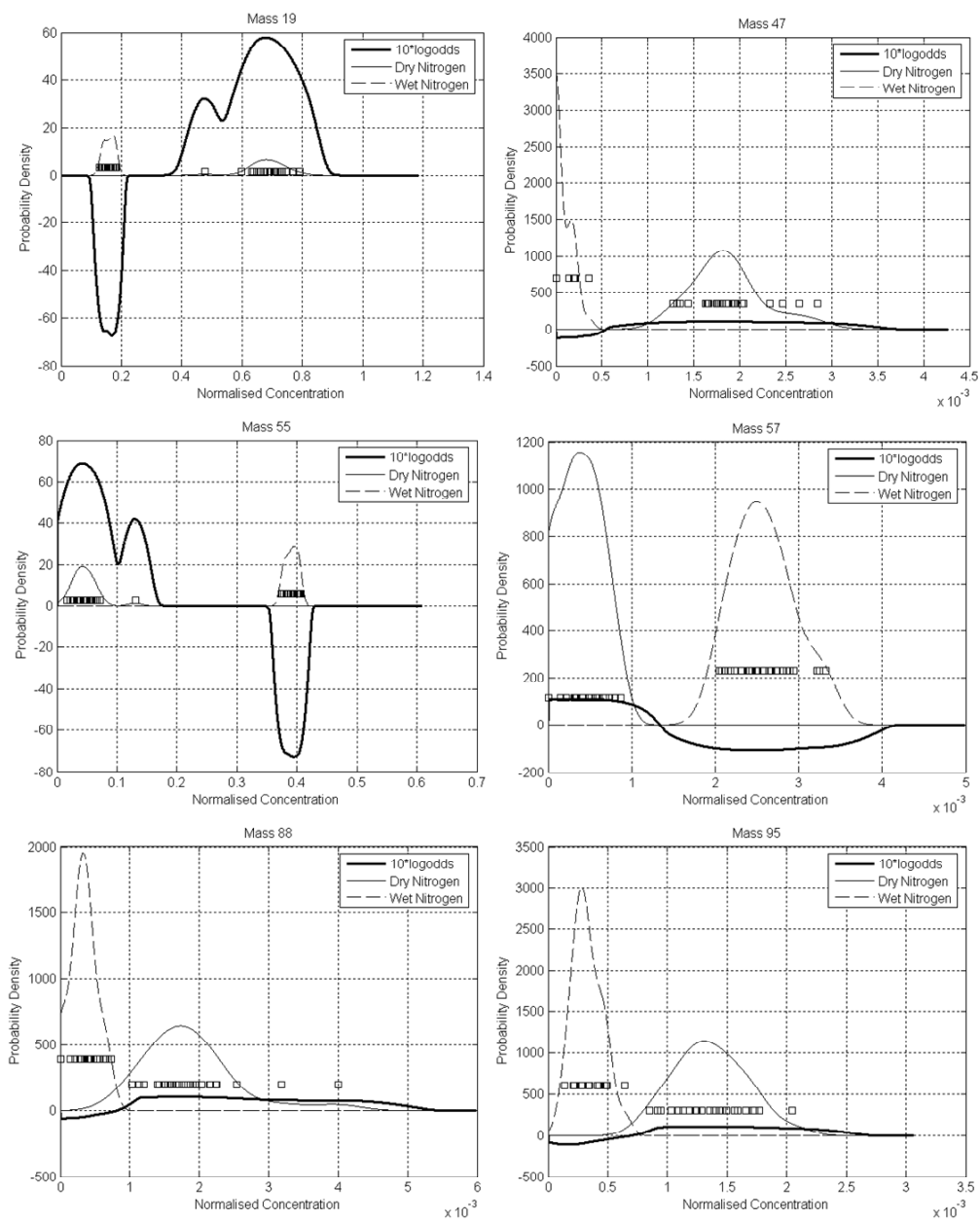


Figure 2.10 Selected probability density profiles using H_3O^+ precursor

2.4.1.2 Biomarkers

The classification model found that the masses indicated in Table 2.2 were most useful in aiding towards a correct classification, and they are ranked with the best biomarker having the smallest overlap between density profiles. Their log-odds density profiles are shown in Figure 2.11.

Table 2.2 Biomarkers for H_3O^+ classification in validation study

Precursor ions	Product Mass	Explanation	Rank
H_3O^+ and its water clusters	19, 55, 73	The wet nitrogen group showed much higher concentrations at masses 55 (and 73), corresponding to the water clusters of H_3O^+ .	3, 4, 5
Isotope of H_3O^+ and its water clusters	57	The wet nitrogen group showed higher concentrations at mass 57, corresponding to the water clusters of H_3O^+ , (and lower concentrations at mass 21, corresponding to the mass of the H_3O^+ isotope (D_3O^+) with no water cluster).	2
$C_4H_9NO.H^+$ (product of N,N-dimethyl acetamide)	88	Due to the solubility of $C_4H_9NO.H^+$ in water, by venting the nitrogen through the water bottle, the concentration at mass 88 decreased dramatically, (and increased at mass 106 - its water cluster).	7
$C_6H_6O.H^+$ (product of phenol)	95	Due to the solubility of $C_6H_6O.H^+$ in water, by venting the nitrogen through the water bottle, the concentration at mass 95 decreased dramatically.	6
$N_2H^+.H_2O$	47	Water cluster of N_2H more prevalent when N_2 passes through water.	1

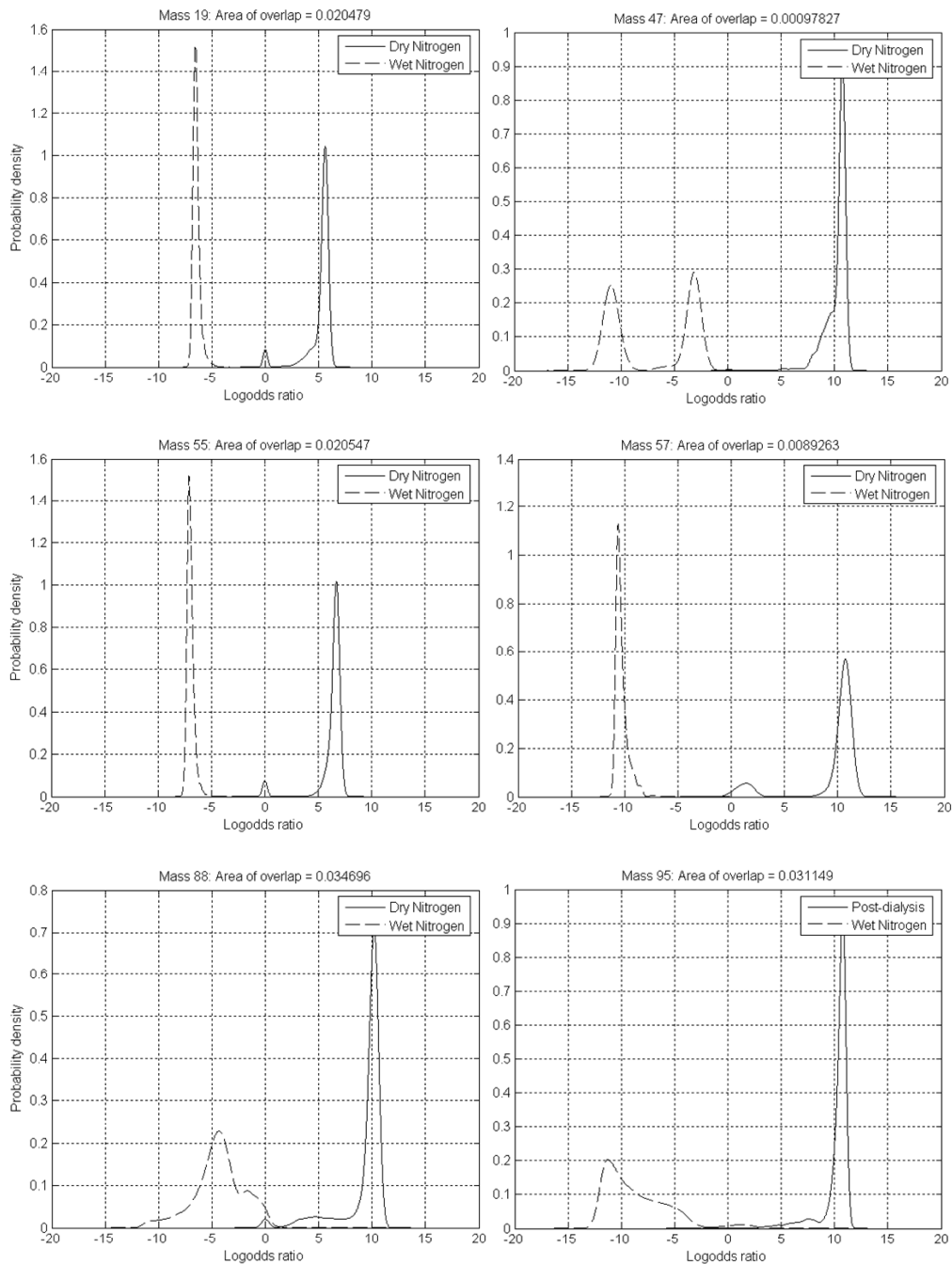


Figure 2.11 Log-odds density profiles for biomarker selection in validation study

2.4.1.3 Reliability

Density profiles were created from the log-odds values obtained from each bootstrap sample entry for each of the test groups, with Dry Nitrogen represented as Group j and Wet Nitrogen represented as Group k . It is observed in Figure

2.12 that there is excellent separation between the two profiles, with consistently large log-odds values obtained. The relatively flat gradient of the reliability curve indicates that if an unknown sample were classified with a small log-odds ratio, the reliability of correct classification would be relatively low. The model is highly sensitive and highly specific, with an area under the Receiver Operating Characteristic (ROC) curve of 0.9998, as shown in Figure 2.13.

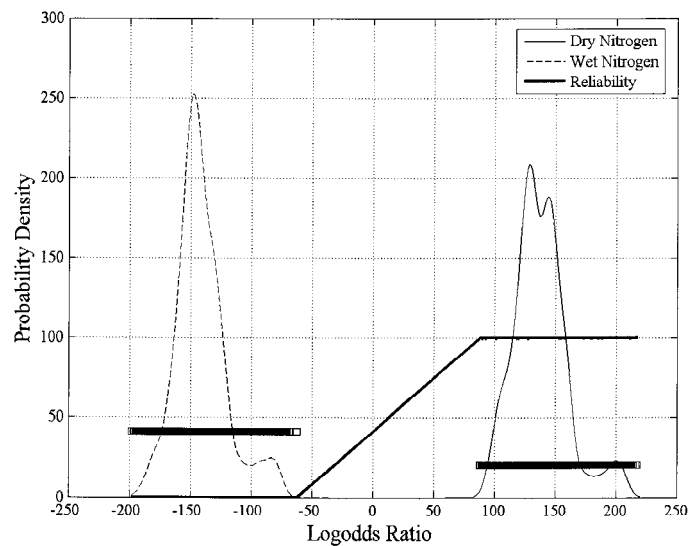


Figure 2.12 Reliability curve for validation study classification model

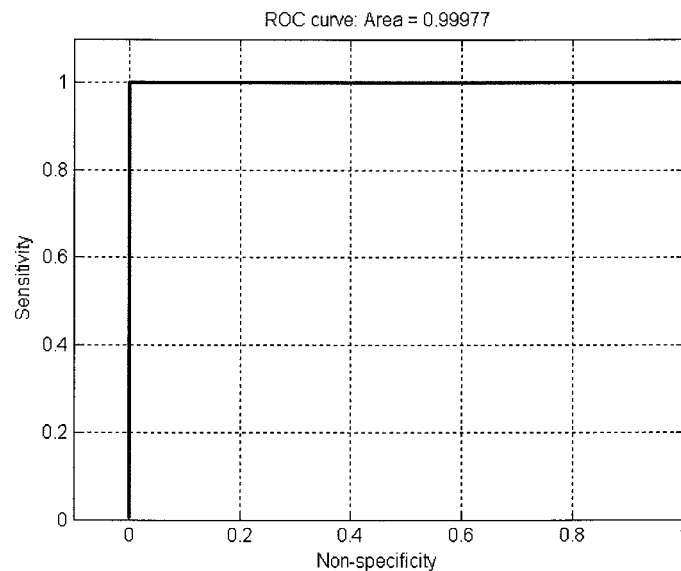


Figure 2.13 ROC curve for validation study classification model

It should be noted that these ideal results are the expectation for this model classification validation study. Hence, the results match the expectation set in designing this test. Thus, the method appears suitable for a more rigorous test.

2.4.2 Dialysis Proof-Of-Concept Study

Seven repeat mass scans were taken of one dialysis patient over the course of 6 months. These mass scans were taken at time $t = 1$ hour and $t = 4$ hours into dialysis treatment. Mass scans were analysed for key biomarkers that aid in a classification between the pre and post -dialysis datasets. A sample size of seven was much smaller than desired, but sufficient to test the classifier concept.

With $B = 1000$ using the H_3O^+ precursor, the overall prediction error was estimated at 11.2%, with error in classifying pre-dialysis readings contributing 16.7%, error in classifying post-dialysis readings contributing 18.8%, and biased error contributing 0%. Due to the equal sample sizes in the pre and post dialysis groups and the zero biased error, the overall estimated prediction error in Equation (2.5) reduces to 0.632 x average of the pre and post dialysis errors. Using the NO^+ precursor, the overall prediction error was 26.0%, with pre-dialysis, post-dialysis, and biased errors contributing 19.3%, 46.4%, and 14.3%, respectively. Using the O_2^+ precursor, the overall prediction error was 18.2%, with pre-dialysis, post-dialysis, and biased errors contributing 19.8%, 37.8%, and 0%, respectively.

2.4.2.1 Probability Density Profiles

Density profiles including log-odds ratios are shown in Figure 2.14 for a selection of the biomarkers indicated in the following section. It can be seen that the density profiles were relatively strong for the 4-hour dialysis group (Group j), because after dialysis treatment, levels of ammonia (masses 18, 36 and 54) and other VOCs fall to normal levels. Depending on factors such as diet and the length of time since the last dialysis treatment, VOC levels can vary dramatically prior to treatment, as seen by the spread of data in the 1-hour dialysis group (Group k).

Note that the density profiles of the 1 hour data at mass 89 and the 4 hour data at mass 35 are undistinguishable in the figure. This issue occurs because all repeat mass scans had the same zero concentration reading for these masses at those time points, and the density profiles are therefore spikes on the y axis. Overall, it should be observed that the result is considerably less *clean* than the

Nitrogen validation study. Note that all density profiles are shown for the H_3O^+ precursor only.

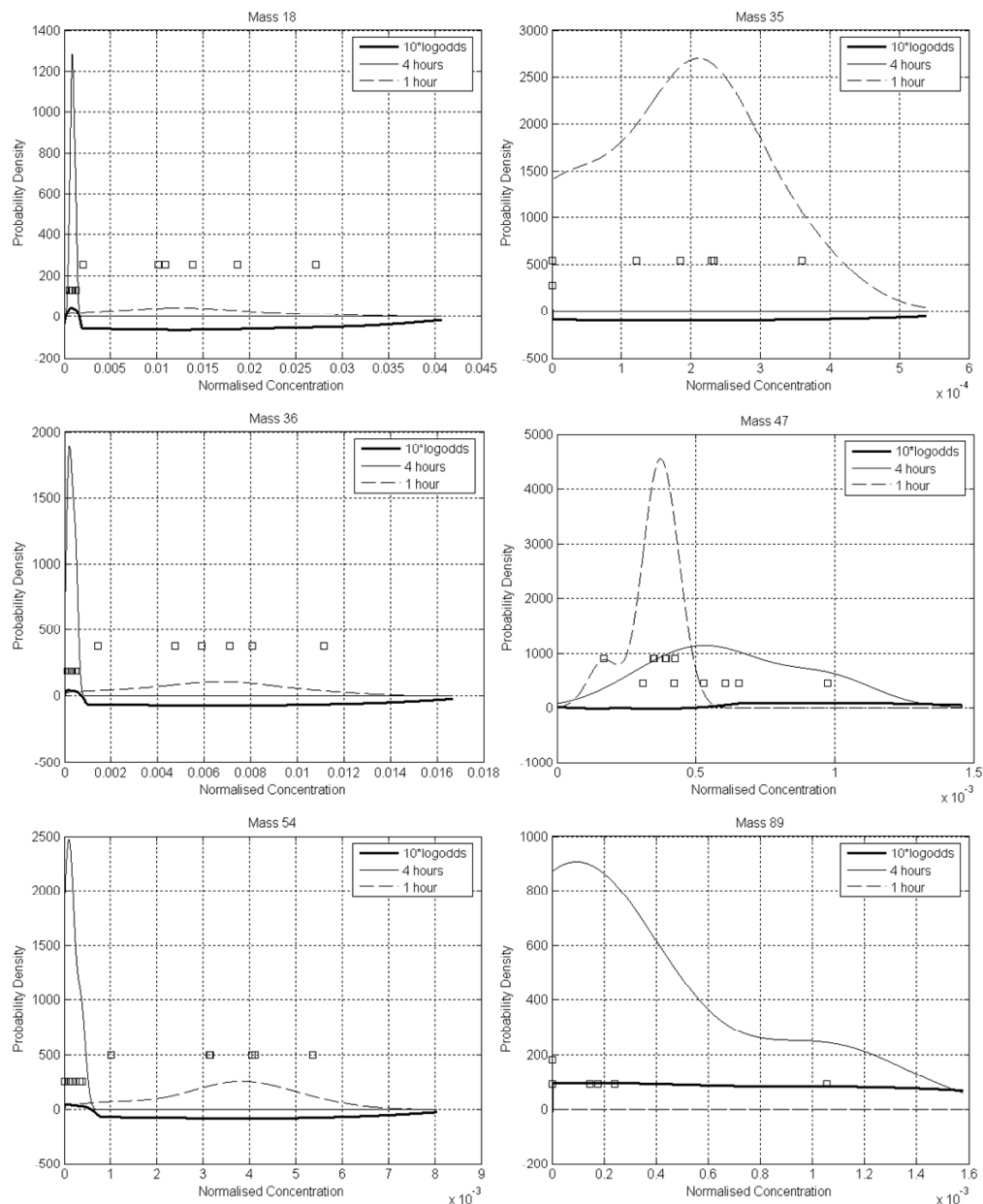


Figure 2.14 Probability density profiles obtained using H_3O^+ precursor on dialysis concentration data

2.4.2.2 Biomarkers

The classification model found that the masses indicated in Table 2.3 were most useful in aiding towards a correct classification, and they are ranked accordingly.

A selection of their log-odds density profiles obtained using the H_3O^+ precursor are shown in Figure 2.15. Note that smoother profiles would be obtained with a greater sample size than what was available in this limited clinical proof-of-concept test case.

It is observed that masses relating to ammonia and its water clusters are most useful in distinguishing between pre- and post- dialysis datasets. This result is expected since it is well documented that ammonia concentration is seen to decrease during dialysis treatment [Narasimhan et al., 2001], as further evidenced by the fact that it is the urea reduction ratio (URR) that is used to measure dialysis efficacy.

Table 2.3 Biomarkers for classification in Dialysis study

Precursor ions	Product Mass	Explanation	Rank
H_3O^+	18, 36, 54	Ammonia and its water clusters	2, 1, 5
	35, 17	Unknown	3, 4
	89	Acetaldehyde	6
	47	Ethanol	7
NO^+	18, 36	Ammonia	2,3
	47	Unknown	1
O_2^+	53	Ammonia, isoprene	1
	17, 18, 35, 36, 53, 54	Ammonia and clusters	4,3,6,5,1,2
	77, 58	Acetone	7,8

2.4.2.3 Reliability

Density profiles were created from the log-odds values obtained from each bootstrap sample entry for each of the test groups. Post-dialysis (4 hours) was represented as Group j and Pre-dialysis (1 hour) was represented as Group k . It is observed in Figure 2.16 that there was a much greater overlap in the two density profiles compared with the Nitrogen validation study, and an absolute log-odds value of approximately 50 must be obtained to classify with 90% certainty in Figure 2.16. As indicated by the ROC curve in Figure 2.17, the model classified significantly better than random, with an ROC area of 0.89.

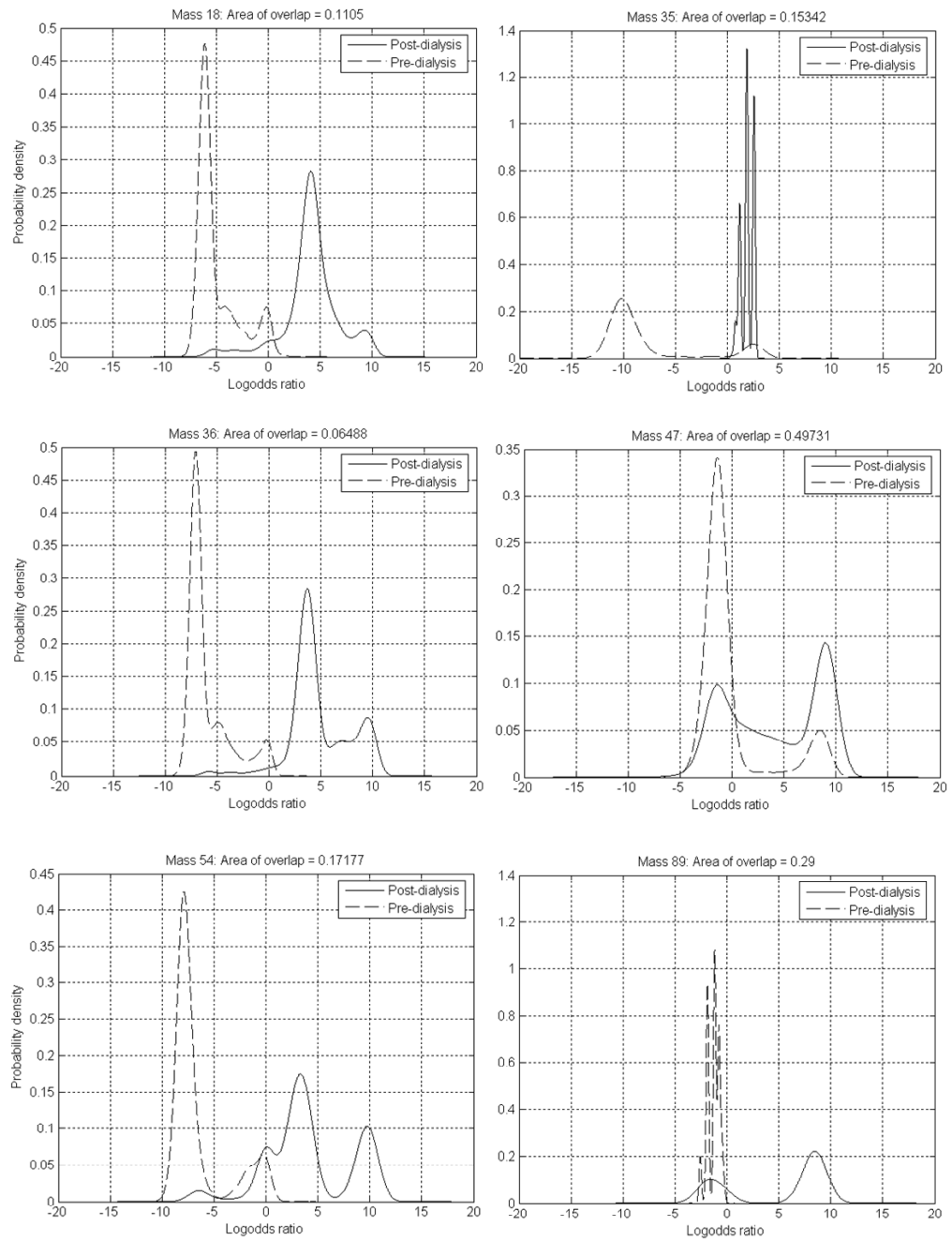


Figure 2.15 Log-odds density profiles for biomarker selection in the dialysis study

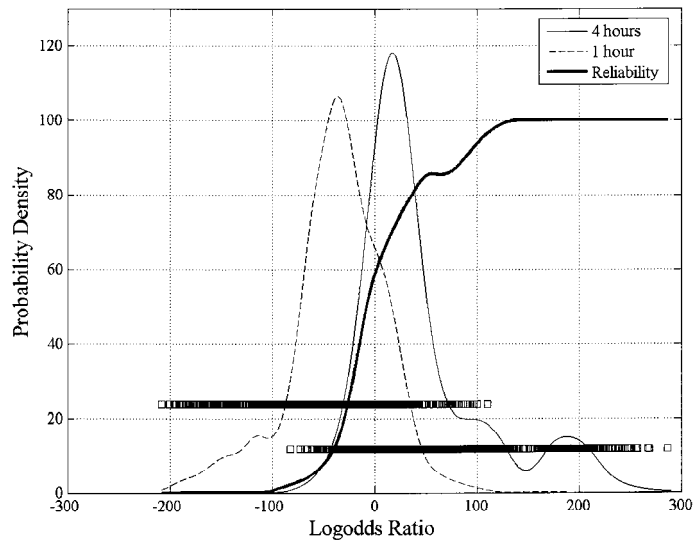


Figure 2.16 Reliability Curve for Dialysis Study Classification Model

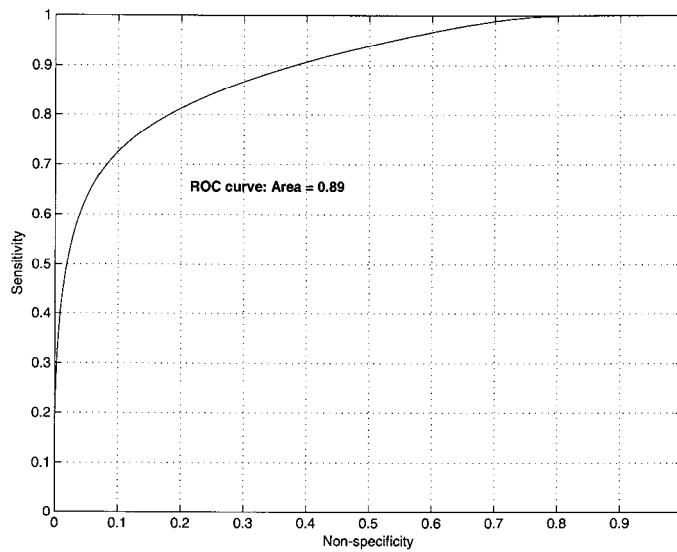


Figure 2.17 ROC Curve for Dialysis Study Classification Model

2.5 Experimental Discussion and Conclusions

A method was presented for the classification of unknown samples. This method was initially validated in a simple study in which saturated nitrogen in tedlar bags was differentiated from dry nitrogen in tedlar bags. There was a 0% predicted

estimation error in classification using the bootstrap error prediction method with 500 bootstrap samples. All expected biomarkers were identified, with the most reliable being $N_2H^+.H_2O$, and isotopes and water clusters of H_3O^+ . In addition, phenol and N,N-dimethyl acetamide products were found to be present in the tedlar bags despite flushing, although levels were reduced in saturated nitrogen samples, presumably related to the solubility of these compounds in water.

Because of the lack of data at low log-odds ratios due to the very distinct sample groups, the reliability curve showed that log-odds ratios of approximately 50 and 70 were required for 90% reliability in classifying saturated and dry nitrogen respectively. However, with 500 bootstrap samples, the minimum log-odds ratios obtained were 70 and 85 for saturated and dry nitrogen respectively. Hence, the high reliability observed. The area under the ROC curve was found to be an expected ideal of 1.00, showing that the classification model was highly sensitive and highly specific in this test case.

After initial validation, the classification model was employed to differentiate patient breath samples after one and four hours of dialysis treatment, thus estimating or measuring kidney function. The sample size of seven was much smaller than desired, but sufficient for this first proof-of-concept. Using 1000 bootstrap samples, estimated prediction errors were found to be 11.2%, 26.0% and 18.2% for the H_3O^+ , NO^+ and O_2^+ precursors, respectively. Density profiles were relatively strong for the 4-hour dialysis group because after dialysis treatment, levels of ammonia and other VOCs fall to normal levels.

Depending on factors such as diet and the length of time since the last dialysis treatment, VOC levels can vary dramatically prior to treatment, as observed by the spread of data in the 1-hour dialysis group. Biomarkers for classification were ammonia, acetaldehyde, ethanol, isoprene and acetone. An absolute log-odds value of approximately 50 must be obtained to classify with 90% certainty. As indicated by the ROC curve, the model classified significantly better than random, with an ROC area of 0.89.

2.6 Classification User Interface

A graphical user interface (GUI) was created in *MATLAB* for use in the classification of cross-sectional sample studies in the Syft laboratory. The GUI is shown in Figure 2.18.

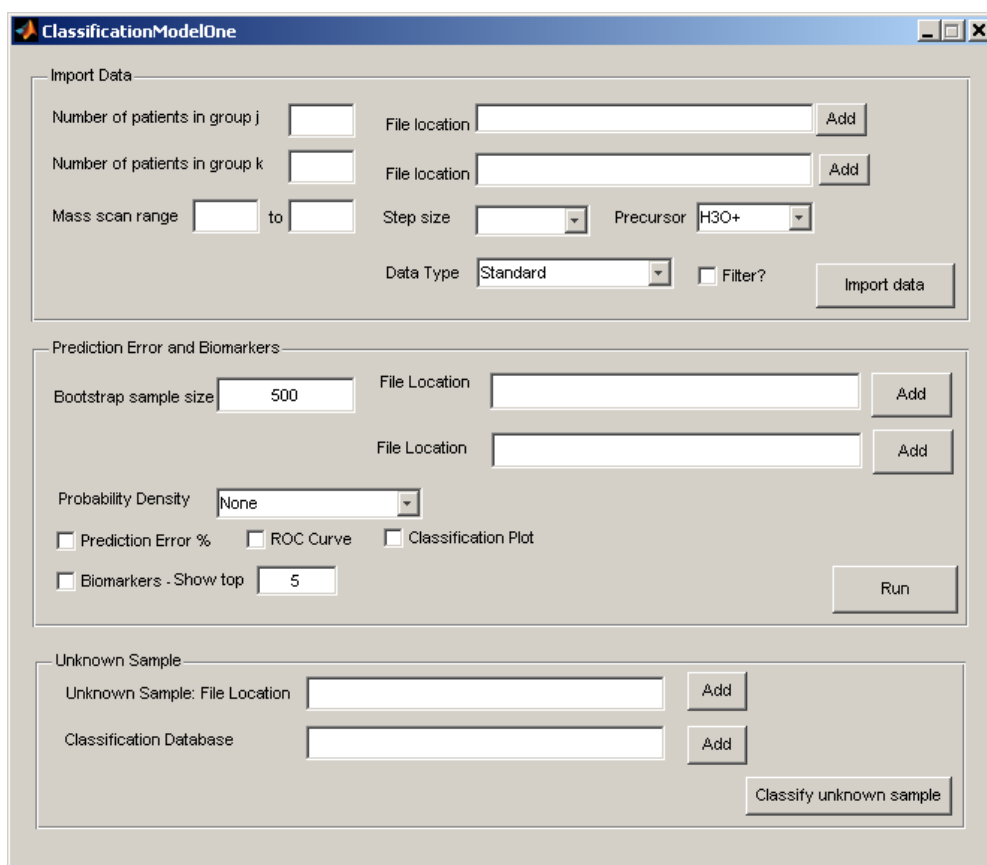


Figure 2.18 Cross-sectional Classification User Interface

The GUI consists of 3 parts:

1. Import Data
2. Prediction Error and Biomarkers
3. Unknown Sample

The *Import Data* block imports data from a specific layout in an excel spreadsheet. The mass scan range (usually 10-180amu) must be specified as well as the step size, which refers to the size mass unit sampled. Options for step size are 0.1 mass unit, 0.2 mass units, or 1 mass unit. However, since the creation of this interface, mass scans are nearly always performed by sampling every whole mass unit. The precursor ion is selected, and the user has the option to filter out the noise, as described in Section 2.2. Lastly, the *Data Type* is selected, where *Standard* refers to a standard cross-sectional classification. The other option is *Longitudinal*, for use in paired datasets, such as the before and after situation in a dialysis trial. Clicking the *Import Data* button imports and sorts the data, storing it as a *.MAT* file.

The *Prediction Errors and Biomarkers* block does just that: determines the prediction error when classifying 2 distinct groups, and identifies the key biomarkers used in that classification. Probability density profiles can be displayed, as selected by the user, and these can be selected either by analyte, by mass, or by top biomarker. For example, the user could decide to see density profiles for all masses associated with ammonia. Alternatively, they could request to see the density profiles of the top n biomarkers. The prediction error, ROC curve, and classification/reliability plot are displayed, if selected by the user.

Unknown Sample allows classification of a single unknown dataset into Group j or Group k , with a determined reliability. A previously established classification database is selected, and the log-odds ratio of the unknown sample is determined. The classification/reliability plot is displayed, hi-lighting the position of the unknown sample, and quoting the reliability of the classification as a percentage.

Chapter 3

Longitudinal Classification Models and Dialysis Study I

The cross-sectional classification model described in the previous chapter is ideal for classifying between two distinct groups: *normal* and *diseased*, where the *normal* datasets are reasonably similar, and the *diseased* datasets express a deviation from that *normal* state. However, when an analysis is performed on longitudinal data, such as for the dialysis proof-of-concept in the previous chapter, the paired nature of the data can be exploited, thus allowing biomarker identification across patient groups.

When monitoring the progression of a disease state, there is no baseline, *normal* starting point (or end-point), and when considering inter-patient populations, one cannot simply take all the *before* samples and classify them against the *after* samples, because, depending on patient specific variables and degree of sickness, starting points and responses to treatment can vary dramatically. In addition, a single patient dataset cannot be considered on its own, because there is usually insufficient data to perform a statistically rigid classification. Hence, an appropriate normalisation method is required to allow interpatient biomarker identification.

This chapter presents a longitudinal classification model, which was validated on a clinical dialysis study.

3.1 Paired Classification Model

3.1.1 Normalisation

The mass scan analysis is interested simply in the magnitude of the relative and absolute change in VOC concentration between two timepoints. Two normalisation methods were considered for the analysis of mass scan data for biomarker detection and evaluation. The first method effectively considers a relative change in VOC concentration. Let C_j refer to the concentration matrix (concentration values at a series of masses) at the healthier timepoint (post-dialysis group in this example), and C_k refer to the concentration matrix at the more unwell timepoint (pre-dialysis group in this example). The data is normalised to twice the average of the two concentrations, as illustrated in Equation (3.1).

$$\begin{aligned} C_{j,norm} &= \frac{C_j}{C_j + C_k} \\ C_{k,norm} &= \frac{C_k}{C_j + C_k} \end{aligned} \quad (3.1)$$

Hence, the concentration data is bounded between $[0 \ 1]$, with values of $C_{k,norm}$ greater than 0.5 representing a decrease in concentration over the course of the dialysis treatment, and values less than 0.5 representing an increase in concentration. This results occurs, because when $C_{k,norm}$ is greater than 0.5, C_k must be greater than C_j , indicating that the analyte concentration *decreases* from C_k to C_j , over the course of dialysis treatment.

The second method effectively considers a normalised absolute change in VOC concentration. This value is measured by shifting the data such that the average of the two timepoint states is at 0. Thus, if the 2 concentrations were 0.2 and 0.4 at sequential time-points C_k and C_j , these values would be replaced by -0.1 and +0.1. This situation is represented in Equation (3.2).

$$\begin{aligned} C_{j,norm} &= \frac{C_j - C_k}{2} \\ C_{k,norm} &= \frac{C_k - C_j}{2} \end{aligned} \quad (3.2)$$

Normalising by Equation (3.2) results in data that is bounded between $(-\infty \infty)$, since C_j and C_k can have any value, and C_j can be less than or greater than C_k . Using this method, a value of $C_{k,norm}$ greater than 0 represents a decrease in concentration over the course of the dialysis treatment, and a value less than 0 represents an increase in concentration. This results occurs because a positive $C_{k,norm}$ indicates that C_k is greater than C_j , such that VOC concentration decreases from C_k in the predialysis state, to C_j in the postdialysis state.

These two normalisation methods allow all patients' data to be combined, thus increasing the sample size for classification, as illustrated by the following example. Consider the artificially generated data in Table 3.1, where concentration data is displayed for 3 patients, DS01-DS03. In this example, DS01 and DS02 have 3 repeat dialysis sessions, and DS03 has 1 dialysis session. Rows *a* and *b* display the raw concentration data obtained for a single mass value measured for all patient sessions. It is observed that one sample (DS02-3) shows an increase in concentration from C_k to C_j , while the rest show a decrease. Note also, that the C_j postdialysis concentration for some patients is higher than the C_k predialysis concentration of other patients (DS01-2 and DS03-1). This example is typical of the raw data obtained. Rows *c* and *d*, show the relative change in concentration, calculated using Equation (3.1), and rows *e* and *f* show the absolute change in concentration, calculated using Equation (3.2).

Table 3.1 Artificially generated longitudinal concentration data for an individual mass, over repeat dialysis sessions in 3 patients

	Patient	DS01			DS02			DS03
		Day 1	Day 2	Day 3	Day 1	Day 2	Day 3	Day 1
a	C_k	0.6	0.4	0.5	0.2	0.25	0.15	0.9
b	C_j	0.25	0.2	0.2	0.1	0.15	0.3	0.5
c	$C_{k,rel}$	0.705	0.665	0.715	0.665	0.625	0.335	0.645
d	$C_{j,rel}$	0.295	0.335	0.285	0.335	0.375	0.665	0.355
e	$C_{k,abs}$	0.175	0.1	0.15	0.05	0.05	-0.075	0.2
f	$C_{j,abs}$	-0.175	-0.1	-0.15	-0.05	-0.05	0.075	-0.2

Using the sets of numbers in Table 3.1, Figure 3.1 is obtained, which demonstrates classifier performance using both non-normalised and normalised techniques. The left figure displays probability density profiles derived from the 6 raw concentration datapoints in rows *a* and *b*. The centre figure displays probability density profiles derived from the relative normalisation in rows *c* and *d*.

Lastly, the right figure displays probability density profiles derived from the absolute normalisation data in rows e and f . It is observed that more meaningful results, with greater separation of density profiles between states, can be obtained with a carefully chosen normalisation method. Probability density profiles such as that shown in Figure 3.1, *left*, are not useful for classification or biomarker detection, since the profiles in the pre and post dialysis states overlap significantly. However, the density profiles shown in Figure 3.1 *centre* and *right*, show much better separation and can therefore be much more useful in classification and biomarker identification.

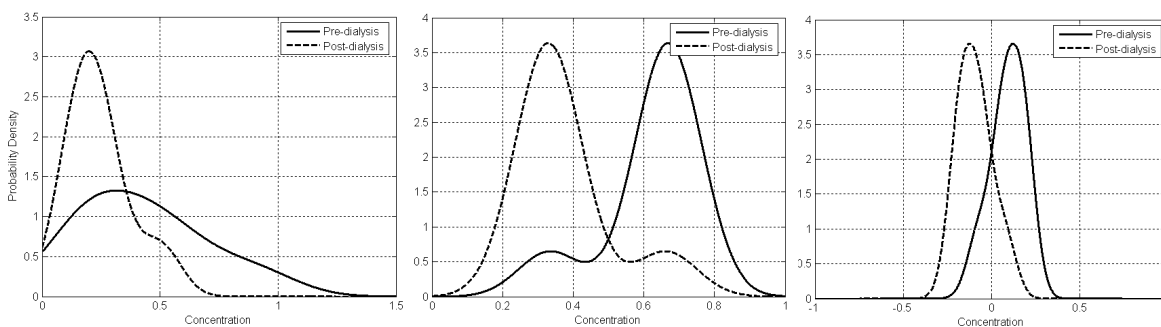


Figure 3.1 Normalisation Illustration: Left-no normalisation; Centre-Relative normalisation, Equation (3.1); Right-Absolute normalisation, Equation (3.2)

Top biomarkers can be identified using the classification method described in Chapter 2 and [Moorhead et al., 2008], with groups $C_{j,norm}$ and $C_{k,norm}$, where the best biomarkers are those with minimal log-odds density overlap profiles.

Classification can be performed using all masses, or using only a selection of masses as biomarkers, thus providing a measure of the sensitivity and specificity for a particular biomarker or group. For example, it is known that masses 18, 36 and 54 found using the H_3O^+ precursor relate to ammonia. Thus, the classifier model can be run using just those 3 masses to determine the sensitivity and specificity of ammonia as a biomarker for this particular disease progression or to monitor dialysis treatment.

3.1.2 Visualisation of Results

To obtain a result that allows easier and more visual identification of biomarkers, a variation to the method presented in Section 3.1.1 is presented, in which biomarkers are displayed visually on an image plot using the difference between

the group datasets. A relative change in analyte concentration, Δrel , is described by Equation (3.3).

$$\Delta rel = \frac{C_j - C_k}{\max(C_j, C_k)} \quad (3.3)$$

Note in Equation (3.3), that an increase in concentration over treatment from C_k to C_j results in a Δrel value that is equal and opposite to the Δrel value obtained for the reciprocal decrease in concentration. The absolute change in analyte concentration, Δabs , is defined:

$$\Delta abs = C_j - C_k \quad (3.4)$$

Density profiles are created from the means of successful bootstrap samples using Δrel and Δabs , and are combined into an image plot. A typical image plot is shown in Figure 3.2. Because the distribution of the mean is the same as the distribution of the raw data [Hastie and Friedman, 2001], the density profiles can be created from the means, making key biomarkers more identifiable in the image plot.

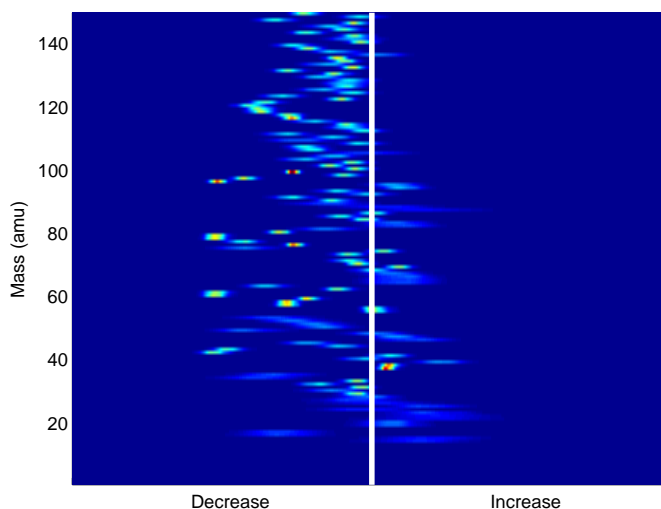


Figure 3.2 Typical image plot highlighting top biomarker masses by probability density profiles created from the mean to standard deviation ratio of subsequent bootstrap datasets.

For comparison, the best biomarkers are those with the highest mean to standard deviation ratio. In an image plot, these good biomarkers are recognised as those masses with a narrow distribution centered far from the increase/decrease interface. A distribution profile that crosses the increase/decrease interface indicates that sometimes the concentration of that mass is seen to increase and other times to decrease, which is not useful in a biomarker.

3.2 Introduction to Dialysis

When renal function is impaired, the kidneys lose the ability to effectively filter and excrete wastes. Hence, salts, water and metabolic wastes accumulate in the blood. The management of chronic renal failure typically involves restricting water, salt and dietary protein intake to reduce the strain on the urinary system by reducing the volume of urine produced and the generation of nitrogenous wastes. Acidosis is commonly encountered with renal failure and can be countered in mild cases with bicarbonate ingestion to restore acid/base homeostasis.

However, if chronic renal failure can not be controlled by diet or drugs, the blood must be artificially filtered using a dialysis machine to regulate the composition of the blood. In haemodialysis, a patient's blood flows through an artificial dialysis chamber consisting of a dialysis fluid separated from the blood by a semipermeable membrane. This membrane contains pores large enough to allow the diffusion of ions, but small enough to prevent plasma proteins escaping. The *cleansed* blood, is then returned to the body. The composition of the dialysis fluid is extremely important, and can be modified for each patient. The concentration of phosphate ions, sulphate ions, urea, creatinine and uric acid must be *lower* in the dialysis fluid to allow these substances to diffuse out of the blood. Similarly, the concentrations of bicarbonate ions and glucose must be *higher* in the dialysis fluid so that they can diffuse into the blood. The concentrations of all other electrolytes must remain the same between the dialysis fluid and blood. Dialysis can also adjust the patient's blood volume, by altering the osmotic pressure of the dialysis fluid, ie the water concentration. Figure 3.3 shows a circuit diagram for the dialysis system [Martini, 2006].

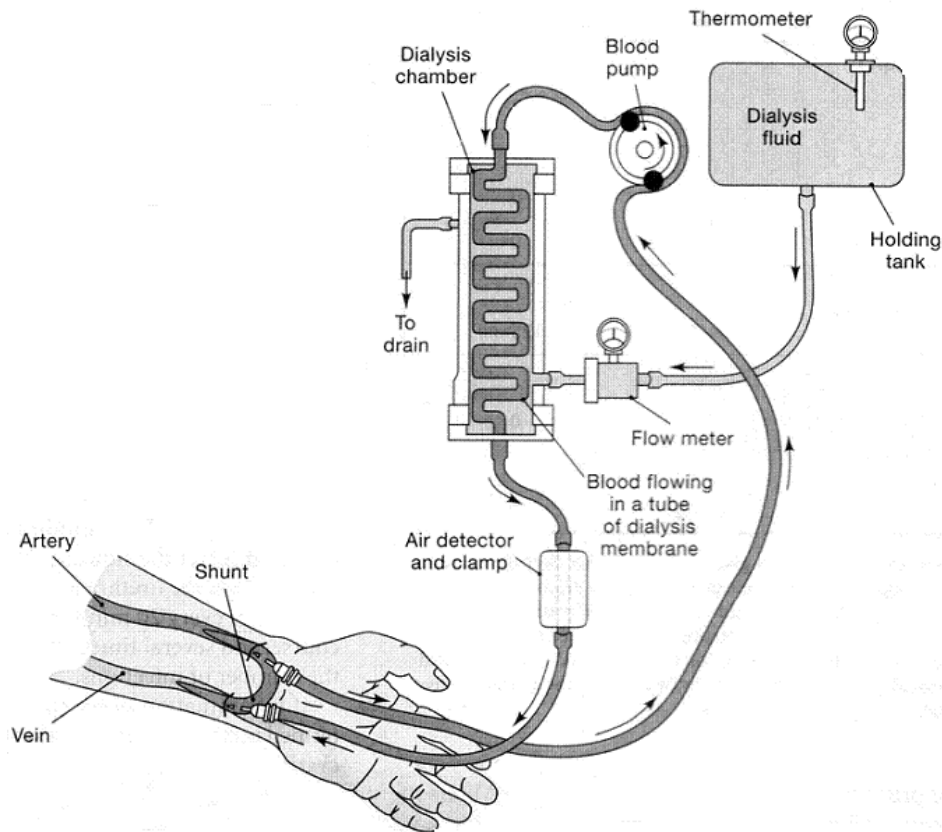


Figure 3.3 Dialysis circuit diagram illustrating external filtering of wastes from the blood in patients with renal failure Martini [2006]

Dialysis treatment can maintain patients suffering from a temporary kidney dysfunction, or those patients awaiting a kidney transplant. However, there are risks and drawbacks associated with this treatment:

- Typically 3-4 dialysis sessions are required per week, each lasting up to 5 hours;
- Hypotension can result due to fluid loss during dialysis;
- There is an increased risk of exposure to blood borne infections;
- There is a risk of embolism if air bubbles in the tubing get into the body.

Dialysis efficacy is most simply measured by the Urea Reduction Ratio (URR), which is a measure of the relative change in Blood Urea Nitrogen (BUN) over the course of the dialysis treatment. BUN decreases over the course of dialysis, as urea diffuses out of the blood and into the dialysis fluid. To calculate the URR,

blood samples must be taken and sent to the laboratory for analysis. As such, results cannot be provided quickly enough or sufficiently frequently to define individual responses to treatment or spontaneous clinical changes [Narasimhan et al., 2001].

SIFT-MS can offer potential benefits in dialysis treatment via the ability to measure dialysis efficiency non-invasively, and in real time, with a simple breath test to determine the reduction ratio of key analytes. By observing specific patient trends, one can determine the timing of the next required dialysis treatment, and thus avoid secondary organ failure due to delayed treatment. SIFT-MS can also be used to calculate the optimal time for dialysis treatment, to minimise patient time and maximise machine availability for others. Lastly, SIFT-MS can be used to identify key markers of renal function, as dialysis treatment effectively takes a patient from a sick to a healthy state over a few hours.

Several others have attempted to correlate breath markers with kidney function via a variety of techniques, with mixed results. [Handelman et al., 2003] measured breath ethane in patients undergoing peritoneal and haemodialysis via Gas Chromatography Mass Spectrometry (GC-MS). They reported that breath ethane was not altered by a single dialysis session. [Capodicasa et al., 1999] also found that ethane was not altered during dialysis, and also reported no change in propane, butane, and pentane. However, they did report an increase in breath isoprene, a finding repeated by [Davies et al., 2001], who used SIFT-MS to demonstrate elevated breath isoprene concentrations in predialysis patients compared to normal controls. Isoprene was then found to increase further during dialysis, with statistical significance.

[Davies et al., 1997] and [Narasimhan et al., 2001] analysed breath ammonia in patients with a renal impairment. [Davies et al., 1997] reported that breath ammonia, as measured by SIFT-MS is substantially elevated in uremia. [Narasimhan et al., 2001] attempted to correlate reduction in breath ammonia with the reduction in BUN and Creatinine using laser spectroscopy. Good correlation was observed, but inter-patient results varied substantially. Lastly, [Bain et al., 2006] monitored TMA and TMNO in patients with end-stage renal disease undergoing haemodialysis, and found that TMA and TMNO accumulate between dialysis sessions but are efficiently reduced to normal levels during a single haemodialysis session.

3.3 Dialysis Clinical Study Design

A clinical study was designed to monitor the change in key breath analytes as measured by SIFT-MS over the course of dialysis treatment, and correlate these changes with the simplest gold standard for dialysis efficacy, the URR, and the current gold standard for kidney function, the plasma creatinine concentration. In addition, mass scans were performed on the breath samples in order to determine possible new biomarkers of kidney function in comparison to these gold standards.

Key analytes monitored in SIM scan mode were ammonia, TMA and acetone. Ammonia is mostly formed from the catabolism of proteins. Ingested and cellular proteins are hydrolysed to form a pool of amino acids. Any amino acids not used in protein production are catabolised to ammonia, which is either excreted, or converted to urea via the Urea Cycle in the liver. When renal function is compromised, blood ammonia increases.

Acetone is formed in the liver by decarboxylation of excess acetyl-CoA. It is derived from acetoacetate, a product of lipid peroxidation. Lipid peroxidation occurs when the body uses fats instead of sugars for energy. Hence, acetone increases when fasting or suffering uncontrolled diabetes mellitus when the body cannot utilise glucose. Acetone is excreted in the urine as a *ketone body*. In chronic kidney disease, acetone cannot be excreted and its concentration in the blood increases.

TMA is a nitrogenous base, normally produced by gut bacteria and oxidised in the liver to produce TMNO, which is excreted in the urine [Tjoa and Fennessey, 1991]. Elevated TMA can therefore be due to increased bacterial proliferation in the gut, or to lack of excretion. Thus, TMA may serve, if it can be measured accurately enough in breath, as a useful marker of kidney function.

This study was carried out in two parts over two years, with Study I carried out on the older *Voice100TM* SIFT-MS instrument. Advances in the SIFT-MS instrument lead to the development of the smaller, quieter, portable *Voice200[®]* SIFT-MS instrument, which was used in Study II. The remainder of this chapter describes the initial study, and chapter 4 presents the improved methodology and results from the second dialysis study.

Patients from the acute haemodialysis unit of Christchurch Hospital were recruited to this clinical study, as approved by the Upper South B Regional Ethics Committee (URB/05/12/178). All dialysis sessions commenced between 8 and 9 am, and were 5 hours in duration. The goal was to obtain datasets from 5 dialysis sessions for each patient, however due to the volatility of the study population, many patients were lost to the study due to:

- Renal transplantation
- Intercurrent illness
- Changing from haemodialysis to peritoneal dialysis
- Home dialysis training
- Death
- Loss of vascular access

The exclusion criteria for these studies were:

- Critically unstable patients
- Patients with inconsistent vascular access
- Patients still adjusting to haemodialysis
- Patients unlikely to be available for 5 sessions (criterion added part-way through clinical trial)
- Patients who did not consent

The relative change biomarker identification method (Δ_{rel} and Equation (3.3)) was considered the most appropriate technique for the identification of biomarkers. This method allowed identification of significant changes in VOC concentrations that occurred at high, as well as low, concentrations detectable by SIFT-MS. This choice was considered reasonable since dialysis efficiency is usually determined by the Urea Reduction Ratio (URR), which is effectively a relative change. Mass scans results are shown using the relative change biomarker identification method (Equation (3.3)), the classification method on the normalised

data, (Equation (3.1)), and the classification method on the raw data. All these approaches are shown for comparison and completeness in evaluating their metrics.

3.3.1 Dialysis Study I Methodology

Table 3.2 shows those patients recruited to the study. The study population was made up of males and females of mixed ethnicity, mixed age (26-78 years), mixed cause of end stage renal failure, and mixed comorbidities. All patients had been undergoing haemodialysis treatment for between 6 months and 2 years.

Table 3.2 Dialysis Study I Sample Population

Study ID	Gender	Age	Ethnicity	Years since commencing dialysis	# completed dialysis sessions
DS101	Male	50	NZ European	0.5	5
DS102	Female	45	NZ European	1	6
DS103	Male	78	NZ European	0.5	1
DS104	Male	48	NZ European	0.5	1
DS105	Male	69	NZ European	0.5	1
DS106	Male	67	NZ Maori	2	1
DS107	Male	52	NZ Maori	1	1
DS108	Male	28	Chinese	0.5	1
DS109	Male	39	NZ European	0.5	1
DS110	Female	26	NZ Maori	0.5	1
DS111	Male	77	NZ European	0.5	4
DS113	Male	37	NZ European	0.5	5
DS114	Male	73	NZ European	0.5	5
DS115	Male	43	NZ Maori	0.5	5

Prior to dialysis, 30mins post-dialysis, and at hourly intervals during dialysis, patients filled a 1L tedlar bag with as few breaths as required. Each bag was delivered to the *Voice100TM* for mass scan and SIM scan analysis within 5 minutes of being inflated. For comparison, blood specimens were collected for creatinine and BUN analysis prior to commencing dialysis and at the completion of the treatment.

SIM scans monitored the concentration of ammonia, acetone and TMA over

the course of treatment, with the concentration of each sample determined as the average concentration in the bag as recorded over a 30 second sampling time. In the mass scan mode, masses 10-150 were monitored at every 0.2 of a mass unit, requiring filtering to extract the concentration at each integer value, as described in Section 2.1.

3.4 Dialysis Study I Results

3.4.1 SIM Scans

SIM scan results monitoring concentrations of ammonia, acetone and TMA for patients with repeat dialysis sessions (DS101, DS102, DS111 and DS113-DS115) are shown in Figures 3.4 to 3.9.

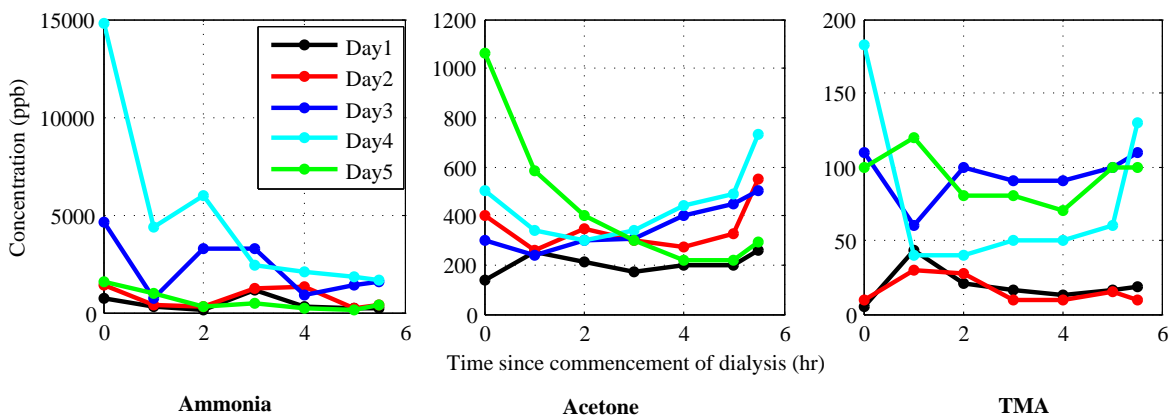


Figure 3.4 DS101 SIM Scan

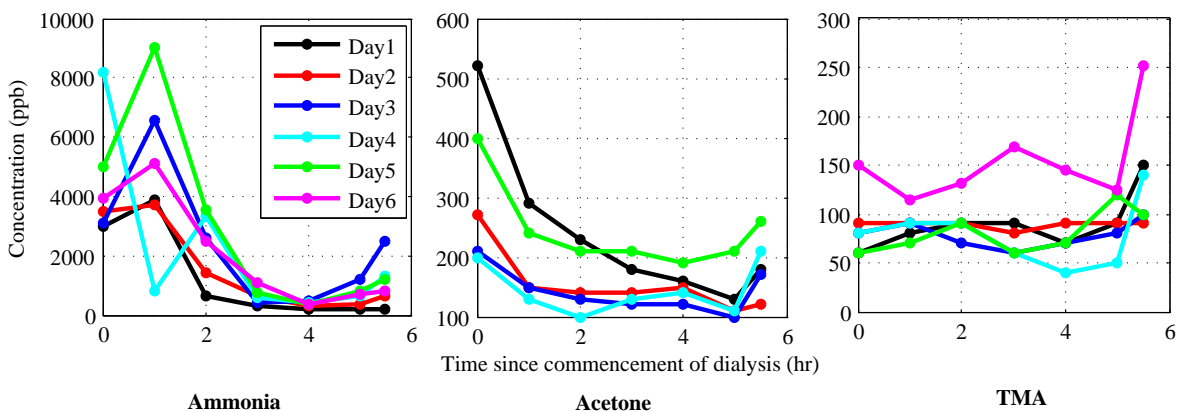


Figure 3.5 DS102 SIM Scan

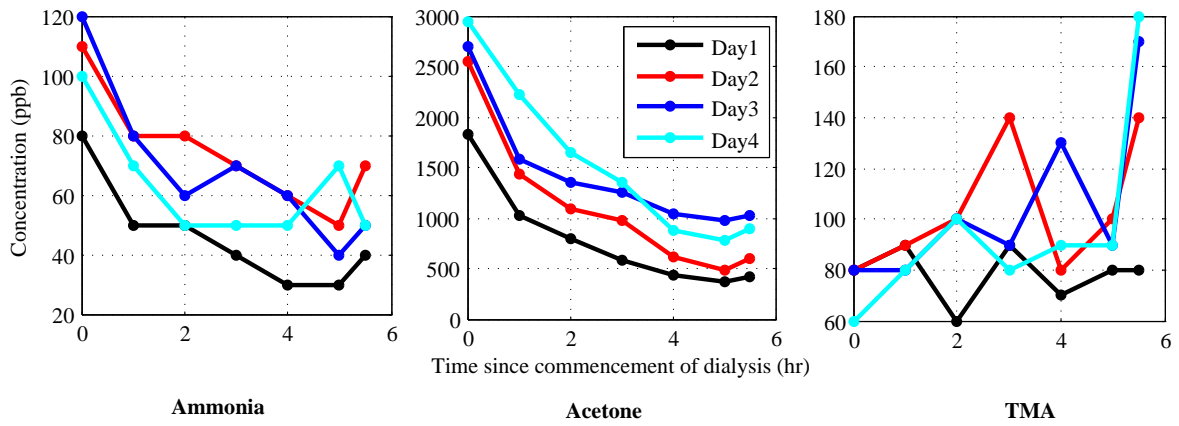


Figure 3.6 DS111 SIM Scan

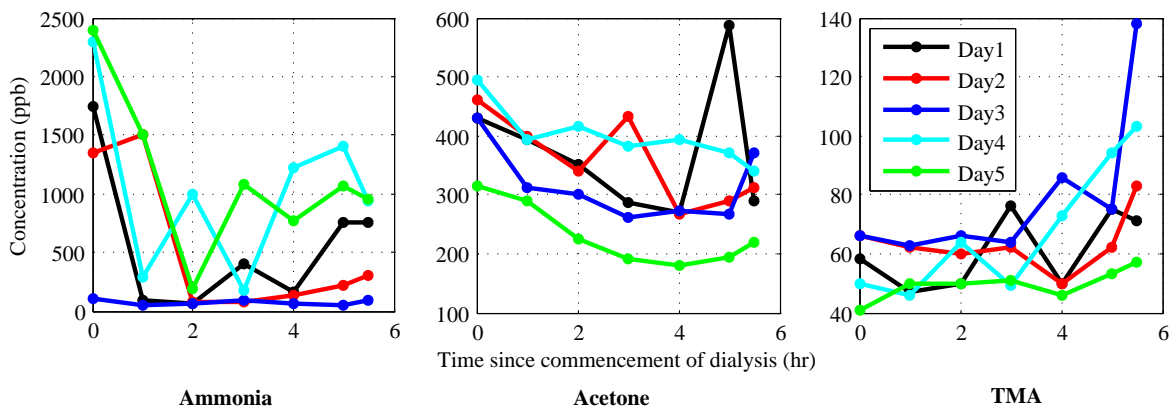


Figure 3.7 DS113 SIM Scan

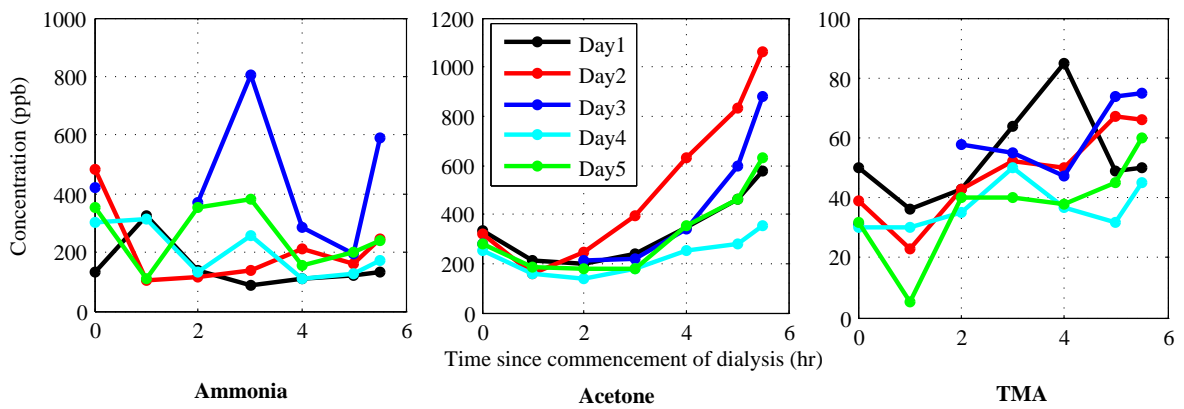


Figure 3.8 DS114 SIM Scan

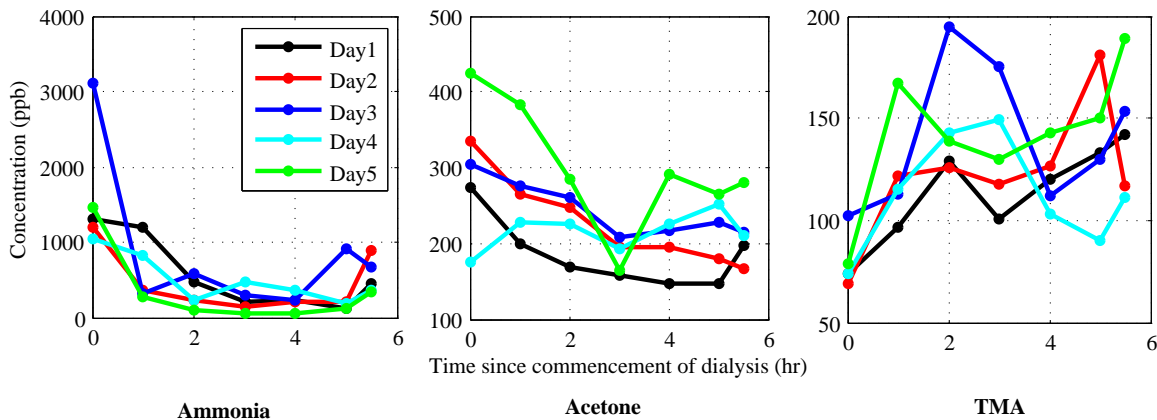


Figure 3.9 DS115 SIM Scan

Three patterns were observed with the ammonia concentration time profiles:

1. Exponential decline, as best described by DS115
2. Increase until 1 hour followed by progressive decline, best described by DS102
3. Oscillatory pattern, best described by DS114

It is postulated that patients who have a low starting ammonia concentration tend to oscillate and finish low because they are near their equilibrium concentration. Patients that have a high starting concentration have more ammonia to clear from the blood and thus will have a high ammonia reduction ratio (ARR). The reason for the rise in ammonia concentration in DS102 is unclear. These intra-patient differences observed between sessions could be due to diet, and time since the last dialysis session. For example, ammonia concentrations are usually higher on Mondays when no dialysis sessions have been performed over the weekend. Similarly, a high-protein meal prior to dialysis can raise the starting concentration.

Acetone appeared to decrease during dialysis for most patients, with DS114 being the exception. Acetone tends to increase as the time since the last meal increases. However, in this study it was not recorded which patients were eating during treatment. This shortfall was remedied in Study II.

TMA concentration appeared to be extremely variable both between dialysis

sessions and between patients, although the general pattern was a steady increase. However, this result could be due to sampling error introduced particularly at low concentrations.

The correlations of breath ammonia, TMA and acetone are shown in Table 3.3. It was observed that only 2 datasets showed statistically significant correlation. Absolute change in breath ammonia was correlated with absolute change in BUN with a *p-value* of 0.027. Absolute change in breath acetone was negatively correlated with absolute change in BUN, with a *p-value* of 0.009.

Table 3.3 Dialysis Study I Correlation

		Creatinine	Ammonia	TMA	Acetone
BUN	Relative	0.9346*	0.0963	0.2521	0.0554
	Absolute	0.5281**	0.4250†	0.1477	-0.4954‡
Creatinine	Relative	1.0000	0.1312	0.2414	0.0884
	Absolute	1.0000	0.3052	-0.1145	-0.3187
* p<<0.001		** p< 0.005	† p<0.03	‡ p<0.01	

It is postulated that creatinine and BUN have different re-equilibration dynamics at the completion of dialysis to ammonia measured in breath. Thus, a blood sample taken while the patient was still connected to the dialysis machine would have been a more appropriate comparison. In addition, hourly sampling appeared to be insufficient to define patients trends. Hence, 30 minute sampling was introduced in Study II.

3.4.2 Mass Scans

Mass scan analysis was performed on all bagged breath samples. However, results here compare the concentrations between the *predialysis* state and the last measurement whilst on dialysis, referred to here as the *postdialysis* state. These states would correlate to state *k* and *j*, in Section 3.1, respectively. Mass scans results are shown using the classification method on the raw data (Chapter 2), the classification method on the normalised data, (Equation (3.1)), and the relative change biomarker identification method (Equation (3.3)), for comparison.

Top biomarkers identified using each method and each precursor are shown

in Table 3.4, where top biomarkers with the classification method have minimal overlap between log-odds density profiles and thus a *low* score. In contrast, top biomarkers with the biomarker identification method have a high mean to standard deviation ratio, and thus a *high* score.

Table 3.4 Dialysis Study I Top Biomarkers

	Classification Method				Biomarker ID	
	Raw Data		Relative Data		Method	
	Mass	Score	Mass	Score	Mass	Score
H_3O^+	18	0.4709	36	0.0866	36	16.92
Precursor	36	0.4710	18	0.1055	18	16.65
	17	0.5023	54	0.2785	54	8.31
	54	0.5268	59	0.4289	17	6.27
	35	0.5278	77	0.4415	78	5.85
NO^+	36	0.5016	18	0.2126	18	10.07
Precursor	18	0.5215	36	0.3848	36	6.87
	47	0.5500	88	0.4919	47	5.04
	77	0.6290	47	0.5400	88	4.48
	59	0.7034	63	0.5698	63	3.40
O_2^+	17	0.4305	17	0.1259	17	15.57
Precursor	35	0.5786	36	0.1463	54	13.83
	53	0.5840	54	0.1580	36	11.49
	54	0.6019	53	0.1662	35	10.07
	18	0.6088	35	0.1672	53	9.41

3.4.2.1 H_3O^+

Using the H_3O^+ precursor, Figure 3.10 was obtained from classification from the raw data. A 18.58% classification error and a ROC area of 0.781 was observed with a bootstrap sample size of 200.

The overlap of log-odds density profiles occurred largely because the method does not take into account the paired nature of the data. When the relative change method was employed (Equation (3.1)), Figure 3.11 was obtained, with a

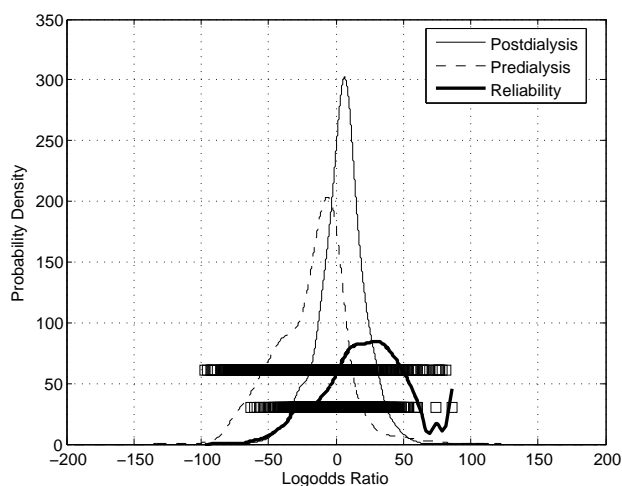


Figure 3.10 Classification on *raw* data over all masses with the H_3O^+ precursor, as determined by Equation (2.3)

2.04% classification error and a 0.994 ROC area with a bootstrap sample size of 200.

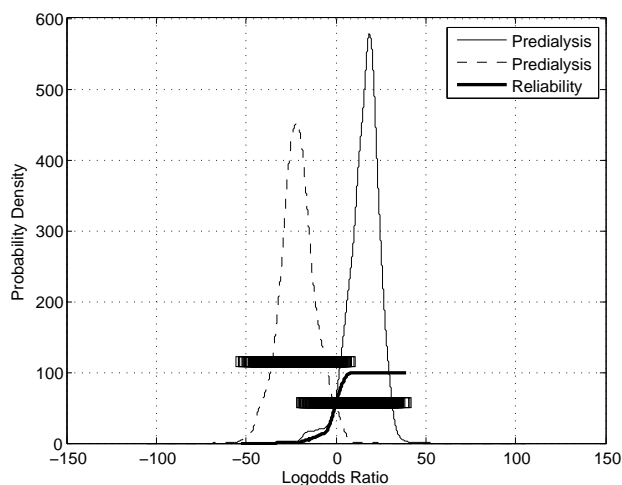


Figure 3.11 Classification on *normalised* data over all masses (Equation (3.1)) with the H_3O^+ precursor, as determined by Equation (2.3)

Using the biomarker identification method, which displays the density profiles of the means of 200 bootstrap samples (Equation (3.3)), Figure 3.12 was obtained.

The top 3 biomarkers corresponding to ammonia and its water clusters are shown in Figures 3.13-3.15. The *left* plot shows the density profile of the raw data. The *centre* plot shows the density profile of the *normalised* data. The *right* plot shows the density profile of the log-odds ratio of the *normalised* data. The reaction with H_3O^+ proceeds as shown in Equation (3.5) for masses 18, 36 and 54.

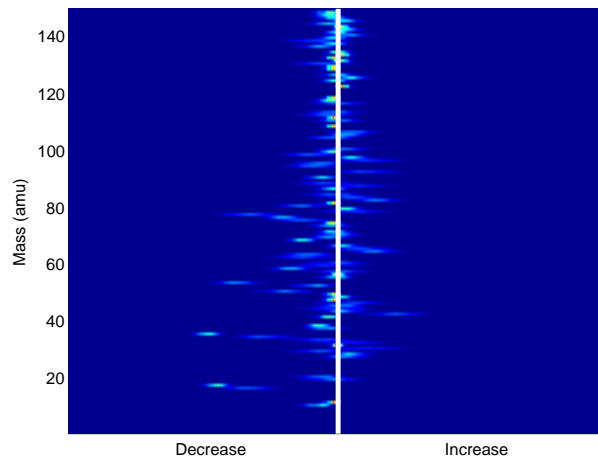


Figure 3.12 Biomarker identification in Dialysis Study I with the H_3O^+ precursor

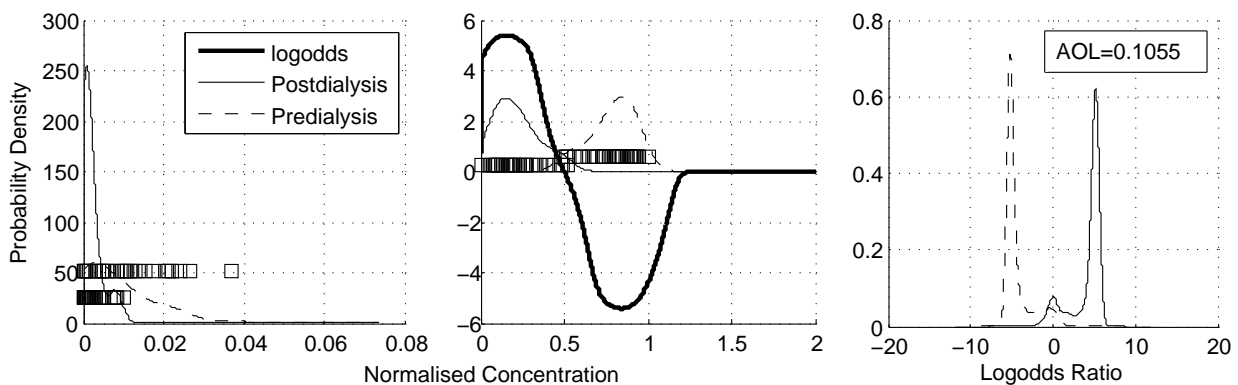
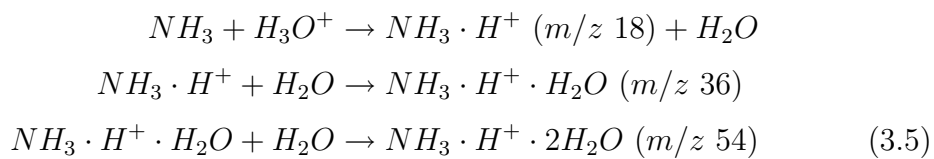


Figure 3.13 Probability density profiles for Mass 18 obtained via raw and normalised, pre and post dialysis datasets. Log-odds probability density profile for identification of biomarkers is shown, *right* with Area of Overlap (AOL) indicating the degree of overlap of the density profiles.

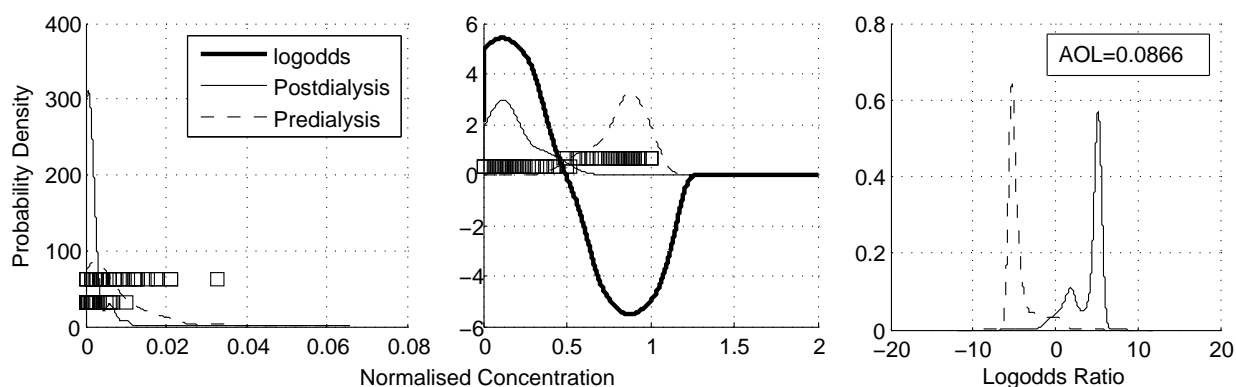


Figure 3.14 Probability density profiles for Mass 36 obtained from raw and normalised, pre and post dialysis datasets.

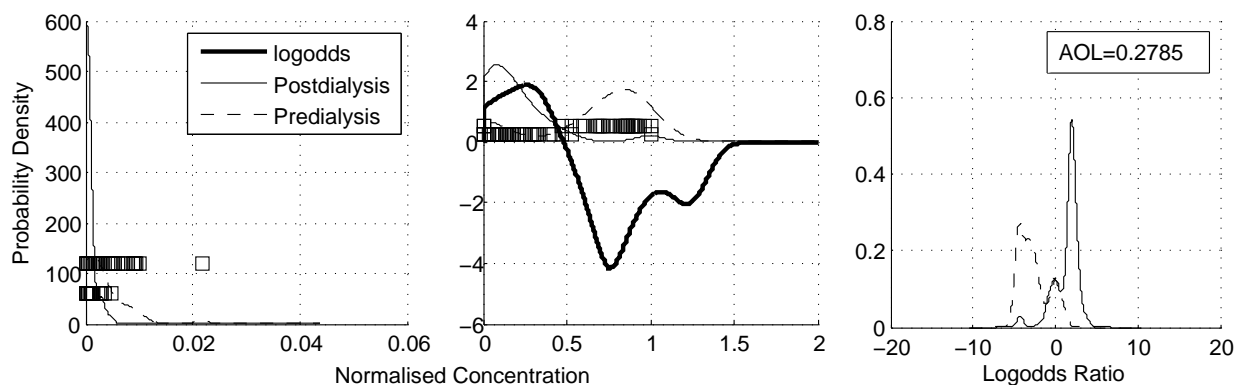


Figure 3.15 Probability density profiles for Mass 54 obtained from raw and normalised, pre and post dialysis datasets.

3.4.2.2 NO^+

Using the NO^+ precursor, Figure 3.16 was obtained from classification off raw data. A 19.72% classification error and a ROC area of 0.791 was observed with a bootstrap sample size of 200.

Again, an improvement was observed when classification was carried out on the normalised data, as seen in Figure 3.17, where the classification error was 9.82% and the ROC area was 0.940 with a bootstrap sample size of 200. Using the biomarker identification method which displays the density profiles of the means of 200 bootstrap samples (Equation (3.3)), Figure 3.18 was obtained.

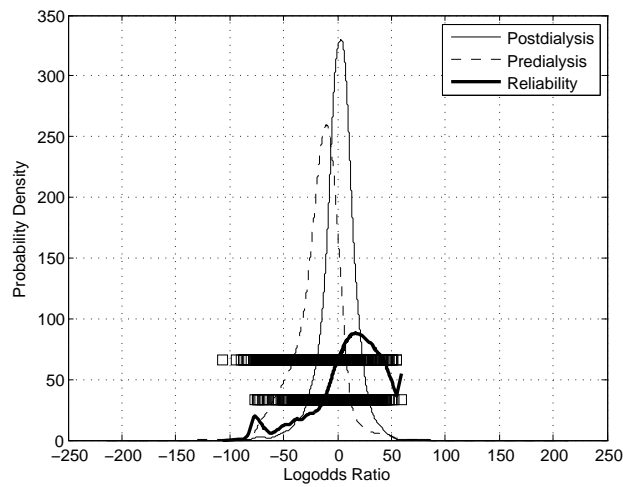


Figure 3.16 Classification on *raw* data over all masses with the NO^+ precursor, as determined by Equation (2.3)

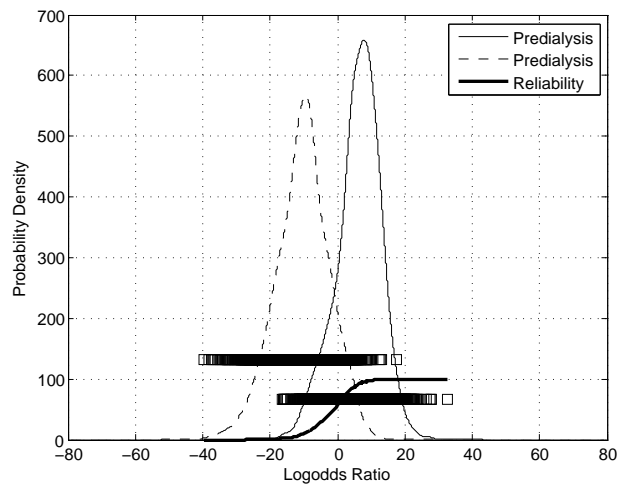


Figure 3.17 Classification on *normalised* data over all masses (Equation (3.1) with the NO^+ precursor, as determined by Equation (2.3)

It is observed in Figure 3.18 that no biomarkers stand out in the image plot. This result was expected, since ammonia, the only biomarker to stand out in this study, cannot be detected with the NO^+ precursor. This result was further highlighted by the relatively larger overlap in density profile in Figure 3.17, and the higher classification error of 9.82%, even when normalisation was used.

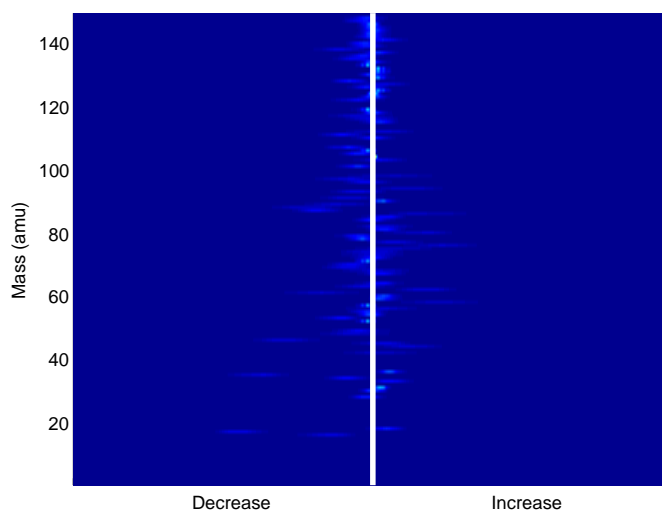
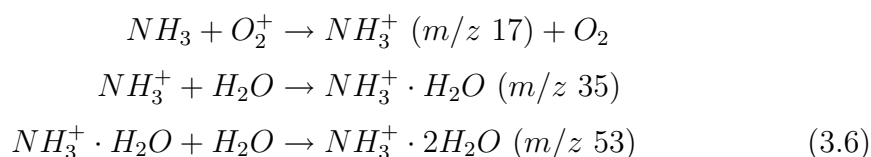


Figure 3.18 Biomarker identification in Dialysis Study I with the NO^+ precursor

3.4.2.3 O_2^+

Using the O_2^+ precursor, Figures 3.19 and 3.20 were obtained from classification from the raw and normalised data, respectively. Using a bootstrap sample size of 200 in both cases, a 24.79% classification error and 0.651 ROC area, and a 2.67% classification error and a 0.992 ROC area were observed from the raw and normalised data, respectively. Using the biomarker identification method, which displays the density profiles of the means of 200 bootstrap samples (Equation (3.3)), Figure 3.21 was obtained.

The top 3 biomarkers correspond to ammonia and its water clusters, and are shown in Figures 3.22-3.27. The reaction with O_2^+ proceeds as shown in Equations (3.6) and (3.7), resulting in the observed peaks at 17, 18, 35, 36, 53 and 54 amu.



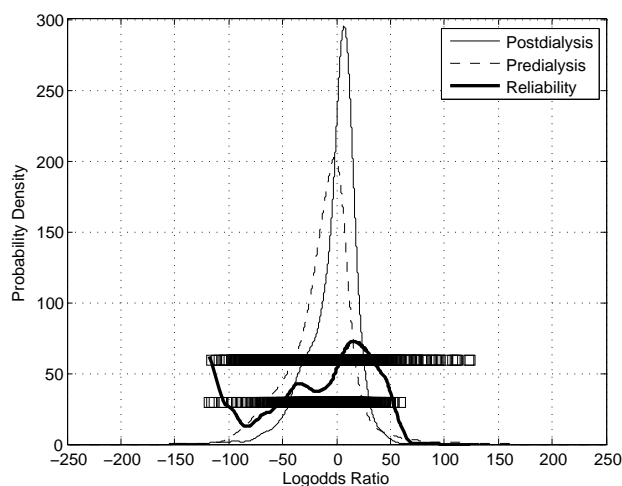


Figure 3.19 Classification on *raw* data over all masses with the O_2^+ precursor, as determined by Equation (2.3)

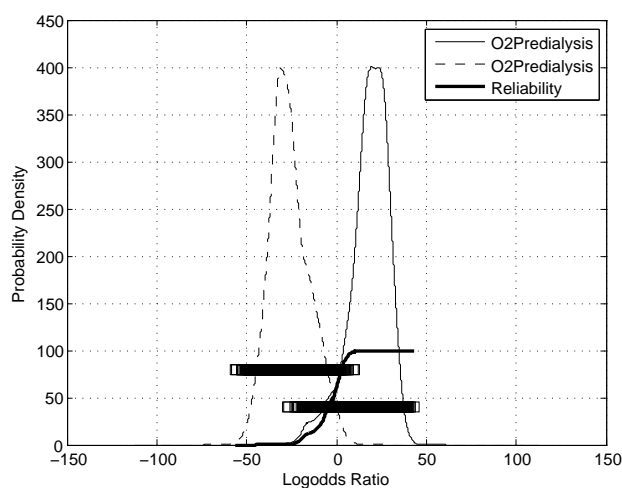
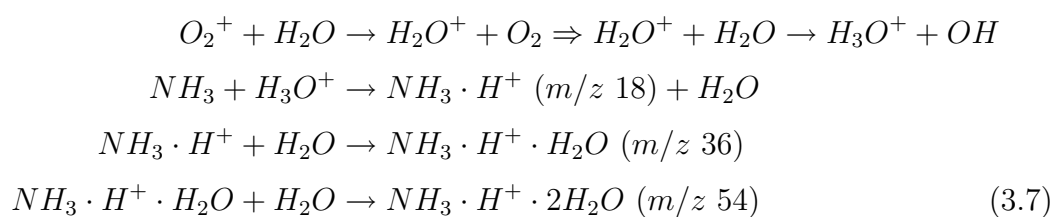


Figure 3.20 Classification on *normalised* data over all masses (Equation (3.1) with the O_2^+ precursor, as determined by Equation (2.3)



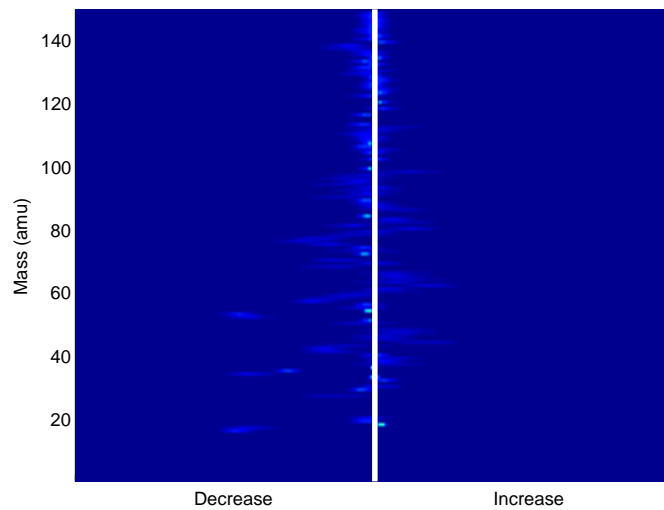


Figure 3.21 Biomarker identification in Dialysis Study I with the O_2^+ precursor

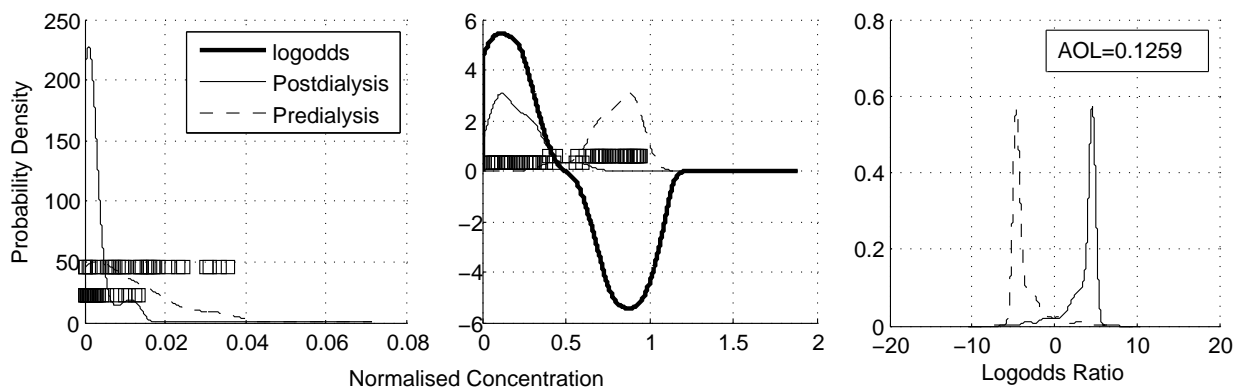


Figure 3.22 Probability density profiles for Mass 17 obtained from raw and normalised, pre and post dialysis datasets using the O_2^+ precursor.

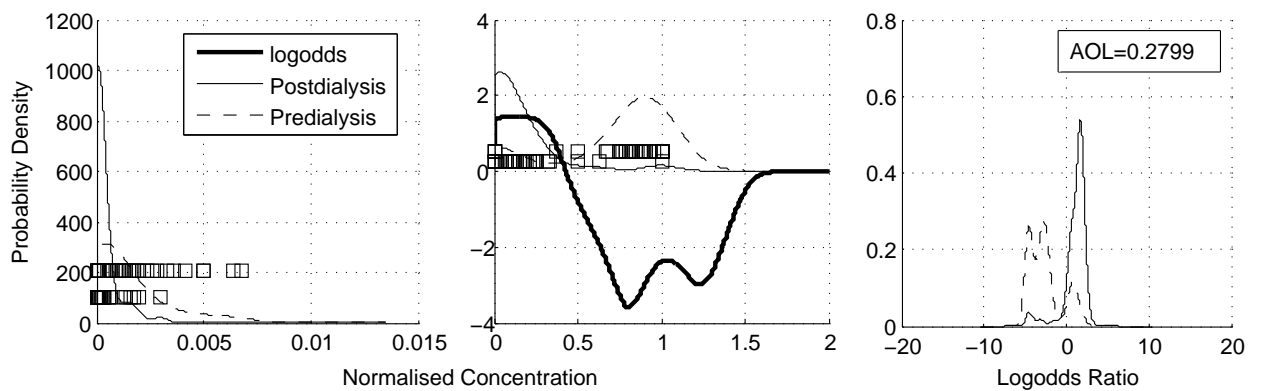


Figure 3.23 Probability density profiles for Mass 18 obtained from raw and normalised, pre and post dialysis datasets using the O_2^+ precursor.

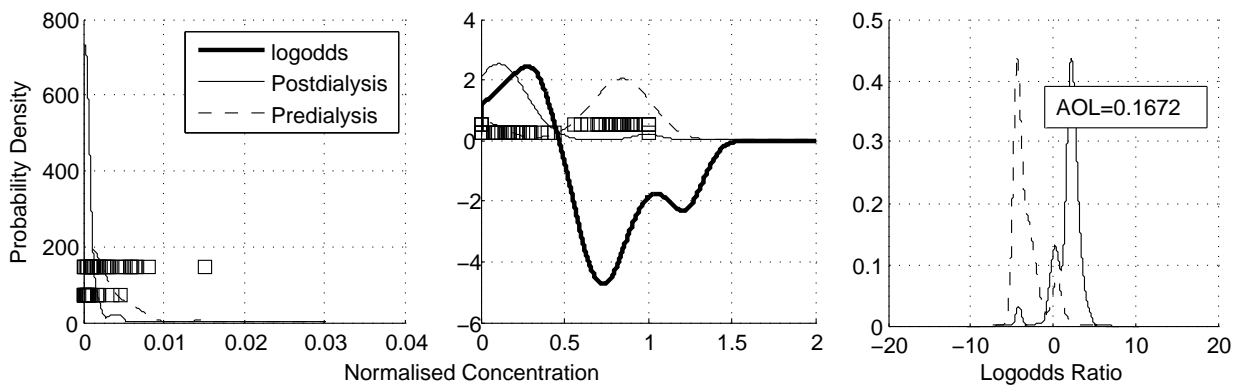


Figure 3.24 Probability density profiles for Mass 35 obtained from raw and normalised, pre and post dialysis datasets using the O_2^+ precursor.

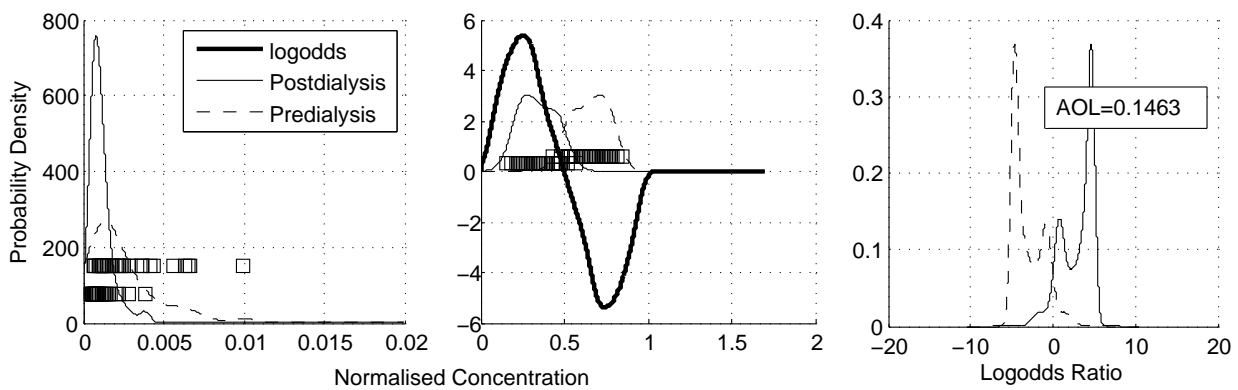


Figure 3.25 Mass Probability density profiles for Mass 36 obtained from raw and normalised, pre and post dialysis datasets using the O_2^+ precursor.

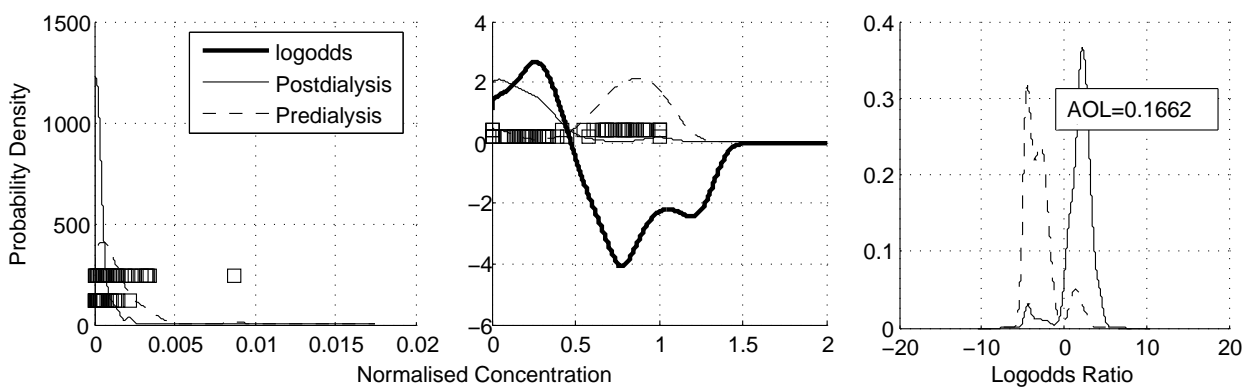


Figure 3.26 Mass Probability density profiles for Mass 53 obtained from raw and normalised, pre and post dialysis datasets using the O_2^+ precursor.

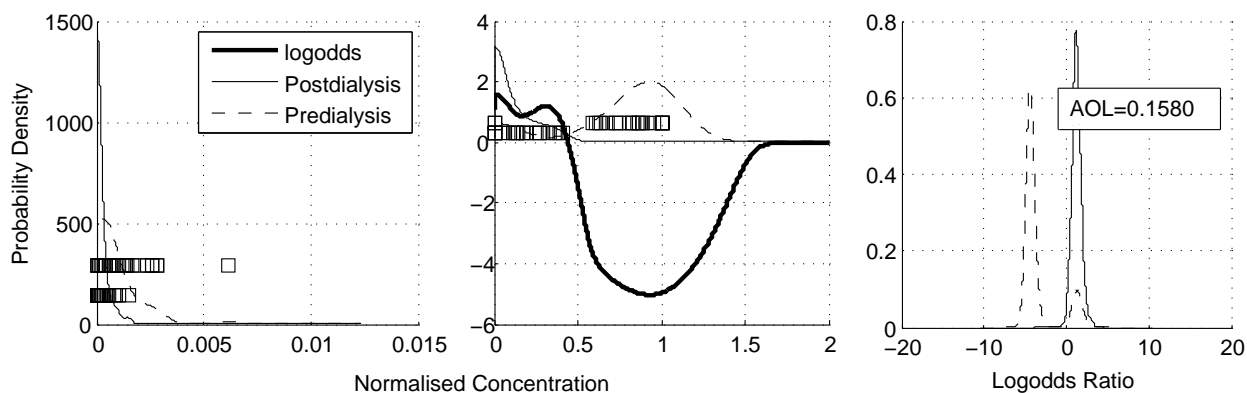


Figure 3.27 Mass Probability density profiles for Mass 54 obtained from raw and normalised, pre and post dialysis datasets using the O_2^+ precursor.

3.5 Summary

A method was presented for biomarker identification using longitudinal classification models. The model exploits the paired nature of the data by normalisation to a relative change of the time course of the treatment. Ethics approval was obtained to carry out a clinical trial, which was carried out in two parts, the first of which was presented in this chapter.

The clinical trial monitored the change in ammonia, TMA and acetone as measured by SIFT-MS over the course of dialysis treatment. In renal failure, the kidney fails to effectively excrete metabolic wastes and hence these accumulate in the blood, and can be measured in the breath. The relative and absolute changes in analyte concentration were compared with the changes in BUN and creatinine, the gold standards of kidney function.

Mass scan analysis was performed on breath samples collected in tedlar bags, for the purpose of detecting biomarkers of kidney function revealed when comparing the predialysis and postdialysis breath samples. Since dialysis efficacy is reported as the URR, a reduction ratio, mass scan analysis was performed using the relative change in states between the beginning and end of dialysis treatment. The only key biomarker identified was ammonia, with a log-odds density profile overlap of 0.0866 and a biomarker score of 16.92, as measured with the H_3O^+ precursor. Estimated prediction errors ranged from 2-10% over the 3 precursors.

Chapter 4

Dialysis Study II

Advances in the SIFT-MS instrument led to the development of the smaller, quieter, portable *Voice200*[®] SIFT-MS instrument, which was used in Dialysis Study II. This portability meant that the SIFT-MS instrument could be taken to the home dialysis training unit, allowing direct breath sampling in the SIM scan mode. Because this trial was carried out in the home dialysis training unit, a more stable patient cohort was ensured. Lastly, more frequent breath monitoring was carried out, to allow better determination of patient trends. Exclusion criteria were the same in Study II as for Study I.

4.0.1 Dialysis Study II Methodology

The introduction of the *Voice200*[®] SIFT-MS instrument allowed direct breath sampling for SIM scan analysis during dialysis treatment. With the use of a mouth piece and biological filter, the patient could breath directly into the machine, making collection into tedlar bags unnecessary. However, direct breath sampling for mass scan analysis was not possible and thus tedlar bags were still required in this instance. The patient cohort is described in Table 4.1.

Breath samples for mass scan analysis were collected into tedlar bags prior to dialysis, at hourly intervals during dialysis and 30 minutes after the completion of dialysis. The *Voice200*[®] instrument analysed samples at 1.0 integer mass units from mass 15-200. SIM scan analysis was performed on direct breath samples collected every 30 minutes during dialysis, as well as prior and 30 minutes after. Blood samples were analysed for creatinine and BUN before and after treatment, as previously.

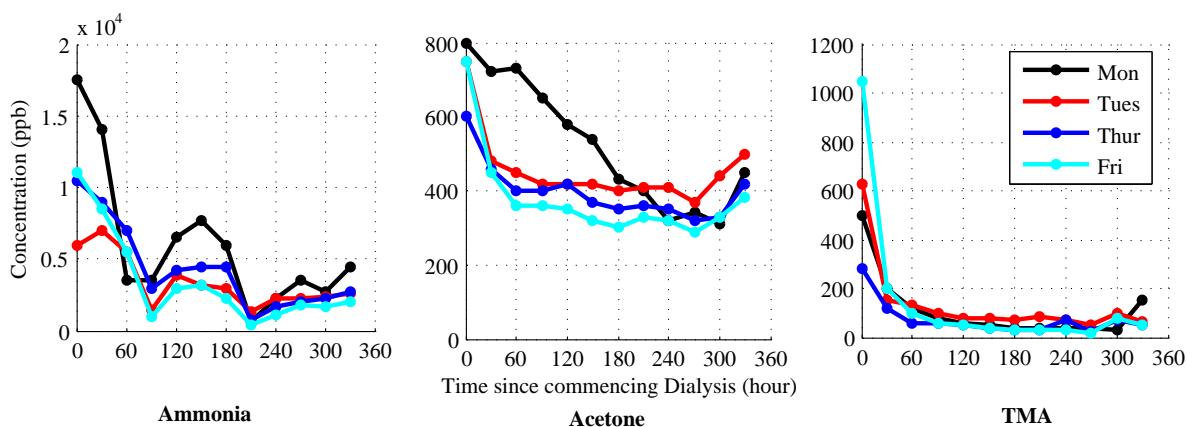
Table 4.1 Dialysis Study II Sample Population

Study ID	Gender	Age	Ethnicity	Months since commencing dialysis	# completed dialysis sessions
DS201	Female	54	NZ European	4	4
DS202	Male	39	NZ European	4	3
DS203	Male	53	NZ European	59	5
DS204	Male	75	European	8	3
DS205	Male	73	NZ European	1	3

4.1 Dialysis Study II Results

4.1.1 SIM Scans

SIM scan results monitoring concentrations of ammonia, acetone and TMA for patients DS201-DS205 are shown in Figures 4.1 to 4.5.

**Figure 4.1** DS201 SIM Scan

It was observed that there were different patterns of behaviour between patients, which was largely dependent on the starting analyte concentration. For ammonia, these starting values ranged from 600 to 17000ppb. Higher starting concentrations generally occurred on days when there was a longer time since the previous dialysis session, as expected. Starting concentrations higher than 5000ppb, such as patients DS201-DS203, displayed an exponential decline with a *bouncing ball* effect part way through treatment as the concentration rose slightly.

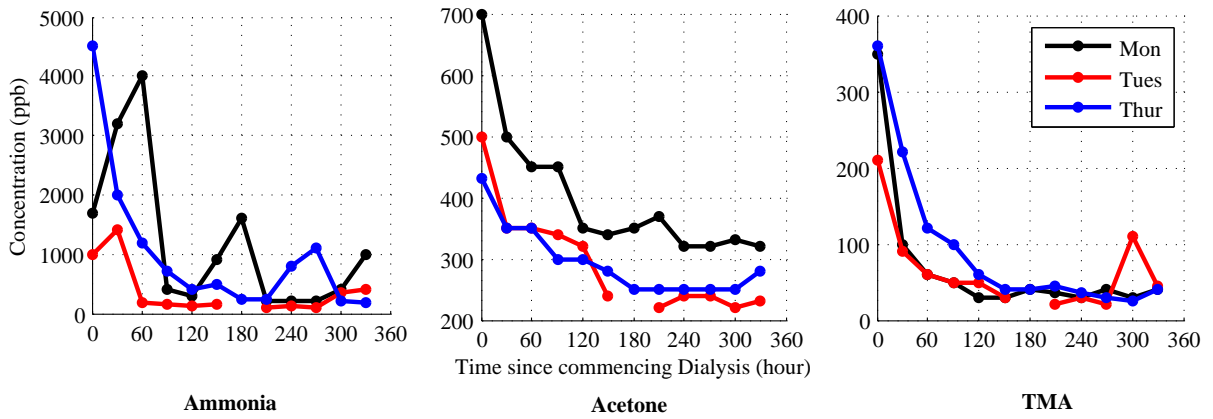


Figure 4.2 DS202 SIM Scan

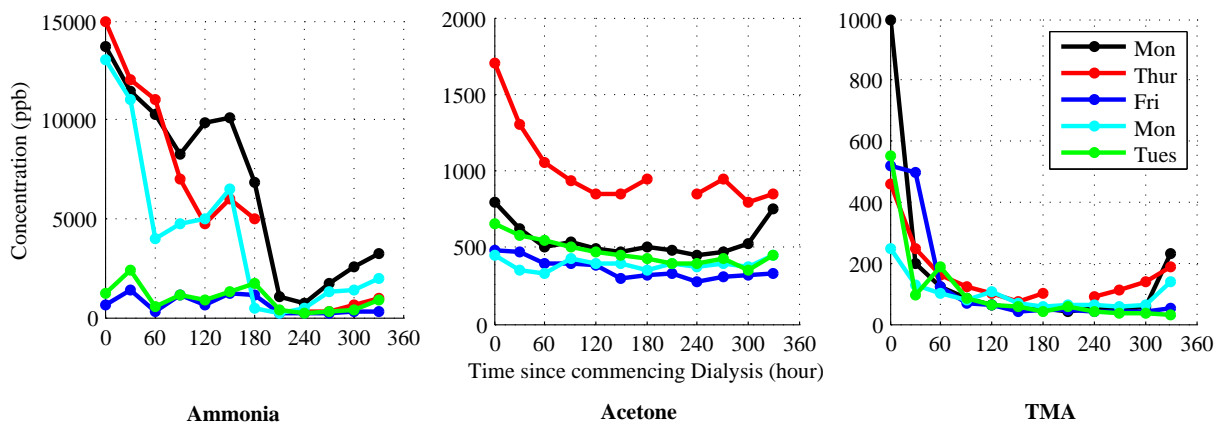


Figure 4.3 DS203 SIM Scan

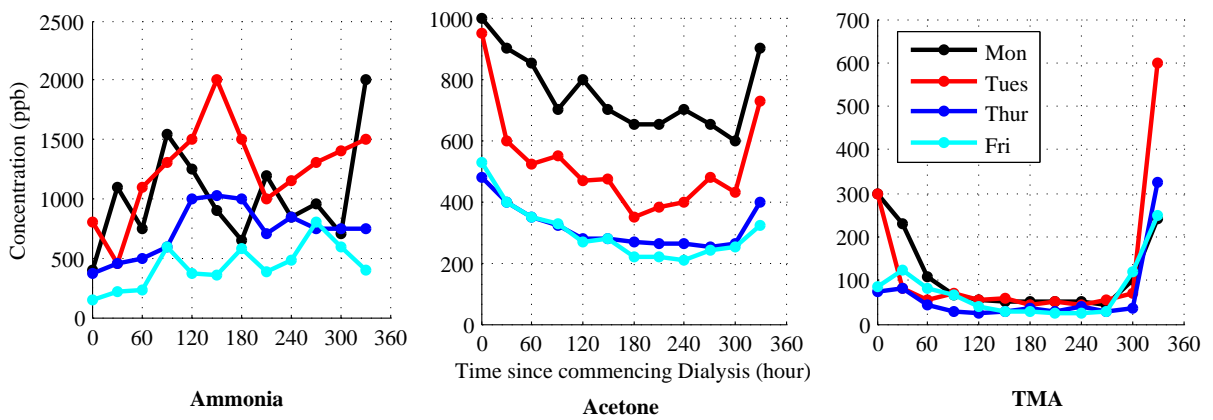


Figure 4.4 DS204 SIM Scan

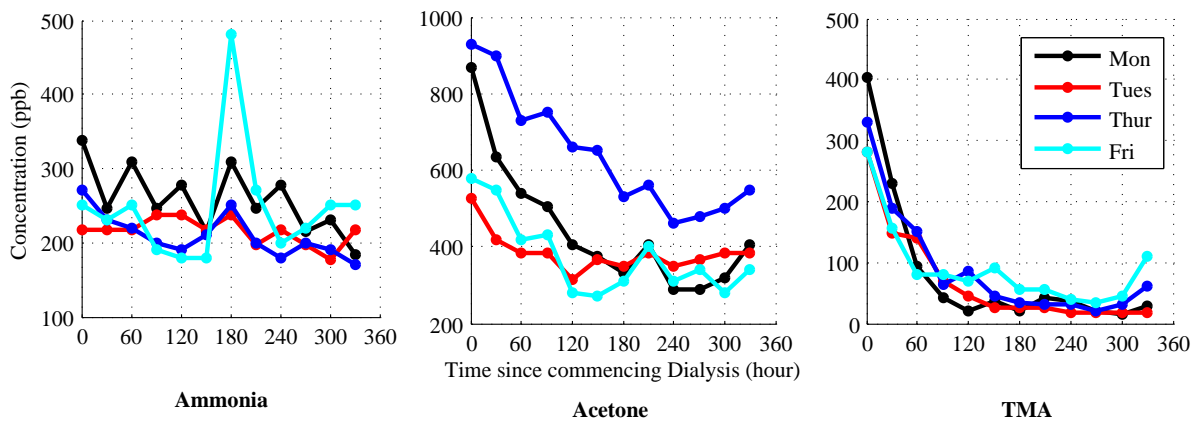


Figure 4.5 DS205 SIM Scan

At initial concentrations lower than 1000ppb, such as in patients DS204 and DS205, and the next day sessions of DS203, an oscillatory pattern was observed, where the average ammonia concentration did not change significantly over treatment. DS202 displayed a profile in at least one session whereby the ammonia concentration was seen to rise for the first 30-60 minutes after the onset of treatment and to subsequently fall to a lower concentration, a pattern that was also observed in Study I, for patient DS102.

Starting concentrations of acetone ranged from 450 to 1700ppb. Again, most patients showed a decline over the course of treatment, although the relative size of the decline varied between patients. Several patients had an increase in concentration in the sample 30 minutes after the completion of dialysis, as re-equilibration occurred.

TMA appeared to be the most repeatable measure over subsequent dialysis sessions, with starting concentrations varying from 100 to 1000ppb. In addition, equilibrium concentrations were relatively constant for each patient, with no intra-dialysis rises. Correlation results are shown in Table 4.2.

Table 4.2 Dialysis Study II Correlation of breath ammonia, TMA and acetone with gold standard BUN and Creatine values

		Creatinine	Ammonia	TMA	Acetone
BUN	Relative	0.8760*	0.5755†	0.6581**	0.3352
	Absolute	0.7378*	0.8046*	0.2792	-0.0633
Creatinine	Relative	1.0000	0.6758**	0.5302†	0.3086
	Absolute	1.0000	0.4978†	-0.1313	-0.2285

* $p < 0.001$ ** $p < 0.005$ † $p < 0.05$

The reduction ratios of breath ammonia and TMA correlated, statistically significantly, with the reduction ratios of BUN and creatinine. In addition, the absolute decrease in breath ammonia correlated significantly with the absolute decrease in BUN and creatinine. The correlation with these results was much greater than in Study I. This improvement could be due to the use of direct breath measurements rather than those collected in tedlar bags, greater accuracy of the *Voice200*[®] over the *Voice100*TM, improved sampling techniques, or a more stable patient cohort due to the patients being in home dialysis training rather than the acute unit.

4.1.2 Mass Scans

Mass scan analysis was performed on all bagged breath samples, but results here compare the concentrations between the *predialysis* state and the last measurement whilst on dialysis, referred to here as the *postdialysis* state. These 2 states are thus the k and j states, respectively, from Section 3.1. Mass scans results are shown using the classification method on the raw data (Chapter 2), the classification method on the normalised data, (Equation (3.1)), and the relative change biomarker identification method (Equation (3.3)), for comparison.

4.1.2.1 H_3O^+

Using the H_3O^+ precursor, Figure 4.6 was obtained from classification off raw data. A 9.9% classification error and a ROC area of 0.936 was observed with a bootstrap sample size of 200.

The overlap of log-odds density profiles occurred largely because the method does not take into account the paired nature of the data. When the relative change method was employed (Equation (3.1)), Figure 4.7 was obtained, with a 0% classification error and a 0.999 ROC area with a bootstrap sample size of 200.

Using the biomarker identification method, which displays the density profiles of the means of 200 bootstrap samples, (Equation (3.3)), Figure 4.8 was obtained.

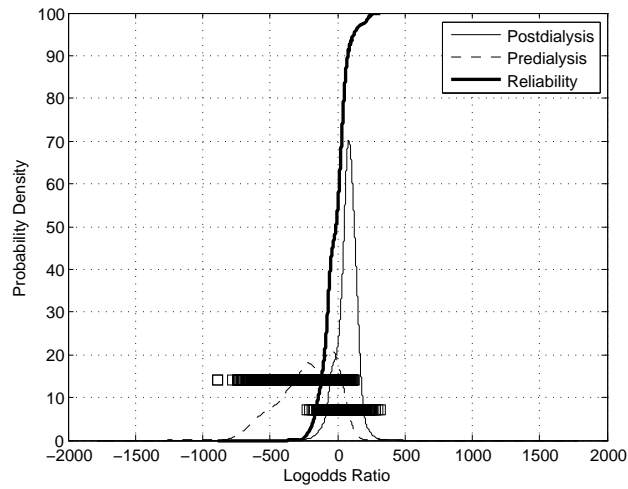


Figure 4.6 Classification from *raw* data over all masses using the H_3O^+ precursor

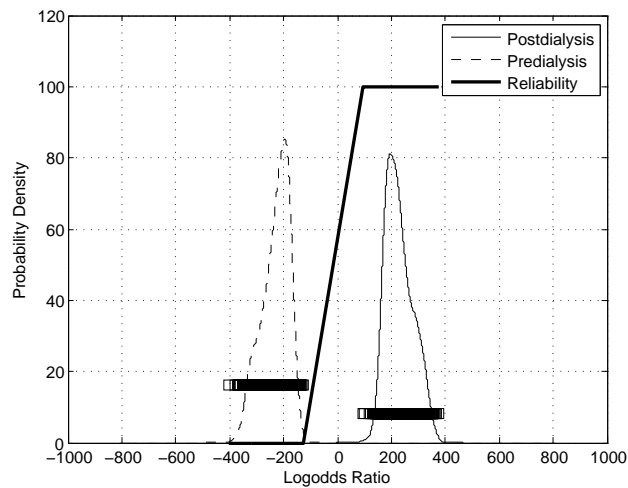


Figure 4.7 Classification from *normalised* data over all masses using the H_3O^+ precursor

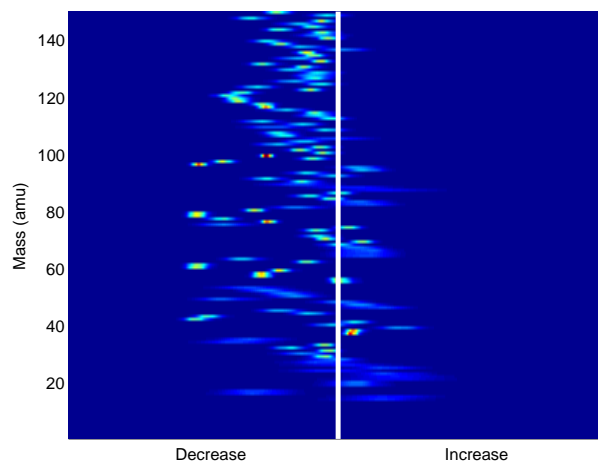


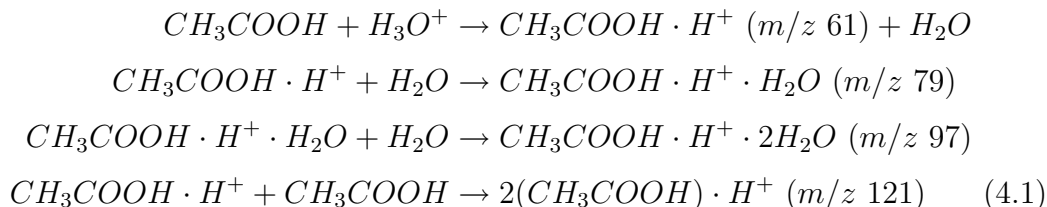
Figure 4.8 Biomarker identification using the H_3O^+ precursor

A summary of the top biomarkers identified using each method is shown in Table 4.3, with their respective scores. Using the classification method, top biomarkers have minimal overlap between log-odds density profiles and thus a *low* score. Using the biomarker identification method, top biomarkers have a high mean to standard deviation ratio, and thus a *high* score.

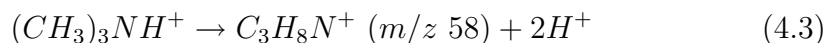
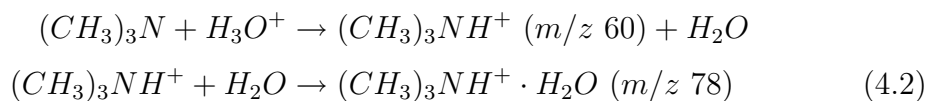
Table 4.3 Dialysis Study II Top Biomarkers with H_3O^+ precursor

Classification Method				Biomarker ID	
Raw Data		Relative Data		Method	
Mass	Score	Mass	Score	Mass	Score
80	0.0950	78	0.0000	97	27.67
62	0.1173	121	0.0000	79	23.59
97	0.1199	118	0.0001	80	23.41
43	0.1329	58	0.0011	61	21.51
44	0.1498	100	0.0014	62	19.79
98	0.1500	79	0.0037	100	18.58
61	0.1641	61	0.0041	43	17.52
79	0.2038	77	0.0054	98	17.42
121	0.2186	119	0.0093	44	15.10
152	0.2411	80	0.0127	119	14.35

Although the order of top biomarkers varied between methods, the same top biomarkers appeared. Several of the markers appeared with attached additive multiples of 18, suggesting the presence of water clusters. For example, masses 61, 79, and 97 appeared as top biomarkers corresponding to acetic acid, as shown in Equation (4.1).



A similar trend was observed with masses 44, 62, 80 and 98, however it is not known which compound this relates to. Masses 58, 60, and 78 all refer to TMA, and the reaction proceeds as shown in Equations (4.2) and (4.3).



Figures 4.9-4.19 show the density profiles of the top biomarkers. The *left* plot shows the density profile of the raw data. The *centre* plot shows the density profile of the *normalised* data. Finally, the *right* plot shows the density profile of the log-odds ratio of the *normalised* data.

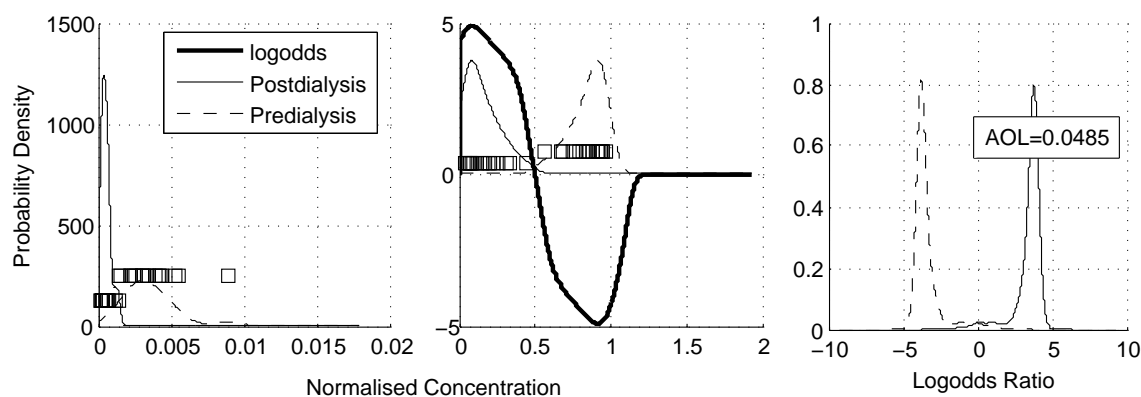


Figure 4.9 Probability density profiles for Mass 43 obtained via raw and normalised, pre and post dialysis datasets with the H_3O^+ precursor. Log-odds probability density profile for identification of biomarkers is shown, *right*.

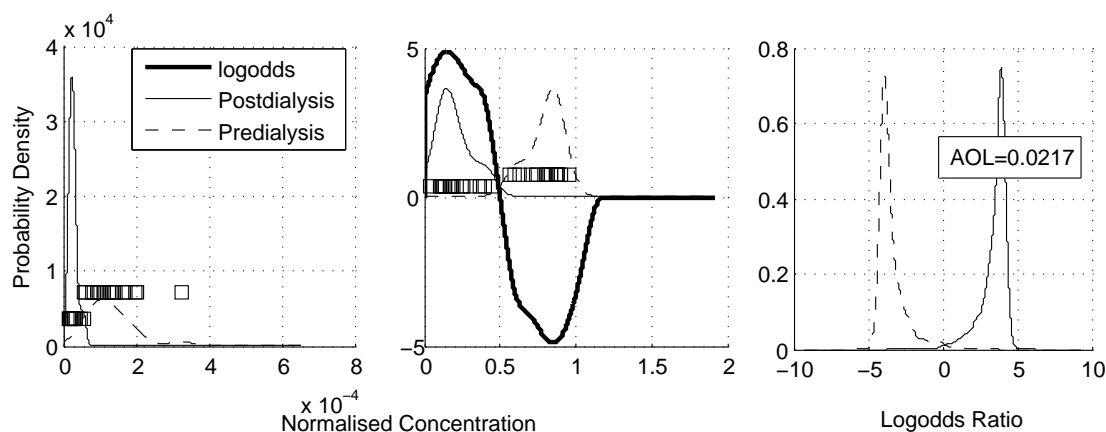


Figure 4.10 Probability density profiles for Mass 44 obtained via raw and normalised, pre and post dialysis datasets with the H_3O^+ precursor.

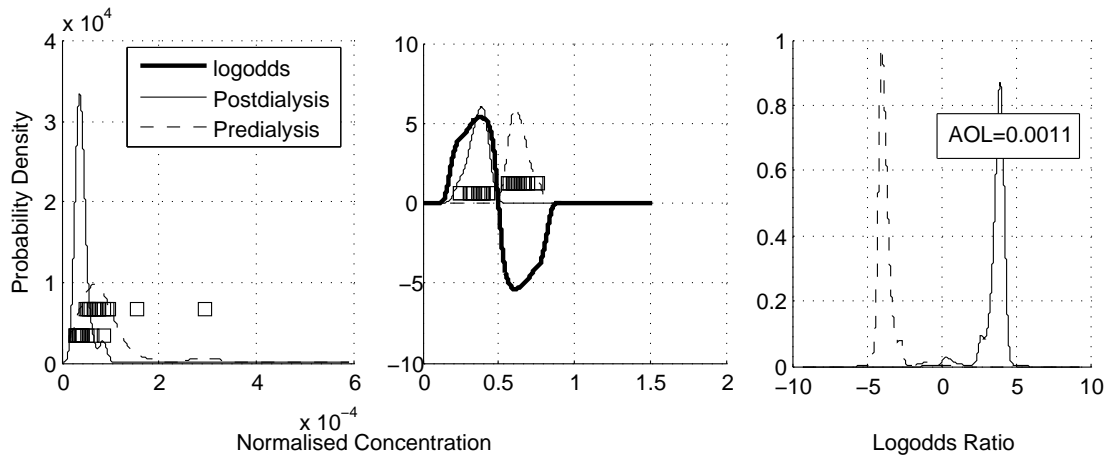


Figure 4.11 Probability density profiles for Mass 58 obtained via raw and normalised, pre and post dialysis datasets with the H_3O^+ precursor.

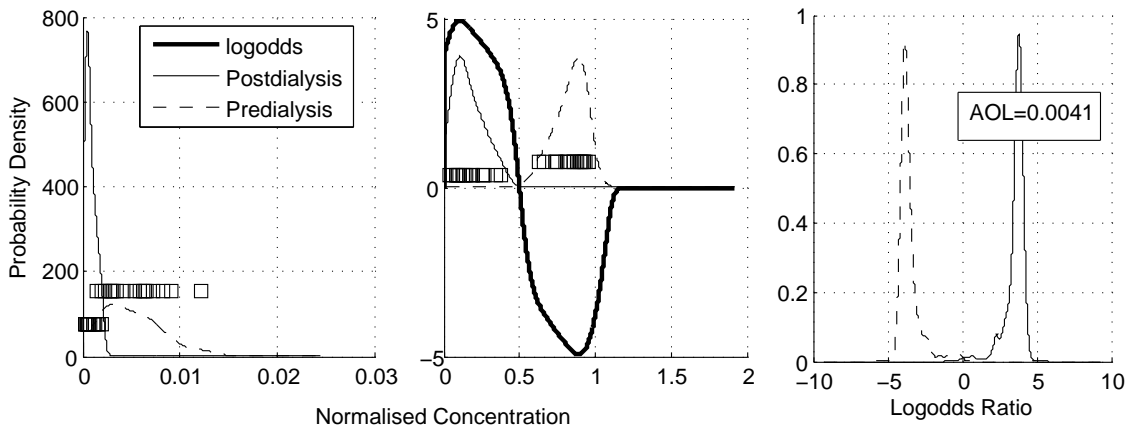


Figure 4.12 Probability density profiles for Mass 61 obtained via raw and normalised, pre and post dialysis datasets with the H_3O^+ precursor.

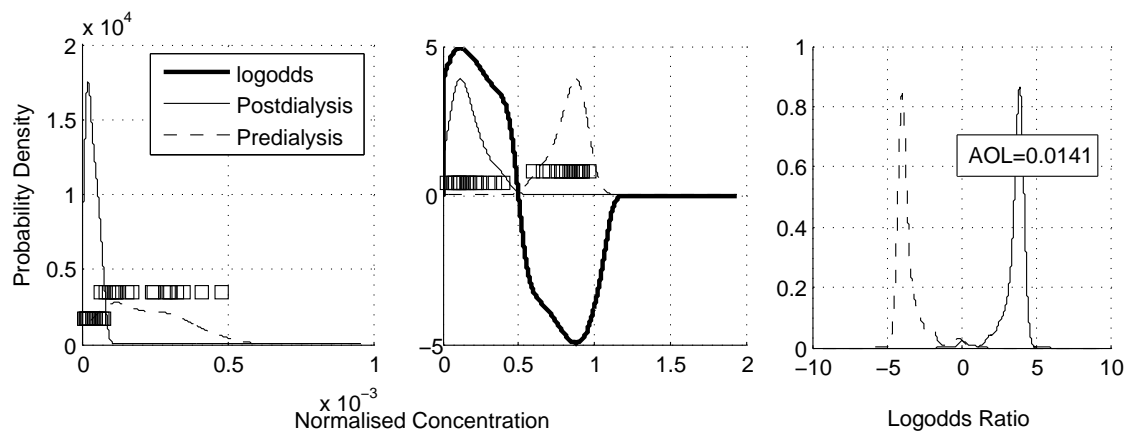


Figure 4.13 Probability density profiles for Mass 62 obtained via raw and normalised, pre and post dialysis datasets with the H_3O^+ precursor.

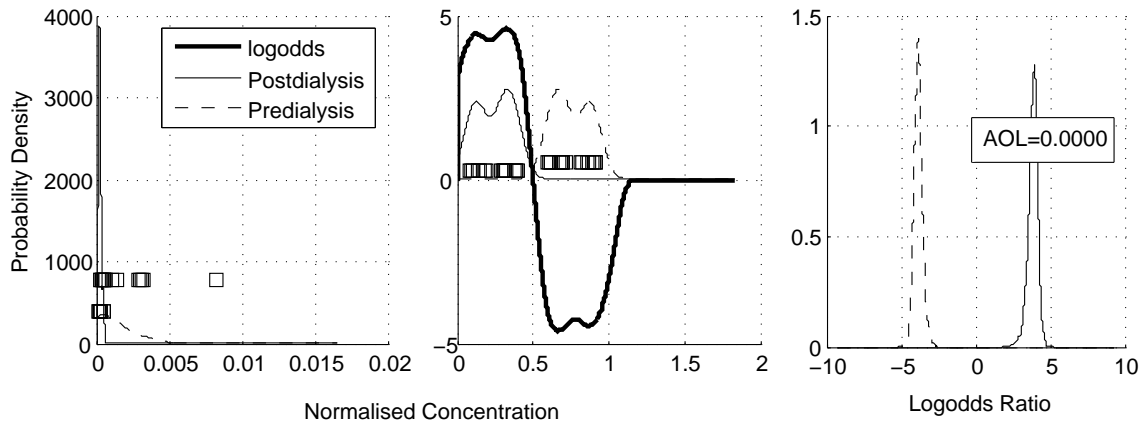


Figure 4.14 Probability density profiles for Mass 78 obtained via raw and normalised, pre and post dialysis datasets with the H_3O^+ precursor.

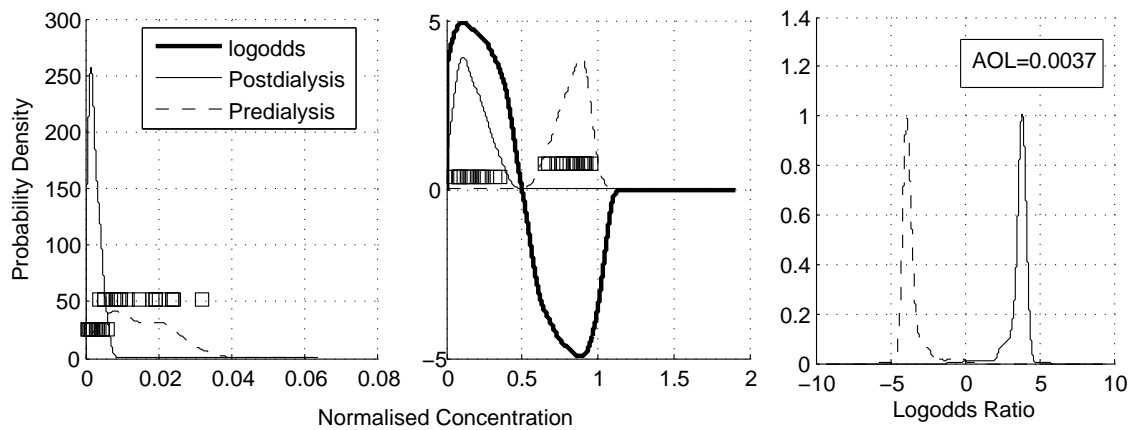


Figure 4.15 Probability density profiles for Mass 79 obtained via raw and normalised, pre and post dialysis datasets with the H_3O^+ precursor.

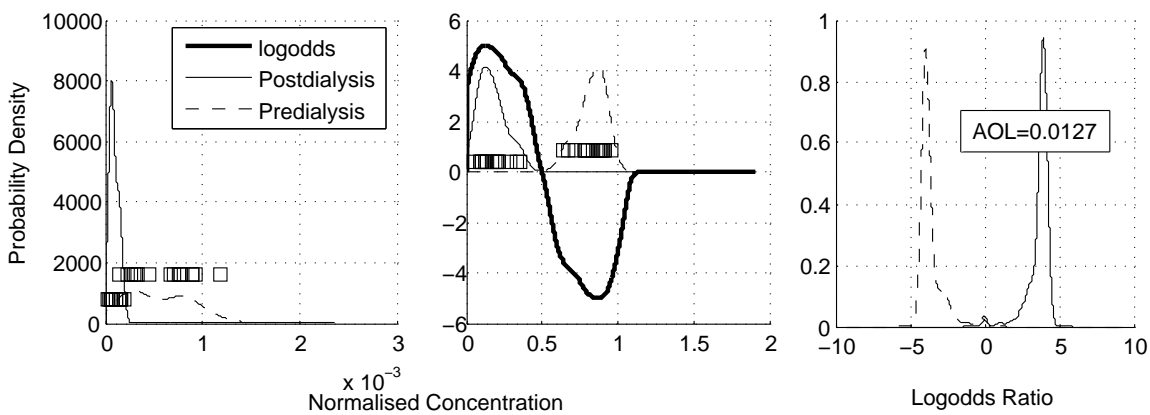


Figure 4.16 Probability density profiles for Mass 80 obtained via raw and normalised, pre and post dialysis datasets with the H_3O^+ precursor.

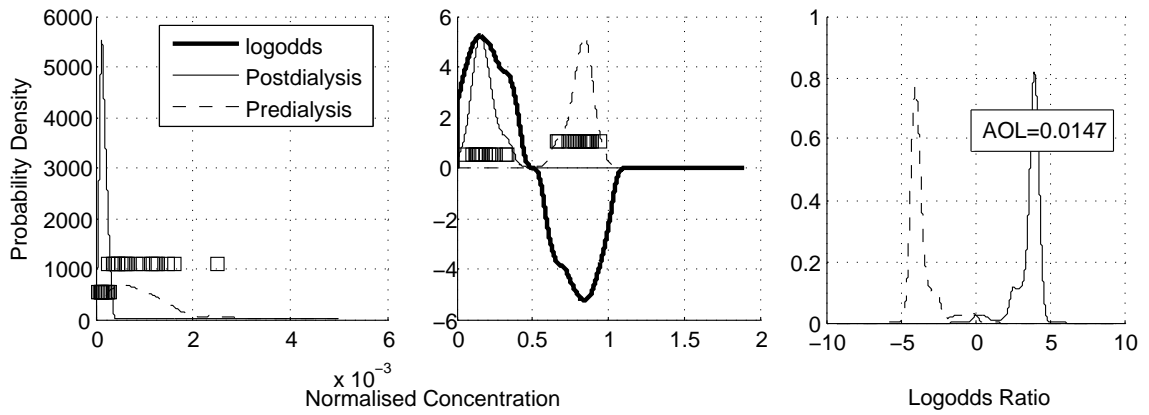


Figure 4.17 Probability density profiles for Mass 97 obtained via raw and normalised, pre and post dialysis datasets with the H_3O^+ precursor.

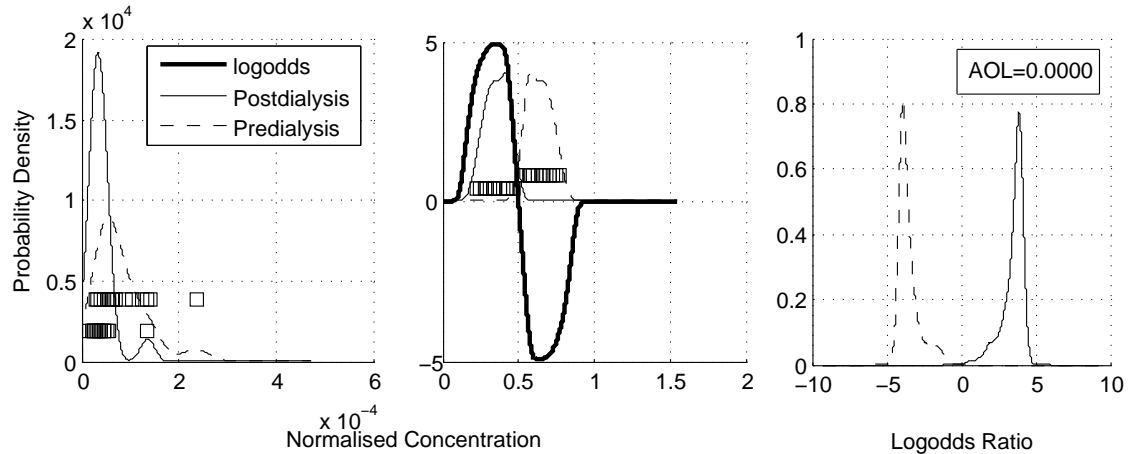


Figure 4.18 Probability density profiles for Mass 118 obtained via raw and normalised, pre and post dialysis datasets with the H_3O^+ precursor.

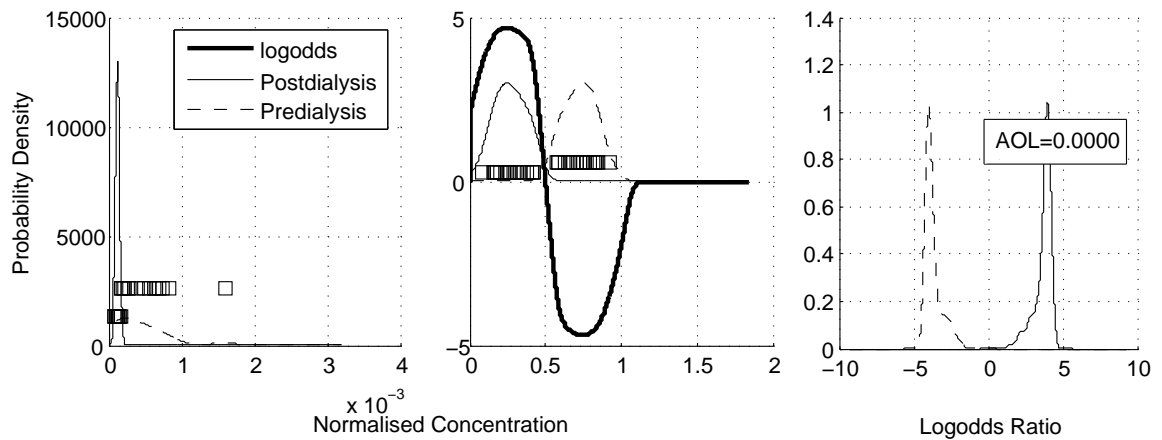


Figure 4.19 Probability density profiles for Mass 121 obtained via raw and normalised, pre and post dialysis datasets with the H_3O^+ precursor.

It is noted in Figures 4.9-4.19 that probability density profiles created from the raw concentration data did not display good separation between pre and post dialysis states. However, the *centre* figures show that this limitation was greatly alleviated by adoption of the relative change normalisation technique from Section 3.1. The *right* figures then show that the classification model could indeed easily distinguish between the pre and post dialysis states, as observed by the very low AOL of probability density profiles.

4.1.2.2 NO^+

Using the NO^+ precursor, Figure 4.20 was obtained from classification of the raw data. A 20.0% classification error and a ROC area of 0.797 was observed with a bootstrap sample size of 200.

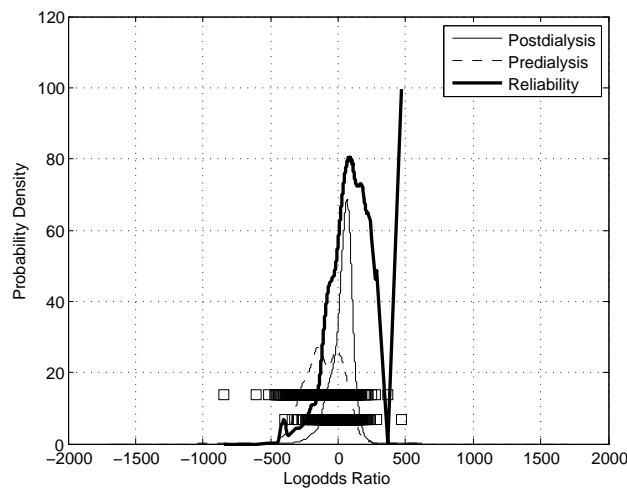


Figure 4.20 Classification on *raw* data over all masses with the NO^+ precursor, as determined by Equation (2.3)

When the relative change method was employed (Equation (3.1)), Figure 4.21 was obtained, with a 0% classification error and a 0.999 ROC area with a bootstrap sample size of 200. Using the biomarker identification method (Equation (3.3)), Figure 4.22 was obtained.

A summary of the top biomarkers identified using each method for the NO^+ precursor is shown in Table 4.4, with their respective scores.

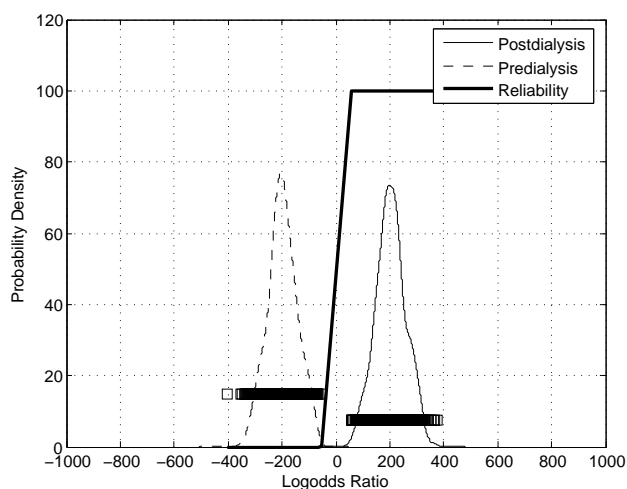


Figure 4.21 Classification on *normalised* data over all masses (Equation (3.1) with the NO^+ precursor, as determined by Equation (2.3)

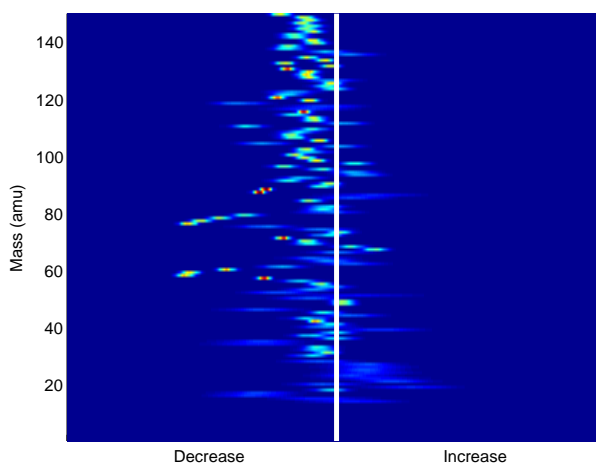


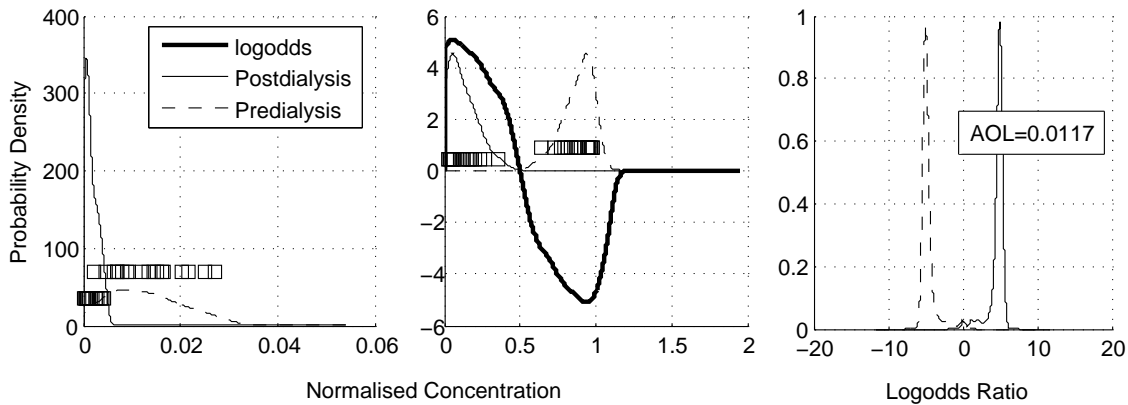
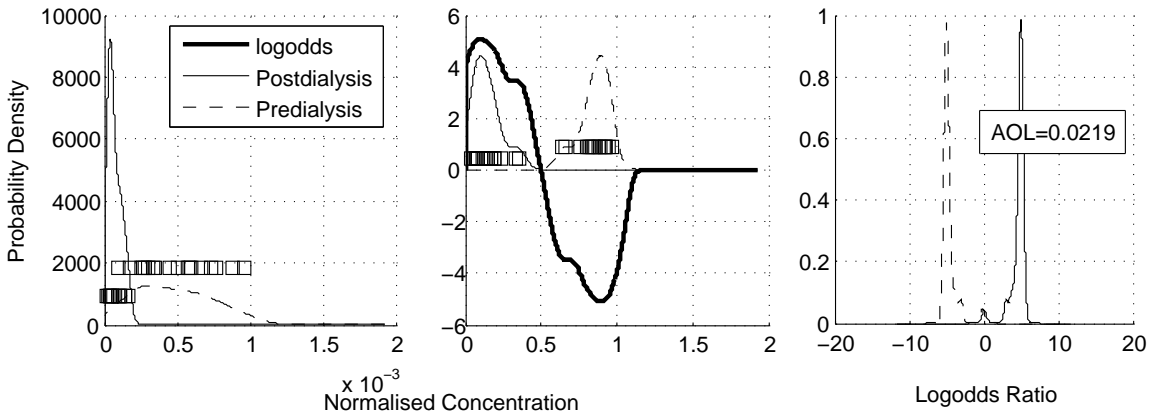
Figure 4.22 Biomarker identification in Dialysis Study II with the NO^+ precursor

Masses 59 and 77 are products of the reaction with TMA, masses 60 and 78 are products of the reaction with acetic acid, and mass 88 arises from the reaction with acetone. The origin of mass 61 is unknown. However, masses 79 and 97 are mass 61 associated with water clusters.

Figures 4.23- 4.32 show the density profiles of the top biomakers. Left, density profile of the raw data; centre, density profile of the relative data; right, density profile of the log-odds ratio of the relative data.

Table 4.4 Dialysis Study II Top Biomarkers with NO^+ precursor

Classification Method				Biomarker ID	
Raw Data		Relative Data		Method	
Mass	Score	Mass	Score	Mass	Score
60	0.1103	89	0.0000	77	26.82
59	0.1149	152	0.0000	59	26.47
78	0.1616	79	0.0000	60	25.28
77	0.2085	61	0.0001	78	21.10
80	0.3004	72	0.0012	88	19.86
61	0.3058	77	0.0035	61	19.00
79	0.3223	78	0.0046	89	18.97
151	0.3248	88	0.0069	58	16.79
121	0.3723	58	0.0103	79	16.31
97	0.3906	154	0.0111	154	13.39

**Figure 4.23** Probability density profiles for Mass 59 obtained from raw and normalised, pre and post dialysis datasets using the NO^+ precursor.**Figure 4.24** Probability density profiles for Mass 60 obtained from raw and normalised, pre and post dialysis datasets using the NO^+ precursor.

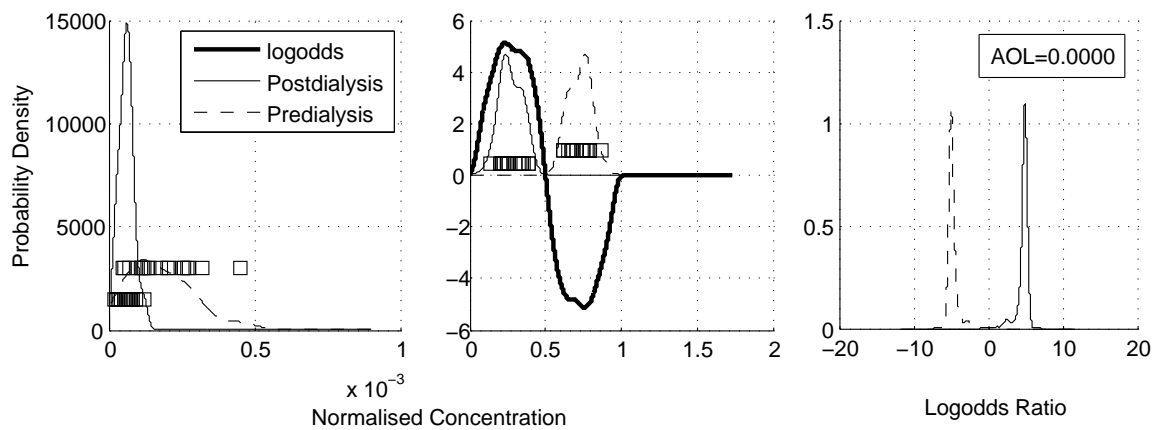


Figure 4.25 Probability density profiles for Mass 61 obtained from raw and normalised, pre and post dialysis datasets using the NO^+ precursor.

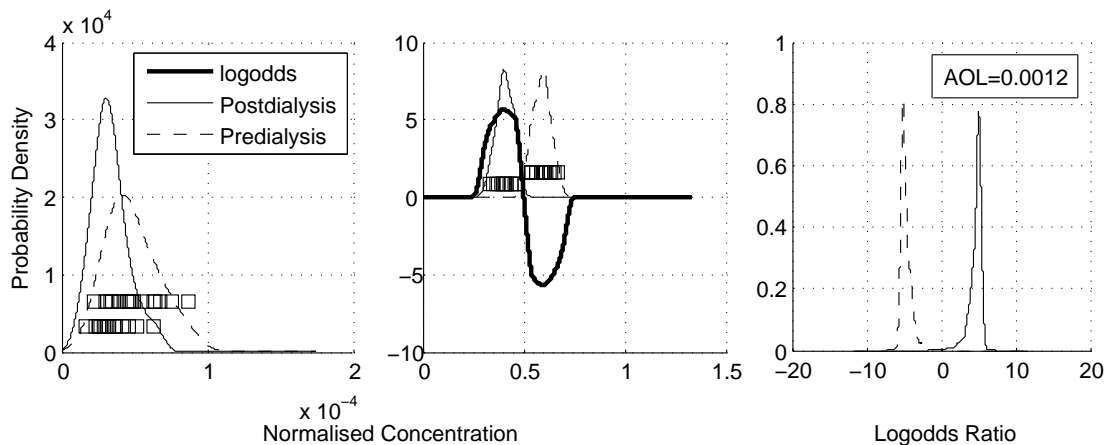


Figure 4.26 Probability density profiles for Mass 72 obtained from raw and normalised, pre and post dialysis datasets using the NO^+ precursor.

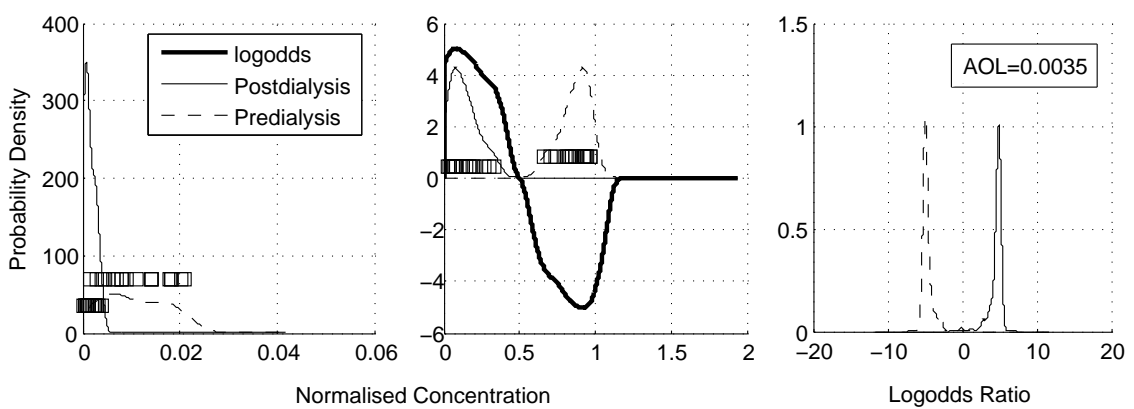


Figure 4.27 Probability density profiles for Mass 77 obtained from raw and normalised, pre and post dialysis datasets using the NO^+ precursor.

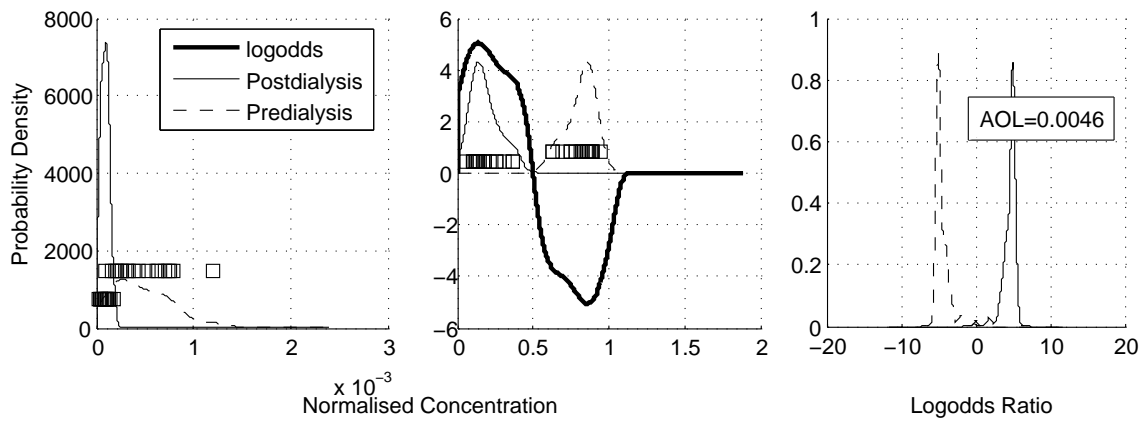


Figure 4.28 Probability density profiles for Mass 78 obtained from raw and normalised, pre and post dialysis datasets using the NO^+ precursor.

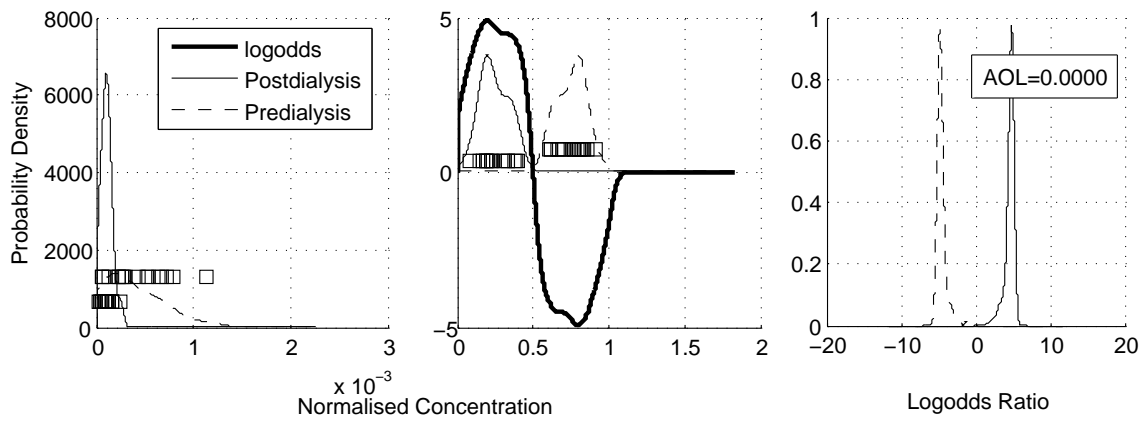


Figure 4.29 Probability density profiles for Mass 79 obtained from raw and normalised, pre and post dialysis datasets using the NO^+ precursor.

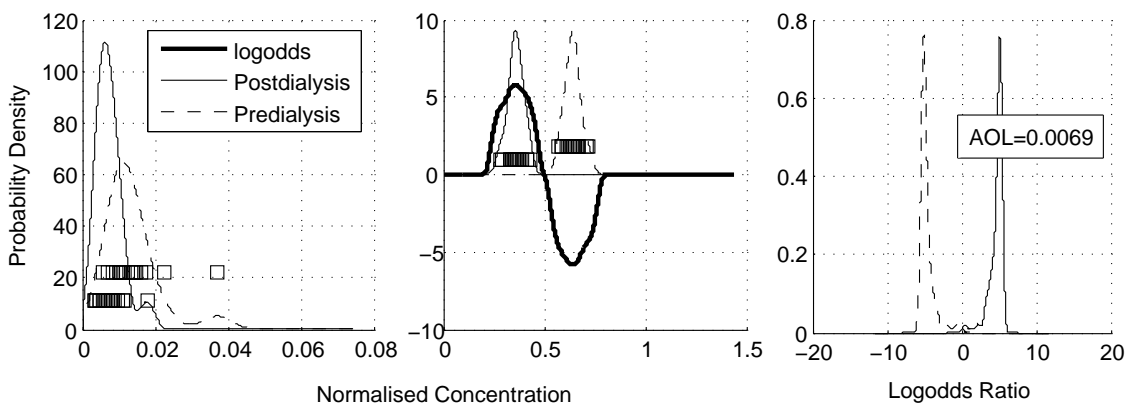


Figure 4.30 Probability density profiles for Mass 88 obtained from raw and normalised, pre and post dialysis datasets using the NO^+ precursor.

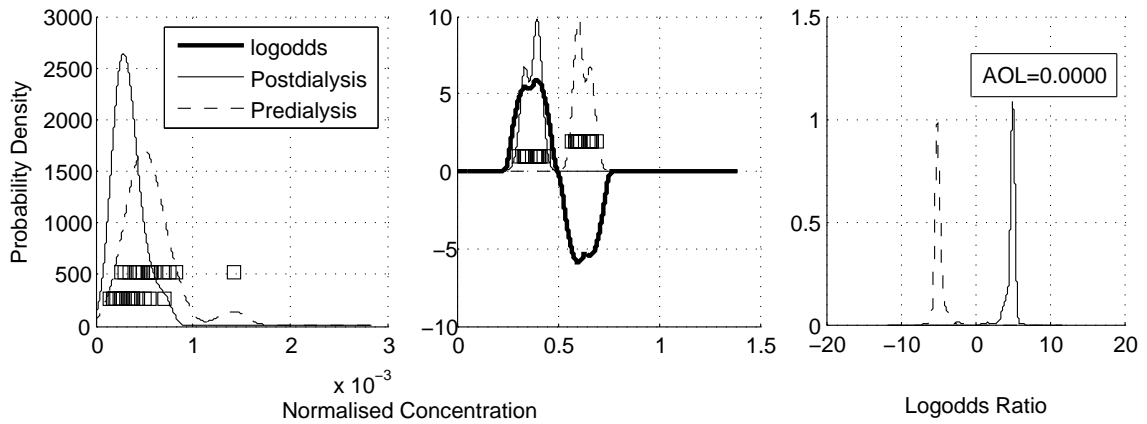


Figure 4.31 Probability density profiles for Mass 89 obtained from raw and normalised, pre and post dialysis datasets using the NO^+ precursor.

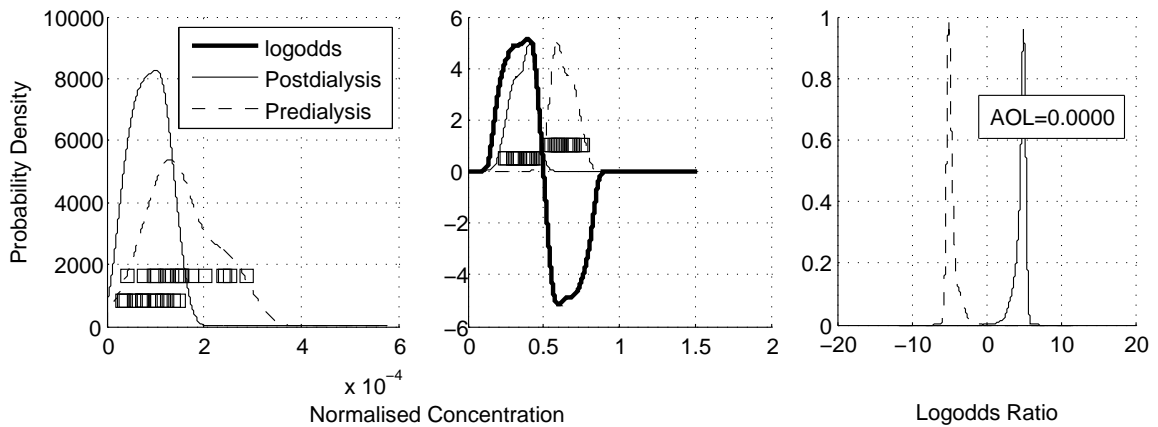


Figure 4.32 Probability density profiles for Mass 152 obtained from raw and normalised, pre and post dialysis datasets using the NO^+ precursor.

4.1.2.3 O_2^+

Using the O_2^+ precursor, Figure 4.33 was obtained from classification off raw data. A 20.2% classification error and a ROC area of 0.790 was observed with a bootstrap sample size of 200. When the relative change method was employed (Equation (3.1)), Figure 4.34 was obtained, with a 0% classification error and a 0.998 ROC area with a bootstrap sample size of 200. Using the biomarker identification method (Equation (3.3)), Figure 4.35 was obtained.

A summary of the top biomarkers identified using each method is shown in Table 4.5, with their respective scores.

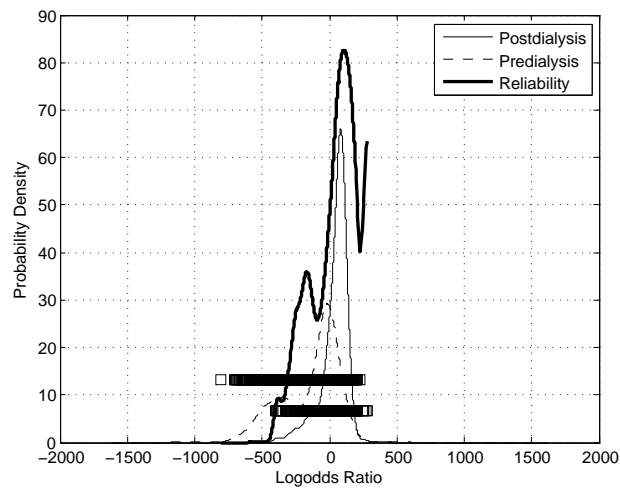


Figure 4.33 Classification on *raw* data over all masses with the O_2^+ precursor, as determined by Equation (2.3)

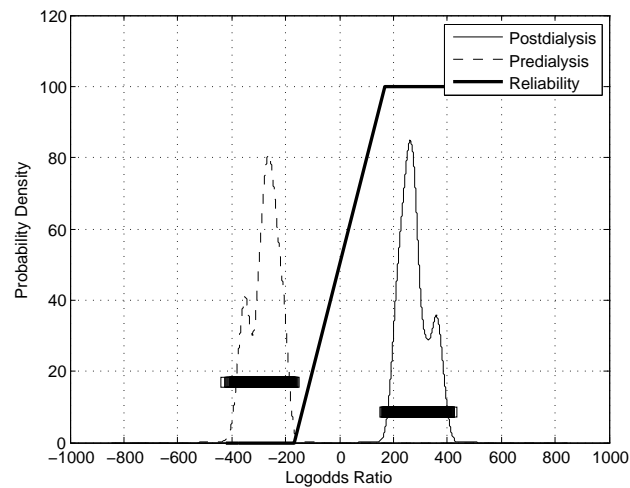


Figure 4.34 Classification on *normalised* data over all masses (Equation (3.1)) with the O_2^+ precursor, as determined by Equation (2.3)

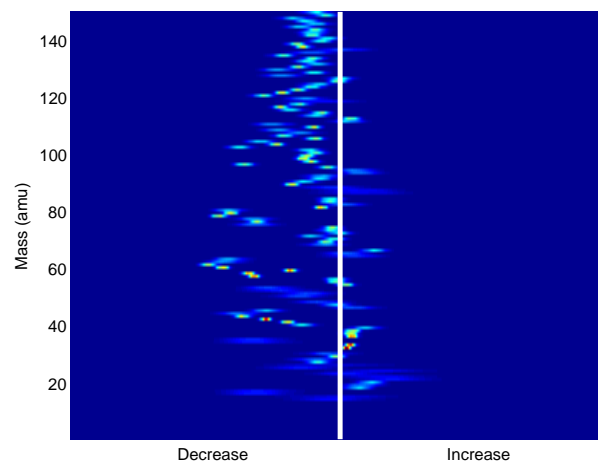


Figure 4.35 Biomarker identification in Dialysis Study II with the O_2^+ precursor

Table 4.5 Dialysis Study II Top Biomarkers with O_2^+ precursor

Classification Method				Biomarker ID	
Raw Data		Relative Data		Method	
Mass	Score	Mass	Score	Mass	Score
81	0.1103	43	0.0000	61	28.06
44	0.1149	151	0.0000	80	24.60
45	0.1616	58	0.0000	62	24.51
103	0.2085	79	0.0001	79	24.03
151	0.3004	60	0.0003	58	22.94
80	0.3058	80	0.0010	59	22.18
63	0.3223	59	0.0015	43	21.95
64	0.3248	78	0.0017	44	19.38
188	0.3723	97	0.0033	97	15.96
62	0.3906	42	0.0038	77	14.99

With the O_2^+ precursor, several of the key masses overlap. Masses 43, 60, 61, 79 and 97 are associated with acetic acid; masses 43, 58, 59, 61, 77, 79, 97 are associated with acetone; and masses 58, 59 and 77 are associated with TMA.

Figures 4.36-4.46 show the density profiles of the top biomarkers. The *left* plot shows the density profile of the raw data. The *centre* plot shows the density profile of the *normalised* data. Finally, the *right* plot shows the density profile of the log-odds ratio of the *normalised* data.

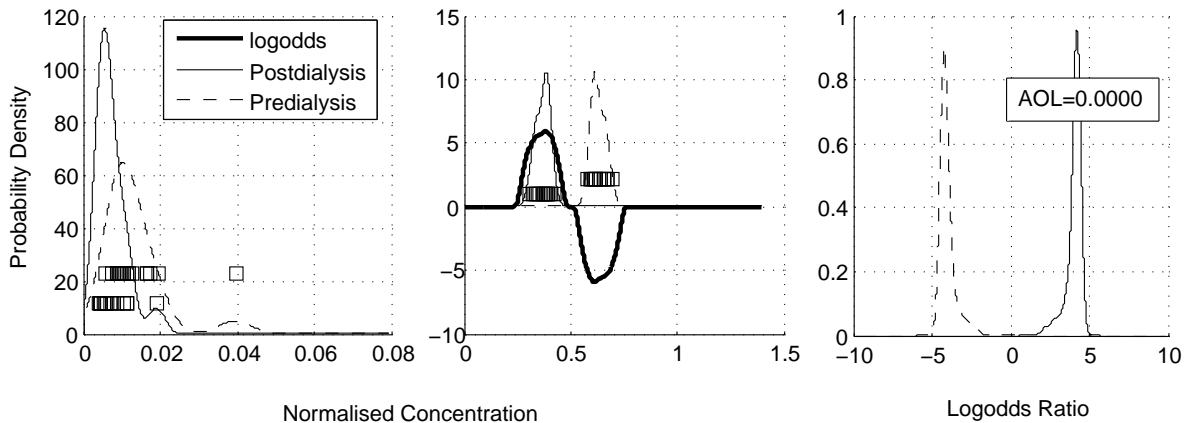


Figure 4.36 Probability density profiles for Mass 43 obtained from raw and normalised, pre and post dialysis datasets using the O_2^+ precursor.

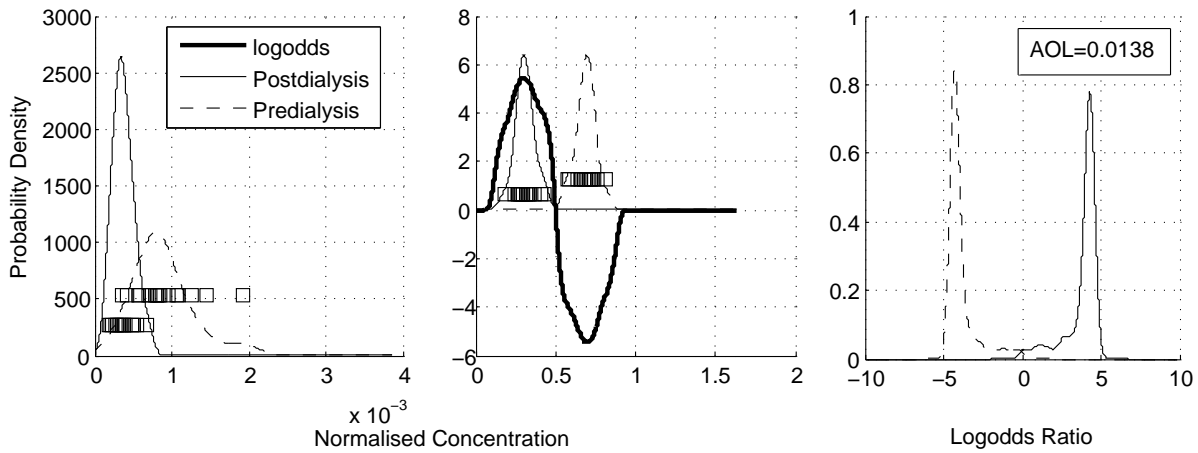


Figure 4.37 Probability density profiles for Mass 44 obtained from raw and normalised, pre and post dialysis datasets using the O_2^+ precursor.

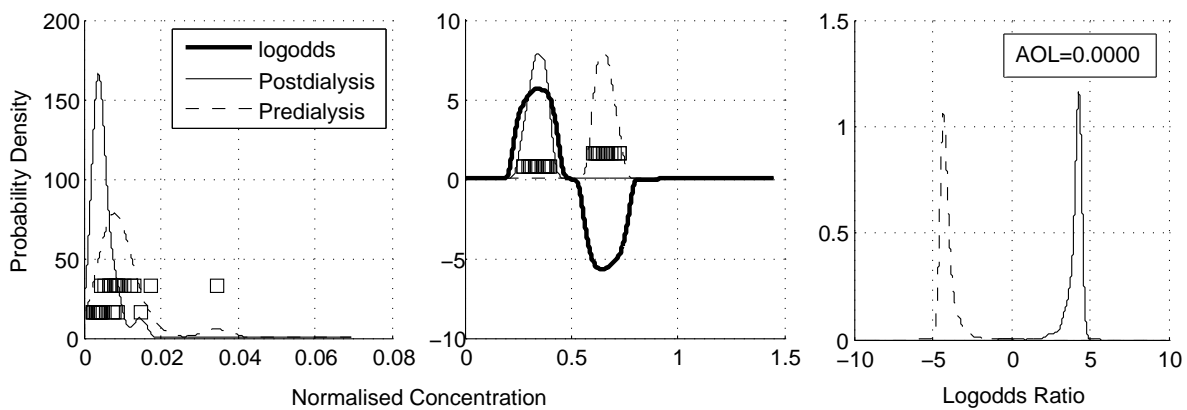


Figure 4.38 Probability density profiles for Mass 58 obtained from raw and normalised, pre and post dialysis datasets using the O_2^+ precursor.

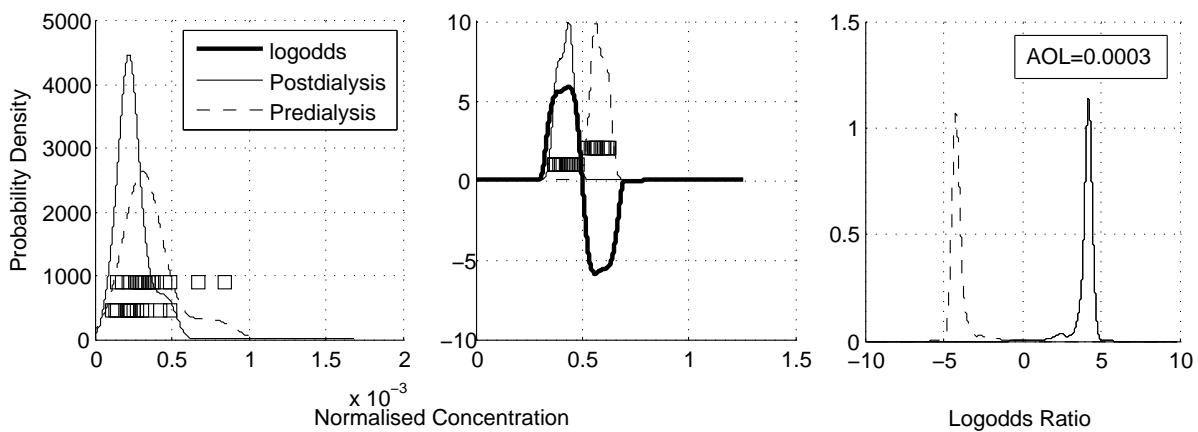


Figure 4.39 Probability density profiles for Mass 60 obtained from raw and normalised, pre and post dialysis datasets using the O_2^+ precursor.

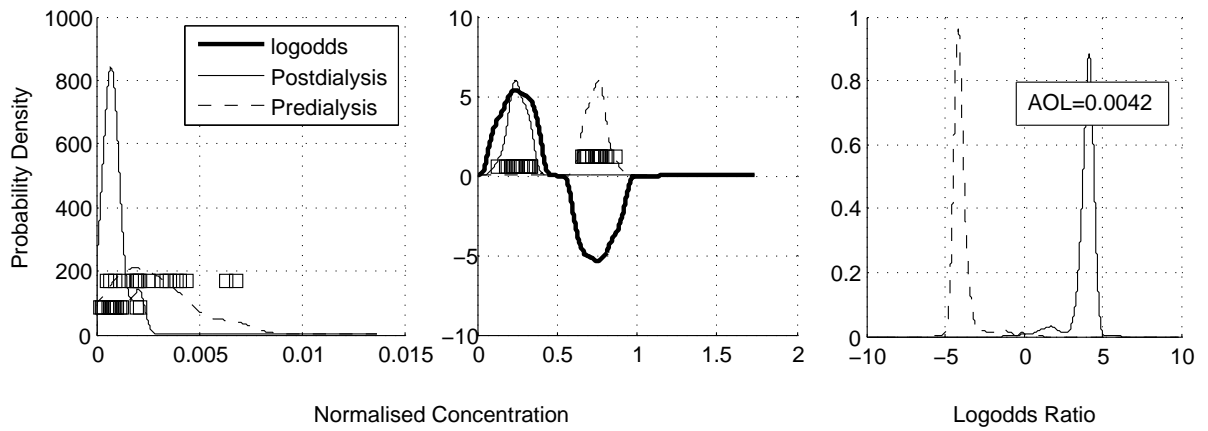


Figure 4.40 Probability density profiles for Mass 61 obtained from raw and normalised, pre and post dialysis datasets using the O_2^+ precursor.

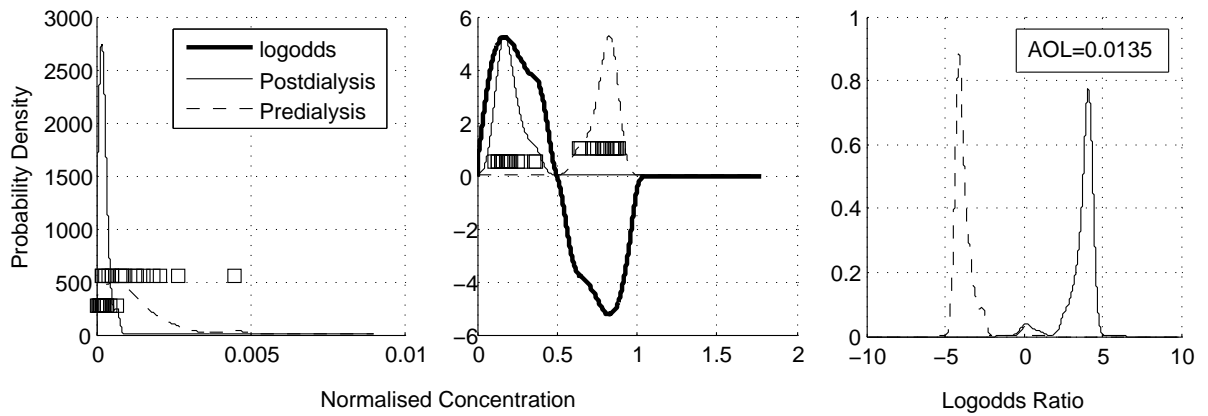


Figure 4.41 Probability density profiles for Mass 62 obtained from raw and normalised, pre and post dialysis datasets using the O_2^+ precursor.

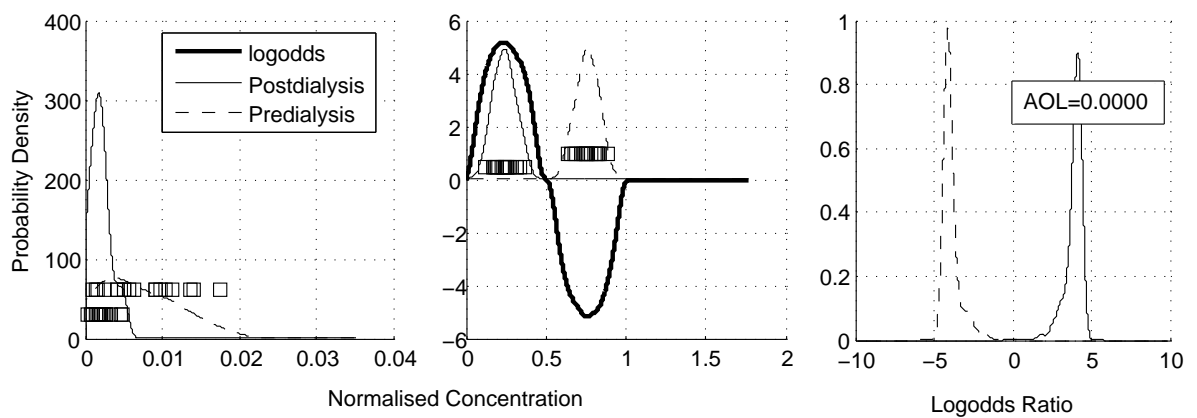


Figure 4.42 Probability density profiles for Mass 79 obtained from raw and normalised, pre and post dialysis datasets using the O_2^+ precursor.

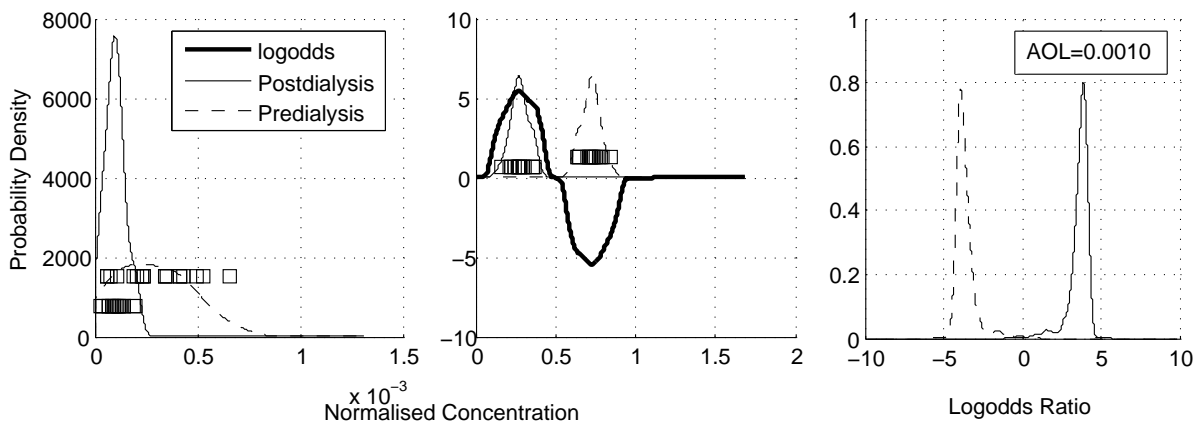


Figure 4.43 Probability density profiles for Mass 80 obtained from raw and normalised, pre and post dialysis datasets using the O_2^+ precursor.

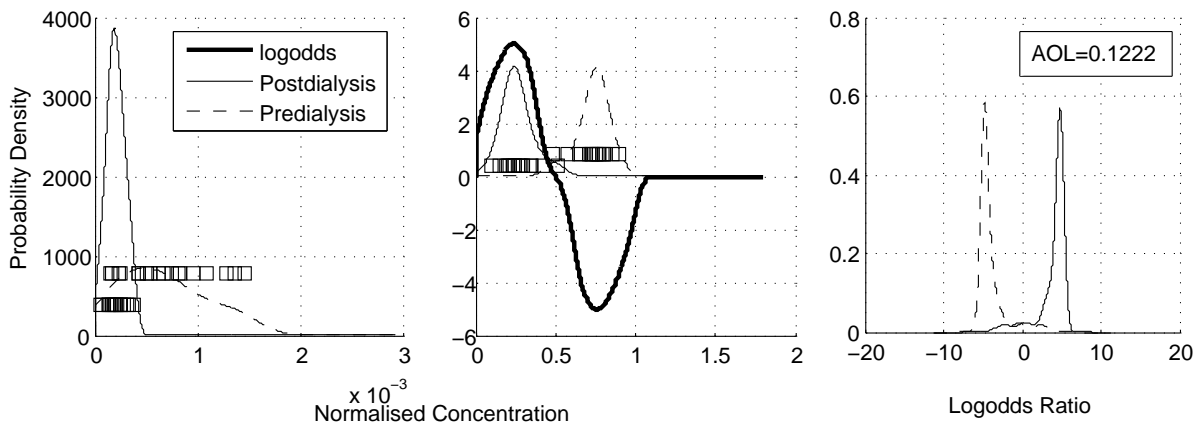


Figure 4.44 Probability density profiles for Mass 81 obtained from raw and normalised, pre and post dialysis datasets using the O_2^+ precursor.

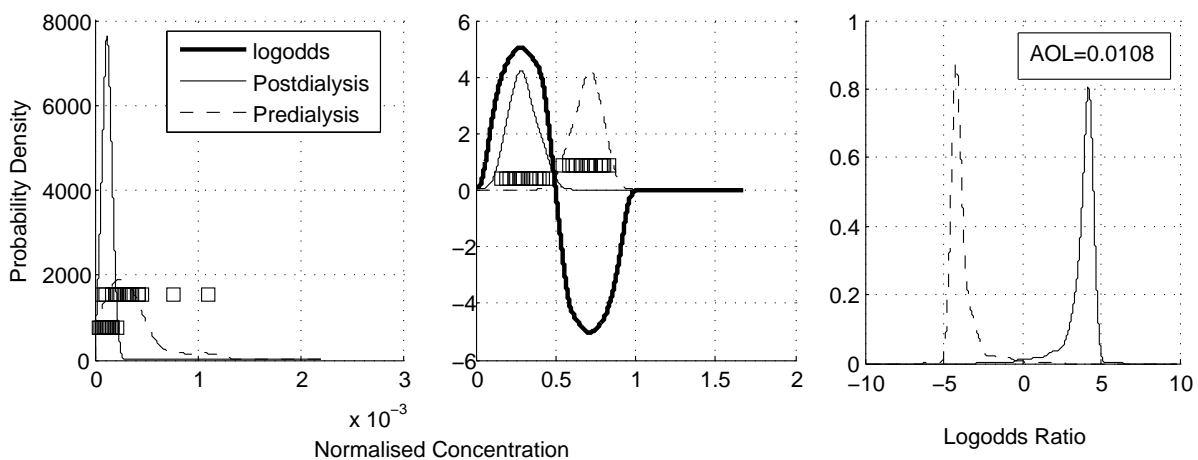


Figure 4.45 Probability density profiles for Mass 103 obtained from raw and normalised, pre and post dialysis datasets using the O_2^+ precursor.

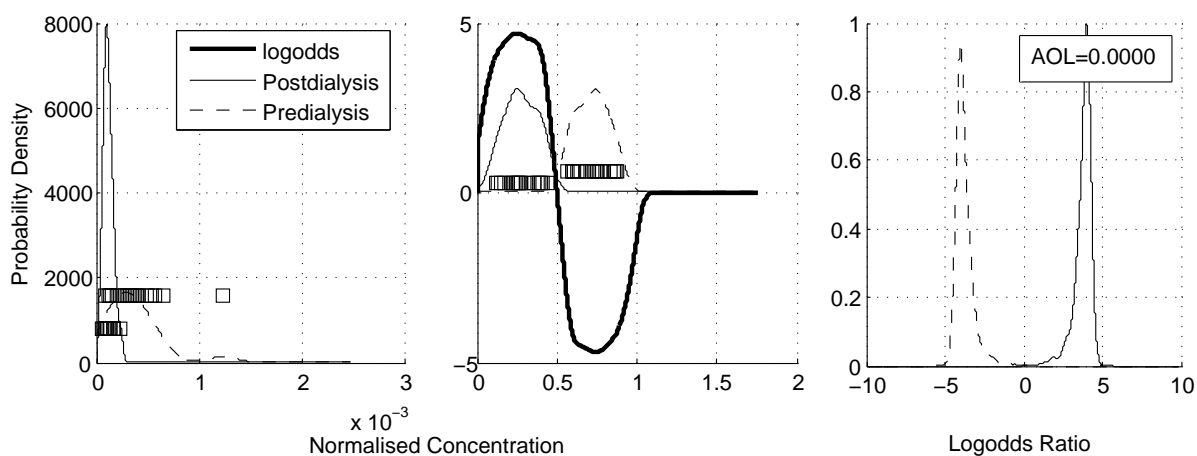


Figure 4.46 Probability density profiles for Mass 151 obtained from raw and normalised, pre and post dialysis datasets using the O_2^+ precursor.

4.2 Summary and Future Work

A clinical study was carried out in two parts to monitor the change in ammonia, TMA and acetone as measured by SIFT-MS over the course of dialysis treatment. In renal failure, the kidney fails to effectively excrete metabolic wastes and hence these accumulate in the blood, and can be measured in the breath. The relative and absolute changes in analyte concentration were compared with the changes in BUN and creatinine, the gold standards of kidney function. Correlations were much improved in the second part of the study, with the introduction of the *Voice200*[®] SIFT-MS instrument, direct breath sampling methods, and a more stable patient cohort. Statistically significant correlations were observed between the reduction ratios of breath ammonia, breath TMA, BUN and creatinine in the second study.

Mass scan analysis was performed on breath samples collected in tedlar bags, for the purpose of detecting biomarkers of kidney function revealed when comparing the predialysis and postdialysis breath samples. Since dialysis efficacy is most simply reported as the URR, a reduction ratio, mass scan analysis was performed using the relative change in states between the beginning and end of dialysis treatment. Several biomarkers were identified, including TMA, acetic acid and acetone, all of which scored better than ammonia in the first study. Since acetic acid is usually metabolised to by the liver to CO_2 and water, its identification in this study as a biomarker is more likely to be related to the fact that patients were eating during the dialysis session, than to any indication of

renal impairment in CRF. A 0% classification error was recorded for all precursors in the second study, whereas in the first study, estimated prediction errors ranged from 2-10% over the 3 precursors.

Future work aims to develop a predictive model for determining the optimal time to dialyse a patient. Results from Study II indicate that TMA would be a good analyte to monitor, since its concentration decreases rapidly regardless of starting concentration, and is maintained at a relatively constant, low concentration during dialysis. As such, it is suggested that breath TMA measured over the first 30 minutes of a dialysis session gives a good measure of the efficacy of clearance from the plasma. A clinical study is currently underway to collect breath samples from patients who have undergone a kidney transplant, in the weeks following their recovery. It is envisaged that analysis of breath analytes could help predict rejection episodes by observing deviations from the improvement of renal function, as monitored by changes in key breath analytes.

Carrying out a trial in a human setting poses difficulties, since all patients present with a differing degree of impairment, have differing diets, and differing genetic predispositions. It was considered that running an animal trial would alleviate many of these difficulties, since in-bred animals could be used in the study. In addition, sample sizes, diet, and daily behaviour, as well as degree of renal impairment, could all be more easily controlled. Lastly, easy comparison with gold standard measures of renal function would be possible, since several techniques in addition to creatinine and BUN blood tests would be available. Such techniques include radioactive tracer methods, which cannot be performed in a human clinical trial. Hence, an animal trial was designed for the identification of biomarkers of acute renal failure in rats, as described in Chapter 5.

Chapter 5

Acute Renal Failure in Rats - Animal Study Design

5.1 Kidney Anatomy and Physiology

5.1.1 Kidney Structure and Function

The kidney is the major vertebrate organ for excretion and salt and water balance. It is also involved in acid-base balance, hormone production, and long-term control of blood pressure. The functional unit of the kidney is the nephron, which consists of the malpighian body and the tubule. The malpighian body is found in the renal cortex and consists of the glomerulus encased in *Bowman's capsule*, as shown in Figure 5.1.

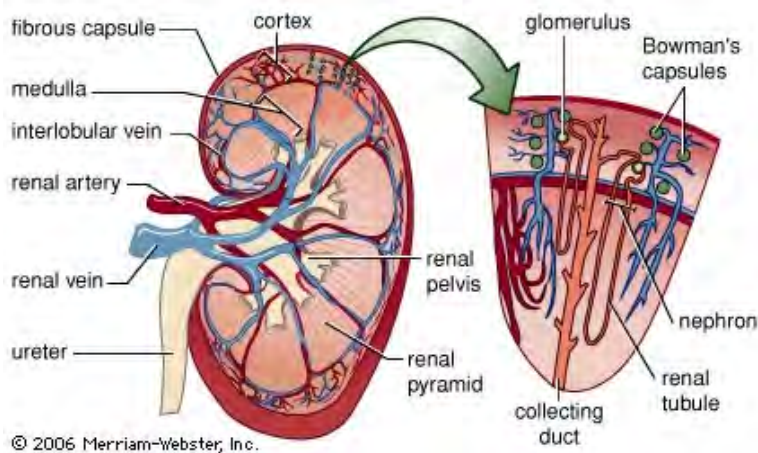


Figure 5.1 Kidney Anatomy, Merriam-Webster [2006]

The glomerulus is a bundle of capillaries, originating from an afferent arteriole from the renal artery, and exiting to an efferent arteriole where it diverges into the peritubular capillary network. Blood plasma is filtered from the glomerulus into Bowman's capsule by a process called ultrafiltration. The ultrafiltrate, or primary urine, contains glucose, amino acids, ions and nitrogenous wastes in the same concentrations as in the blood plasma, but lacks the large plasma proteins, which do not fit through the small pores in the glomerular capillary wall.

From Bowman's capsule, primary urine enters the proximal convoluted tubule (PCT), which descends into the loop of Henle in the renal medulla. The ascending limb of the loop of Henle comes back to the cortex and becomes the distal convoluted tubule (DCT). The DCTs of many nephrons join in a common collecting duct in the cortex, and then run back through the medulla to empty into the ureter at the tips of the renal pyramid, as shown in Figure 5.2.

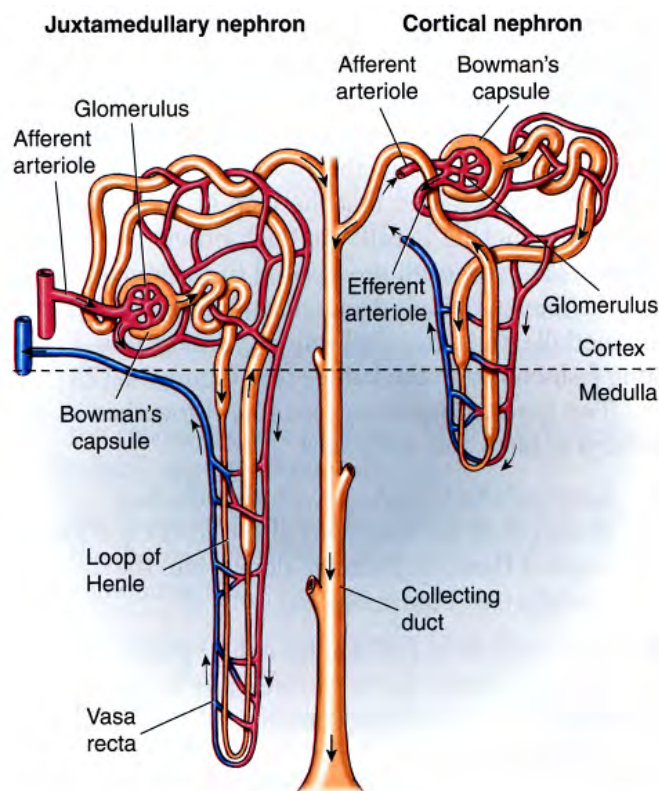


Figure 5.2 Structure of a nephron, Randall et al. [2002]

Once entering the tubules, the composition of the primary urine changes as secretion and reabsorption takes place. Most of the water and solutes filtered by the glomerulus are reabsorbed in the PCT. Na^+ , amino acids and other solutes are actively transported out of the tubular fluid and into the interstitial fluids, and

water follows passively to maintain osmotic pressure. Other passively reabsorbed substances include Cl^- , HCO_3^- , and urea. Reabsorbed water and solutes are taken up by the peritubular capillaries and exit the kidney via the renal vein. The epithelial cells in the PCT are structured for massive salt and water reabsorption, with numerous microvilli forming a brush border which increases the surface area available for reabsorption. Details of the PCT epithelial cell are shown in Figure 5.3.

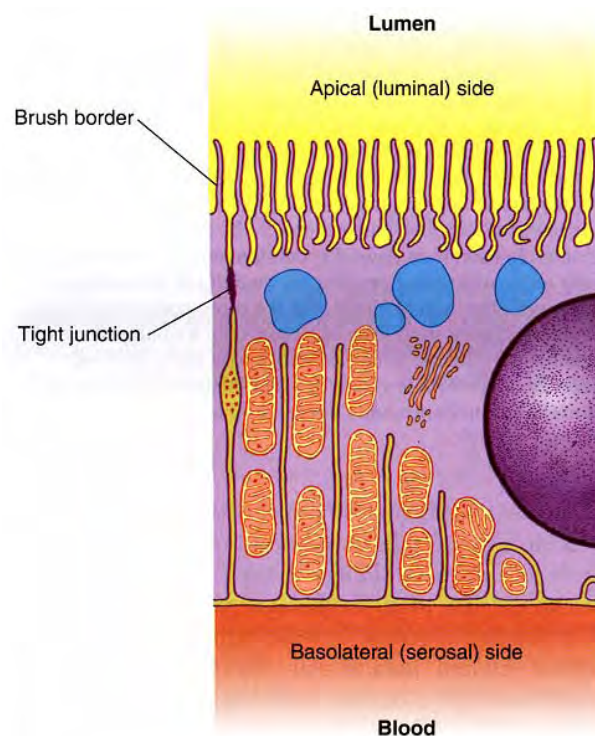


Figure 5.3 PCT Epithelial Cell, Randall et al. [2002]

The loop of Henle acts as a countercurrent multiplier to establish a concentration gradient in the renal medulla. Cells in the descending limb are non-specialised and allow passive transport of water out of the tubular fluid, but have very low permeability to salt. In the ascending limb, salt is actively transported out into the interstitial fluid, but water cannot follow because this region of the tubule is impermeable to water. Salt in the interstitial fluid then diffuses back around the descending limb of the loop of Henle, where the osmotic gradient causes water to move out into the interstitial fluid, thus concentrating the tubular fluid as it passes down the descending limb. The active transport of salt out of the ascending limb results in a tubular fluid that is more dilute when it enters the DCT than when it entered the PCT. Salt continues to be actively transported out in the DCT, and water follows passively. Tubular fluid entering the collecting duct from the DCT is much more dilute than the interstitial fluid in the medulla,

and so when it passes down the collecting duct, which is permeable to water but not to ions, water is reabsorbed to maintain the osmotic potential, and the urine becomes more concentrated.

As well as reabsorbing desired substances back into the plasma, the tubules are also capable of secreting substances directly into the tubular fluid. Such substances include K^+ and H^+ ions, ammonia, and organic acids and bases, such as foreign or toxic substances and endogenous products of metabolism. Secretion is mostly active, driven by the sodium gradient established by the Na^+/K^+ pumps in the tubular membrane. Some of these pumps are non-specific, and can allow the elimination of many potentially dangerous substances, such as drugs and toxins directly from the liver. However, this non-specificity also means that various organic ions can be competing for the same secretory pathway, and therefore elevated levels of one organic compound can reduce the secretion of another. Secretion of ammonia and H^+ are intimately related and are important in the regulation of acid-base homeostasis. Ammonia excretion is discussed further in the next section.

The kidneys are primarily responsible for the excretion of organic wastes. This process occurs via filtration of the blood in the glomerulus of individual nephrons, and reabsorption and secretion of solutes and water in the renal tubules. The resulting tubular fluid is excreted as urine.

5.1.2 Ammonia Excretion

Ammonia is mostly formed from the catabolism of proteins. Ingested and cellular proteins are hydrolysed to form a pool of amino acids. Any amino acids not used in protein production are catabolised to ammonia. This ammonia is either excreted, or converted to urea via the Urea Cycle in the liver.

Ammonia exists biologically as NH_3 and NH_4^+ , with the relative amounts of each governed by the buffer reaction $NH_3 + H^+ \rightleftharpoons NH_4^+$. In most biological fluids, where the pH is less than 7.4, most ammonia is present as NH_4^+ . NH_3 is relatively small and uncharged, thus it can diffuse across most lipid bilayers in the tubular membrane. NH_4^+ has very limited permeability and must be transported across the apical tubular membrane.

Since ammonia is very toxic, it is transported in the blood as glutamine, and on reaching the proximal tubule, it is converted back to ammonia via ammoniogenesis. At this point, ammonia is either transported into the urine as NH_4^+ , mainly via the apical Na^+/H^+ exchanger, or returns to the systemic circulation to be metabolised to urea in the liver, in a ratio governed by acid-base homeostasis. Ammonia can also enter the tubular fluid as NH_3 , by diffusing across the apical membrane, as seen in Figure 5.4. Several different types of ammonia transporters have been identified, of which the family of Rh glycoproteins has been the most recent. The RhBG glycoprotein is expressed in a wide variety of organs involved in ammonia metabolism, including the kidney, liver, skin, stomach and gastrointestinal tract [Weiner and Hamm, 2007].

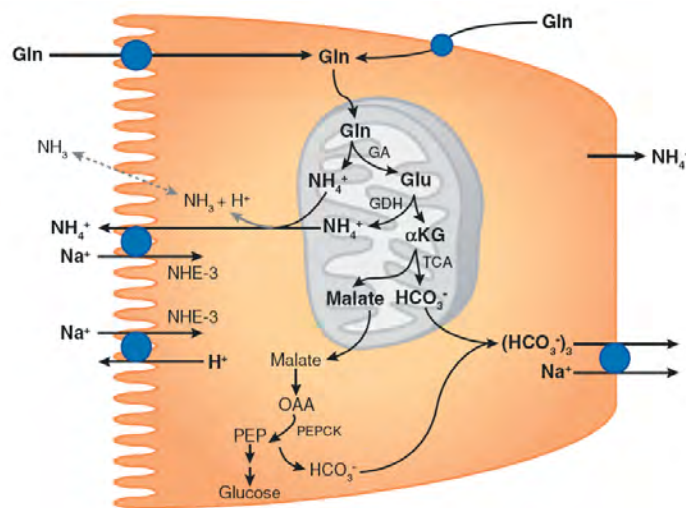


Figure 5.4 Tubular Excretion of Ammonia (Gln-Glutamine; GA-Glutaminase; Glu-Glutamate; GDH-Glutamate Dehydrogenase, Weiner and Hamm [2007])

5.1.3 Glomerular Filtration Rate

Pressure in the glomerular capillaries is relatively high to maintain the Glomerular Filtration Rate, GFR . Autoregulation ensures that GFR remains relatively constant as mean pressure, ΔP , in the renal artery changes, by vasoconstriction and vasodilation of afferent and efferent arterioles. These changes alter the resistance, R , to blood flow, Q , through the kidney, Equation (5.1).

$$Q = \frac{\Delta P}{R} \quad (5.1)$$

This autoregulatory function is achieved through several mechanisms. By

myogenic autoregulation, an increase in blood pressure causes a stretch in the afferent arteriole wall, triggering contraction of smooth muscle cells surrounding the vessel, thus reducing the vessel diameter and increasing the vessel resistance, R :

$$R = \frac{8\mu l}{\pi r^2} \quad (5.2)$$

where μ is the dynamic viscosity of blood, l is the length of the vessel, and r is the radius of the vessel. This increase in resistance counteracts the increase in blood pressure, thus maintaining a constant flowrate, Q , through the vessel. The converse situation is also true, with vessels dilating when blood pressure decreases.

Renal blood flow is also modulated by secretion of substances from cells in the *juxtaglomerular apparatus*. The juxtaglomerular apparatus contains two types of cells: modified distal tubule cells which form the *macula densa* and monitor sodium chloride flux in the distal tubule; and modified smooth muscle cells, called juxtaglomerular or granular cells, which are located mostly in the afferent arterioles and secrete substances which indirectly affect blood flow, as shown in Figure 5.5.

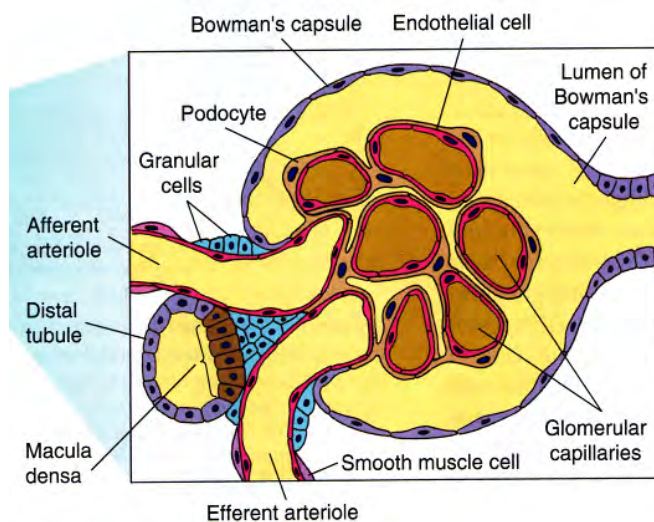


Figure 5.5 Juxtaglomerular Complex for monitoring renal blood flow, Randall et al. [2002]

A reduction in renal blood flow or systemic blood pressure produces a decrease in GFR, which decreases solute delivery to the distal tubule. This decreased solute delivery reduces the sodium chloride flux in the macula densa cells, which in turn

triggers the release of renin from the granular cells, as well as directly producing tubuloglomerular feedback relaxation of efferent arteriolar smooth muscle. When renin is released, the level of the hormone angiotensin II in the blood increases, causing constriction of all arterioles in the body. A rise in angiotensin II also stimulates the release of aldosterone from the adrenal cortex which promotes the tubular reabsorption of salts. Angiotensin II also stimulates an increase in the synthesis of Antidiuretic Hormone (ADH) in the hypothalamus and its release from the posterior pituitary, which increases the water permeability of the distal tubule and collecting duct, thus promoting water reabsorption. Increase in the reabsorption of salts and water increases blood volume and therefore blood pressure, thus restoring GFR via this autoregulatory route.

5.1.4 Renal Histology

The PCT, DCT, collecting ducts and thick segments of the Loop of Henle are lined by a simple cuboidal epithelium, and the thin segments of the loop of Henle are lined with a simple squamous epithelium. The PCT and DCT are found in the renal cortex, whereas the loops of Henle and collecting ducts run mainly through the medulla. The length of a PCT tends to be several times greater than that of a DCT, so sections of proximal tubules are much more common than those of distal tubules in a typical histological slide of renal cortex.

A section of PCT is distinguishable by the brush border of microvilli on the apical end of each cell which provides an increased surface for absorption of substances from the tubular fluid. PCT cells and cells of the thick ascending limb of the loop of Henle have the highest proportion of mitochondria in their cytoplasm, to provide the energy for pumping ions and molecules against their concentration gradient.

The plasma membranes of adjacent PCTs and DCTs are extensively interdigitated to increase the basal membrane surface area available for pumping molecules out the basal end of each cell. Collecting ducts merge and become larger as they descend through the medulla, so different sizes of collecting ducts may be observed at different levels in the kidney, with the smallest in the cortex and the largest near the renal pelvis at the base of the medulla. Normal histological preparations are shown in Figures 5.6-5.8.

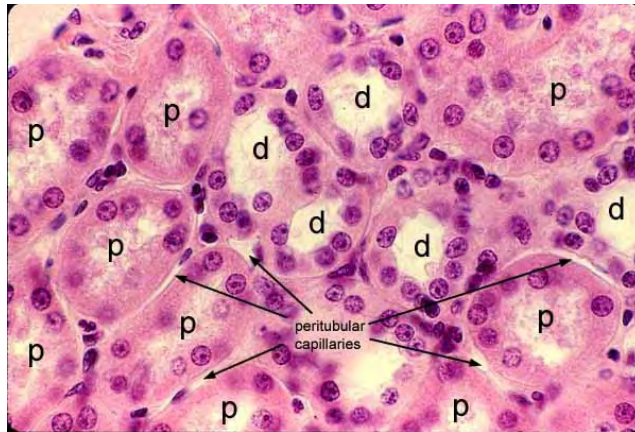


Figure 5.6 Normal Tubular Histology: *p* - Proximal Convoluted Tubule; *d* - Distal Convoluted Tubule, King [2007]

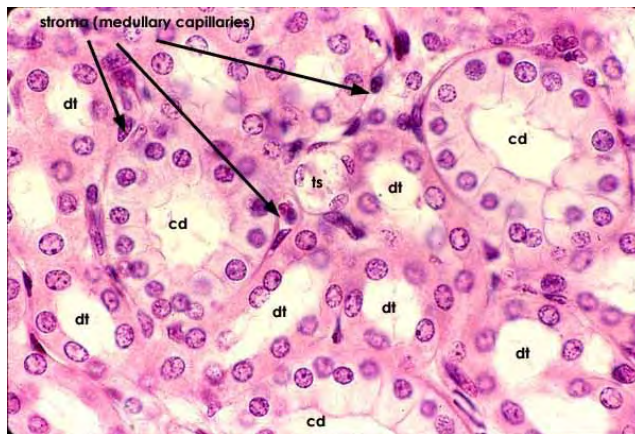


Figure 5.7 Normal Tubular Histology: *cd* - Collecting Duct; *ts* - Thin Segment of Loop of Henle; *d* - Distal Convoluted Tubule, King [2007]

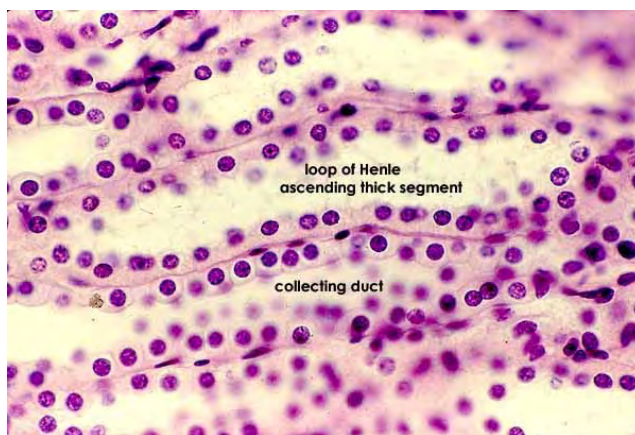


Figure 5.8 Normal Tubular Histology: Longitudinal Section of Collecting Duct and Thick Segment of Loop of Henle, King [2007]

5.1.5 Acute Renal Failure

GFR is the most widely accepted measure of kidney function. It refers to the volume of plasma that can be filtered through the glomerulus per unit time. Therefore, the ability to measure GFR in real-time would be very useful for the early detection of Chronic Kidney Disease (CKD). It would also be of great use in the management of patients presenting with Acute Renal Failure (ARF), also known as Acute Kidney Injury, (AKI), in which GFR is significantly decreased.

Knowing the GFR is particularly useful when determining drug dosage, since a drug will continue to act whilst in the blood, and many drugs are excreted by the kidney in proportion to GFR. However, it is important to note that kidney function, quoted as GFR, is therefore dependent on the functioning of the glomerulus, and does not consider tubular injury, which is nearly always present in ARF [Solomon and Segal, 2008]. When glomerular filtration is compromised, substances cannot be excreted, and therefore build up in the blood. Therefore, a biomarker for kidney function would be any substance that changes concentration in the blood in a manner *specific* to ARF and *sensitive* to the degree of change in GFR and/or kidney function. On the other hand, a biomarker for ARF/AKI reflecting tubular injury could be present prior to any change in GFR.

GFR is currently estimated in a clinical setting from the reciprocal of serum creatinine concentration, as discussed later in this chapter. At low GFR, creatinine secretion in the tubules increases. Hence, the serum creatinine concentration appears smaller, resulting in an over-estimated GFR. In addition, the steady-state assumption of GFR prediction models becomes invalid in ARF, since serum creatinine levels do not remain constant [Hosten, 1990]; [Bellomo et al., 2004]; [Erley et al., 2001]; [Doolan et al., 1962]. The creatinine production rate is also observed to decrease in ARF, associated with decreasing muscle mass [Shemesh et al., 1985]. Lastly, in chronic kidney disease, serum creatinine levels are very slow to react to changes in GFR, because the half life of creatinine is 48-72 hours. Hence, serum creatinine levels often do not increase until the kidney injury is relatively severe, resulting in a delay in the diagnosis of ARF [Solomon and Segal, 2008]. The converse of this is also true, and the kidney could have stopped deteriorating or even begun to improve, before any discernible difference is observed in the serum creatinine level. Regardless, a decrease in GFR, as indicated by an increase in serum creatinine concentration, remains the current definition of

ARF, despite these limitations.

The clinical condition of ARF is said to occur in anywhere from 1% to 25% of critically ill patients, depending on the population being studied and the criteria used to define its presence [Bellomo et al., 2004]. ARF can be classified in humans using the *RIFLE* system, in which deviation from a baseline (normal) GFR is determined based on the following criteria:

- **Risk of renal dysfunction:** serum creatinine increased 1.5 times OR urine production <0.5 mL/kg body weight for 6 hours;
- **Injury to the kidney:** serum creatinine increased 2.0 times OR urine production <0.5 mL/kg body weight for 12 hours;
- **Failure of kidney function:** serum creatinine increased 3.0 times OR creatinine >355 $\mu\text{mol/L}$ (with a rise of >44) or urine output below 0.3 mL/kg for 24 hours;
- **Loss of kidney function:** persistent ARF or complete loss of kidney function for more than four weeks;
- **End-stage kidney disease:** complete loss of kidney function for more than three months.

ARF can be caused by *pre-renal*, *renal*, or *post-renal* factors. Pre-renal refers to causes in the blood supply, such as ischaemia, hypovolemia or sepsis. Renal refers to damage to the kidney itself, which could be caused by toxins or medications, haemolysis, acute glomerulonephritis, or rhabdomyolysis, the latter of which is the breakdown of muscle tissue and release of myoglobin into the blood caused by a crush or blunt trauma injury. Post-renal refers to obstructive causes in the urinary tract, caused by anticholinergic medication, abdominal cancers, or kidney stones.

Histologically, an ischaemic insult to the kidney results in no morphological change to the glomeruli, however many studies have reported tubular, vascular, and inflammatory perturbations in ARF. This discussion will focus on the tubular abnormalities observed in ARF. ARF is characterised by tubular dysfunction with impaired sodium and water reabsorption, and is associated with

the shedding and excretion of proximal tubule brush border membranes and epithelial tubule cells into the urine. In vitro studies using chemical anoxia have revealed abnormalities in the proximal tubule cytoskeleton that are associated with translocation of Na^+/K^+ -ATPase from the basolateral to the apical membrane [Schrier et al., 2004]. Such a translocation could explain the decrease in tubular sodium reabsorption that occurs with ARF since it interferes with the transporter responsible for sodium uptake.

This tubular perturbation is insufficient to cause the fall in GFR that leads to nitrogenous-waste retention. However, loss of brush border membranes, loss of proximal tubule cells, and decreased proximal tubule sodium reabsorption may combine to result in a decreased GFR during ARF [Thurau and Boylan, 1976]. Brush border membranes and cellular debris could obstruct the tubular lumen. Microdissection of individual nephrons of kidneys from patients with ARF demonstrated obstructing casts in distal tubules and collecting ducts [Oliver et al., 1951], which could explain the dilated proximal tubules that are observed upon renal biopsy of ARF kidneys.

The decrease in proximal tubular sodium reabsorption that is associated with acute ischaemic injury would increase sodium chloride delivery to the macula densa and thereby activate the tubuloglomerular feedback mechanism and decrease GFR [Thurau and Boylan, 1976]. Micropuncture perfusion studies delivering increased sodium chloride to the macula densa have demonstrated a decrease in single-nephron GFR by as much as 50% through tubuloglomerular feedback [Schnermann and Homer, 2003]. The loss of the tubular epithelial cell barrier and/or the tight junctions between cells during acute renal ischemia could lead to a leak of glomerular filtrate back into the circulation [Molitoris et al., 1989]. If this occurs and normally non-reabsorbable substances leak back into the circulation, then a falsely low GFR will be measured, if based on the clearance of that substance. Dextran sieving studies in patients with ARF demonstrated that only a 10% decrease in GFR could be explained by backleak of filtrate [Myers et al., 1979].

Early detection and intervention in ARF can greatly improve a patient's prognosis. Therapy for ARF depends on the cause, but if GFR is not improved with fluid resuscitation, therapy-resistant hyperkalemia, metabolic acidosis, or fluid overload, then dialysis is required. Hence, real-time, high resolution biomark-

ers would offer a significant advantage in early detection and monitoring of the therapeutic intervention.

5.2 Study Design

Current measurements of renal function rely on daily measurements of plasma creatinine. Consequently, when most glomerular filtration function is lost, the diagnosis of kidney failure is delayed by up to 3 - 5 days in clinical situations. This delay results in unacceptable delays in instituting treatment. Consequently, there have been no improvements in mortality in the management of ARF for over 50 years, despite the availability of many useful experimentally effective treatments. SIFT-MS has the potential to offer non-invasive determination of renal function in real-time, and hence this study aims to correlate renal function as determined via SIFT-MS with current clinical and research gold standard techniques. Clinical gold standards refer to those methods currently used commonly in standard medical practice. Research gold standards refer to those techniques which are generally too time consuming or expensive to be appropriate in a clinical setting, although they usually give a more accurate result.

In this study, approved by the Animal Ethics Committee (C09/ 07601), female Sprague-Dawley rats (280-320g, n=11) were housed at 21°C in a 12 hour light/dark cycle, and allowed free access to food and water. Under ketamine/domitor anaesthesia, an in-dwelling cannula was inserted into the jugular vein for the purposes of fast serial blood sampling. GFR was monitored via plasma creatinine, SIFT-MS breath sampling, and bolus inulin clearance for 5 days while the animal recovered from surgery.

In a subsequent surgery, the renal arteries were exposed via a single mid-ventral incision, and clamped for 60 minutes, creating ARF via an ischemic event. GFR was monitored for 7 days using the same 3 techniques, as the animal recovered and renal function returned to normal levels. Rats were euthanised at the completion of the trial, and histological preparations were made from the excised kidneys. The GFR monitoring schedule is shown in Table 5.1.

Pilot studies were conducted to develop the techniques required for this study. The following factors were considered in relation to surgical techniques:

Table 5.1 GFR Monitoring Schedule

Method	Monitoring Timepoints	
	Post-cannulation	Post-ARF
Plasma Creatinine	6hr, 2day	1hr, 6hr, 20hr, 30hr, 2day, 4day, 7day
Inulin Clearance	6hr, 2day	6hr, 30hr, 2day, 4day, 7day
SIFT-MS Breath	-4hr, 1hr, 6hr, 20hr, 30hr, 2day,	-4hr, 1hr, 6hr, 20hr, 30hr, 2day, 3day, 4day, 7day

- Method of induction of ARF
- Blood sampling, blood loss, and blood transfusion
- Method of inserting indwelling jugular vein cannula
- Choice of anaesthetic agent, duration of anaesthesia, and number of surgeries
- Inulin clearance modelling
- Breath collection techniques

5.3 Induction of Acute Renal Failure

In this study, ARF was induced via ischaemia. Under anaesthesia, oxygen was prevented from reaching the kidneys for a period of time via a bilateral renal artery clamp. Rats typically recover from this type of surgery over the course of approximately 1 week [Gobé et al., 2000].

A non-volatile anaesthetic agent was required so as not to interfere with the breath sampling experiments. For this reason, Halothane and Isoflurane were not considered, although access to the neck region for the cannulation surgery would have been very difficult with the rat in a vaporiser in any event. In addition, the agent could not interfere with kidney function. Sodium Pentobarbitone (Pentobarb-300) was originally selected due to its low cost. However, this drug is intended for use as an euthanasia solution, and although it is commonly used

as an anaesthetic in rats, its variable quality and low margin of safety deemed it ultimately an unsuitable option for this study.

Subsequently, a domitor/ketamine mixture was selected. Domitor is an alpha-2 adrenoceptor agonist, which is ideal as a sedation agent. The action of domitor can be reversed with anti-sedan administered at equal dosage. Due to its poor analgesic properties, domitor is usually administered with ketamine, a dissociative drug. No reversal agent is available for ketamine, and the adverse effect of drying of the cornea must be prevented with ophthalmic ointment. Domitor causes diuresis, by inhibiting ADH release from the pituitary. This does not effect glomerular filtration, but due to the high urine flowrate (approximately 10mL urine is passed over the duration of surgery), the fluid lost must be replaced. Thus, 10mL saline was injected subcutaneously after the rat entered the surgical plane to compensate for fluid loss during surgery. Domitor can also cause cardiovascular and respiratory depression. Hence, it is usually administered in conjunction with atropine sulphate, an antimuscarinic alkaloid which helps prevent bradycardia, and reduces bronchial secretions.

Two analgesics were considered for post-operative pain relief. Marcain is a rapid-onset, long-acting local anaesthetic which is applied topically. It can be applied to the wound area during suturing, but therefore cannot be used for pain relief in the days following surgery. Better recovery was observed for rats treated with temgesic, a long-acting synthetic opioid, which can be administered subcutaneously as required following surgery. Table 5.2 summarises the drug regime.

Table 5.2 Rat Anaesthetic and Analgesic Drug Regime

Drug	Dose (<i>mg/kg</i>)	Admin Route*	Purpose
Domitor	0.5	SC	Sedation
Ketamine	75	SC	Sedation & analgesia
Atropine	0.05	SC	Prevent bradycardia and bronchial secretions
Saline	10mL	SC	Compensate diuretic effect of domitor
Antisedan	0.5	SC	Reverse effect of domitor
Temgesic	0.05	SC	Post-operative pain-relief

*SC Subcutaneous

Because it was intended that the rat survived this surgery, it was necessary to use as noninvasive a technique as possible when inducing ARF. The first technique considered was to access the kidneys via two flank incisions, through which it would be possible to *pop out* the kidney in order to clamp the renal arteries. Such a technique had been performed by the surgical team in previous laboratory work, and could be achieved with very small incisions that did not disturb other organs. However, this technique required decapsulating the kidney to get to the vessels, and due to the position of the vein and artery, it was extremely difficult to separate the vein from the artery without piercing the vein, as seen in Figure 5.9. It was also difficult to actually locate the artery. Hence, the solution was to clamp the vein and artery together. However, using this technique, it was very difficult to know how adequate the ischaemia was.

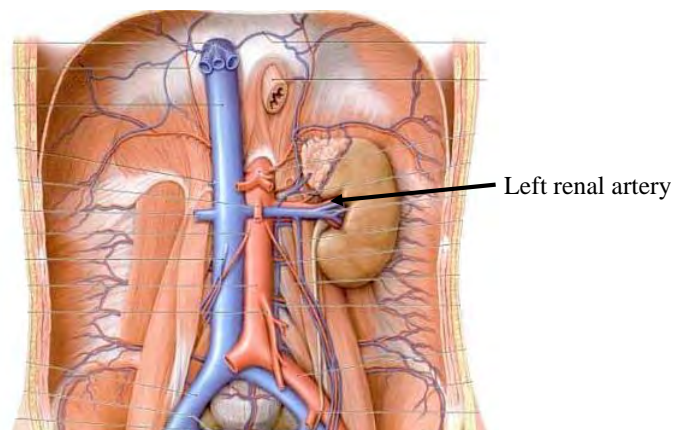


Figure 5.9 Renal circulation, highlighting position of the renal vein, University of Debrecen [2009]

The second method investigated was to access the kidneys via a single mid-ventral incision. Although this technique requires a larger incision, it was through the *linea alba*, a fibrous structure running down the midline of the abdomen. The *linea alba* contains thinner tissue layers, and is devoid of important nerves and blood vessels. Therefore, an incision here causes the recovering animal significantly less discomfort.

Using this technique, the renal arteries can be clamped close to the aorta, where it is much easier to separate the artery from surrounding tissue. Therefore the artery can be isolated and clamped, and the discolouration of the kidney caused by blood draining out of it can be detected almost immediately. This approach ensures adequate, controlled damage to the kidney.

In total, 8 pilot studies were carried out on inducing ARF via bilateral renal artery clamping. These studies and outcomes are summarised in Table 5.3. Other studies in the literature performed renal artery clamping for between 30 and 60 minutes with good survival rates [Gobé et al., 2000]. For this study, a 60-minute bilateral renal artery clamp was selected. The surgical technique is summarised in Figure 5.10.

Table 5.3 Pilot Studies on ARF

Rat	Anaesthetic	Incision Type	Clamp Time	Outcome
370g female	Pentobarb	midventral	60 mins	50mm incision seemed quite large. Tried to clamp renal arteries close to the kidney. Decision to try 2 flank incisions. Difficult to find vessels without decapsulating the kidney.
520g male	Pentobarb	2 x flank	30 mins	Quicker to access kidney via flank incision, but tissue layer much thicker. Easier to find vessels when kidneys decapsulated.
325g female	Pentobarb	2 x flank	45 mins	Successful experiment, but left kidney went quite black, and right kidney remained pink.
326g female	Pentobarb	NA	NA	Rat died due to respiratory failure after cannulation prior to renal artery clamp.
336g female	Pentobarb	2 x flank	45 mins	Rat euthanised due to respiratory difficulties after clamping complete.
318g female	Pentobarb	midventral	45 mins	Rat died overnight after surgery, but pre-clamp and post-clamp bolus inulin clearances were carried out and a 25% decrease in function was observed.
297g female	Domitor/ Ketamine	midventral	45 mins	Kidneys did not change colour - need to tie the clamps shut. Post-clamp inulin clearance indicated insufficient kidney damage.
248g female	Domitor/ Ketamine	midventral	60 mins	50% decrease in GFR as estimated by bolus inulin clearance.

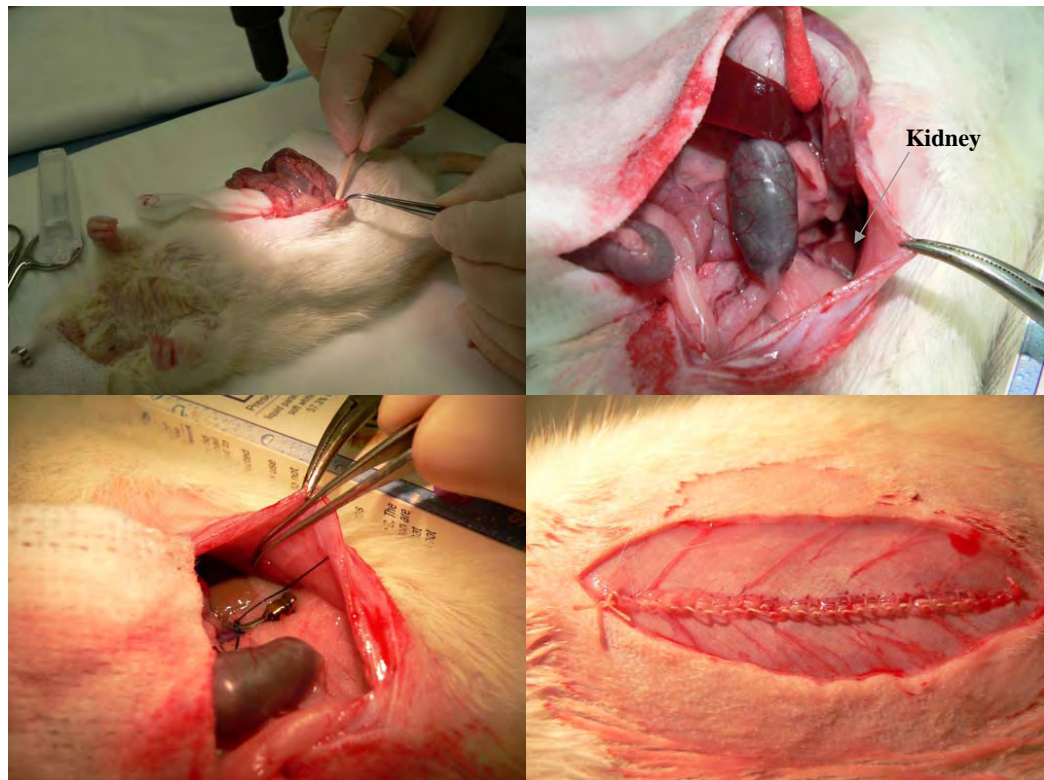


Figure 5.10 ARF Surgical Technique: Top left, mid-ventral incision; top right, locating kidney; bottom left, clamping renal artery; bottom right, suturing each tissue layer with a running stitch.

Under domitor/ketamine anaesthesia, atropine and saline were administered subcutaneously. During surgery and recovery, body temperature was maintained via use of a heat pad. Corneal drying was prevented using eye ointment. Under surgical conditions, a 5cm mid-ventral incision was made and a blunt dissection technique was used to expose the renal arteries close to the aorta. Both renal arteries were clamped for 60 minutes, and adequate clamping was ensured by observing the kidneys become pale. Saline-soaked gauze was used to prevent internal organs drying out during the 60 minute clamping time. After 60 minutes, the clamps were removed and each tissue layer was sutured separately with a running stitch. Anti-sedan was administered to reverse the anaesthetic effect of domitor, and the rat began to twitch within 2 minutes. Temgesic was administered subcutaneously as indicated for pain relief for 2 days post-surgery. The rat was monitored using animal welfare score sheets until recovery, and at least twice daily for the remainder of the trial.

5.4 Inulin Clearance Tests for Determining GFR

5.4.1 Clearance Techniques

The most widely accepted measure of kidney function is the volume of ultrafiltrate that can be filtered by the glomerulus per unit time, the *GFR*. The renal clearance of any substance which can be freely filtered by the glomerulus without being secreted or reabsorbed by the renal tubules can thus be used to estimate GFR. Key elements include the ability to safely administer the substance, and to measure its concentration in the plasma. It is essential that there be no other means by which the body can clear the specific substance, so that clearance is specific for the GFR.

Inulin is a large starch-like fructose polymer, which is uncharged, and does not bind to plasma proteins. Therefore, it passes readily through the glomerular capillary basement membrane. In addition, it is not reabsorbed, secreted or metabolised by the renal tubules, making it an ideal filtration marker. Inulin clearance can be measured using two main approaches: constant infusion method (CIM), requiring plasma samples and timed urine collection; or bolus techniques, requiring modelling of the tracer (inulin) distribution and elimination kinetics.

The constant infusion method (CIM) is considered the research gold standard measure of kidney function, and is the method commonly quoted in textbooks [Cameron, 1992]. Using this method, inulin is injected into the plasma at a constant rate until a steady state is achieved. Once in the steady state, a blood sample is taken, and the inulin plasma concentration determined. The appearance of inulin in the urine is determined by its concentration in the urine and the volume of urine produced per minute. GFR is then determined by Equation (5.3).

$$GFR = \frac{(Urine\ concentration)(Urine\ flow)}{Plasma\ concentration} \quad (5.3)$$

In practice, this technique has limitations, because it is difficult and slow to achieve a steady state. In addition, it is very cumbersome and difficult, in *man*, to obtain an accurate timed urine collection [Cameron, 1992]. Several techniques

have been suggested in the literature to alleviate these difficulties, ranging from catheterisation to overcome the problem of deadspace in the urinary tract, to rationalising against the need for urine collection at all.

[Earle and Berliner, 1946] and [Berger et al., 1948] argued that for subjects with reasonable kidney function (inulin clearance more than 60% of normal), the rate of excretion must be equal to the rate of infusion, provided the plasma concentration and volume of distribution do not change. In this case, only the plasma concentration and infusion rate were required to calculate GFR. Many subsequent studies have illustrated the unreliability of this technique due to failure to obtain a constant inulin concentration in the plasma [Zeier et al., 1992].

[Van Acker et al., 1995] investigated the validity of the steady-state constant infusion method by carrying out 3 hourly clearances of inulin and *p*-aminohippuric acid (PAH) over 27 hours in 25 patients with renal disease. As estimated without urine collection, this overestimated clearance calculated using urinary recovery by 10%. Additionally, neither inulin nor PAH plasma concentrations became fully constant.

In contrast to constant infusion techniques, bolus methods can be carried out quickly, and require only a single injection of the exogenous marker into the plasma, and fast serial blood sampling thereafter at defined intervals. Urine collection is not required. However, data analysis requires the application of a well defined mathematical model. For accurate results, the exact amount of inulin injected must also be known, all of which must enter the circulatory system.

Several models have been proposed in the literature. One-compartment models such as [Sapirstein et al., 1952], are inaccurate because they assume that the mixing time between the plasma and interstitial compartments is negligible, and as demonstrated in [Sturgeon et al., 1998], this situation is not the case. Some models such as [Peters et al., 1999] are single compartment and recognise that GFR is overestimated in that type of model, but then try to correct for GFR using a *sliding factor* that assumes the distribution phase between the plasma and interstitial compartment is constant for all subjects.

Other models, such as [Prescott et al., 1991], calculate clearance as the amount of inulin present in the urine divided by the area under the plasma-inulin

concentration curve. Such a model requires adequate blood sampling in both the distribution (plasma to interstitial compartments), and elimination (plasma compartment to urine) phases, as well as prolonged sampling until near-zero plasma concentrations to obtain an accurate plasma-inulin concentration curve. The model of [Prescott et al., 1991] maintains that inulin clearance changes as the time after bolus administration increases, however it is likely that insufficient sample points were obtained in the early distribution phase to adequately define the pharmacokinetics in this model.

[Qi et al., 2004] calculated GFR in mice using a bolus FITC-inulin injection (a fluorescence technique). In this study, 7 blood samples were collected over 75 minutes, and a 2-compartment exponential decay curve was fitted using nonlinear regression in *Prism*. [Qi et al., 2004] also calculated GFR using only the later timepoints and a single compartment model, and found that GFR was overestimated by 34% using this method. After a 5/6 nephrectomy, GFR was found to decrease to approximately 14% (1/6) of its previous value, as expected. However, their model does not appear to fit well to sample data points.

Other models insist that clearance can be calculated using only 1 or 2 sample points [Russell et al., 1989]; [Bubeck et al., 1992]. In this method, the ratio of the markers' dose to serum activity at a pre-specified time point(s) after intravenous administration is used as its volume of distribution, which is then logarithmically transformed to obtain the Tubular Extraction Rate, TER. As this ratio becomes smaller, such as during impaired renal function, it becomes closer to a critical threshold, $e^{1.75e^{0.005t}}$ calculated using the half life of $^{99m}\text{Tc} - \text{MAG}_3$, below which value *negative* values are obtained.

In this study, pilot experiments were carried out to attempt to correlate constant infusion and bolus clearance results in 5 rats. All rats had CIM and bolus inulin clearances performed under anaesthesia in the same surgery: 2 rats received CIM followed by bolus inulin clearance, and 3 rats received the bolus experiment followed by CIM. It was found that it was preferable to carry out the bolus experiment prior to the CIM experiment so as not to have to account for a background/starting inulin concentration in the bolus kinetic model.

Using CIM, urine was collected via catheterisation of both ureters; serial blood sampling was carried out via a jugular vein cannula (described in Section

5.4.2) and inulin was infused via tail or femoral vein, as summarised in Table 5.4.

Table 5.4 Clearance Experiments

Rat (male)	Infusion Method	Infusion Route	GFR (mL/min)	Outcome
665g	CIM	Femoral	3.77*	Inulin infused at 3mL/hr following a 0.38mL bolus. Mannitol greatly improved urine output. Constant plasma and urine concentrations not achieved after 70 minutes, Figure 5.11.
665g	Bolus	Femoral	3.94*	Background inulin concentration at time zero not evaluated. Monitoring only carried out for 10 minutes - subsequently deemed too short to describe the elimination phase. Inulin concentration injected too low.
*Expected GFR is 3.92-5.05mL/min.				
700g	CIM	Femoral	2.37*	Inulin infused at 2mL/hr following a 0.28mL bolus. Constant plasma and urine concentrations not achieved after 70 minutes, Figure 5.12. Block in ureteric cannula at 40-50 minutes.
700g	Bolus	Femoral	4.50*	Background inulin concentration at time zero estimated. 7 samples collected over 10 minutes. Inulin concentration injected too low.
*Expected GFR is 4.13-5.32mL/min.				
590g	Bolus	Jugular	3.82*	2 bolus clearances performed prior to CIM. Monitored for 6 minutes.
590g	Bolus	Jugular	3.86*	Estimated background inulin concentration at time zero. Monitored for 6 minutes.
590g	CIM	Tail	0.40*	Inulin infused at 2mL/hr following a 0.28mL bolus. Steady state not achieved after 70 minutes. Rat deteriorating.
*Expected GFR is 3.48-4.48mL/min.				
606g	Bolus	Jugular	3.76*	4 samples collected over 10 minutes.
606g	CIM	Femoral	2.69*	Inulin infused at 2mL/hr following a 0.3mL bolus. Extremely variable urine collections.
*Expected GFR is 3.58-4.61mL/min.				
570g	Bolus	Jugular	4.07*	6 samples collected over 10 minutes.
570g	CIM	Femoral	3.54*	Inulin infused at 3mL/hr following a 0.38mL bolus. Steady state achieved, Figure 5.15.
*Expected GFR is 3.36-4.33mL/min.				

The main problems encountered with CIM were:

- Infusion into the tail vein was difficult under anaesthesia because the rat temperature decreased making it harder to cannulate the vein. During these experiments a lump appeared in the tail indicating that not all the inulin was being delivered to the circulatory system.
- Urinary output was insufficient and the deadspace volume was too large. Mannitol in the ratio 1:10 with saline was used to make up the inulin solution to increase urine volume, and the catheters were cut as short as possible to reduce deadspace.

Using the bolus inulin injection method, serial blood sampling was carried out via a jugular vein cannula, and an inulin bolus was injected into the femoral or jugular vein over 2-3 seconds. The main problems encountered were:

- Cannulating the jugular vein and femoral vein was time consuming and less practical for ambulatory experiments, therefore infusion into the jugular vein was tested, and provided the cannula and needles were well flushed, injecting and sampling from the same cannula was found not to contaminate results.
- The optimal concentration of inulin to be injected was unknown. Results were improved with higher concentrations (1:4 opposed to 1:19) and sampling over a longer period of time (70 minutes opposed to 10 minutes).

Expected GFR results were calculated based on body weight, as shown in Equation (5.4) [Löwenborg et al., 2000].

$$0.59 \times \text{Body weight} \leq \text{GFR} \leq 0.70 \times \text{Body weight} \quad (5.4)$$

For all 5 rats, GFR estimated using the bolus method resulted in a value within the expected range. However, using CIM, only 1 rat obtained a GFR within the expected range, with the remaining 4 rats underestimating GFR.

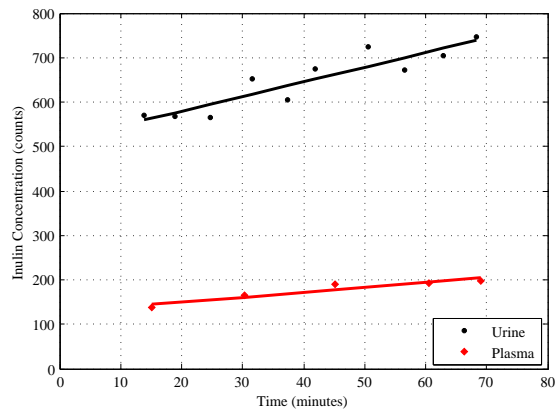


Figure 5.11 CIM for Pilot Rat 1

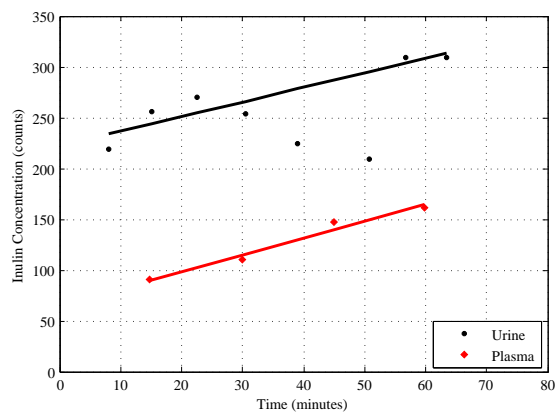


Figure 5.12 CIM for Pilot Rat 2

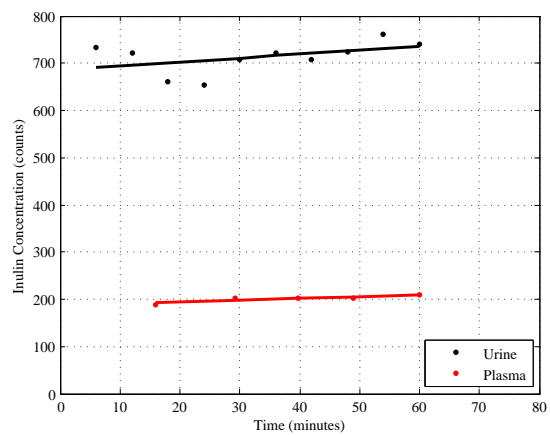


Figure 5.13 CIM for Pilot Rat 5

Bolus experiments in 3 subsequent rats were performed with each rat undergoing the clearance test while anaesthetised, *and* in the ambulatory state 1-4 days after surgery. Inulin was injected in ratio 1:4 with saline, and sampling continued over 70-90 minutes. Table 5.5 shows that rats 1 and 3 obtained a GFR that was repeatable over more than 1 bolus clearance experiment. All GFR estimations were within expected values except the rat 2 anaesthetised bolus clearance. This result was somewhat expected since the rat suffered extensive blood loss during surgery, and after the clearance experiment received a blood transfusion from another rat, all of which may have effected the results.

Table 5.5 Bolus Experiments

Rat (male)	Expected GFR (mL/min)	GFR (mL/min)	Estimation % error	Figure
415g	2.45-3.15	3.12	9.9%	5.14
415g	2.45-3.15	3.11	12.0%	5.14
386g	2.28-2.93	1.92	7.4%	5.15
386g	2.28-2.93	2.38	6.6%	5.15
276g	1.70-2.19	2.06	8.8%	5.16
276g	1.70-2.19	2.18	1.5%	5.16

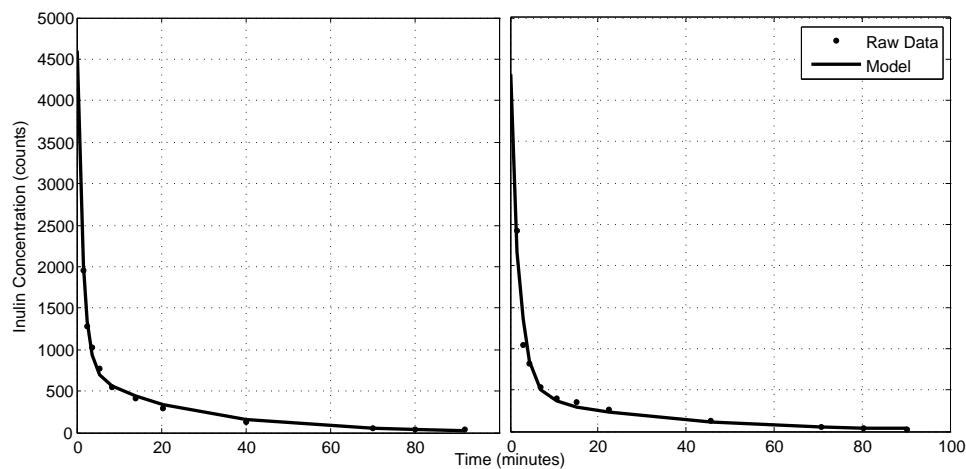


Figure 5.14 Subsequent bolus clearances for Pilot Rat 6 - Model fitted to raw data

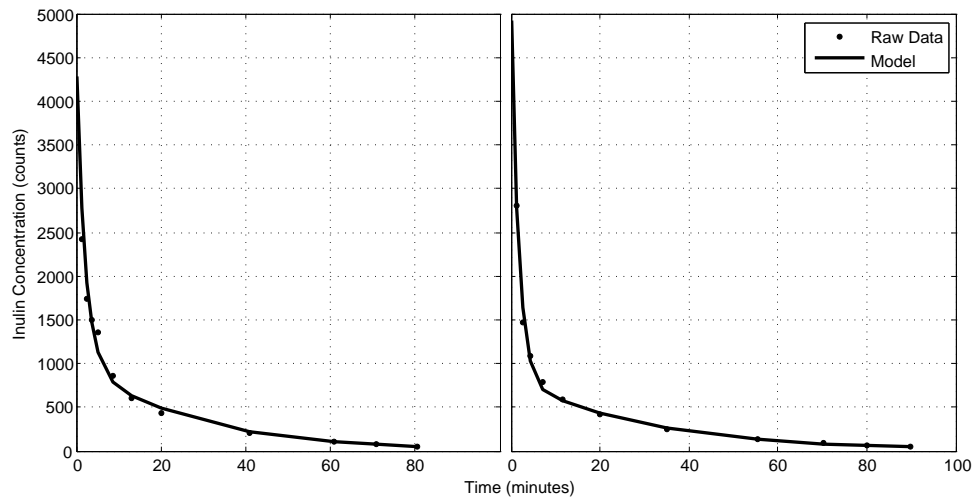


Figure 5.15 Subsequent bolus clearances for Pilot Rat 7

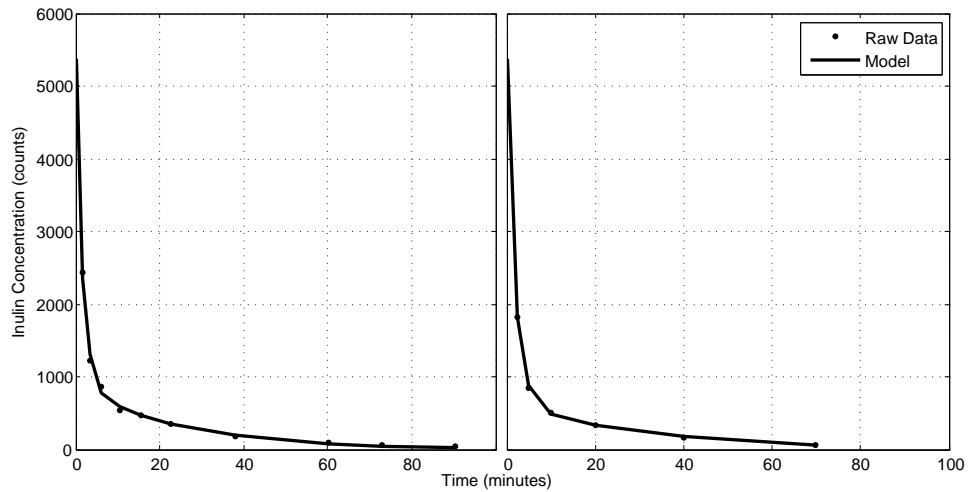


Figure 5.16 Subsequent bolus clearances for Pilot Rat 8

5.4.2 Serial Blood Sampling and Cannulation

Serial blood sampling for bolus inulin clearance can best be achieved via cannulation, requiring a surgical intervention to insert the cannula. Important points to consider are:

- How to tie the cannula in place
- How to keep the cannula patent for the duration of the trial
- How to prevent the animal attacking the cannula
- Sampling time-points and blood volumes

- Length of time of surgery
- Control experiments

Two methods for jugular vein cannulation were considered. The first was the double-blunt needle technique described by [Bakar and Niazi, 1982] in which a 23-gauge needle is forced into a bent 20-gauge needle. A cannula of appropriate size then fits snugly onto the other end of the 23-gauge needle, as seen in Figure 5.17.

The cannula is then inserted into the jugular vein by threading the bent 20-gauge needle into and out of the vein, as seen in Figure 5.18. The 20-gauge needle is then removed from the assembly, leaving the cannula and smaller needle behind in the vein to be sutured in place.

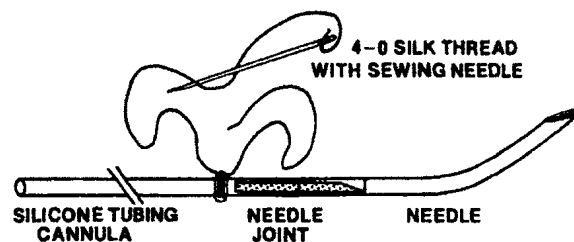


Figure 5.17 Double blunt needle assembly Bakar and Niazi [1982]

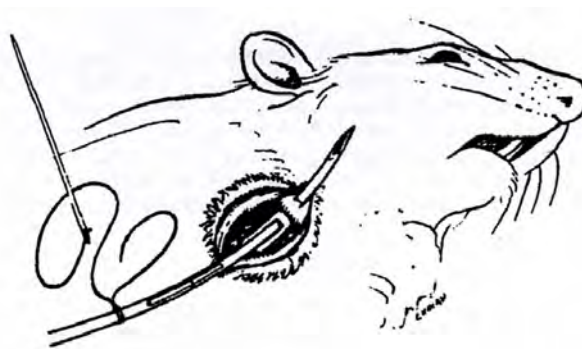


Figure 5.18 Double blunt needle cannulation technique Bakar and Niazi [1982]

The second and easier to perform method is similar to that described by [Wyman et al., 1994]. In this method, 0.8/0.5mm 15° bevel-tipped cannula filled with heparinised saline attached to a 1mL syringe via a blunt 24-gauge needle is inserted approximately 40mm into the jugular vein, through the sinus at the

junction of the subclavian vein, and into the superior vena cava, as shown in Figure 5.19.

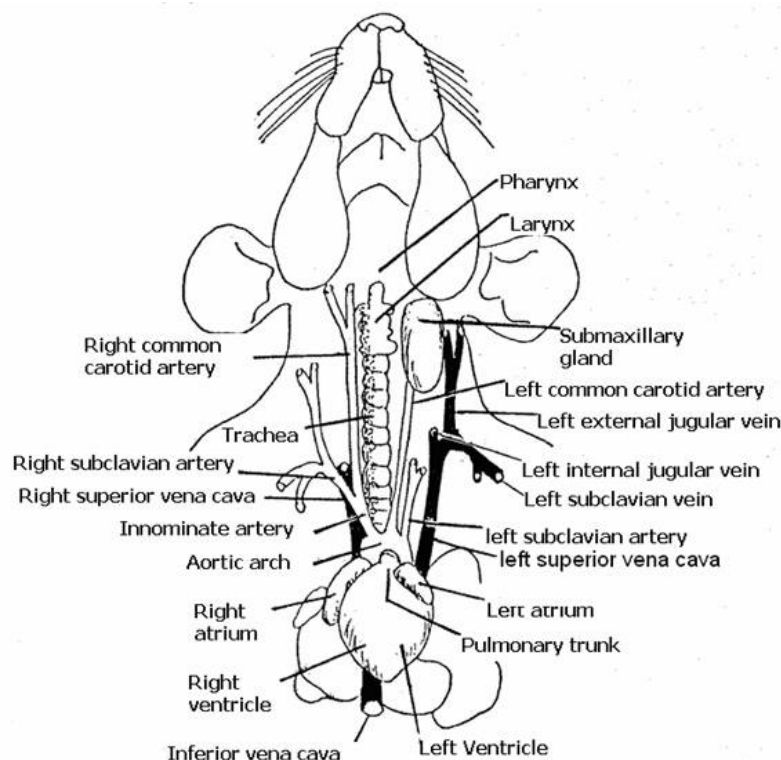


Figure 5.19 Position of the jugular vein

The angle of the bevel is important, because although a sharper bevel makes it easier to insert into the vein, it also increases the risk of piercing the vessel wall, or of occluding the cannula due to suction onto the vessel wall when blood is withdrawn from the cannula. It is often difficult to manoeuvre the cannula into position. However, lifting the chest cavity and/or injecting saline into the cannula to open the vessel can usually overcome this difficulty. The position of the cannula is verified by drawing back on the syringe to see if blood flows freely. The cannula is held in place by suturing to the muscle. Next, the cannula is threaded subcutaneously to the back of the neck, where the animal cannot easily reach it.

Pilot studies found that the animal was still able to pull the cannula out of position. Hence, a coat was fashioned to protect the cannula, as seen in Figure 5.20. The cannula was temporarily blocked off with a 24g needle and nylon thread providing a tight seal to prevent blood being drawn back up the cannula when blood was not being sampled.



Figure 5.20 Rat coat to prevent rat accessing the indwelling cannula

The surgical technique is shown in Figures 5.21 and 5.22.

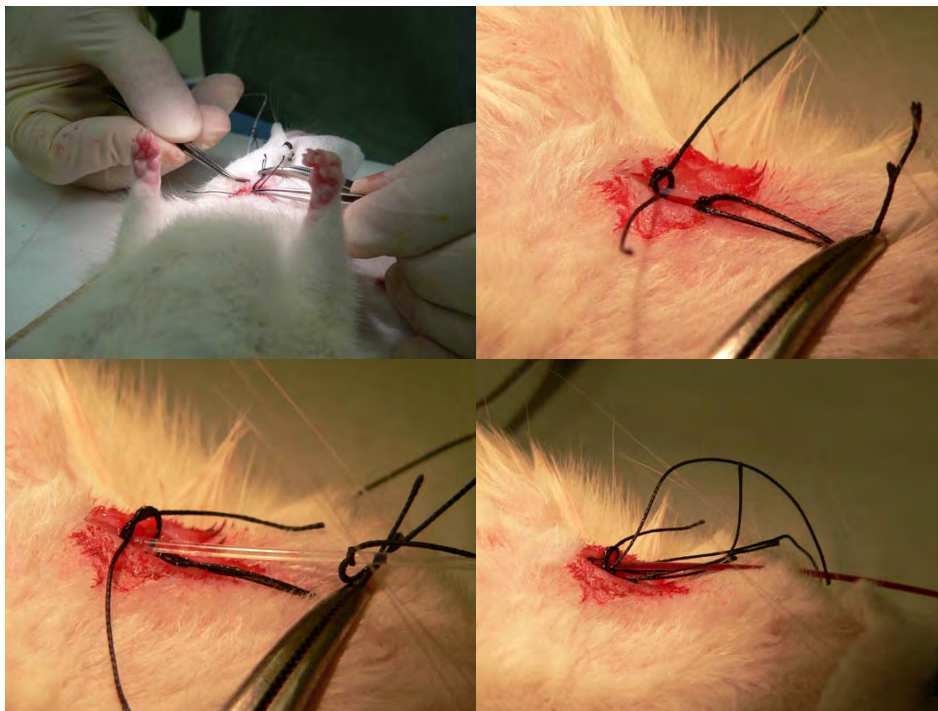


Figure 5.21 Cannulation Surgery: Top left, rat positioned for surgery; top right, isolating the jugular vein; bottom left, inserting the cannula; bottom right, obtaining blood from cannula.

Heparinised saline was used daily to flush the cannula to keep it patent and prevent clotting, however, by the end of the 2-week experiment, there was typically a buildup of fibrous tissue over the tip of the cannula in most animals which caused either partial or complete occlusion. It is thought that this buildup is most

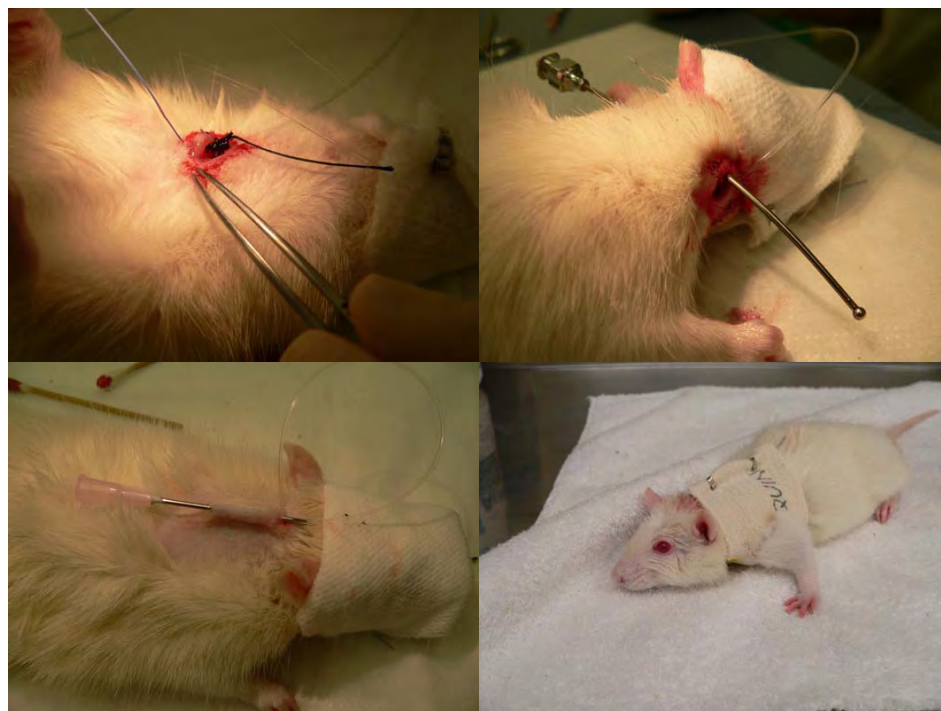


Figure 5.22 Cannulation Surgery: Top left, tying cannula in place; top right, gavage needle to thread the cannula sub-cutaneously to the back of neck; bottom left, positioning cannula at the back of neck; bottom right, wrapped in cannula-protecting coat.

likely an immune response to the cannula. Because of the difficulty in keeping the cannula patent for 2 weeks, it was considered to perform both the bilateral renal artery clamp and jugular vein cannulation in the one surgery. However, the length of surgery was a significant concern in the design of experiments.

In particular, the time required to perform an ARF surgery was approximately 2 - 2.5 hours from administration of the anaesthetic to administration of the reversal agent. To insert a jugular vein cannula could take up to 1 hour, and because a control, *pre-ARF-induction* inulin clearance test was desired, a 70 minute inulin clearance test would also have to be performed during the surgery. These tests made the surgery too long, and pilot animals did not survive. In addition, the heparin required to keep the jugular vein cannula patent caused excess blood loss around the large mid-ventral incision, and an inulin clearance test under surgical conditions can not act as a control with non-anaesthetised animals. Therefore, it was determined to perform 2 surgeries, allowing approximately 5 days for the animal to recover from the cannulation surgery before undergoing the ARF surgery.

Pilot studies were used to determine the optimal blood sampling time points for inulin clearance, with consideration to allowable blood loss volumes and maintaining adequate blood volume and pressure. Blood volume, BV , in the rat is estimated by Equation (5.5), where BW is the body weight in grams [Lee and Blafox, 1985].

$$BV(mL) = 0.06BW + 0.77 \quad (5.5)$$

For multiple survival collections, 13% of an animals' blood volume in any 2-week period is the permissible collection volume. For 300g rats in the current study, this equated to a total allowable collection volume of 2.44mL. 50 μ L plasma was required for scintillation analysis, and with an average haematocrit of 40%, and allowing a margin of error, 150 μ L blood was required for each inulin sampling time point. Figure 5.23 shows the model fitted clearance curve for a pilot animal.

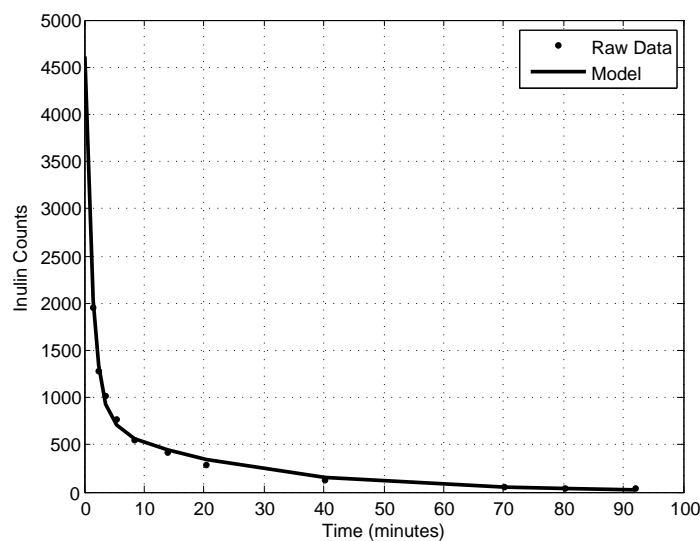


Figure 5.23 Pilot Animal Inulin Clearance Curve

Hence, the following time-point sampling selections were determined:

- Pre-inulin bolus
- 1.5 minutes post-bolus
- 3 minutes post-bolus

- 6 minutes post-bolus
- 12 minutes post-bolus
- 20 minutes post-bolus
- 40 minutes post-bolus
- 70 minutes post-bolus

With an additional $200\mu\text{L}$ blood sample required for creatinine analysis at each inulin clearance test, a total of 1.4mL blood was required at each inulin clearance. As seen in Figure 5.24, GFR as estimated via inulin clearance did not vary significantly between 22 and 50 hour sample time-points. Hence, it was determined to perform inulin clearance tests at 6 hours, 30 hours, 2 days, 4 days and 7 days, as well as well as 6 hour and 2 day clearances following the cannulation surgery to provide an experimental control. Therefore, the total blood volume required was significantly greater than the allowable collection volume for survival experiments.

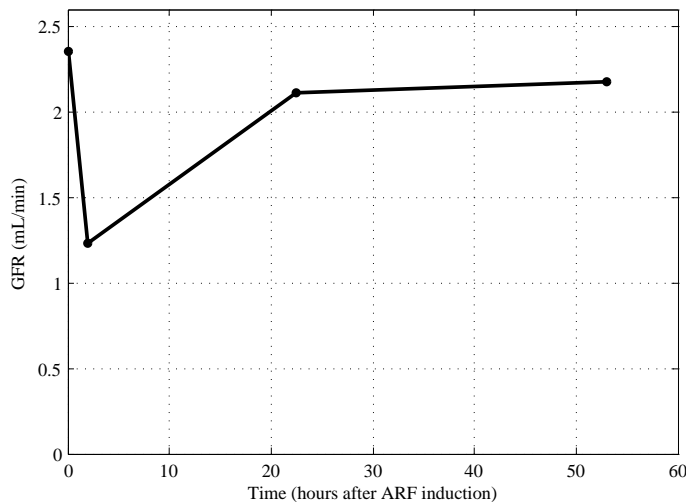


Figure 5.24 Pilot Animal Day 2 Inulin Clearance

The solution to this problem was to perform a blood transfusion. Initially, other rats from the colony were considered for this role. However, since only the blood plasma is required for testing, it was determined that after separating the plasma from the red blood cells, the red blood cells could be mixed with a

volume of saline equal that that lost in plasma, and returned to the animal at the completion of the inulin clearance test via the jugular vein cannula.

5.4.3 Final Inulin Clearance method

^{14}C labelled inulin ($1\ \mu\text{Ci}$ of $1.12\ \text{uCi}/\text{mg}$ dissolved in 0.1mL ionised water, diluted 1:4 with saline) was injected into the jugular vein cannula of a conscious animal over 2-3 seconds, and flushed with heparinised saline. A $150\ \mu\text{L}$ blood sample was collected via the jugular vein cannula at -1, 1.5, 3, 6, 12, 20, 40, 70 minutes post-bolus, and the separated plasma was sent for scintillation analysis. Red cells and remaining blood plasma were returned to the animal with saline via the jugular vein after each complete clearance experiment.

5.5 Creatinine Clearance for GFR Determination

Measuring GFR by calculating the clearance of an exogenous marker is time consuming, expensive, and thus not appropriate in most clinical settings. Hence, GFR is usually estimated using an endogenous marker, such as creatinine. Creatinine is formed from creatine phosphate in muscle tissue, and as such, creatinine production varies greatly with muscle mass. Serum creatinine concentration also varies with diet. Cooking converts creatine in meat to creatinine, which when eaten, raises serum creatinine concentration. Hence there can be large variation in creatinine concentration, particular during illness.

In addition to the variable rate of generation, creatinine is also not an ideal filtration marker because, as well as being filtered by the glomerulus, it is also secreted by the proximal tubules, resulting in a clearance that exceeds GFR, particularly in ARF when secretion increases. Figure 5.25 shows that steady state creatinine is approximately inversely proportional to GFR as measured by inulin clearance at normal values (GFR > dashed line) [Shemesh et al., 1985]. However, when the full spectrum of GFR values is considered, the relationship between creatinine concentration and GFR is hyperbolic, indicating that creatinine clearance is a poor measure of kidney function at low GFR where it would be most useful.

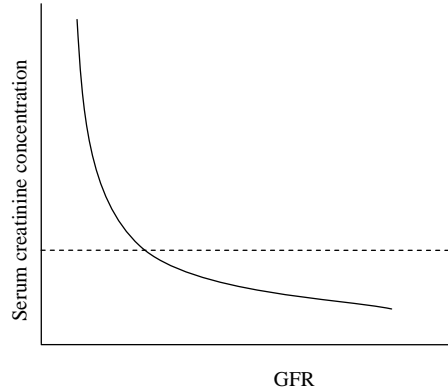


Figure 5.25 Relationship between creatinine clearance and GFR in humans

When renal failure is advanced, there is a significant decrease in glomerular filtration. However, this decrease is accompanied by an increase in tubular secretion, extra-renal elimination of creatinine via intestinal bacteria, and often a decrease in creatinine production. Therefore, in chronic renal failure, creatinine concentration becomes an unreliable measure of renal function, usually overestimating GFR.

Because of the difficulties in collecting timed urine samples, GFR is often estimated using plasma creatinine samples alone, as opposed to calculating the creatinine clearance. Equations such as the Cockcroft-Gault and the MDRD equations, (5.6) and (6.16) respectively, have been developed to try to correct for the limitations of GFR estimation by plasma creatinine, by accounting for age, sex, weight and race [Cockcroft and Gault, 1976]; [Levy et al., 1999]. GFR estimated using either the Cockcroft-Gault or the MDRD equations is the current clinical gold standard.

$$C_{cr}(mL/min) = \frac{(140 - age(years))(weight(kg))(0.85 \text{ if female})}{72P_{cr}(mg/dL)} \quad (5.6)$$

$$C_{cr}(mL/min/1.73m^2) = (186.3)(P_{cr}^{1.154})(age^{-0.203})(1.212 \text{ if black})(0.742 \text{ if female}) \quad (5.7)$$

All animals recruited for the present study were female albino rats and were

approximately the same age. Hence, the variations observed between individuals in a typical clinical setting were not considered relevant to this study. Therefore, the GFR was estimated based on rat weight and plasma creatinine concentration as described further in the next chapter.

A 200 μ L blood sample was required for creatinine analysis at each point that GFR by plasma creatinine was to be compared with GFR by inulin clearance and GFR by breath analysis. Blood was obtained via the jugular vein cannula if patent, or by tail vein if it was not. Blood was centrifuged, and plasma creatinine concentration was determined using the HPLC creatinine assay, in which precision studies have shown the coefficient of variation to be 2% for both within batch and between batch variation. Plasma concentration was determined at 6 hour and 2 day post cannulation surgery, and at 6 hour, 30 hour, 2 day, 4 day and 7 day post ARF surgery.

5.6 Breath Collection for Determination of GFR

The most common method for breath testing in large animals is via a face-mask with a non-rebreathing valve, and collecting the breath exhalate into a bag. In small animals, the animal is usually placed in a sealed chamber until desired analytes reach detectable levels. In anaesthetised animals, breath is usually collected directly using endotracheal intubation, [Wyse et al., 2005]. All 3 of these options were investigated, before settling on a combined method.

Due to the results from the previously described dialysis study, direct breath was deemed preferable to breath collection in tedlar bags. The tidal volume of the rat had to be validated to ensure that the volume flowrate was greater than the sampling rate, to ensure the breath sample was not too diluted. [Pass and Freeth, 1993] report the rat volume flowrate as approximately 2.7mL/sec for a 250-300g rat, based on a respiratory rate of 85-110 breaths per minute and a tidal volume of 1.5-1.8mL. Monitoring respiratory rate during surgery found that it drops from approximately 100 breaths per minute at rest, to 40 breathes per minute during anaesthesia for a 300g rat. Tidal volume was thus measured crudely by the water displacement method, in which a beaker of water was inverted in a shallow dish, also containing water. Tubing was placed under the lip of the beaker, and the

other end was attached to a latex rat mask, into which the rat was held, forming a seal. As the rat exhaled, a volume of water was displaced, equal to the volume of air exhaled. A 300g rat was found to displace 23.5mL water in 10 seconds, a value just higher than the SIFT-MS sampling rate of 2mL/sec. Because this method is very crude for measuring flowrate, it was decided to use the values reported by [Pass and Freeth, 1993].

Endotracheal intubation was not considered for the primary breath sampling method in the main trial because it requires the animal to be anaesthetised. Due to the number of breath samples required, this method was deemed impractical, considering the risks of repeated anaesthesia, and animal ethics. However, endotracheal intubation was considered as a validation technique for future breath sampling methods. Unfortunately, due to difficulties with the anaesthetic, the learning curve associated with intubation, and the desire to minimise animal numbers, intubation, while attempted in 5 rats, was unsuccessful.

The option to place the animal in a sealed chamber, and wait for analyte concentrations to build up was discarded for two main reasons. Firstly, to simply wait for detectable analyte levels to be obtained is insufficient, since the analyte will continue to build up until an equilibrium is obtained. To wait for an equilibrium would be dangerous for the rat, since it would be re-breathing and thus concentrating CO_2 in the blood and risking hypercapnia. Secondly, the sample collected would be contaminated from the fur and waste products, for example if the animal urinated whilst in the chamber.

The face-mask option with re-breathing valve commonly used for breath sampling in large animals was attempted for the rat. A latex mask was created from a plaster mould generated off a deceased rat. A rat cage (Figure 5.10) was designed to fit and hold a variable sized rat in position in the mask. The mask was attached to straw with a simple reed valve, allowing the rat to breath from the room air, and forcing breath unidirectionally down the straw to the mass spectrometer.

Due to the low pressures involved because of the small size of the animal, combined with the difficulty in forming a seal around the mask, activating the valves was very difficult. In addition, because of the small tidal volume, deadspace was a significant problem. Lastly, it was very stressful for the rat to be forced

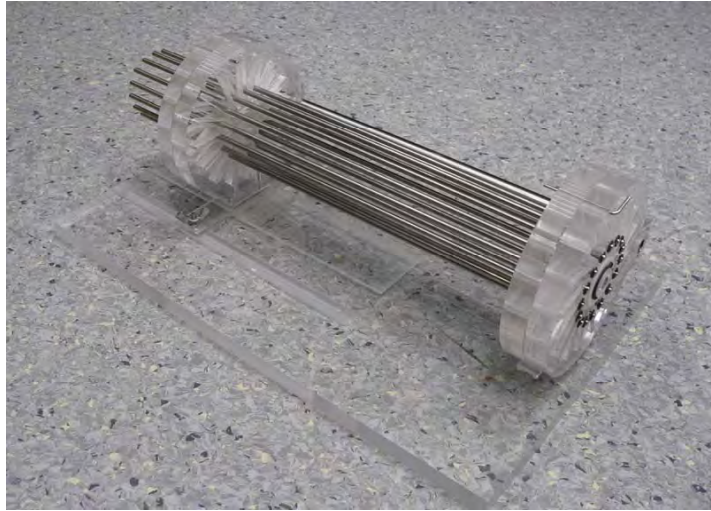


Figure 5.26 Rat restraining device

into the mask, likely elevating stress markers, such as pentane in the breath. Hence, this method was abandoned. Valved methods such as utilised in humans for discarding the dead-space portion of the breath and maintaining the alveolar breath for sampling were also discarded as impractical in the rat.

Finally, a method was defined in which direct breath was collected from a conscious rat by wrapping the rat in a towel and placing it snugly into a 300mL bottle as seen in Figure 5.27.

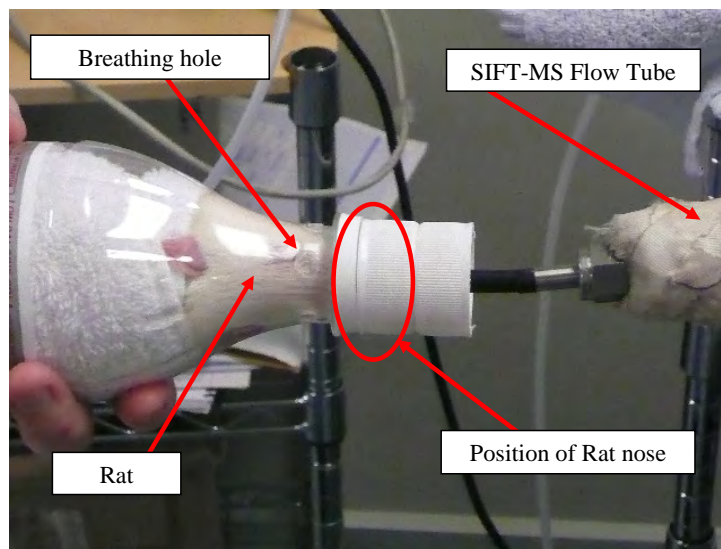


Figure 5.27 Breath collection apparatus

A background air sample was also obtained at each rat breath sample time-point. The tightness of the fit in the bottle combined with wrapping the rat in a towel minimised contamination from the fur and waste products. Breathing holes were located posterior to the position of the rats' nose. Breath was drawn directly from the bottle through the SIFT-MS machine at 2mL/sec via a small straw attached to the end of the bottle. Background air plays a significant role in this experimental set-up, and the pilot studies and mathematical models to account for this are described in the next chapter.

The effect of the anaesthetic was tested to ensure that there were not any metabolites interfering with experimental results. The selected anaesthetic (domitor/ketamine) is metabolised mainly in the liver, and excreted mainly in the urine. Hence, it was not expected to interfere with breath VOCs. A pilot experiment was performed in which breath VOCs were monitored in 2 anaesthetised rats. Breath was sampled prior to administering the anaesthetic, and again at 30 minutes and 60 minutes post-anaesthetic with H_3O^+ , NO^+ and O_2^+ precursors. At this time, the reversal agent was administered and breath was sampled again 1 and 2 hours later.

Acetone was seen to increase over the course of the experiment, due to the enforced fast, as seen in Figures 5.28, 5.29, and 5.30.

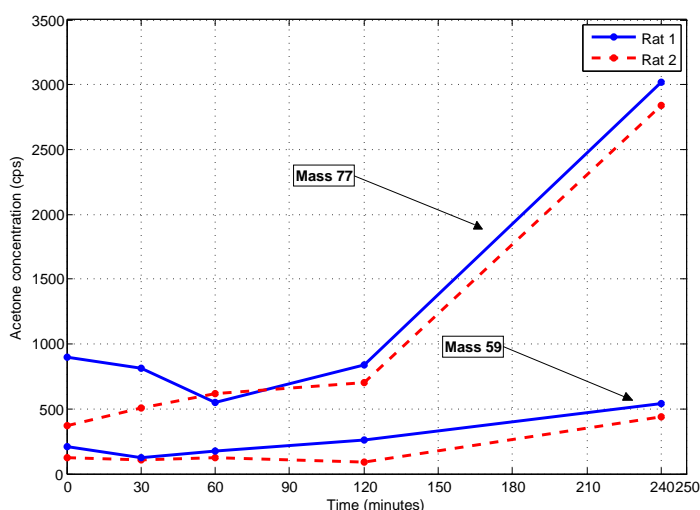


Figure 5.28 Increase in acetone as measured with H_3O^+ precursor over duration of anaesthesia

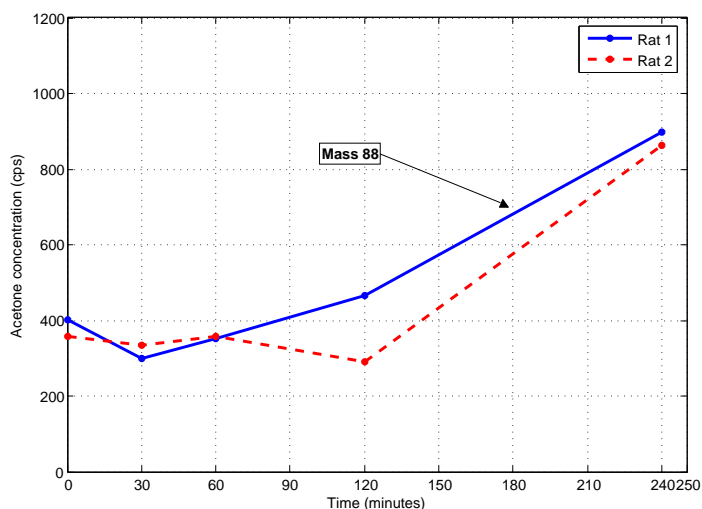


Figure 5.29 Increase in acetone as measured with NO^+ precursor over duration of anaesthesia

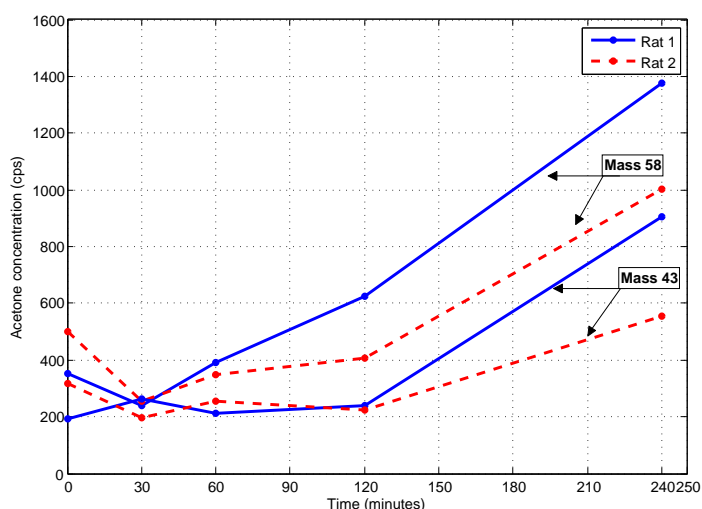


Figure 5.30 Increase in acetone as measured with O_2^+ precursor over duration of anaesthesia

Isoprene was observed to decrease over the course of the experiment, although this trend was more pronounced in Rat 2, as seen in Figures 5.29, and 5.30. Isoprene has been reported to be increased in patients with end-stage renal failure, [Davies et al., 2001]. Hence, it was an important analyte to monitor in the main trial.

Lastly, because breath sampling occurs both following cannulation surgery and following surgery for ARF induction, any VOC present because of the surgery or anaesthetic would be identified in the control post-cannulation breath experiments, and therefore not attributed to the reduction in renal function.

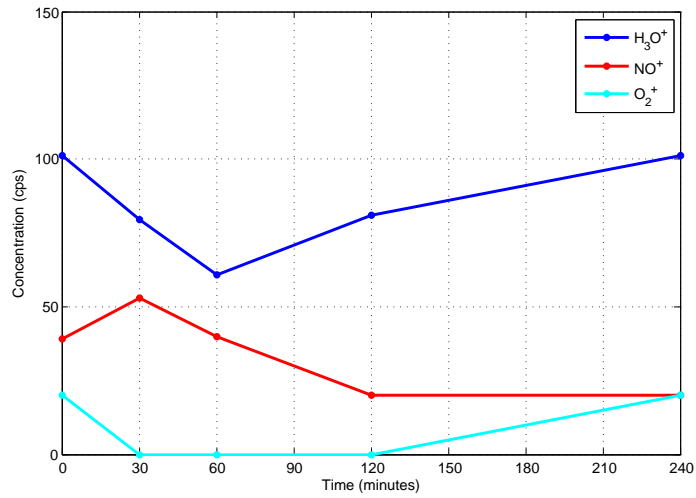


Figure 5.31 Decrease in isoprene in Rat 1 over duration of anaesthesia

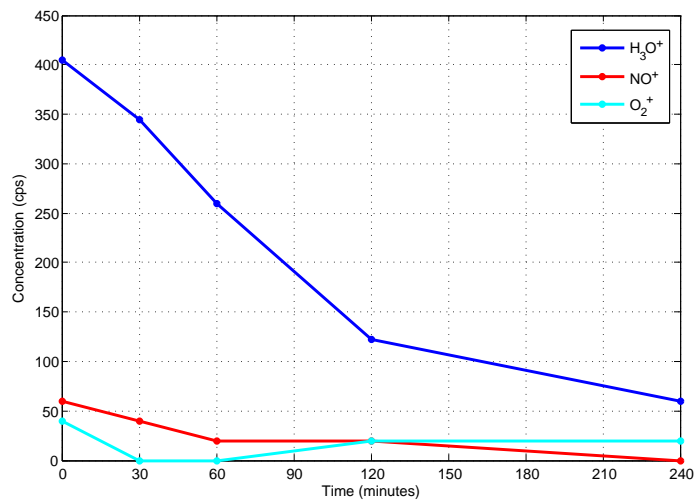


Figure 5.32 Decrease in isoprene in Rat 2 over duration of anaesthesia

5.7 Summary

Kidney structure and function was described, with specific reference to GFR and acute renal failure. Current clinical and research gold standard methods for determining renal function via the clearance of endogenous (creatinine) and exogenous (inulin) markers, was summarised, along with a discussion of the difficulties and limitations with these techniques.

An experimental design was presented for monitoring breath analyte concentration in rats for the purpose of determination of renal function after induction of ARF. Methods for determining GFR via a bolus inulin clearance and plasma creatinine sampling were also presented. Results from these latter methods al-

low comparison of the breath monitoring technique with current gold standard measures.

Pilot studies were described that were conducted to refine the techniques required for the main clinical trial. Pilot study considerations included surgical techniques, anaesthetic agents, serial blood sampling, bolus clearance modelling and breath collection techniques.

Chapter 6

ARF in Rats - Mathematical Methods

6.1 Inulin Clearance Modelling for GFR Determination

Injection of an inulin bolus into the blood is described by the 2-compartment model in Figure 6.1, where the bolus is injected into the plasma compartment, P , (with distribution volume V_P), and moves bi-directionally between the interstitial compartment, Q , (distribution volume V_Q), as described by n_2 and n_3 before being eliminated from the plasma via the kidneys, as described by n_1 .

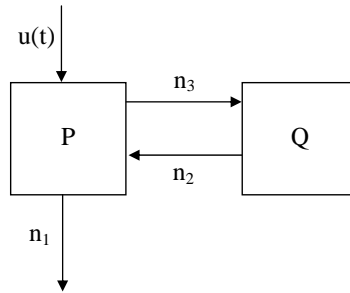


Figure 6.1 Two-Compartment Model of Kidney Function

The differential equations describing the amount of inulin in the 2 compartments are dependent on the rate constants $n_1 - n_3$, and the inulin mass in both compartments, $p(t)$ and $q(t)$, as described in Equations (6.1) and (6.2).

$$\frac{d}{dt}p(t) = -(n_1 + n_3)p(t) + n_2q(t) + u(t) \quad (6.1)$$

$$\frac{d}{dt}q(t) = -n_2q(t) + n_3p(t) \quad (6.2)$$

In terms of concentrations, where $P = \frac{p}{V_P}$ and $Q = \frac{q}{V_Q}$, and defining $\alpha = \frac{V_Q}{V_P}$, Equations (6.1) and (6.2) become:

$$\dot{P} = -(n_1 + n_3)P(t) + n_2\alpha Q(t) + \frac{u(t)}{V_P} \quad (6.3)$$

$$\dot{Q} = -n_2Q(t) + \frac{n_3}{\alpha}P(t) \quad (6.4)$$

Since transport is assumed to be passive between plasma and interstitial compartments, the volume flowrate between compartments must be equal, indicating a diffusion-based transport, as defined in Equation (6.5).

$$n_3V_P = n_2V_Q \quad (6.5)$$

It is assumed that the bolus is given so quickly that the concentration in the interstitial compartment, $Q(t)$, is initially zero (as verified by the -1 minute blood sample). The bolus is therefore modelled as a unit impulse function at time zero, as described in Equation (6.6), where $P(0)$ is the inulin concentration in the plasma compartment at time zero, and $\delta(t)$ is the Dirac delta function.

$$u(t) = P(0)V_P\delta(t) \quad (6.6)$$

Equation (6.6) is a reasonable simplification given there is no extra information to be obtained by modelling the initial rise in plasma inulin concentration, giving the physical limitations of gaining a sufficient number of accurate sample datapoints within the first minute after injection of the bolus. This assumption also indicates that the initial concentration in the plasma compartment is determined from the size of the injected bolus and the plasma volume.

Combining Equations (6.3), (6.4), (6.5) and (6.6) yields:

$$\dot{P} = -n_1P(t) - n_2\alpha(P(t) - Q(t)) + P(0)\delta(t) \quad (6.7)$$

$$\dot{Q} = n_2(P(t) - Q(t)) \quad (6.8)$$

An analytical approach for solving this type of problem is to differentiate Equation (6.7) to obtain a second order ODE in $P(t)$:

$$\ddot{P} = -n_1\dot{P} - n_2\alpha(\dot{P} - \dot{Q}) \quad (6.9)$$

Equations (6.7) and (6.8) are rearranged for Q and \dot{Q} , and are substituted into Equation (6.9), which yields:

$$\ddot{P} + (n_1 + n_2\alpha + n_2)\dot{P} + n_1n_2P = 0 \quad (6.10)$$

Equation (6.10) can be solved analytically to yield an equation of the form $P(t) = Ae^{-k_1t} + Be^{-k_2t}$. However, this solution is highly non-linear in the unknown parameters n_1 and n_2 , and would require a non-linear optimisation routine to solve. Thus, although the problem is simplified at one level by finding an analytical solution to Equation (6.10), the inverse problem of identifying n_1 and n_2 is made non-linear and non-convex. Hence it is more difficult to find a global minima, and would require many computationally expensive simulations over multiple starting points to ensure the correct solution is obtained.

An alternative method is to recognise that identification of the parameter n_1 required for determination of *GFR*, can be achieved without computing an analytical or a numerical solution, by using measured concentration data and an iterative integral fitting method, [Hann et al., 2005].

This parameter identification method uses integrals of Equations (6.7) and (6.8) to reduce the nonlinear estimation problem to a set of linear equations that can be solved using linear least squares. The result is a convex relaxation to a well known optimisation problem, which is linear and requires minimal computation. In addition, integral functions have the advantage of being robust to noise in the measured data, by effectively providing a low-pass filter in the summations involved in numerical integration.

First, Equation (6.7) is integrated to obtain an approximation to $P(t)$ in terms of the unknowns n_1 and n_2 . A system of equations is then set up as defined in Equation (6.11), and solved for n_1 and n_2 using linear least squares.

$$\left[\int_0^t P(t)dt \quad \alpha \int_0^t (P(t) - Q(t))dt \right] \begin{bmatrix} n_1 \\ n_2 \end{bmatrix} = \begin{bmatrix} P(0) - P(t) \end{bmatrix} \quad (6.11)$$

Note that Equation (6.11) will have to be integrated over several different time intervals in the test to yield a solvable system of equations.

The initial approximation of $P(t)$ is a linear piecewise approximation obtained from the measured time and concentration data, and $P(0)$ is the estimated average inulin concentration in the plasma immediately after injection of the bolus, defined as the product of the bolus volume and concentration, divided by the estimated plasma volume of the animal based on its weight. Using the obtained solution for n_1 and n_2 , a new approximation for $P(t)$ is generated. Constraints are added to the least squares solution to keep the approximation within known physiological ranges. However, there are no measurements for $Q(t)$, hence a different approach is required to analyse the interstitial compartment.

Given the approximation for $P(t)$, $Q(t)$ can be found analytically using the convolution integral solution to Equation (6.8), given in (6.12).

$$Q(t) = n_2 \int_0^t P(\tau) e^{-n_2(t-\tau)} d\tau \quad (6.12)$$

Iterations between $P(t)$ and new estimates of $Q(t)$ to update $P(t)$ in Equation (6.11) continue until convergence is achieved in the parameter values. The method is repeated for α values within the physiologically reported range of 2.2 - 4.5 [Levitt, 2003] and [Poulsen et al., 1977], until a least squares solution is found for α .

[Levitt, 2003] and Poulsen et al. [1977] both determined the volume of distribution in humans. Therefore, to determine the volume of distribution in rats, 2 pilot experiments were performed, in which the renal arteries were tied off, and

an inulin bolus was injected. Plasma samples were collected over 90 minutes, by which time it was assumed that equilibrium would be obtained. Note that in this model, the volume of distribution is equal to the sum of the plasma and interstitial volumes ($V_P + V_Q$). The volume of distribution was then calculated using Equation (6.13),

$$(\text{volume of distribution}) = \frac{(\text{vol inj})(\text{cts inj})}{SS\text{cts}} \quad (6.13)$$

where vol inj is the volume of the inulin bolus, cts inj is the inulin concentration in the bolus, and $SS\text{cts}$ is the steady state inulin concentration calculated as the area under the plasma inulin concentration curve (AUC) divided by time, after equilibration between compartments. Note that if GFR is reduced to zero, after equilibration between the plasma and interstitial compartments the inulin concentration will remain constant until the end of the experiment, and thus $SS\text{cts}$ will be a true *steady state*. Using this technique, Figures 6.2 and 6.3 were obtained for rats 1 and 2, respectively, and experimental and model identified parameters are shown in Table 6.1.

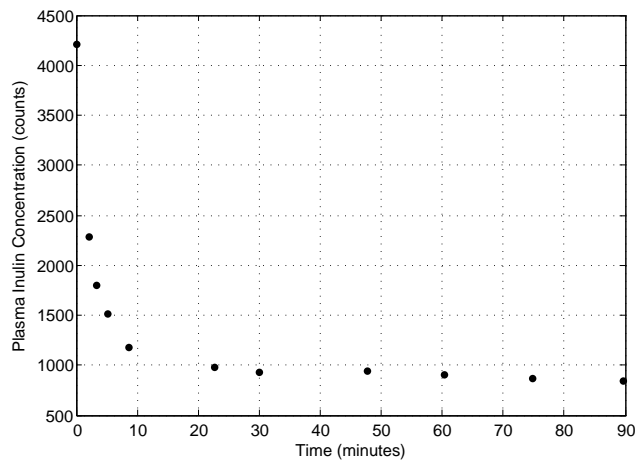


Figure 6.2 Rat 1 Raw inulin concentration data to enable modelling of volume of distribution

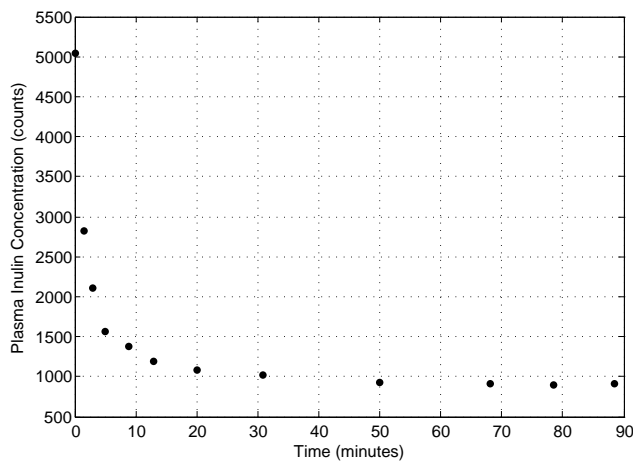


Figure 6.3 Rat 2 Raw inulin concentration data to enable modelling of volume of distribution

Table 6.1 Parameters for Volume of Distribution Determination

Parameter	Rat 1	Rat 2
Volume inulin injected	0.38mL	0.395mL
Concentration inulin injected	183746.7 counts	195411.6 counts
Steady state inulin concentration	896 counts	913.4 counts
Weight	415g	383g
Plasma volume	16.6mL	15.3mL
Volume of distribution	77.9mL	84.5mL
α	3.7	4.5

However, as seen in Figures 6.4 and 6.5, the model fit to this raw inulin concentration data suggests that steady state was not obtained, and thus GFR was not exactly zero. Therefore, the volume of distribution and, subsequently α , were overestimated in this instance. Average and maximum fitting errors were 3.6% and 6.7%, and 5.7% and 10.9% for rats 1 and 2, respectively in Figures 6.4 and 6.5. Note that, as the experiments were designed, the plasma and unmeasured interstitial concentration should approach the same value, as seen in Figures 6.4 and 6.5.

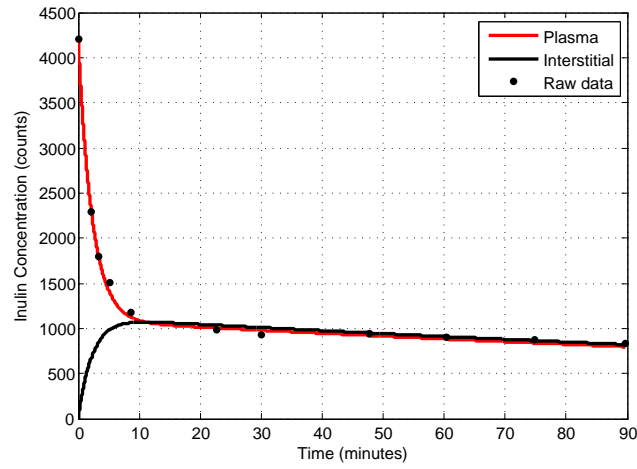


Figure 6.4 Rat 1 Model fit to raw inulin concentration data for volume of distribution determination. The non-zero slope indicates $GFR \neq 0$

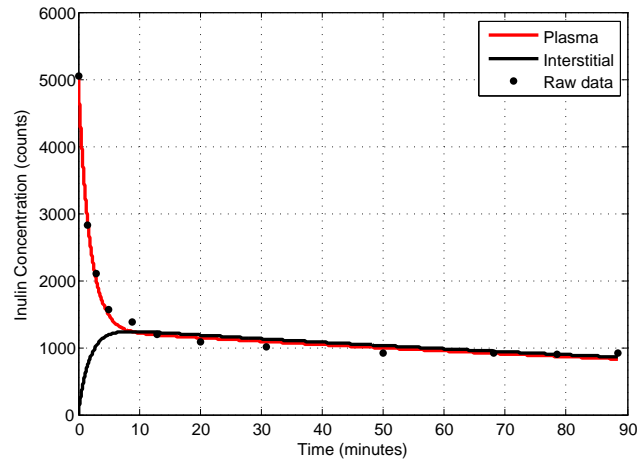


Figure 6.5 Rat 2 Model fit to raw inulin concentration data. The non-zero slope indicates $GFR \neq 0$

Equation (6.14) was employed to account for this situation in which steady state is not achieved,

$$\begin{aligned}
 (\text{volume of distribution}) &= \frac{(\text{vol inj})(\text{cts inj}) - (\text{vol lost})(AUC/\text{time})}{AUC/\text{time}} \\
 &= \frac{(\text{vol inj})(\text{cts inj})}{AUC/\text{time}} - (GFR)(\text{mins}) \quad (6.14)
 \end{aligned}$$

where cts lost is the concentration of inulin excreted, vol lost is the volume of

urine passed over the experiment, *time* is time between equilibration and the end of the experiment, and *mins* is the length of time between injection of the bolus and the end of the experiment.

Using this technique, α was estimated as $\alpha = 2.3$ and $\alpha = 2.2$ for rats 1 and 2 respectively, compared with the $\alpha = 3.7$ and $\alpha = 4.5$ values obtained previously. Therefore, in the integral fitting method, α values of between 2.2 and 4.5 are permitted. This method also allows for a changing volume of distribution between clearance experiments, which is reasonable considering the changing state of the rat over the 2-week course of the trial, including variable blood loss, water consumption, and fluid loading. It is important to recognise that the volume of distribution is a pharmacokinetic parameter, rather than an absolute physiological parameter. Distribution of a substance in the interstitial compartment will vary depending on the substance. Thus, the volume of the interstitial compartment does not have an exact physiological meaning.

After fitting the model to the raw inulin concentration data, the GFR is then equal to the product of n_1 and the plasma volume, where plasma volume is defined in Equation (6.15), and is found analytically using *MapleTM* with Equations (6.1) and (6.2),

$$V_P = \frac{(-bolus)(rawcts)(-1 + e^{-n_1 t bolus})}{(n_1)(P(0))(t bolus)(e^{-n_1 t bolus})} \quad (6.15)$$

where *bolus* is the volume of inulin solution injected, *rawcts* is the concentration of the injected inulin, *t bolus* is the time over which the bolus was injected, and $P(0)$ is the average inulin concentration in the plasma immediately after injecting the inulin bolus. Note that blood sampling over the course of the experiment results in a decreased haematocrit, although blood volume and pressure is maintained by flushing the cannula with an equal volume of saline. For a 300g rat with a 18-19mL blood volume, the 1.4mL of blood required over the experiment results in a 7-8% decrease in haematocrit, which is not accounted for in the model.

Finally, note that the expected plasma volume is approximately 40% body weight, based on a blood volume as defined in Equation (5.5), and an average haematocrit of 40%. Thus, a 300g rat will have a plasma volume of approximately 11-12mL.

6.2 Creatinine Estimates of GFR

All animals recruited for the present study were female Sprague-Dawley rats of approximately the same age. Therefore, GFR was estimated based on rat weight and plasma creatinine concentration. By plotting GFR (mL/min) values generated using the inulin clearance method against $\frac{wt}{P_{cr}}$ for all rats at all time points, Figure 6.6 and Equation (5.4) were obtained, where wt is the rat weight in kg , and P_{Cr} is the plasma creatinine concentration in $\mu mol/L$.

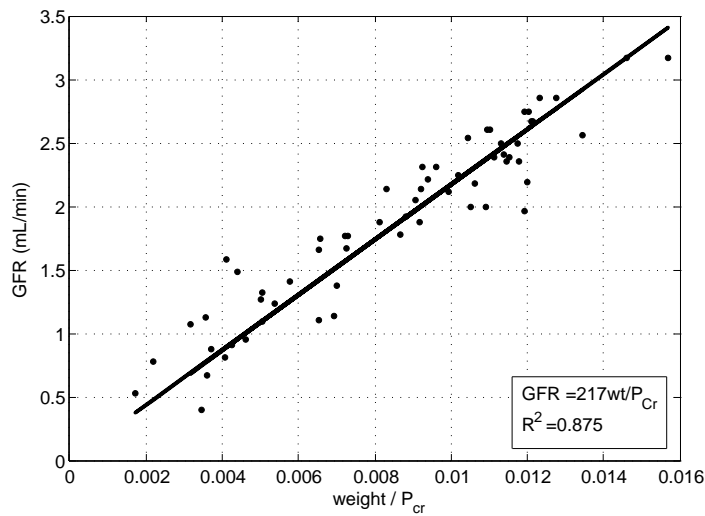


Figure 6.6 Relationship between plasma creatinine and GFR in all rats

$$GFR = 217 \frac{wt}{P_{cr}} \quad (6.16)$$

6.3 Breath collection for GFR estimation

6.3.1 SIM Scans

A pilot study was conducted to determine the relationship between rat breath and background air in the experimental set-up described in Chapter 5. Healthy, conscious rats were allowed to equilibrate in a room containing a controlled concentration of ammonia. By increasing the concentration of the background ammonia, C_B , and measuring the sample collected in the bottle, C_{Tot} , Figure 6.7 was

obtained, relating background ammonia to the concentration in a rat's breath, which is useful for calibration of experimental results.

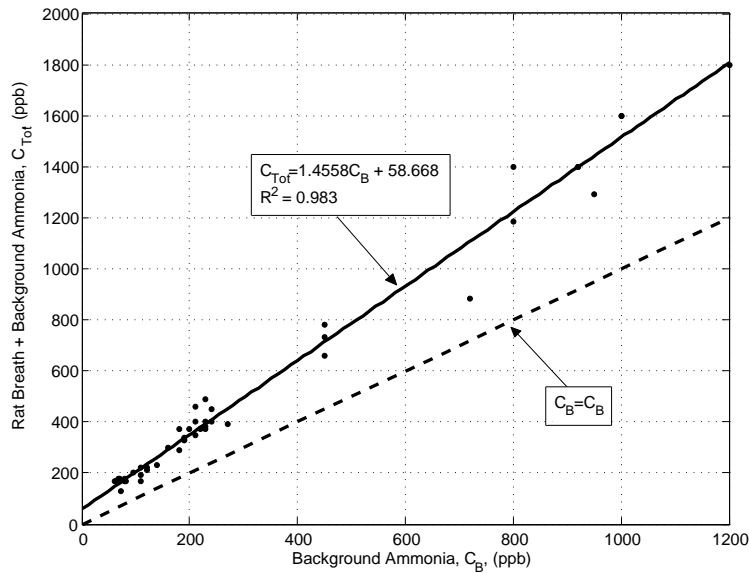


Figure 6.7 Relationship between background and breath ammonia in healthy rats

Linear regression yields Equation (6.17), where the y-intercept can be used to find the concentration of ammonia in breath given a zero concentration in background air.

$$C_{Tot} = 1.46C_B + 59 \quad (6.17)$$

Because of the experimental set-up, the measured concentration, C_{Tot} is actually a combination of the rat breath concentration, C_R , and the background air, C_B . Hence, C_R is even higher than seen in Figure 6.7.

The slope of C_{Tot} in Figure 6.7 illustrates the very important observation that ammonia concentration in rat breath, C_R , is dependent on the concentration of that analyte in the background air, C_B , as expected. However, the slope greater than 1 indicates that ammonia is concentrated in the breath against its concentration gradient from the blood, a finding that has not been previously described.

For simple diffusion down a concentration gradient, as is usually reported for transport across lung epithelial cells, it was expected that when plotted against C_B , the lines C_{Tot} and C_B should intersect at a point where the concentrations are equal. At background air concentrations less than the point of intersection, the analyte diffuses *out of* the blood, and at background air concentrations greater than the point of intersection, the analyte diffuses *into* the blood. Hence, this finding in Figure 6.7 and Equation (6.17) suggests the presence of actively energised ammonia transporters in the lung capillaries or epithelia, which are capable of transporting ammonia against its concentration gradient such that ammonia appears to be exhaled at concentration greater than that of the background air or the blood.

Another possible explanation is that ammonia and its metabolites are removed from the blood and concentrated in the lung tissue, thus providing a sink for diffusion into the alveolar air. Cooper and Freed [2005] injected a [^{13}N]ammonia bolus into the femoral vein of anaesthetised rats and measured its clearance from the blood. Results showed that nearly 30% of the label was removed by the lungs in the first pass, supporting the theory for an ammonia sink. However, they did not measure large quantities of ammonia in the expired air. A third possible explanation is an increase in the action of the enzyme urease in the oral cavity, which converts urea to ammonia.

Equation (6.17) indicates the ammonia concentration in a healthy rat. However, it is not feasible to perform such an experiment on a group of rats with equally impaired renal function. Hence, a generalised model must be developed, and analyte concentration in rats with impaired renal function must be normalised to the healthy rat state.

A lumped parameter model for the breath circuit is shown in Figure 6.8. In this model, the rat is breathing at a volume flow rate of V_R mL/sec, and breathes in and out concentrations of C_{Tot} and C_R , respectively. SIFT-MS draws the sample at 2mL/sec, and thus background air must be drawn into the bottle at $V_B = 2\text{mL/sec}$ to maintain equilibrium. The volume flow rate of rat breath is calculated from tidal volume and respiratory rate, which for a 250-300g rat, is approximately 2.7mL/sec [Pass and Freeth, 1993].

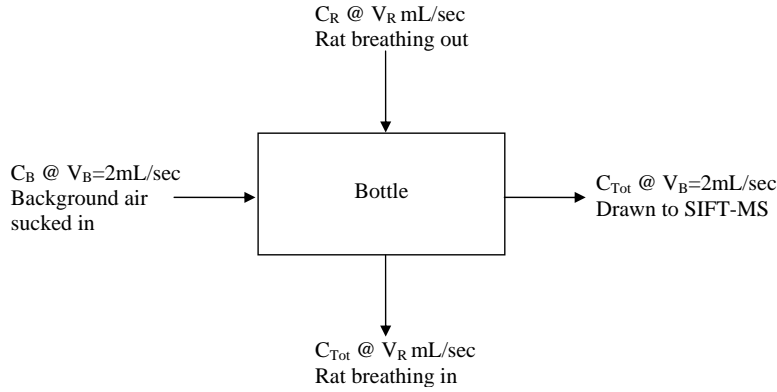


Figure 6.8 Rat Breathing Circuit

Using continuity of mass, C_R can be calculated from Equation (6.18).

$$\begin{aligned}
 C_B V_B + C_R V_R &= C_{Tot} V_B + C_{Tot} V_R \\
 \Rightarrow C_R &= \left(1 + \frac{V_B}{V_R}\right) C_{Tot} - \frac{V_B}{V_R} C_B
 \end{aligned} \tag{6.18}$$

Plotting C_R against C_B and fitting a linear regression as in Figure 6.7 and Equation (6.17), yields (6.19), specific for ammonia.

$$C_R = 1.79C_B + 102 \tag{6.19}$$

Note that the C_R obtained from Equation (6.19) is specific for a healthy rat. Hence, Equations (6.18) and (6.19) are combined to normalise a given rat concentration, C_R , to a healthy rat concentration at that background air concentration, as seen in (6.20).

$$C_{R^*} = \frac{\left(1 + \frac{V_B}{V_R}\right) C_{Tot} - \frac{V_B}{V_R} C_B}{1.79C_B + 102} \tag{6.20}$$

C_{R^*} is plotted against time, following the course of each surgical intervention. Hence, each rat provides their own control from the cannulation surgery to ensure that it was the ARF and not surgery alone causing the rise in breath ammonia. Using this method, a percentage increase in breath ammonia can be reported

for each rat. Subsequently, breath ammonia can be converted to GFR by plotting GFR obtained via inulin clearance against C_{R^*} for each rat, and generating Equation 6.21, where a is a rat-specific parameter.

$$GFR = \frac{a}{C_{R^*}} \quad (6.21)$$

Alternatively, a population metric for GFR can be obtained by plotting GFR obtained via inulin clearance against C_{R^*} for all rats at all time-points, which is shown in Figure 6.9. GFR can then be estimated for any rat in the population from breath ammonia using Equation (6.22). Note that domitor causes a 70% depression in respiration. Therefore, the ratio V_B/V_R in Equation (6.20) is increased during surgery and recovery from anesthesia. A limitation of this method is that the final breath concentration, normalised to the background air, is quite sensitive to changes in the V_B/V_R ratio. This problem is less of an issue in this study, because all rats are a similar weight, receive the same drug dosage, and undergo the same surgical procedures. Hence, the respiratory responses are assumed to be the same between animals.

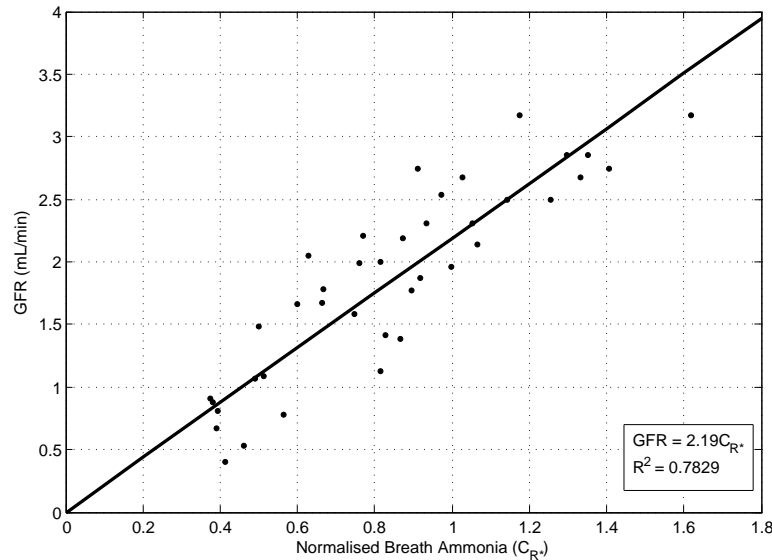


Figure 6.9 Relationship between breath ammonia and GFR, where the $a=2.19$ slope is a population estimate for Equation (6.21)

$$GFR = \frac{2.19}{C_{R^*}} \quad (6.22)$$

SIM scan results were collected not only for ammonia, but also for isoprene in this pilot experiment. Although isoprene concentration in the laboratory air was not varied deliberately, as ammonia was, its concentration was still monitored. Plotting C_{Tot} against C_B for isoprene, Figure 6.10 was obtained.

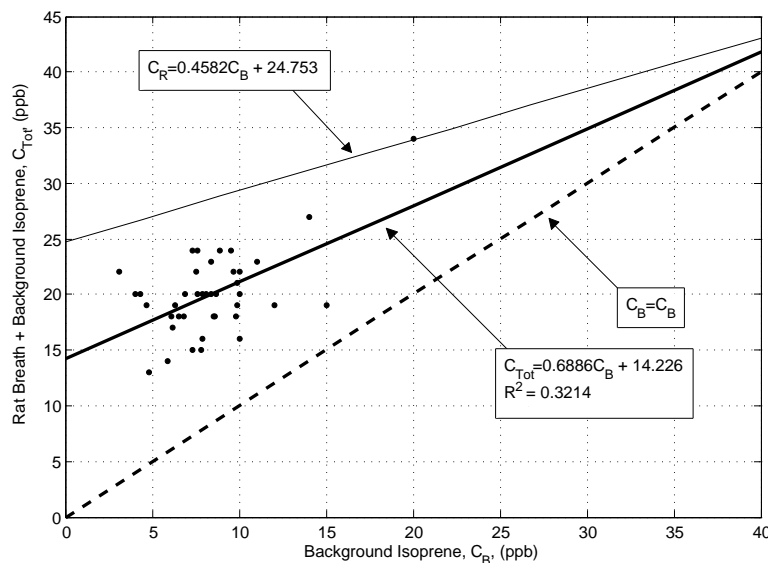


Figure 6.10 Relationship between background and breath isoprene in healthy rats

The correlation is much lower in Figure 6.10 than in Figure 6.7. However, the concentrations involved were much lower, and the variation in background air was a natural variation, rather than an artificially imposed condition. The C_{Tot} and C_R slopes have a value less than 1.0 indicating that isoprene behaves as expected for an analyte travelling passively down its concentration gradient across lung epithelia. The fact that the point of intersection was not reached within the commonly observed isoprene concentrations indicates that isoprene is substantially higher in breath than background air. Hence, there is an almost unlimited sink for isoprene diffusion into the background air.

[Buckley et al., 1999] found that after administering radiolabelled isoprene to rats and following the time course of excretion, 91% of that dose was recovered, of which 94% was excreted unchanged. Specifically, 59% was excreted in the breath, 35% was excreted by the kidney, and the remainder was recovered in the faeces and tissues. With known and reported renal excretion, the slope in Figure 6.10 is reasonable and suggests that the exhaled breath is the result of the combination of endogenous isoprene and background isoprene minus renal excretion.

With lack of evidence to suggest otherwise, it is expected that most other analytes cross the lung epithelia via diffusion, with the precise slope varying depending on excretory pathways specific to the analyte. That is, the amount exhaled will be a result of endogenous production or metabolism combined with the amount of analyte inhaled, minus metabolism or excretion of the analyte via other pathways. Ammonia, with its apparent active transport across the lung epithelia is considered an exception, which could be an evolutionary adaptation to rid the body of dangerous nitrogenous wastes.

6.3.2 Interpreting SIM Scan raw data

A typical SIM scan is shown in Figure 6.11. Error in the GFR estimation is due to the oscillation in ammonia concentration as recorded by the SIFT-MS, and seen in Figure 6.11. A density profile can be created from the SIM scan of background air and sample results, as described in Chapter 2 and shown in Figure 6.12.

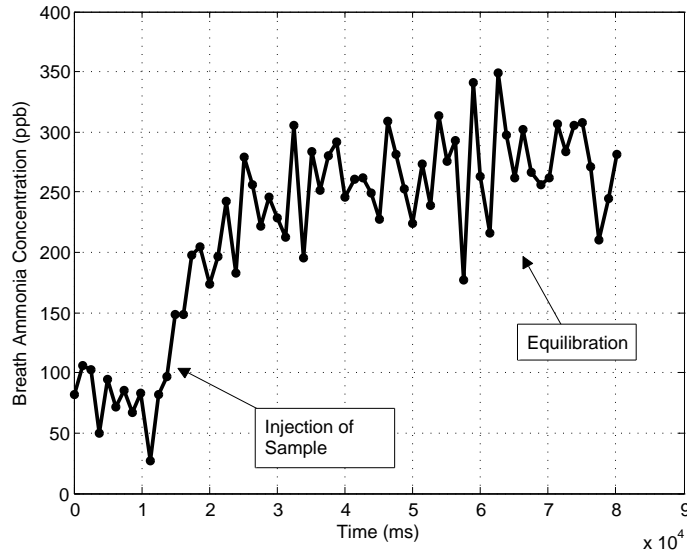


Figure 6.11 Typical SIM scan, showing oscillation in reported concentration at equilibrium

The reported concentration is then the peak of the density profile, with the error in the value obtained via error propagation. Equation (6.22) can then be re-written in full, including errors:

$$GFR \pm \Delta_{GFR} = a \frac{102 + 1.79(C_B \pm \Delta_{C_B})}{\left(1 + \frac{V_B}{V_R}\right)(C_{Tot} \pm \Delta_{C_{Tot}}) - \left(\frac{V_B}{V_R}\right)(C_B \pm \Delta_{C_B})} \quad (6.23)$$

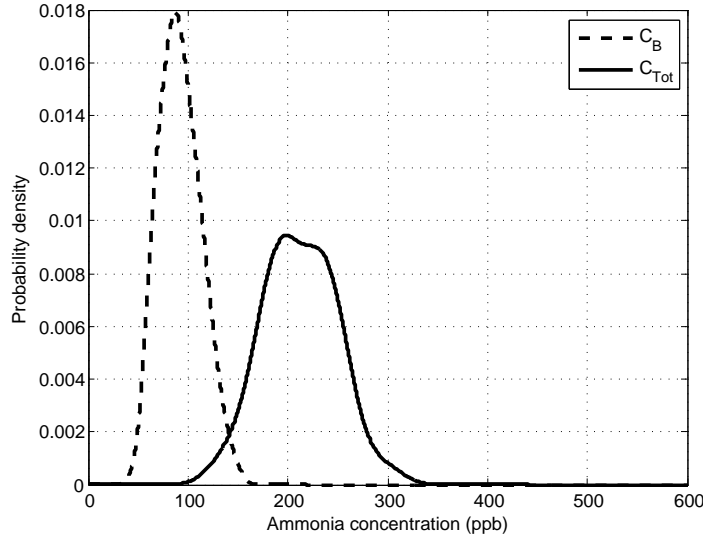


Figure 6.12 Density profile of typical SIM scan for determining *true* analyte concentration

The error on a quantity, Δx , is usually quoted as the standard deviation, σ . Given that the distribution in these SIM scans is largely normal, the 68% confidence limits are \pm one standard deviation from the value. Equations (6.24) and (6.25) are used to determine the error propagation in (6.23).

$$f = aA \pm bB \longrightarrow \sigma_f^2 = a^2\sigma_A^2 + b^2\sigma_B^2 \quad (6.24)$$

$$f = a\frac{A}{B} \longrightarrow \left(\frac{\sigma_f}{f}\right)^2 = \left(\frac{\sigma_A}{A}\right)^2 + \left(\frac{\sigma_B}{B}\right)^2 \quad (6.25)$$

Splitting (6.23) into its numerator, *num*, and denominator, *den*, the error in GFR, σ_{GFR} , is determined, as defined in Equations (6.26) and (6.27).

$$\left(\frac{\sigma_{GFR}}{GFR}\right)^2 = \left(\frac{\sigma_{num}}{num}\right)^2 + \left(\frac{\sigma_{den}}{den}\right)^2 \quad (6.26)$$

$$\Rightarrow \sigma_{GFR} = GFR \sqrt{\left(\frac{(1.79a)^2(\sigma_{C_B})^2}{(a^2)(102 + 1.79C_B)^2}\right) + \left(\frac{2\left(1 + \frac{V_B}{V_R}\right)^2 + 2(\sigma_{C_B})^2 + (\sigma_{C_{Tot}})^2}{\left(\left(1 + \frac{V_B}{V_R}\right)C_{Tot} - \frac{V_B}{V_R}C_B\right)^2}\right)} \quad (6.27)$$

6.3.3 Mass Scans

Mass scans were analysed using the paired model described in Chapter 3. Raw data were collected in triplicate for C_B and C_{Tot} were combined using Equation (6.18), and an Equation (6.20) specific to each mass of interest in the collected spectrum. Masses can appear in the breath from the background air in four main ways:

1. Mass generated endogenously, regardless of presence in background air; passive diffusion down a concentration gradient across lung epithelia; excretion a combination of ventilation, metabolism and renal elimination, eg isoprene. Figure 6.13, Case 1.
2. Mass generated endogenously, regardless of presence in background air; active transport across lung epithelia, eg ammonia. Figure 6.13, Case 2.
3. Mass not generated endogenously; passive diffusion down a concentration gradient across lung epithelia; no excretion or metabolism. Figure 6.14, Case 1.
4. Mass not generated endogenously; passive diffusion down a concentration gradient across lung epithelia; excretion a combination of ventilation, metabolism and renal elimination. Note that if the mass is not produced endogenously, but is metabolised or excreted via the kidneys, then the body is effectively removing a contaminant from the background air. Figure 6.14, Case 2.

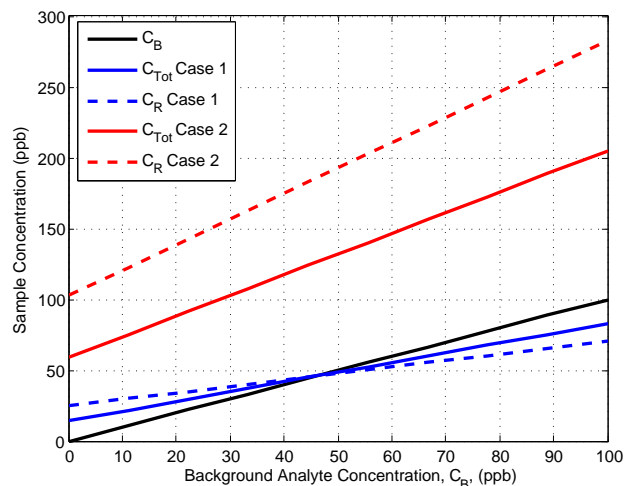


Figure 6.13 Endogenously generated analyte transport into alveolar breath

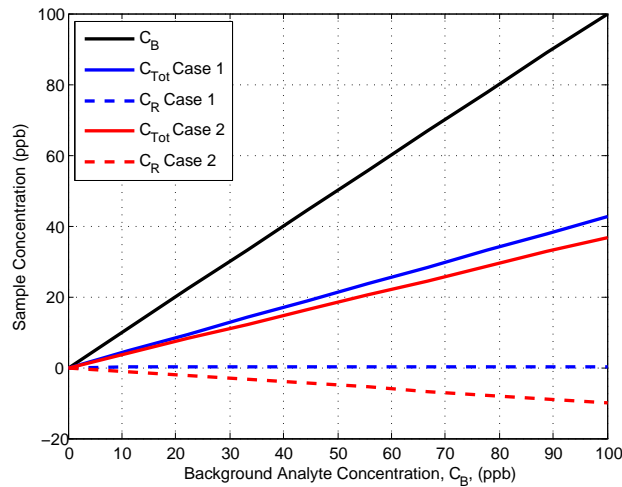


Figure 6.14 Analyte transport out of background air

Two classifications were performed using the paired classification technique of Chapter 3 for biomarker identification:

1. Maximum concentration after cannulation surgery *against* maximum concentration after ARF surgery
2. Healthy concentration (after recovery from cannulation surgery and before ARF surgery) *against* maximum concentration after ARF surgery

These three tests give an indication of the impact of ARF over and above the impact of any surgical stressor, as well as an indication of the degree of recovery within one week of induced ARF.

6.4 Summary

Mathematical models were presented for the determination of GFR from bolus inulin clearance tests, plasma creatinine concentrations, and breath collections. Specifically, a two compartment model described the kinetics of a bolus inulin tracer as it is injected into the plasma and passes out into the urine. Secondly, a population model based on the Cockcroft-Gault equation using plasma creatinine concentrations, was presented and modified for use in rats.

Lastly, it was illustrated how the concentration of analytes in rat breath can be isolated from the background air. This illustration required a pilot study to be carried out, in which the background air ammonia concentration was varied to determine its effect on expired breath. Interestingly, it was found that ammonia can be removed from the body at a concentration greater than that suggested by simple diffusion from the blood, alone.

Chapter 7

ARF in Rats - Results and Discussion

In total, 11 rats participated in the main ARF animal trial. The completeness of the datasets varied between rats, with the cannulae of some rats failing before the end of the trial. In addition, some of the earlier rats do not have control results for post-cannulation surgery. Results are detailed for each rat for correlation between inulin clearance, creatinine concentration and breath SIM scans. Histology slides were examined for evidence of ARF. Finally, the paired mass scan model from Chapter 3 was employed to identify other possible biomarkers of renal failure.

Given the small number of rats in this study, both pseudo-names and numbers were assigned to each, for clarity, and to highlight their contribution to these novel studies. Again, all rats were female Sprague-Dawley rats of 280-320g. They were housed individually at 21°C in a 12 hour light/dark cycle, and allowed free access to food and water. Rats were regularly monitored according to animal ethics guidelines, and approval for this study was granted by the Animal Ethics Committee under protocol C09/07601. Approval to conduct these trials, also required the successful completion of 3 animal ethics modules offered by the University of Otago Animal Welfare Office:

- Module One: Animal Ethics and Legislation
- Module Two: Experimental Animal Techniques
- Module Three: Anaesthesia and Surgery

7.1 Correlation of gold standard renal markers with breath ammonia

7.1.1 Grace - Rat 1

7.1.1.1 Inulin Clearance

Grace underwent a successful cannulation surgery, followed by a recovery inulin clearance test 2 days later. Five days after cannulation surgery, she underwent surgery to induce ARF. Surgery was successful, and the cannula remained patent for 3 post-ARF clearances. Her inulin clearance fitting results are shown in Figure 7.1, and model-fitted parameters are shown in Table 7.1. The good model fit to raw data in this and subsequent rats justifies the integral fitting method selected in Chapter 6.

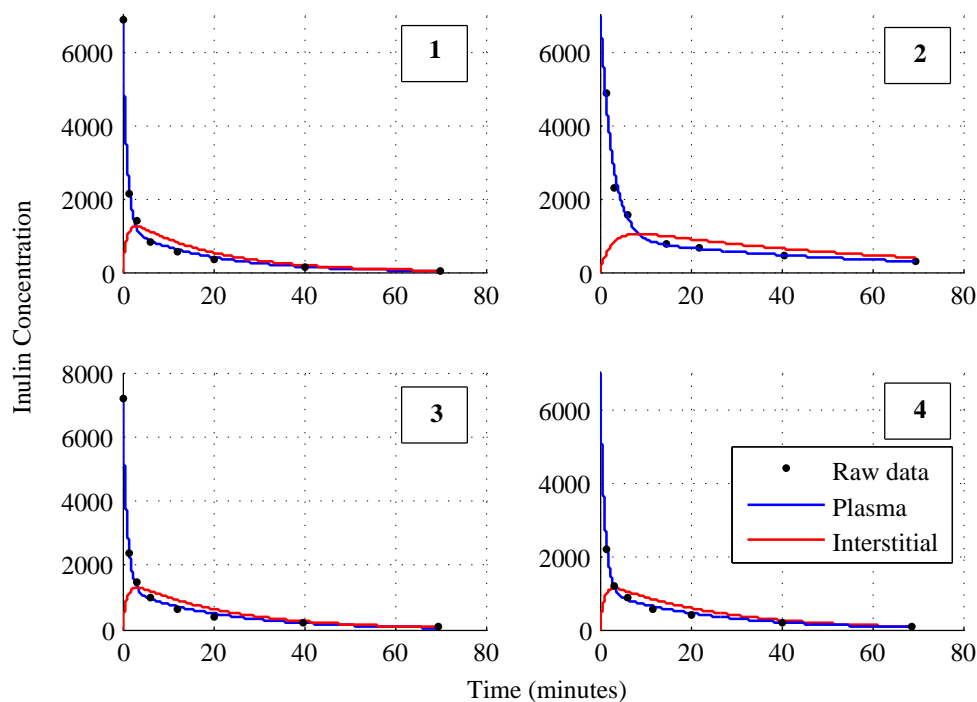


Figure 7.1 Grace: Modelling of inulin concentration in the plasma and interstitial compartments over a 70 minute clearance test conducted on 4 separate occasions. 1: Two days post cannulation surgery; 2-4: Six hours, 30 hours, and two days post ARF induction, respectively

Table 7.1 Grace: Inulin clearance parameters

Parameter	Inulin Clearance Test			
	1	2	3	4
Weight (g)	236.1	255	244	236.2
Plasma Volume (mL)	9.5	10.2	9.8	9.5
n_1	0.24817	0.1024	0.21567	0.22996
n_2	0.21958	0.060525	0.2109	0.17734
α	2.8	3.7	2.9	3.5
GFR (mL/min)	2.35	1.05	2.11	2.18
Average Fitting Error (%)	10.9	7.7	14.3	10.9
Maximum Fitting Error (%)	29.4	22.3	42.8	26.3

7.1.1.2 Creatinine

Five creatinine concentrations were determined using the jugular vein cannula, and a subsequent 3 samples obtained via the tail vein. A pre-ARF measurement was not taken, but was assumed to be similar to the 6 hour post-cannulation measurement.

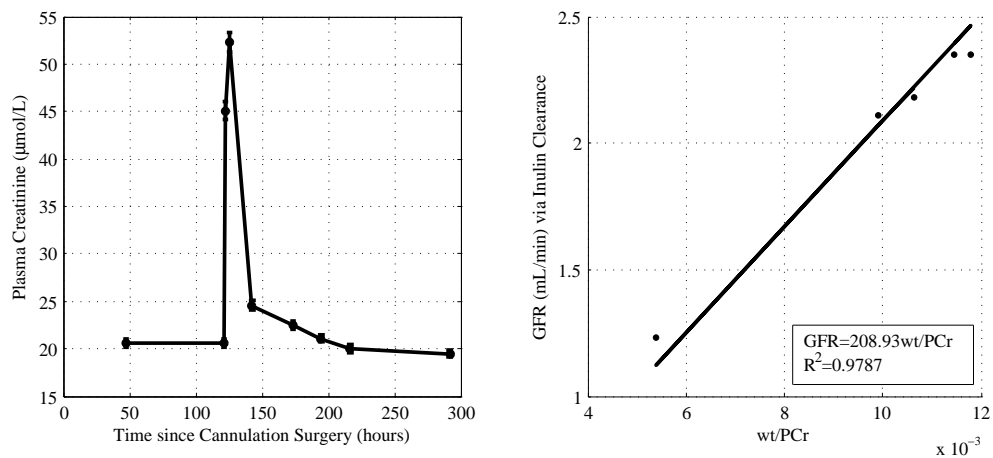


Figure 7.2 Grace: Plasma creatinine concentration and correlation with GFR via inulin clearance

7.1.1.3 Ammonia SIM Scans

Thirteen breath SIM scans were analysed from 1 hour after cannulation surgery until 7 days post-ARF surgery. Figure 7.3 shows the measured breath results for C_B and C_{Tot} , as well as the calculated C_R and C_{R^*} . In addition to displaying the rat breath ammonia concentration, Figure 7.3 highlights the natural variation in background ammonia levels in the laboratory environment.

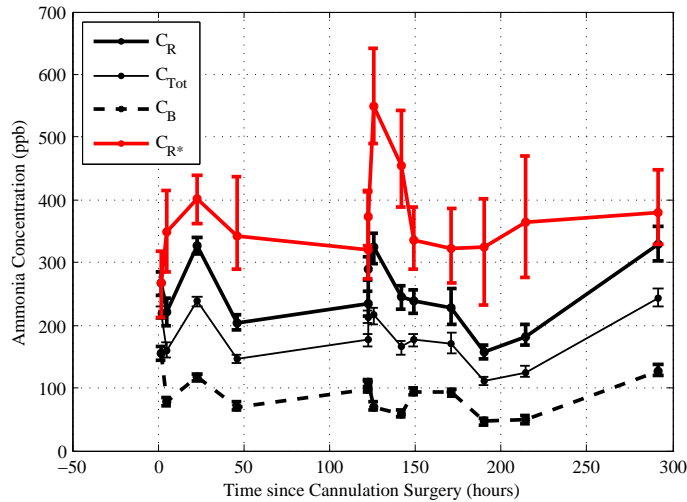


Figure 7.3 Grace: SIM scan analysis of ammonia in breath and background air

Plotting GFR obtained via inulin clearance against $1/C_{R^*}$ for all common test timepoints, resulted in Equation (7.1), with $a = 1.94$ from Equation (6.21), and an R^2 value of 0.74.

$$GFR = \frac{1.94}{C_{R^*}} \quad (7.1)$$

Combining GFR estimation via inulin clearance, plasma creatinine, and breath ammonia resulted in Figure 7.4. As expected, GFR drops after any surgery. However, the magnitude of that decrease is significantly greater after an acute renal injury. In this rat, approximately 90% of renal function was restored within 30 hours of induction of ARF, and renal function appeared to be back within a normal range by the end of the trial, 7 days after that injury. Error bars representing sampling errors and variation in breath measurement were calculated as described in Section 6.3. Errors in GFR estimation via inulin clearance were calculated from average model fitting errors. Lastly, a fixed error of 2% is shown

for errors in GFR calculation via plasma creatinine concentration, as described in Section 5.5.

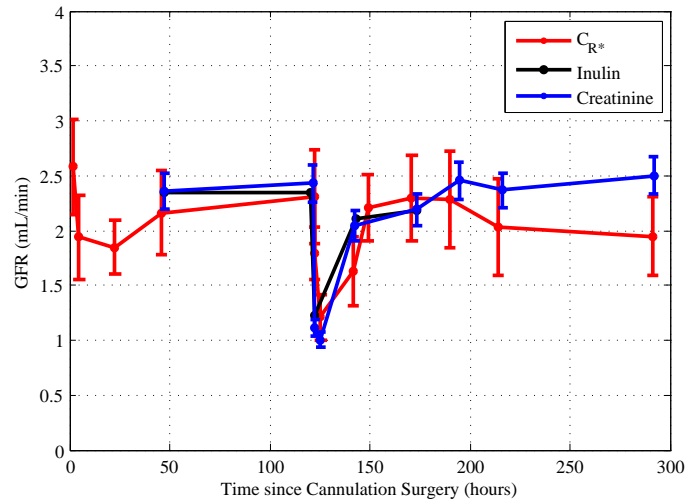


Figure 7.4 Grace: A comparison of GFR estimates via bolus inulin clearance, plasma creatinine concentration, and breath ammonia concentration, following cannulation surgery at 0 hours, and surgery for ARF induction at 120 hours

7.1.2 Heidi - Rat 2

7.1.2.1 Inulin Clearance

Heidi underwent a successful cannulation surgery, followed by a recovery inulin clearance test 2 days later. Five days after cannulation surgery, she underwent surgery to induce ARF. Surgery was successful, and the cannula remained patent for 3 post-ARF clearances. The first of these clearances was performed in a different manner to the rest of the clearance tests, in which blood samples were taken every 30-60 minutes after the bolus for 4 hours, to attempt a GFR estimate immediately after surgery. However, since this was a period when the GFR was increasing rapidly, this method was not particularly successful. Heidi's inulin clearance fitting results are shown in Figure 7.5, and model-fitted parameters are shown in Table 7.2.

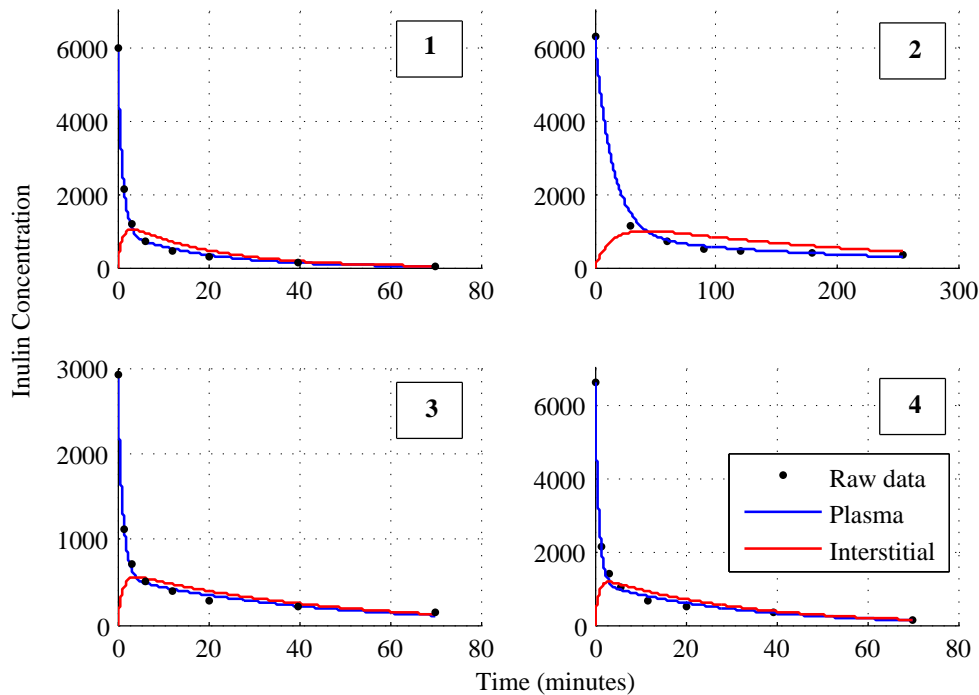


Figure 7.5 Heidi: Inulin clearance summary. 1: Two days post cannulation surgery; 2-4: One, 24 and 48 hours post ARF induction, respectively

Table 7.2 Heidi: Inulin clearance parameters

Parameter	Inulin Clearance Test			
	1	2	3	4
Weight (g)	259.5	273.3	258.4	269.5
Plasma Volume (mL)	10.4	10.9	10.4	10.8
n_1	0.24575	0.022907	0.10988	0.16224
n_2	0.18806	0.012801	0.19054	0.22255
α	2.8	2.8	3.3	3.5
GFR (mL/min)	2.56	0.25	1.14	1.75
Average Fitting Error (%)	9.7	14.9	7.0	9.6
Maximum Fitting Error (%)	31.8	34.0	19.8	17.5

7.1.2.2 Creatinine

Five creatinine concentrations were determined using the jugular vein cannula, with the last 2 samples obtained via the tail vein. A pre-ARF measurement was not taken, but was assumed to be similar to the 6 hour post-cannulation measurement.

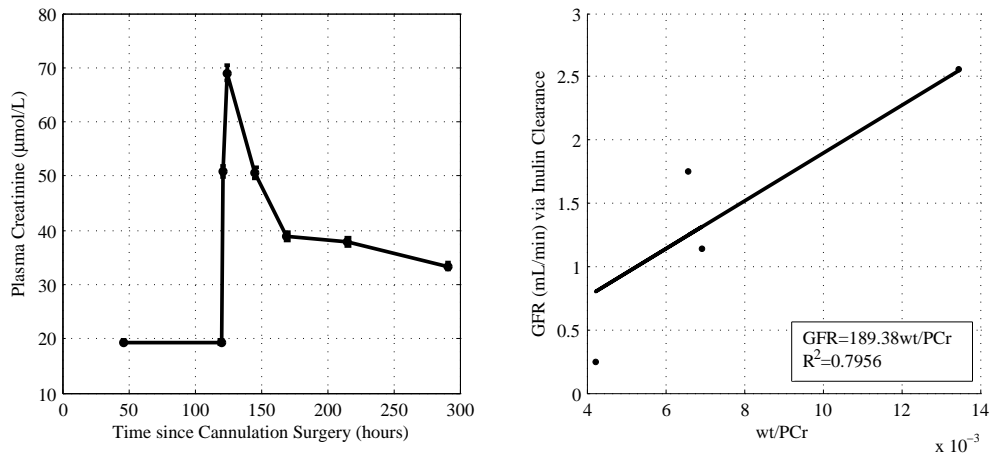


Figure 7.6 Heidi: Plasma creatinine concentration and correlation with GFR via inulin clearance

7.1.2.3 Ammonia SIM Scans

Nine breath SIM scans were analysed from 2 days after cannulation surgery until 7 days post-ARF surgery. Figure 7.7 shows the measured breath results for C_B and C_{Tot} , as well as the calculated C_R and C_{R^*} .

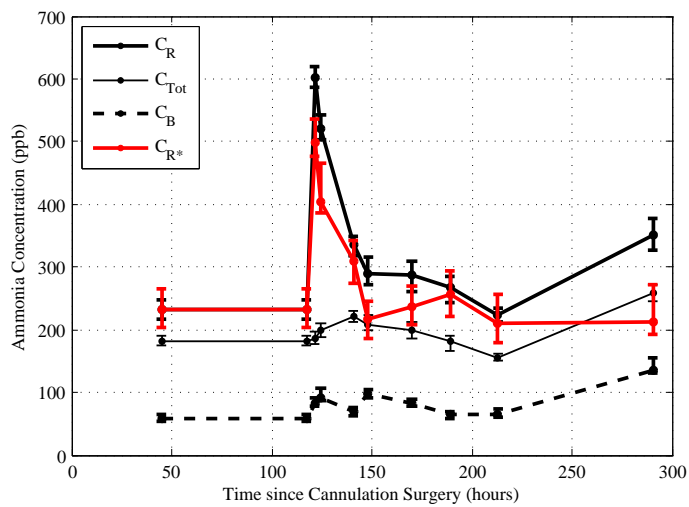


Figure 7.7 Heidi: SIM scan ammonia in breath and background air

Plotting GFR obtained via inulin clearance against $1/C_{R^*}$, resulted in Equa-

tion (7.2), with $a = 2.40$ from Equation (6.21), and an R^2 value of 0.52.

$$GFR = \frac{2.40}{C_{R^*}} \quad (7.2)$$

Combining GFR estimation via inulin clearance, plasma creatinine, and breath ammonia resulted in Figure 7.8.

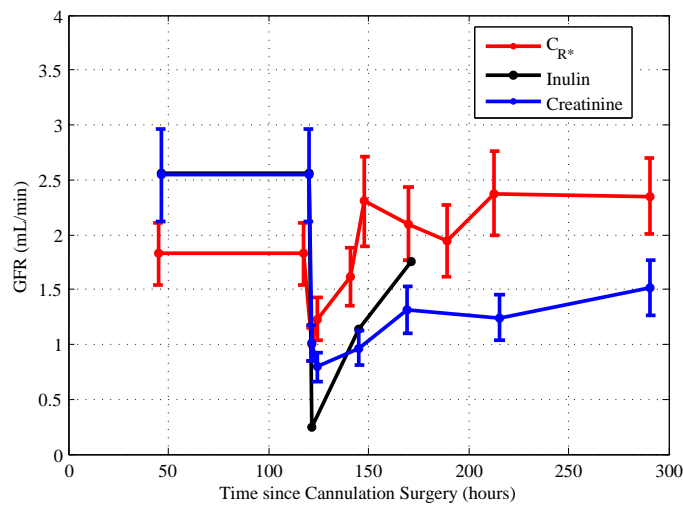


Figure 7.8 Heidi: GFR estimation via bolus inulin clearance, plasma creatinine, and breath ammonia

7.1.3 Isis - Rat 3

7.1.3.1 Inulin Clearance

Isis underwent a successful cannulation surgery, followed by a recovery inulin clearance test 2 days later. Five days after cannulation surgery, she underwent surgery to induce ARF. Surgery was successful, and the cannula remained patent for 5 post-ARF clearances, including an intermediate clearance the day after surgery. Her inulin clearance fitting results are shown in Figure 7.9, and model-fitted parameters are shown in Table 7.3.

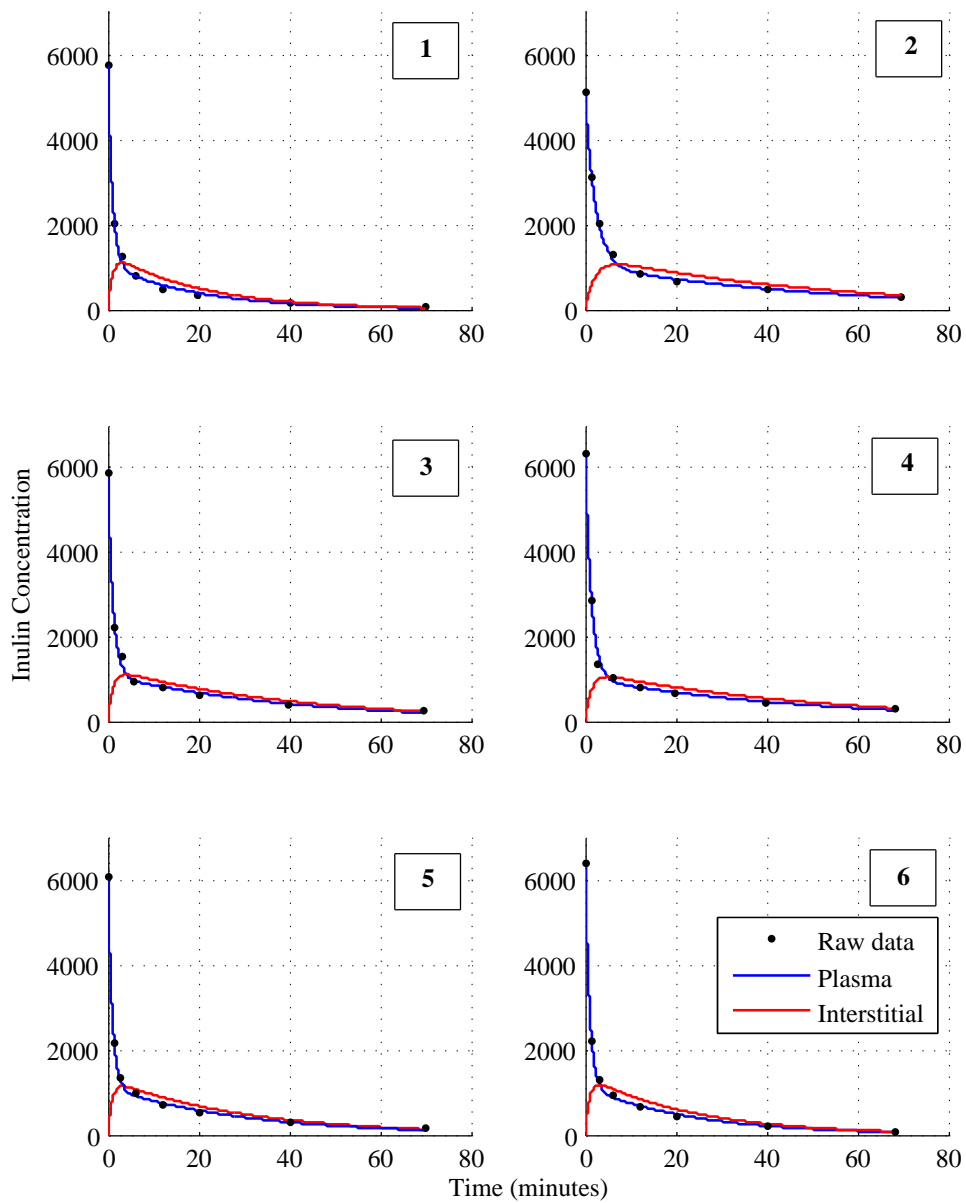


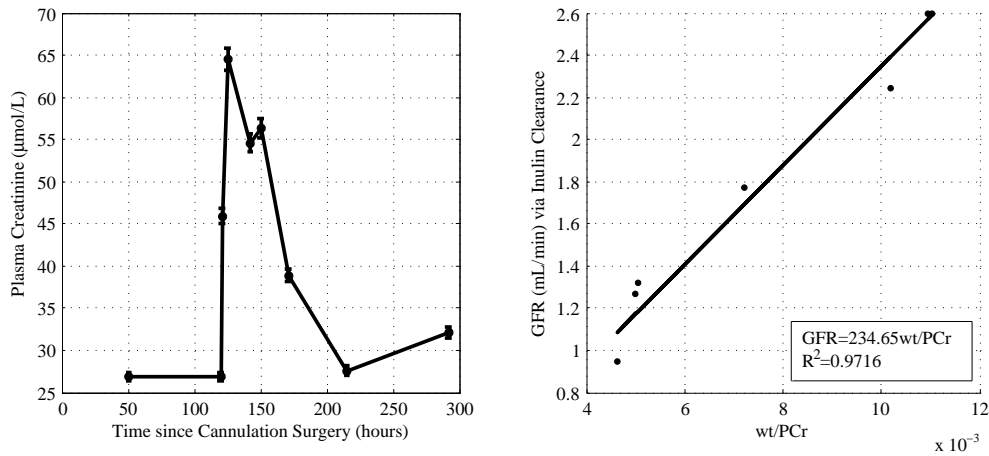
Figure 7.9 Isis: Inulin clearance summary, 1: Two days post cannulation surgery; 2-6: Six hours, 20 hours, 30 hours, 2 days and 4 days post ARF induction

7.1.3.2 Creatinine

The first 7 creatinine concentrations were able to be determined using the jugular vein cannula, with the last sample obtained via tail vein. A pre-ARF measurement was not taken, but was assumed to be similar to the 6 hour post-cannulation measurement.

Table 7.3 Isis: Inulin clearance parameters

Parameter	Inulin Clearance Test					
	1	2	3	4	5	6
Weight (g)	294.4	298.6	273.3	284	280.9	281.6
Plasma Volume (mL)	11.8	12.0	11.0	11.4	11.3	11.3
n_1	0.21967	0.0792	0.1156	0.1074	0.157	0.19817
n_2	0.22243	0.10698	0.185	0.13515	0.21887	0.21706
α	2.7	2.6	3.3	3.3	3.2	3.0
GFR (mL/min)	2.60	0.95	1.27	1.32	1.77	2.24
Average Fitting Error (%)	14.0	3.3	6.6	9.8	8.3	7.5
Maximum Fitting Error (%)	40.1	7.7	14.9	20.1	26.3	18.6

**Figure 7.10** Isis: Plasma creatinine concentration and correlation with GFR via inulin clearance

7.1.3.3 Ammonia SIM Scans

Nine breath SIM scans were analysed from 2 days after cannulation surgery until 7 days post-ARF surgery. Figure 7.11 shows the measured breath results for C_B and C_{Tot} as well as the calculated C_R and C_{R^*} .

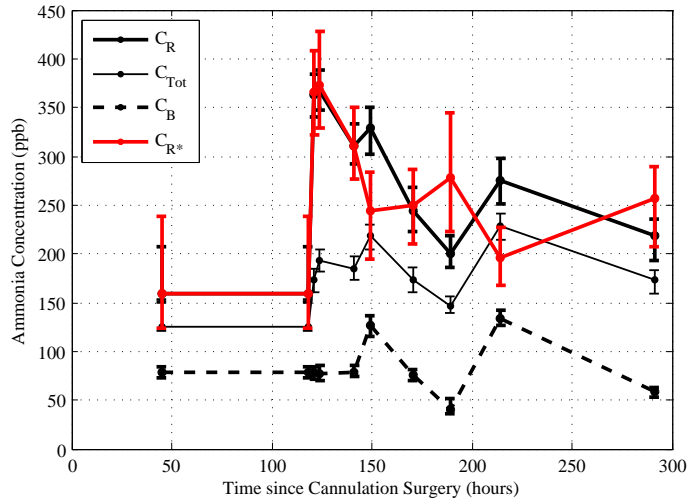


Figure 7.11 Isis: SIM scan ammonia concentration in rat breath and background air

Plotting GFR obtained via inulin clearance against $1/C_{R^*}$, resulted in Equation (7.3), with $a = 1.67$ from Equation (6.21), and an R^2 value of 0.93.

$$GFR = \frac{1.67}{C_{R^*}} \tag{7.3}$$

Combining GFR estimation via inulin clearance, plasma creatinine, and breath ammonia resulted in Figure 7.12.

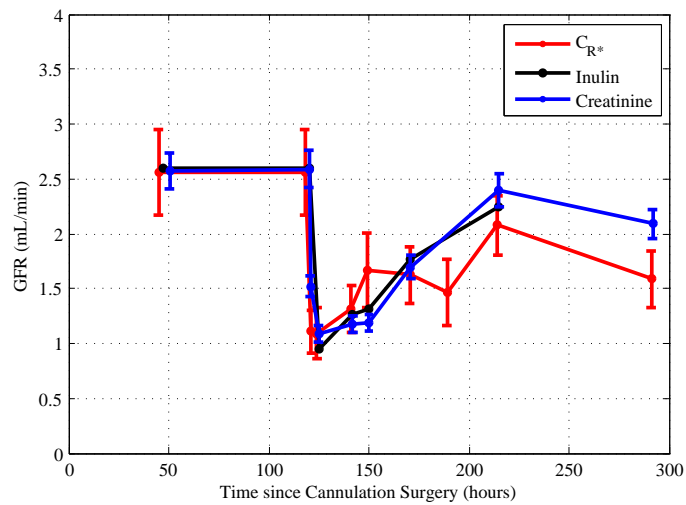


Figure 7.12 Isis: GFR estimation via bolus inulin clearance, plasma creatinine, and breath ammonia

7.1.4 Maya - Rat 4

7.1.4.1 Inulin Clearance

Maya underwent a successful cannulation surgery, followed by the post-operation and recovery inulin clearance tests. Five days later, she underwent surgery to induce ARF. Surgery was successful, and the cannula remained patent for 4 of the 5 post-ARF samples. Her inulin clearance fitting results are shown in Figure 7.13, and model-fitted parameters are shown in Table 7.4.

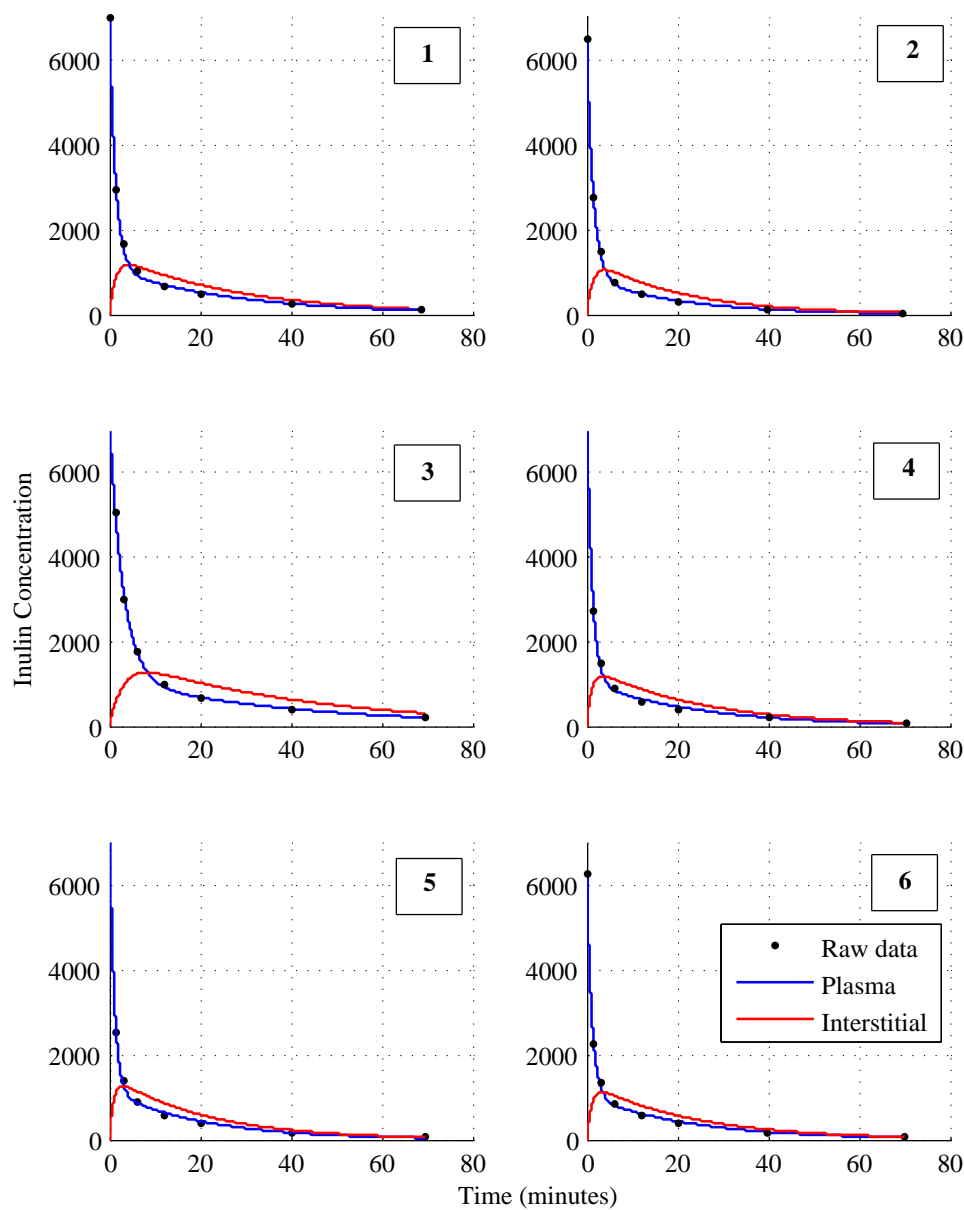


Figure 7.13 Maya: Inulin clearance summary, 1-2: Six hours and 2 days post cannulation surgery, respectively; 3-6: Six hours, 30 hours, 2 days and 4 days post ARF induction, respectively.

Table 7.4 Maya: Inulin clearance parameters

Parameter	Inulin Clearance Test					
	1	2	3	4	5	6
Weight (g)	255.3	238.8	240.1	232.1	237	229.6
Plasma Volume (mL)	10.3	9.6	9.6	9.3	9.5	9.2
n_1	0.18252	0.24892	0.1141	0.22973	0.25366	0.20832
n_2	0.14271	0.13695	0.070757	0.15365	0.18772	0.18312
α	3.1	2.6	2.4	3.4	3.2	2.9
GFR (mL/min)	1.87	2.39	1.10	2.14	2.41	1.92
Average Fitting Error (%)	7.5	6.2	6.2	9.2	11.8	9.0
Maximum Fitting Error (%)	15.1	19.1	10.9	21.4	34.4	21.6

7.1.4.2 Creatinine

The first 8 creatinine concentrations were able to be determined using the jugular vein cannula, with the last sample obtained via tail vein. A pre-ARF measurement was not taken, but was assumed to be similar to the 6 hour post-cannulation measurement.

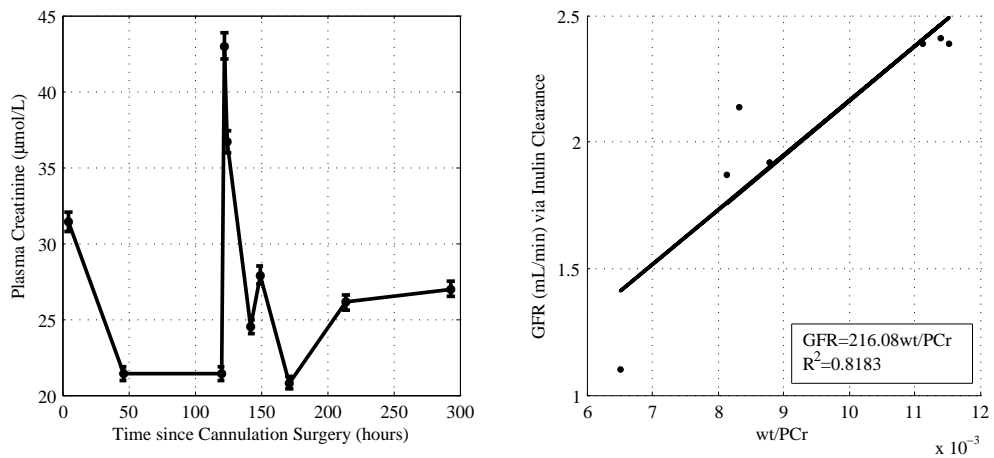


Figure 7.14 Maya: Plasma creatinine concentration and correlation with GFR via inulin clearance

7.1.4.3 Ammonia SIM Scans

All 15 breath SIM scans were analysed from 4 hours prior to cannulation surgery until 7 days post-ARF surgery. Figure 7.15 shows the measured breath results for C_B and C_{Tot} as well as the calculated C_R and C_{R^*} .

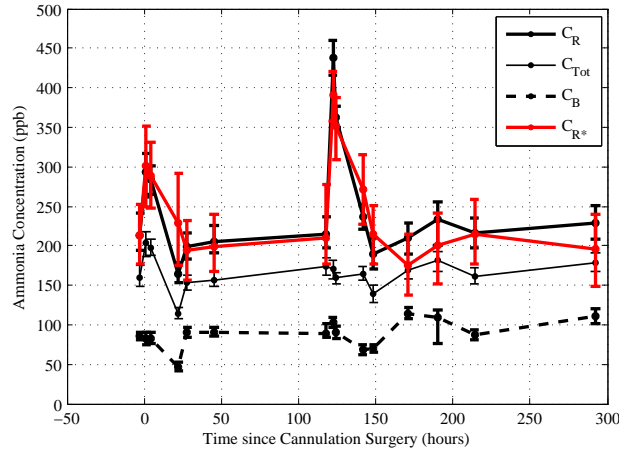


Figure 7.15 Maya: SIM scan ammonia concentration in rat breath and background air

Plotting GFR obtained via inulin clearance against $1/C_{R^*}$, resulted in Equation (7.4), with $a = 1.78$ from Equation (6.21), and an R^2 value of 0.80. Combining GFR estimation via inulin clearance, plasma creatinine, and breath ammonia resulted in Figure 7.16.

$$GFR = \frac{1.78}{C_{R^*}} \quad (7.4)$$

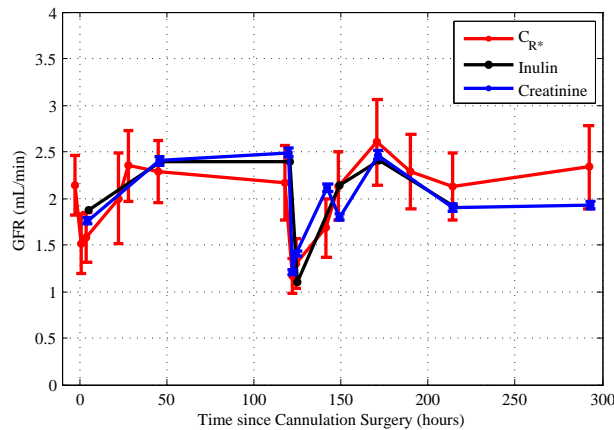


Figure 7.16 Maya: GFR estimation via bolus inulin clearance, plasma creatinine, and breath ammonia

7.1.5 Nell - Rat 5

7.1.5.1 Inulin Clearance

Nell underwent a successful cannulation surgery, followed by the post-operation and recovery inulin clearance tests. Five days later, she underwent surgery to induce ARF. Surgery was successful, and the cannula remained patent for 4 of the 5 post-ARF samples. Her inulin clearance fitting results are shown in Figure 7.17, and model-fitted parameters are shown in Table 7.5.

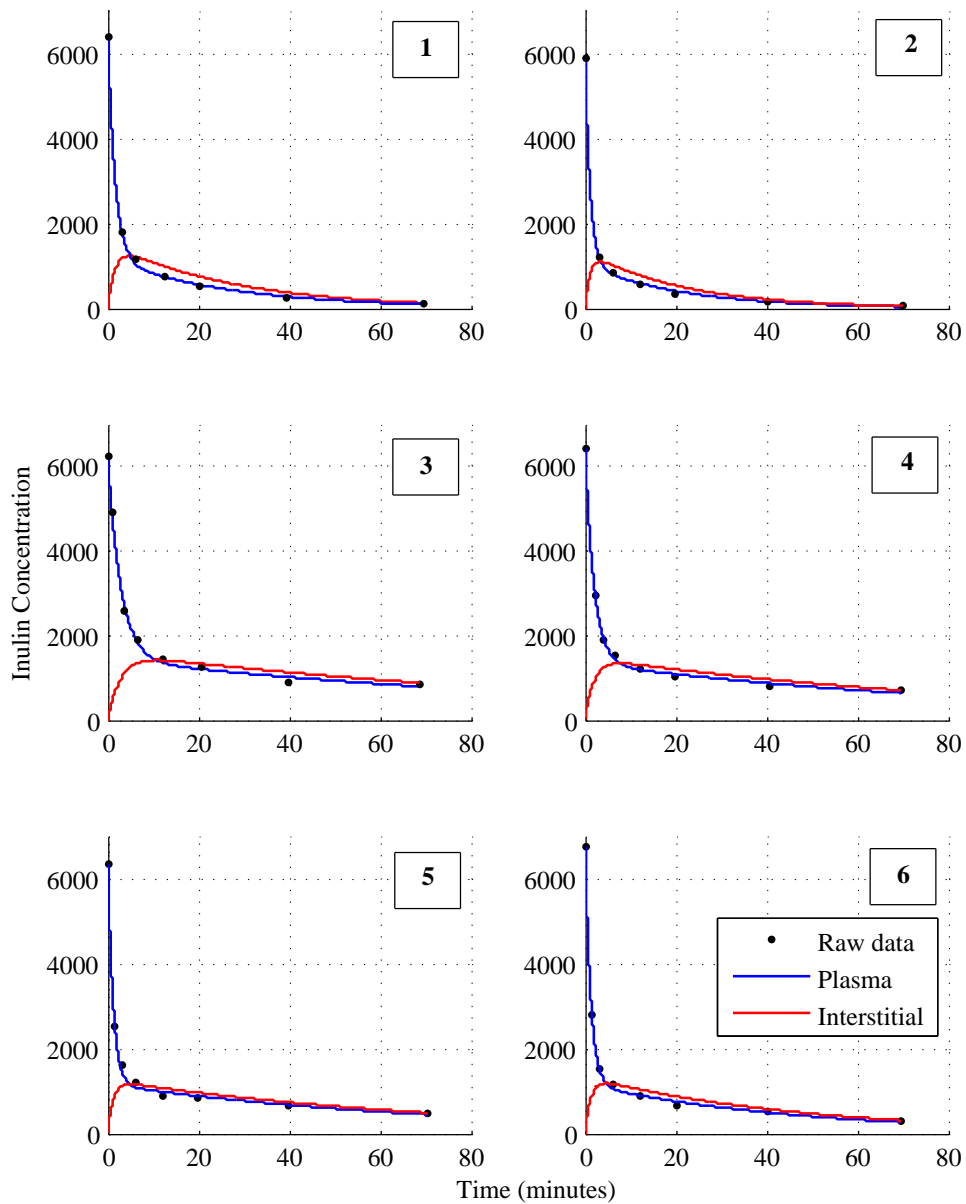


Figure 7.17 Nell: Inulin clearance summary. 1-2: Six hours and 2 days post cannulation surgery, respectively; 3-6: Six hours, 30 hours, 2 days, and 4 days post ARF induction, respectively.

Table 7.5 Nell: Inulin clearance parameters

Parameter	Inulin Clearance Test					
	1	2	3	4	5	6
Weight (g)	285.2	299.8	288	278.6	281.7	262.3
Plasma Volume (mL)	11.4	12.0	11.5	11.2	11.3	10.5
n_1	0.15558	0.2076	0.034497	0.047501	0.068831	0.10753
n_2	0.1403	0.19356	0.086742	0.11323	0.16402	0.15459
α	2.5	2.7	2.7	3.1	3.8	3.6
GFR (mL/min)	1.78	2.50	0.40	0.53	0.78	1.13
Average Fitting Error (%)	9.5	8.9	6.6	4.5	6.9	5.6
Maximum Fitting Error (%)	24.1	27.4	13.3	8.0	13.0	12.6

7.1.5.2 Creatinine

The first 8 creatinine concentrations were able to be determined using the jugular vein cannula, with the last sample obtained via tail vein. A pre-ARF measurement was not taken, but was assumed to be similar to the 6 hour post-cannulation measurement.

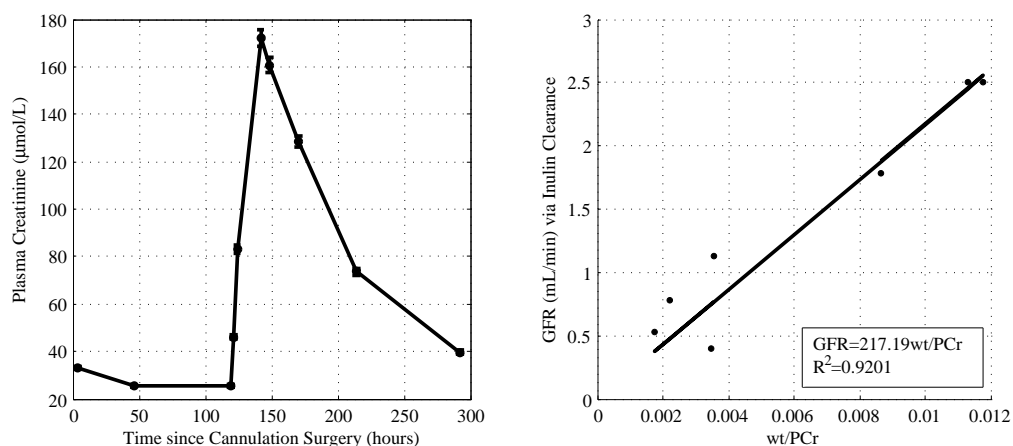


Figure 7.18 Nell: Plasma creatinine concentration and correlation with GFR via inulin clearance

7.1.5.3 Ammonia SIM Scans

All 15 breath SIM scans were analysed from 4 hours prior to cannulation surgery until 7 days post-ARF surgery. Figure 7.19 shows the measured breath results for C_B and C_{Tot} as well as the calculated C_R and C_{R^*} .

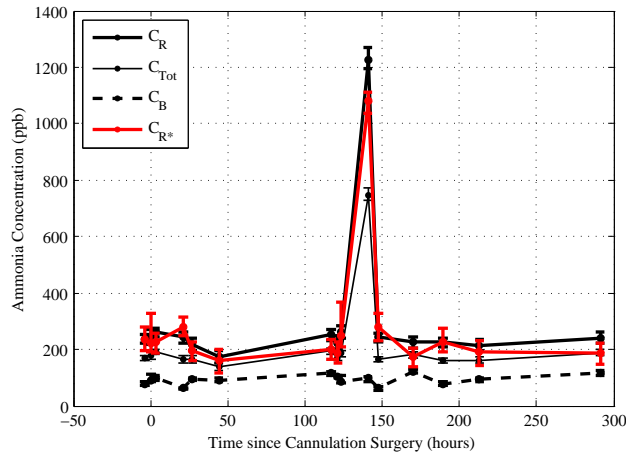


Figure 7.19 Nell: SIM scan ammonia concentration in breath and background air

Plotting GFR obtained via inulin clearance against $1/C_{R^*}$, resulted in Equation (7.5), with $a = 1.74$ from Equation (6.21), and an R^2 value of 0.23.

$$GFR = \frac{1.74}{C_{R^*}} \quad (7.5)$$

This low correlation was further observed in Figure 7.20, where GFR estimated via breath ammonia appeared to return to normal levels much quicker GFR estimated via inulin clearance or plasma creatinine. It is likely that machine error may have contributed to this poor result, because the C_{Tot} value reported by the SIFT-MS instrument did not reach a strict plateau. Instead, the reported concentration continued to rise to a value of approximately 750ppb, which was 3-4 times greater than the highest concentration recorded for any other rat at any other timepoint. Combining GFR estimation via inulin clearance, plasma creatinine, and breath ammonia resulted in Figure 7.20.

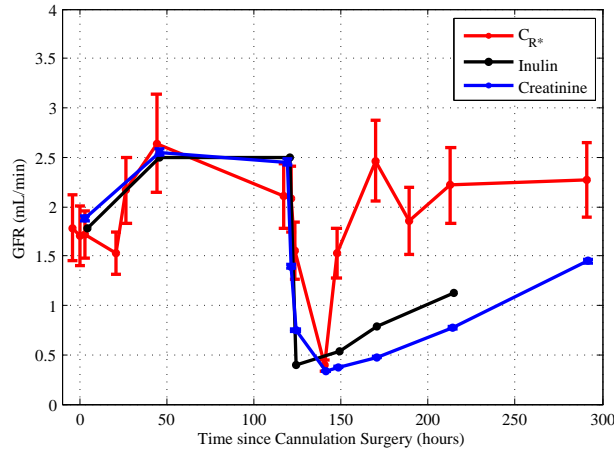


Figure 7.20 Nell: GFR estimation via bolus inulin clearance, plasma creatinine, and breath ammonia

7.1.6 Olive - Rat 6

7.1.6.1 Inulin Clearance

Olive had a successful cannulation surgery, followed by the post-operation and recovery inulin clearance tests. After ARF-induction surgery the cannula remained patent until a 6 day inulin clearance test. Inulin clearance fitting results are shown in Figure 7.21, and model-fitted parameters are shown in Table 7.6.

Table 7.6 Olive: Inulin clearance Parameters

Parameter	Inulin Clearance Test						
	1	2	3	4	5	6	7
Weight (g)	292.3	299.5	278.3	291.8	277	270	276
Plasma Volume (mL)	11.7	12.0	11.1	11.7	11.1	10.8	11.1
n_1	0.1701	0.22264	0.072785	0.12674	0.14959	0.16314	0.15911
n_2	0.13217	0.12815	0.13058	0.21035	0.19531	0.22275	0.23927
α	2.4	3.2	2.4	3.0	3.1	2.9	3.2
GFR (mL/min)	1.99	2.67	0.81	1.48	1.66	1.77	1.81
Average Fitting Error (%)	11.2	7.5	7.8	8.6	7.3	9.8	11.7
Maximum Fitting Error (%)	25.5	18.3	15.5	20.5	16.3	31.9	24.7

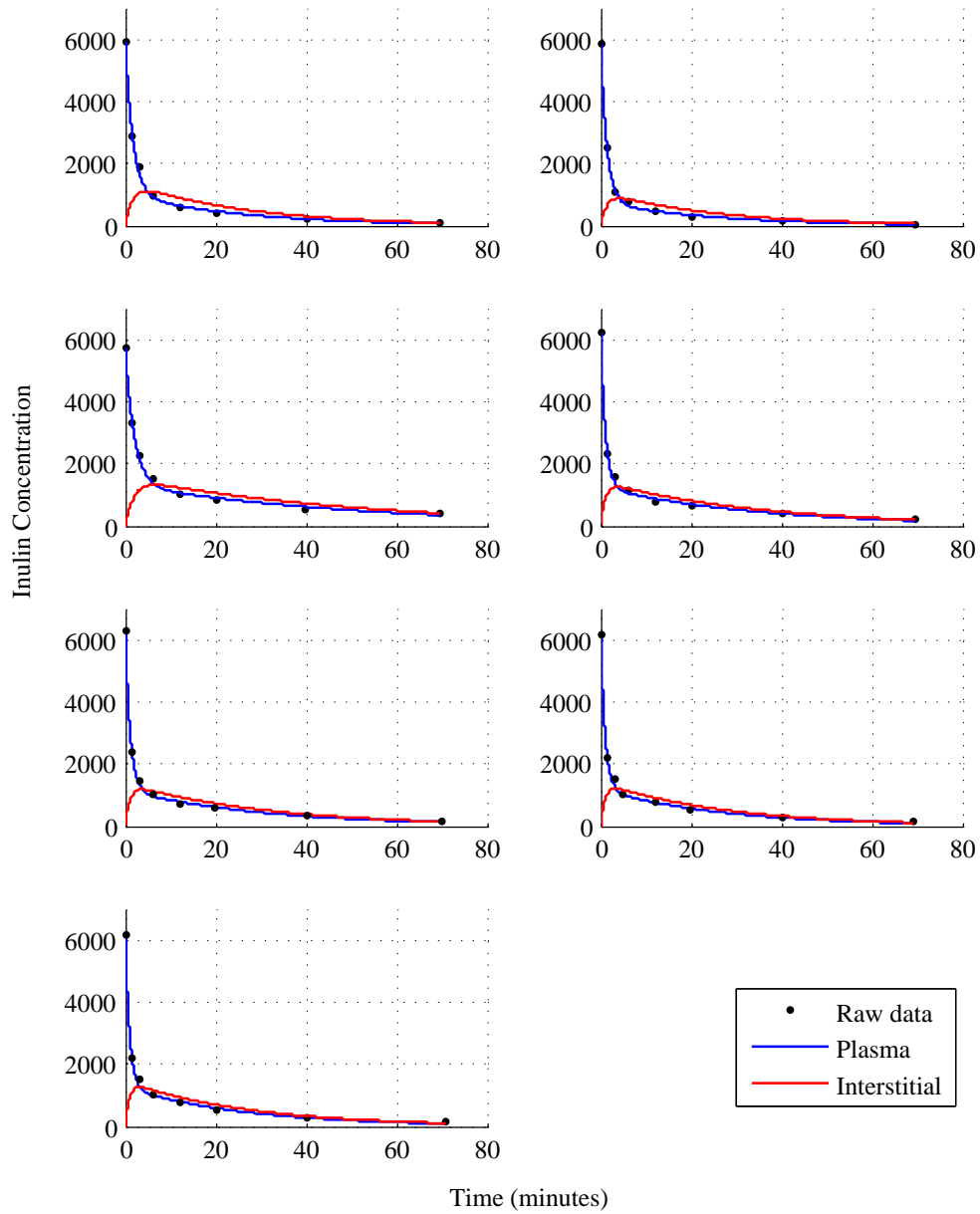


Figure 7.21 Olive: Inulin clearance summary. 1-2: Six hours and 2 days post cannulation surgery; 2-7: Six hours, 30 hours, 2 days, 4 days, and 6 days post ARF induction, respectively

7.1.6.2 Creatinine

The first 8 creatinine concentrations were able to be determined using the jugular vein cannula, with the last sample obtained via tail vein. A pre-ARF measurement was not taken, but was assumed to be similar to the 6 hour post-cannulation measurement.

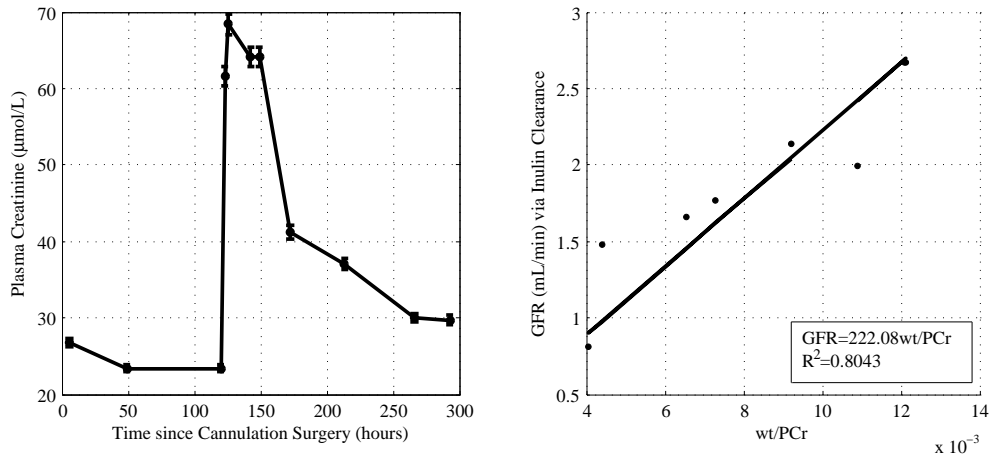


Figure 7.22 Olive: Plasma creatinine concentration and correlation with GFR via inulin clearance

7.1.6.3 Ammonia SIM Scans

All 15 breath SIM scans were analysed from 4 hours prior to cannulation surgery until 7 days post-ARF surgery. Figure 7.27 shows the measured breath results for C_B and C_{Tot} as well as the calculated C_R and C_{R^*} .

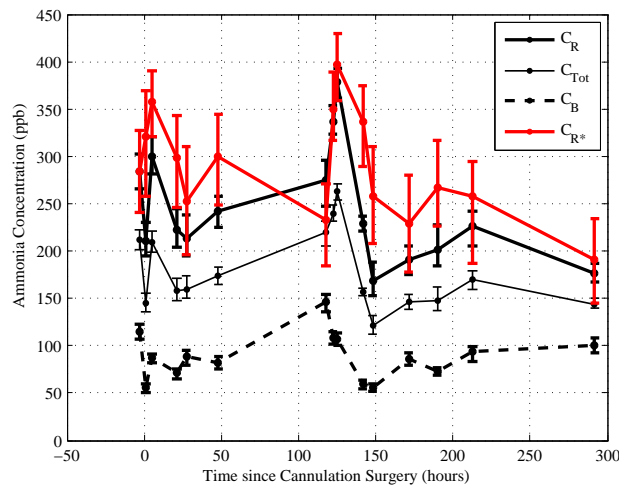


Figure 7.23 Olive: SIM scan ammonia in breath and background air

Plotting GFR obtained via inulin clearance against $1/C_{R^*}$, resulted in Equation (7.6), with $a = 1.71$ from Equation (6.21), and an R^2 value of 0.17. This low R^2 value occurred because the lowest breath ammonia concentration achieved after the cannulation surgery was not too dissimilar to that achieved after ARF

induction. However, if the relative decrease in breath ammonia from a pre-surgery concentration is considered, the relative decrease in renal function after ARF induction is 47% compared with 27% for post-cannulation surgery. Combining GFR estimation via inulin clearance, plasma creatinine, and breath ammonia resulted in Figure 7.24.

$$GFR = \frac{1.71}{C_{R^*}} \quad (7.6)$$

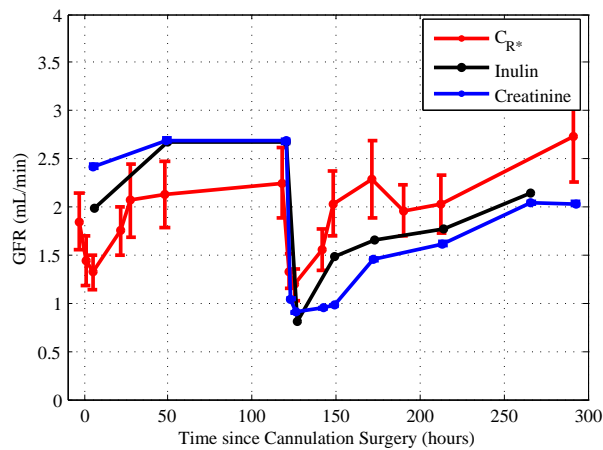


Figure 7.24 Olive: GFR estimation via bolus inulin clearance, plasma creatinine, and breath ammonia

7.1.7 Paige - Rat 7

7.1.7.1 Inulin Clearance

Paige underwent a successful cannulation surgery, followed by the post-operation and recovery inulin clearance tests. Five days later, she underwent surgery to induce ARF. Surgery was successful, and the cannula remained patent up to and including the 4 day post-ARF clearance test. Her inulin clearance fitting results are shown in Figure 7.25, and model-fitted parameters are shown in Table 7.7.

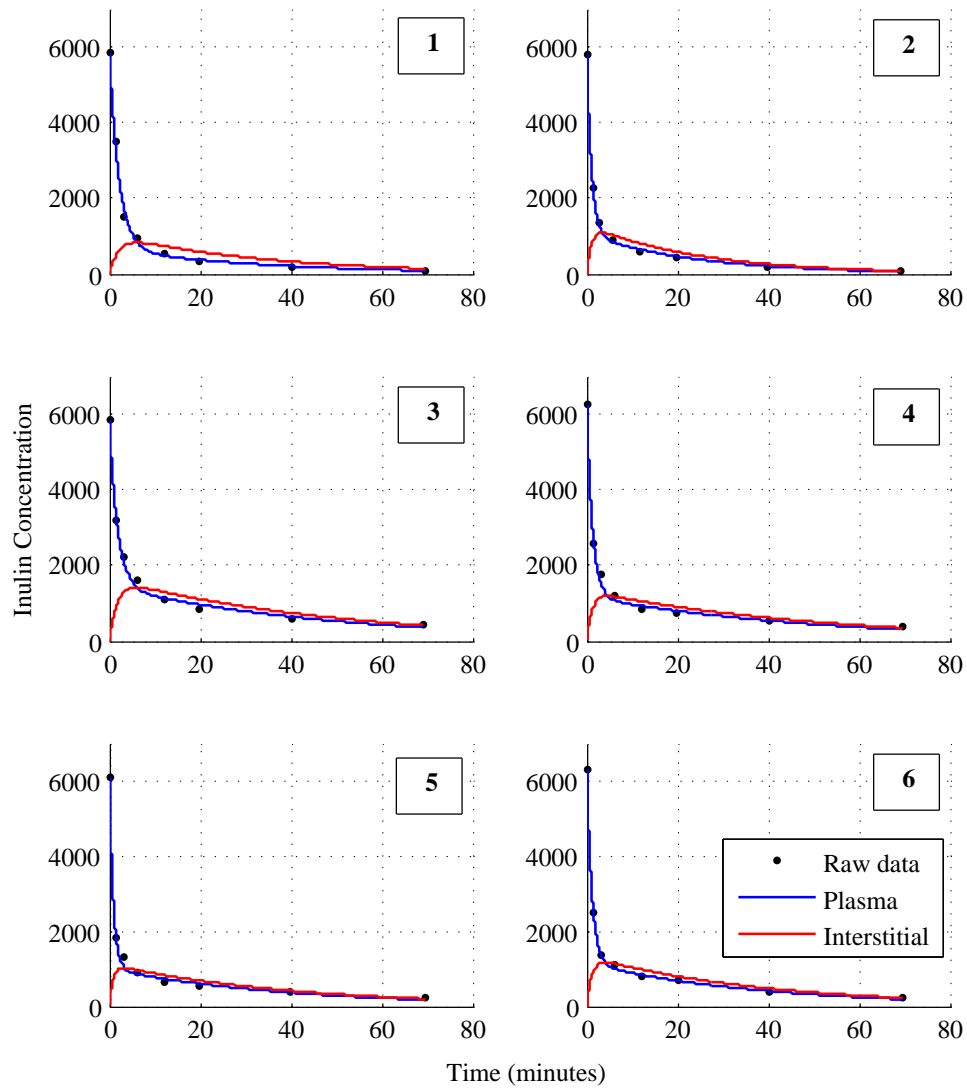


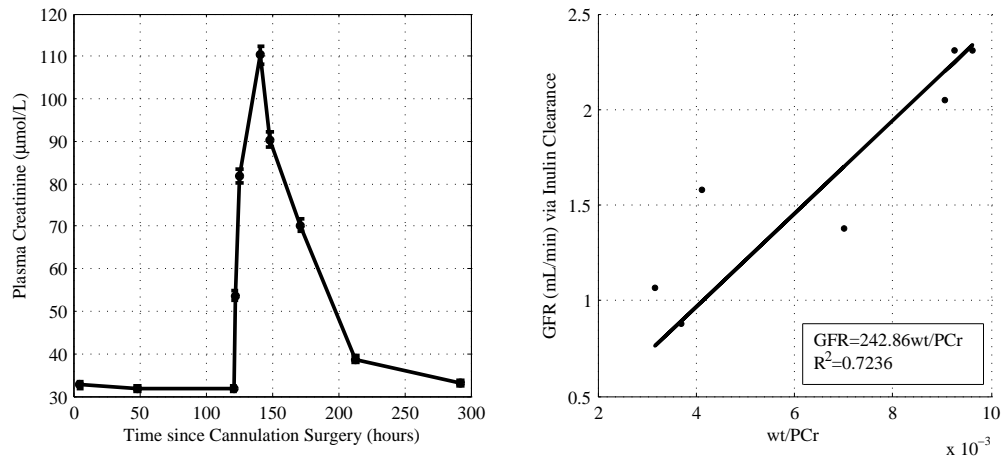
Figure 7.25 Paige: Inulin clearance summary. 1-2: Six hours and 2 days post cannulation surgery; 3-6: Six hours, 30 hours, 2 days, and 4 days post ARF induction, respectively.

7.1.7.2 Creatinine

The first 8 creatinine concentrations were able to be determined using the jugular vein cannula, with the last sample obtained via tail vein. A pre-ARF measurement was not taken, but was assumed to be similar to the 6 hour post-cannulation measurement.

Table 7.7 Paige: Inulin clearance parameters

Parameter	Inulin Clearance Test					
	1	2	3	4	5	6
Weight (g)	295.6	308.9	302.1	284.6	286.2	275.4
Plasma Volume (mL)	11.9	12.4	12.1	11.4	11.5	11.0
n_1	0.17276	0.18666	0.072924	0.09339	0.13762	0.12464
n_2	0.079153	0.19802	0.15279	0.16441	0.21158	0.1782
α	3.1	2.9	2.3	3.4	4.0	3.3
GFR (mL/min)	2.05	2.31	0.88	1.06	1.58	1.38
Average Fitting Error (%)	10.9	9.0	10.1	8.9	10.5	4.8
Maximum Fitting Error (%)	23.8	21.1	20.0	13.9	20.5	7.5

**Figure 7.26** Paige: Plasma creatinine concentration and correlation with GFR via inulin clearance

7.1.7.3 Ammonia SIM Scans

All 15 breath SIM scans were analysed from 4 hours prior to cannulation surgery until 7 days post-ARF surgery. Figure 7.27 shows the measured breath results for C_B and C_{Tot} as well as the calculated C_R and C_{R^*} .

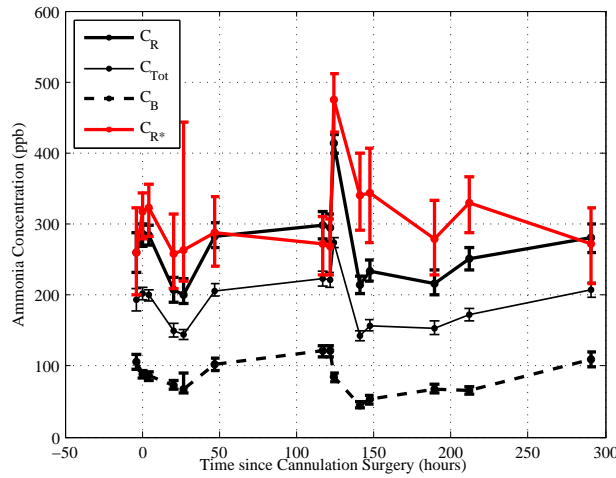


Figure 7.27 Paige: SIM scan ammonia in breath and background air

Plotting GFR obtained via inulin clearance against $1/C_{R^*}$, resulted in Equation (7.7), with $a = 1.86$ from Equation (6.21), and an R^2 value of 0.58. Combining GFR estimation via inulin clearance, plasma creatinine, and breath ammonia resulted in Figure 7.28.

$$GFR = \frac{1.86}{C_{R^*}} \tag{7.7}$$

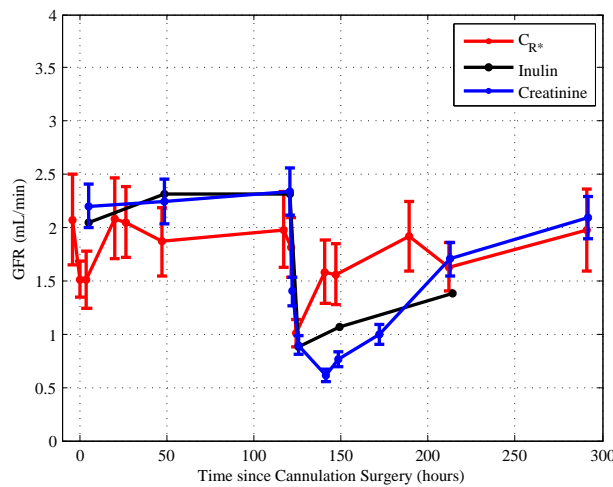


Figure 7.28 Paige: GFR estimation via bolus inulin clearance, plasma creatinine, and breath ammonia

7.1.8 Quin - Rat 8

7.1.8.1 Inulin Clearance

Quin underwent a successful cannulation surgery, followed by the post-operation and recovery inulin clearance tests. Five days later, she underwent surgery to induce ARF. Surgery was successful, and the cannula remained patent up to and including the 30 hour post-ARF clearance test. Her inulin clearance fitting results are shown in Figure 7.29, and model-fitted parameters are shown in Table 7.8.

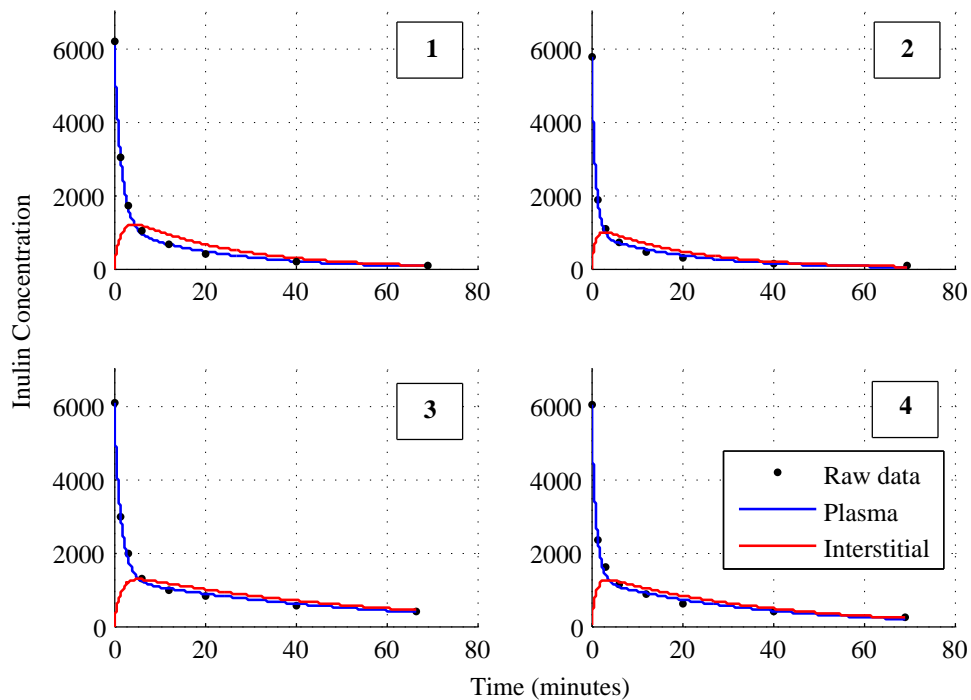


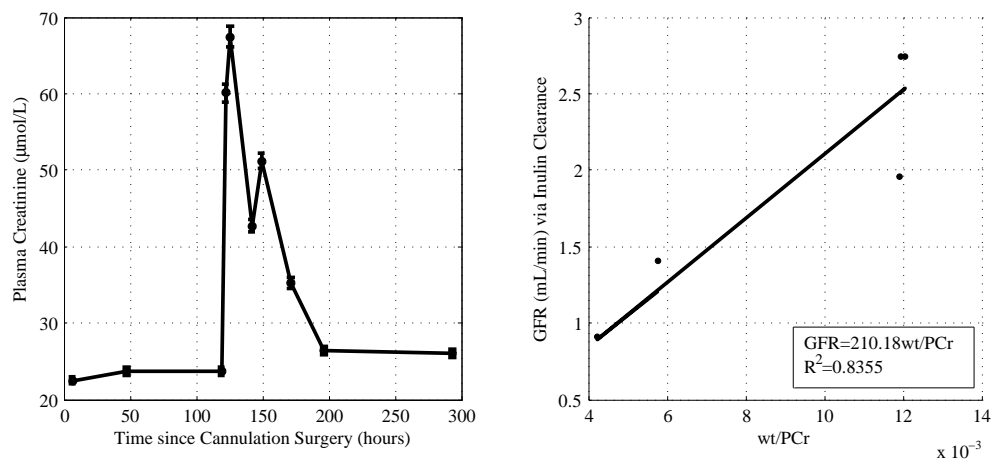
Figure 7.29 Quin: Inulin clearance summary. 1-2: Six hours and 2 days post cannulation surgery; 3-4: Six hours and 30 hours post ARF induction.

7.1.8.2 Creatinine

The first 6 creatinine concentrations were able to be determined using the jugular vein cannula. The remainder of the samples were obtained via the tail vein. A pre-ARF measurement was not taken, but was assumed to be similar to the 6 hour post-cannulation measurement.

Table 7.8 Quin: Inulin clearance parameters

Parameter	Inulin Clearance Test			
	1	2	3	4
Weight (g)	269.1	291.3	285.8	295
Plasma Volume (mL)	10.8	11.7	11.4	11.8
n_1	0.18139	0.23398	0.079097	0.11924
n_2	0.14566	0.20743	0.14921	0.21419
α	2.3	3.1	2.9	2.9
GFR (mL/min)	1.96	2.74	0.91	1.41
Average Fitting Error (%)	10.8	11.2	6.0	7.6
Maximum Fitting Error (%)	30.8	32.1	10.1	17.6

**Figure 7.30** Quin: Plasma creatinine concentration and correlation with GFR via inulin clearance

7.1.8.3 Ammonia SIM Scans

All 15 breath SIM scans were analysed from 4 hours prior to cannulation surgery until 7 days post-ARF surgery. Figure 7.31 shows the measured breath results for C_B and C_{Tot} as well as the calculated C_R and C_{R^*} .

Plotting GFR obtained via inulin clearance against $1/C_{R^*}$, resulted in Equation (7.8), with $a = 1.59$ from Equation (6.21), and an R^2 value of 0.23. Quin's results were similar to Olive's, in that if a relative decrease in renal function from pre to post surgery as measured by breath ammonia is considered, the decrease

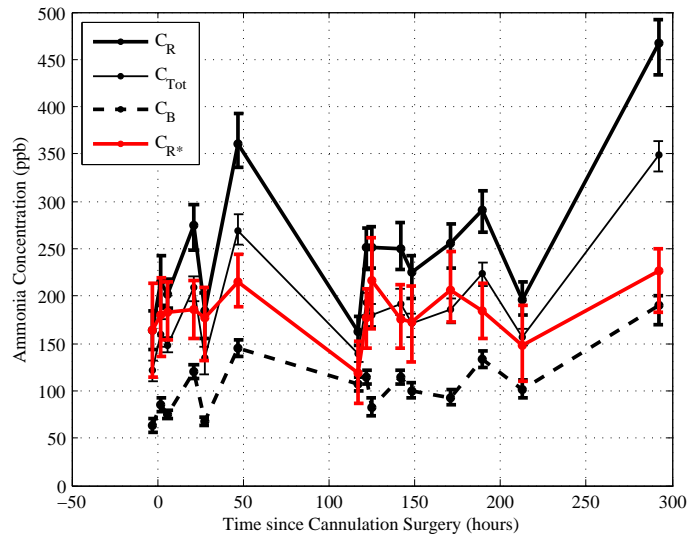


Figure 7.31 Quin: SIM scan ammonia in breath and background air

post-ARF is 50% compared to 19% for post-cannulation.

$$GFR = \frac{1.59}{C_{R^*}} \quad (7.8)$$

Combining GFR estimation via inulin clearance, plasma creatinine, and breath ammonia resulted in Figure 7.32.

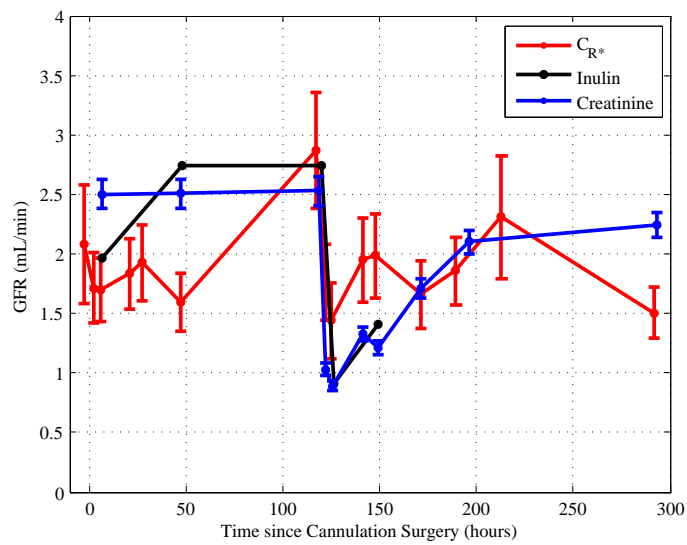


Figure 7.32 Quin: GFR estimation via bolus inulin clearance, plasma creatinine, and breath ammonia

7.1.9 Sophie - Rat 9

7.1.9.1 Inulin Clearance

Sophie underwent a successful cannulation surgery, followed by the post-operation and recovery inulin clearance tests. Five days later, she underwent surgery to induce ARF. Surgery was successful, however the cannula lost patency and no further inulin clearances were possible. Her inulin clearance fitting results are shown in Figure 7.33, and model-fitted parameters are shown in Table 7.9.

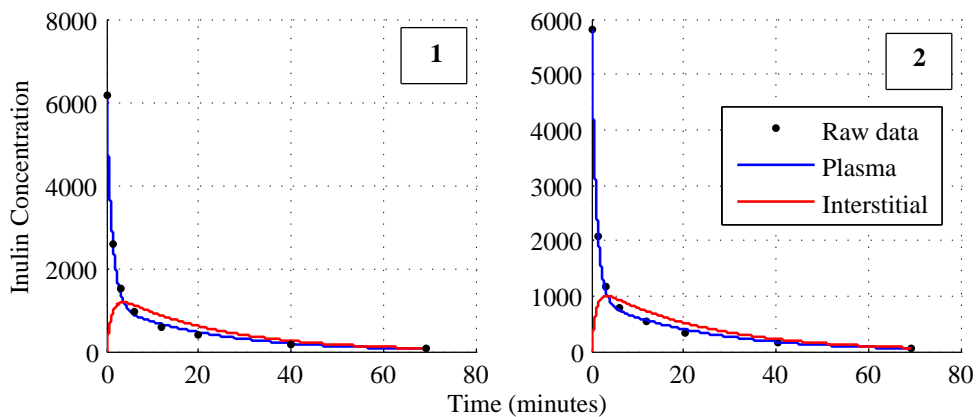


Figure 7.33 Sophie: Inulin clearance summary. 1-2: Six hours and 2 days post cannulation surgery, respectively.

Table 7.9 Sophie: Inulin clearance parameters

Parameter	Inulin Clearance Test	
	1	2
Weight (g)	282.6	300.6
Plasma Volume (mL)	11.4	12.1
n_1	0.19462	0.21105
n_2	0.17991	0.18651
α	2.6	3.1
GFR (mL/min)	2.21	2.55
Average Fitting Error (%)	14.1	11.3
Maximum Fitting Error (%)	39.1	26.3

7.1.9.2 Creatinine

The first 2 creatinine concentrations were able to be determined using the jugular vein cannula. These were the 6 hour and 2 day post-cannulation measurements. After this time, the jugular vein cannula lost patency, and the remainder of the samples were obtained via the tail vein. A pre-ARF measurement was not taken, but was assumed to be similar to the 6 hour post-cannulation measurement.

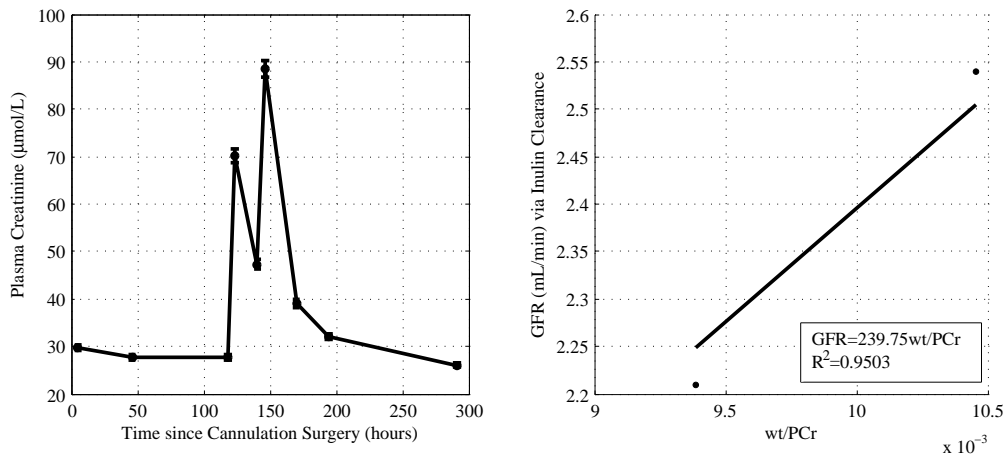


Figure 7.34 Sophie: Plasma creatinine concentration and correlation with GFR via inulin clearance

7.1.9.3 Ammonia SIM Scans

All 15 breath SIM scans were analysed from 4 hours prior to cannulation surgery until 7 days post-ARF surgery. Figure 7.35 shows the measured breath results for C_B and C_{Tot} as well as the calculated C_R and C_{R^*} .

Plotting GFR obtained via inulin clearance against $1/C_{R^*}$, resulted in Equation (7.9), with $a = 1.90$ from Equation (6.21). With only 2 points for correlation, no R^2 value is reported.

$$GFR = \frac{1.90}{C_{R^*}} \quad (7.9)$$

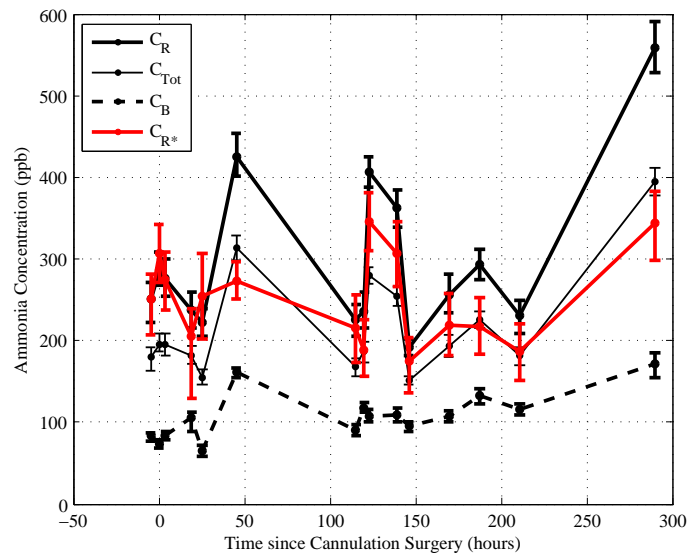


Figure 7.35 Sophie: SIM scan ammonia in breath and background air

Combining GFR estimation via inulin clearance, plasma creatinine, and breath ammonia resulted in Figure 7.36.

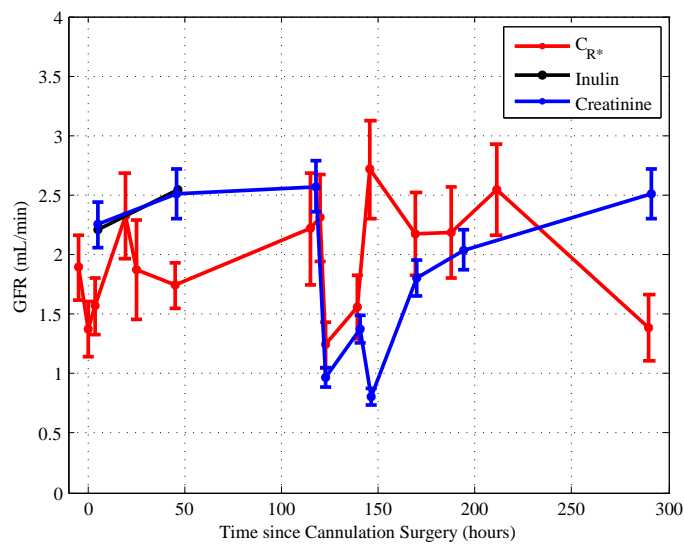


Figure 7.36 Sophie: GFR estimation via bolus inulin clearance, plasma creatinine, and breath ammonia

7.1.10 Tosca - Rat 10

7.1.10.1 Inulin Clearance

Tosca underwent a successful cannulation surgery, followed by the post-operation and recovery inulin clearance tests. After surgery to induce ARF, she was able to participate in the 6 hour, 30 hour, and 2 day post-ARF inulin clearances before her jugular vein cannula failed. Her inulin clearance fitting results are shown in Figure 7.37, and model-fitted parameters are shown in Table 7.10.

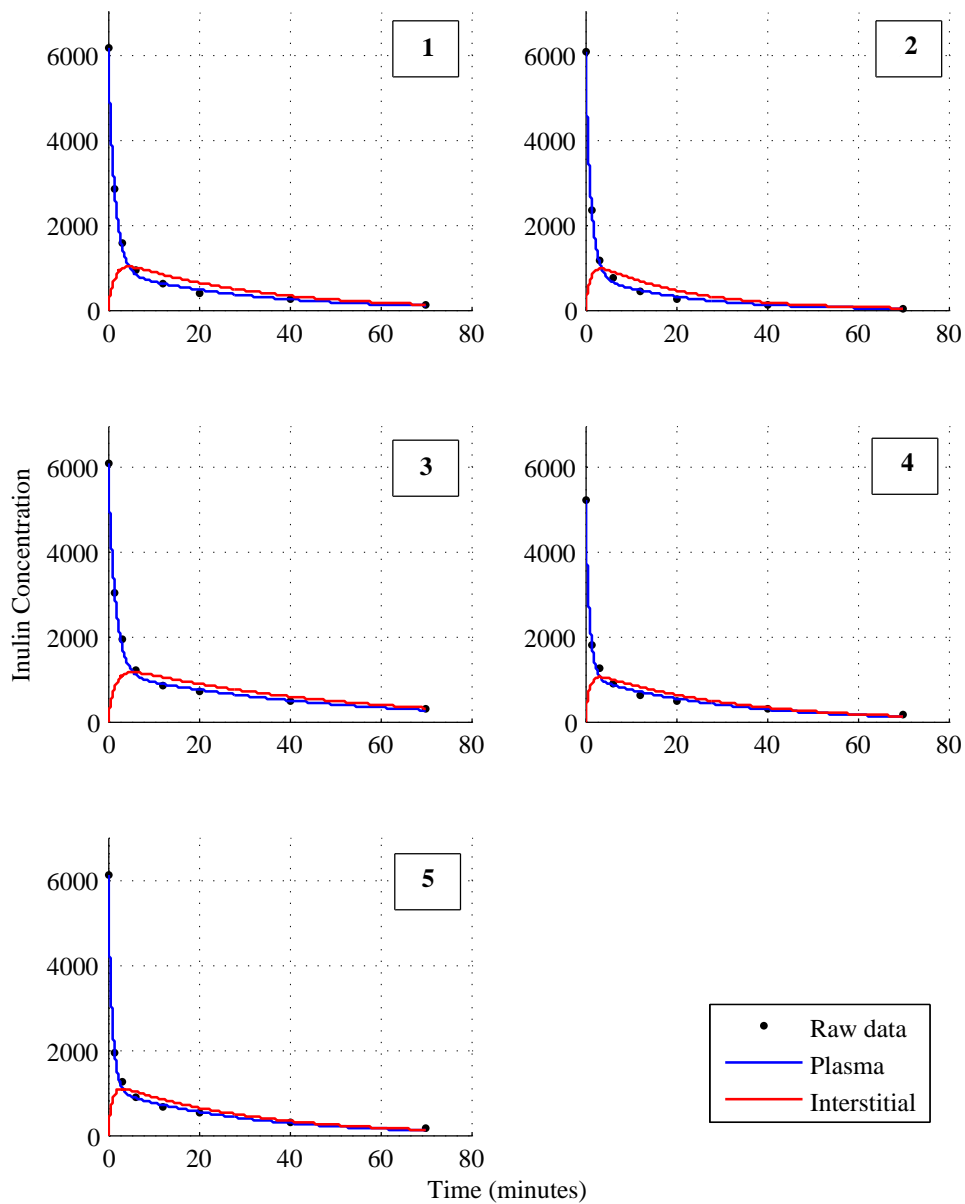


Figure 7.37 Tosca: Inulin clearance summary. 1-2: Six hours and 2 days post cannulation surgery; 3-5: Six hours, 30 hours and 2 days post ARF induction, respectively.

Table 7.10 Tosca: Inulin clearance parameters

Parameter	Inulin Clearance Test				
	1	2	3	4	5
Weight (g)	289.5	306.2	280.8	287.9	282.7
Plasma Volume (mL)	11.6	12.3	11.3	11.5	11.3
n_1	0.17214	0.25786	0.09692	0.14538	0.16666
n_2	0.12608	0.15294	0.13025	0.23833	0.21884
α	3.1	2.9	3.1	3.0	3.4
GFR (mL/min)	2.00	3.17	1.09	1.68	1.89
Average Fitting Error (%)	9.8	8.2	6.1	9.7	8.3
Maximum Fitting Error (%)	26.2	10.7	22.0	31.2	

7.1.10.2 Creatinine

The first 7 creatinine concentrations were able to be determined using the jugular vein cannula. These were the 6 hour and 2 day post-cannulation measurements, and the 1 hour, 6 hour, 20 hour, 30 hour and 2 day post-ARF measurements. 4 day and 7 day samples were obtained via the tail vein. A pre-ARF measurement was not taken, but was assumed to be similar to the 6 hour post-cannulation measurement.

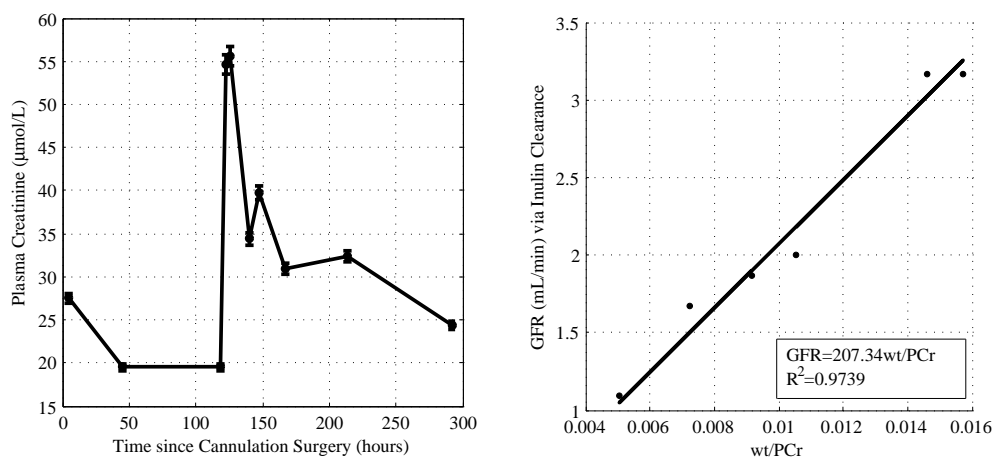


Figure 7.38 Tosca: Plasma creatinine concentration and correlation with GFR via inulin clearance

7.1.10.3 Ammonia SIM Scans

Sixteen breath SIM scans were analysed from 4 hours prior to cannulation surgery until 7 days post-ARF surgery. Figure 7.39 shows the measured breath results for C_B and C_{Tot} as well as the calculated C_R and C_{R^*} .

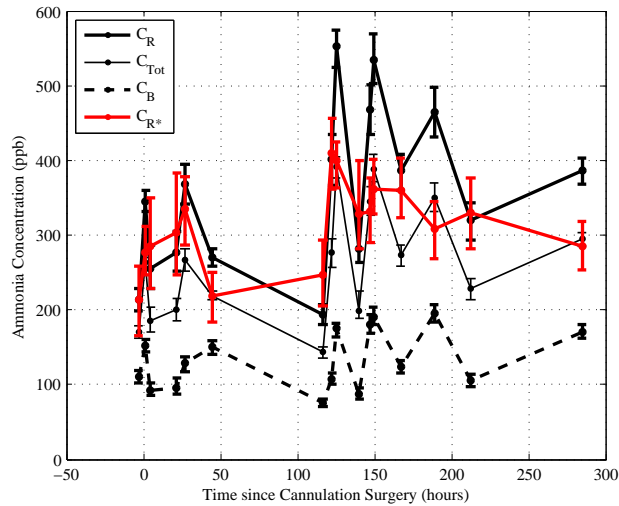


Figure 7.39 Tosca: SIM scan ammonia in rat breath and background air

Plotting GFR obtained via inulin clearance against $1/C_{R^*}$, resulted in Equation (7.10), with $a = 2.22$ from Equation (6.21), and an R^2 value of 0.85. Combining GFR estimation via inulin clearance, plasma creatinine, and breath ammonia resulted in Figure 7.40.

$$GFR = \frac{2.22}{C_{R^*}} \tag{7.10}$$

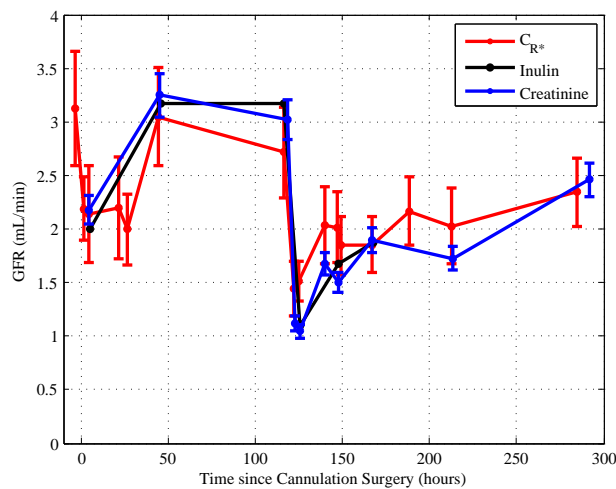


Figure 7.40 Tosca: GFR estimation via bolus inulin clearance, plasma creatinine, and breath ammonia

7.1.11 Ula - Rat 11

7.1.11.1 Inulin Clearance

Ula underwent a successful cannulation surgery, followed by the post-operation and recovery inulin clearance tests. During surgery to induce ARF, she stopped breathing for a short time, however was able to undergo the first post-ARF inulin clearance test. However, she did not survive to participate in the recovery section of the trial. Her inulin clearance fitting results are shown in Figure 7.41, and model-fitted parameters are shown in Table 7.11.

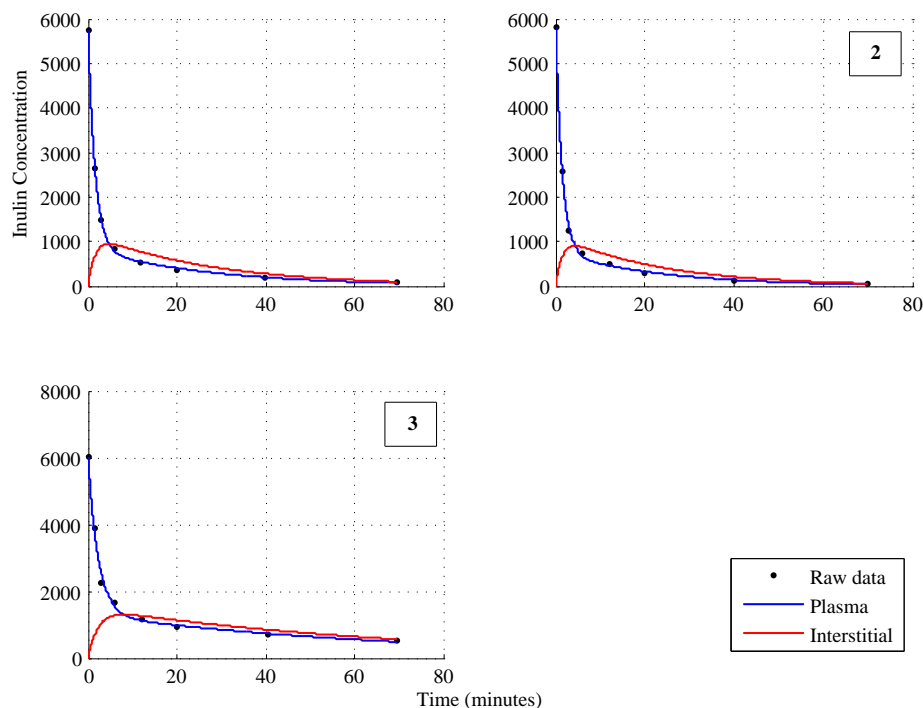


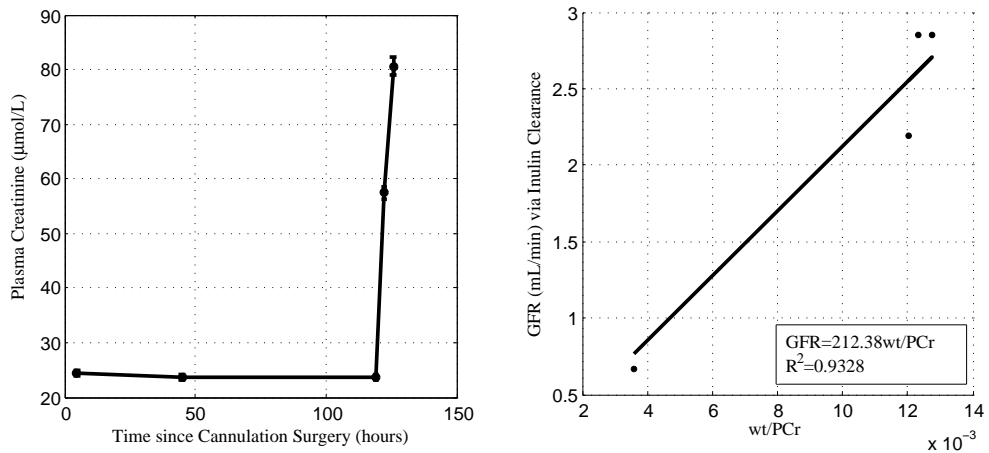
Figure 7.41 Ula: Inulin clearance summary.1-2: Six hours and 2 days post cannulation surgery; 3: Six hours post ARF induction.

7.1.11.2 Creatinine

The first 4 creatinine concentrations were able to be determined using the jugular vein cannula. These were the 6 hour and 2 day post-cannulation measurements, and the 1 hour and 6 hour post-ARF measurements. A pre-ARF measurement was not taken, but was assumed to be similar to the 6 hour post-cannulation measurement.

Table 7.11 Ula: Inulin clearance parameters

Parameter	Inulin Clearance Test		
	1	2	3
Weight (g)	294.3	312.1	289.3
Plasma Volume (mL)	11.8	12.5	10.5
n_1	0.18526	0.22789	0.058394
n_2	0.12261	0.12562	0.10458
α	2.9	2.9	2.7
GFR (mL/min)	2.19	2.86	0.68
Average Fitting Error (%)	8.2	7.7	6.0
Maximum Fitting Error (%)	14.6	17.2	11.1

**Figure 7.42** Ula: Plasma creatinine concentration and correlation with GFR via inulin clearance

7.1.11.3 Ammonia SIM Scans

Nine breath SIM scans were analysed from 4 hours prior to cannulation surgery until 6 hours post-ARF surgery. Figure 7.43 shows the measured breath results for C_B and C_{Tot} as well as the calculated C_R and C_{R^*} .

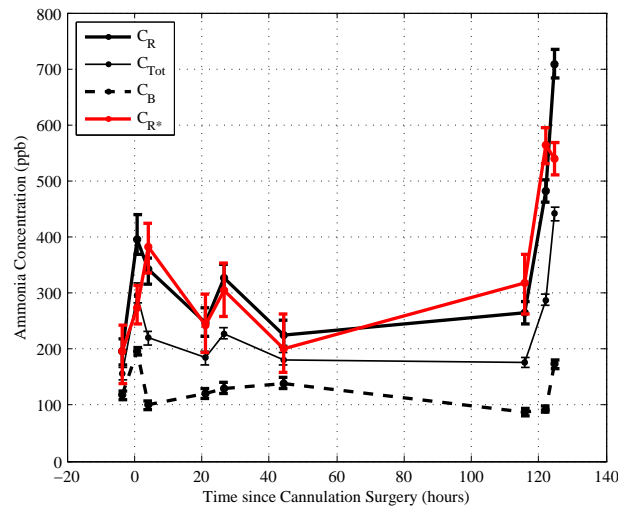


Figure 7.43 Ula: SIM scan ammonia in breath and background air

Plotting GFR obtained via inulin clearance against $1/C_{R^*}$, resulted in Equation (7.11), with α equal to 2.04 from Equation (6.21), and an R^2 value of 0.62.

$$GFR = \frac{2.04}{C_{R^*}} \quad (7.11)$$

Combining GFR estimation via inulin clearance, plasma creatinine, and breath ammonia resulted in Figure 7.44.

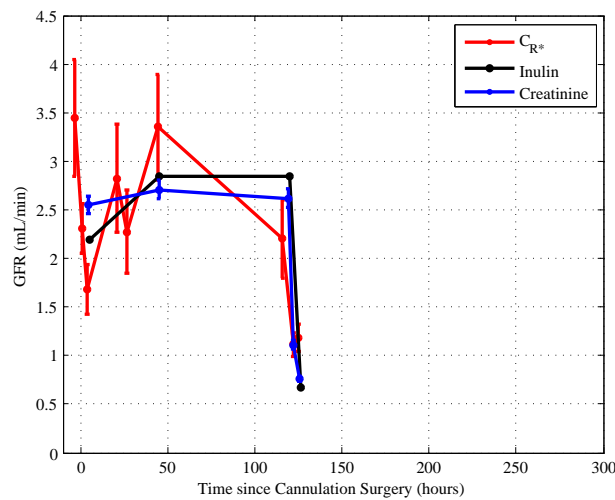


Figure 7.44 Ula: GFR estimation via bolus inulin clearance, plasma creatinine, and breath ammonia

7.1.12 Summary

Eleven rats participated in an animal trial conducted over 2 weeks. In an initial surgery, an in-dwelling cannula was inserted into the jugular vein for the purposes of fast serial blood sampling. Five days after recovery from this surgery, ARF was induced via a 60 minute bilateral renal artery clamp. GFR was monitored via inulin clearance tests, plasma creatinine concentrations, and breath ammonia SIM scans during this trial.

Relative decreases in renal function showed excellent correlation between methods, and indicate good promise for fast, non-invasive determination of renal function via breath testing.

7.2 SIM Scan - Isoprene

Isoprene concentration was monitored via SIM scan analysis, and the results over the course of the trial are shown in Figures 7.45 to 7.55, for each rat. It was observed that while the isoprene concentration in exhaled breath does increase after surgery to induce ARF, it does not appear to increase to an extent greater than that observed in response to a general surgery. Hence, this increase in exhaled isoprene is not necessarily attributable to ARF, but is instead a response to surgery. Therefore, isoprene has potential as a biomarker of acute physiological stress.

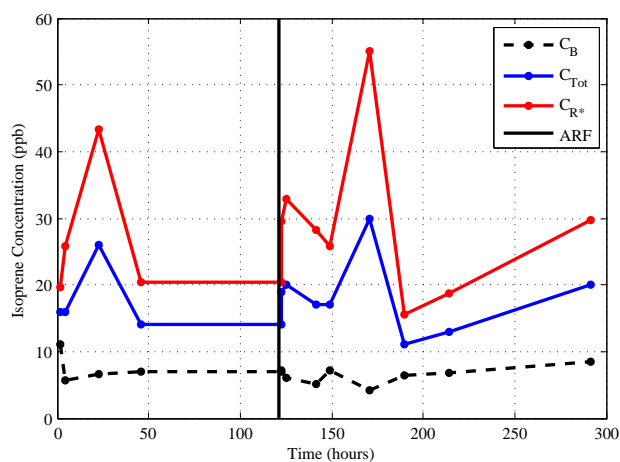


Figure 7.45 Grace, rat #1: Breath Isoprene over ARF Trial

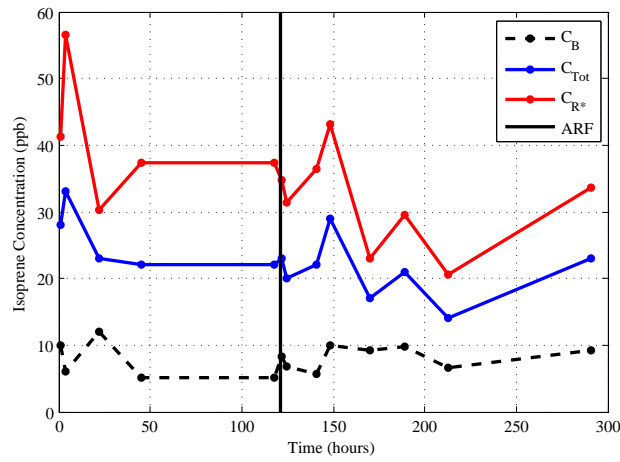


Figure 7.46 Heidi, rat #2: Breath Isoprene over ARF Trial

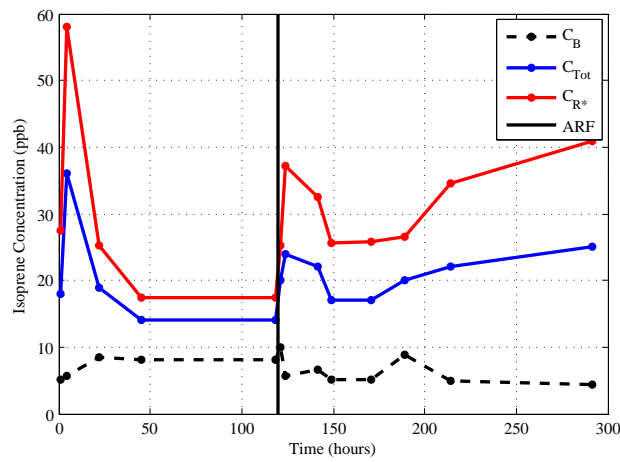


Figure 7.47 Isis, rat #3: Breath Isoprene over ARF Trial

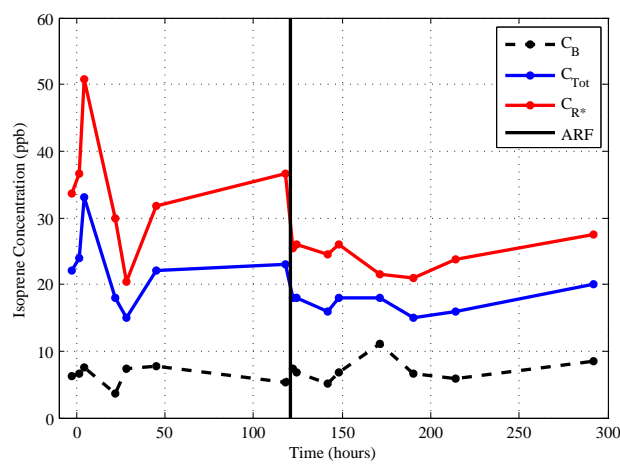


Figure 7.48 Maya, rat #4: Breath Isoprene over ARF Trial

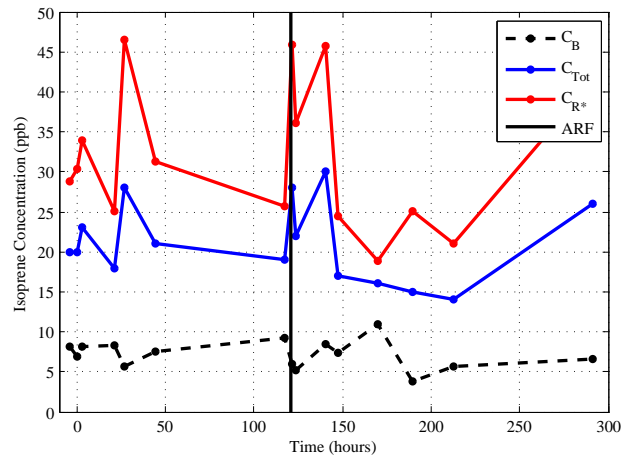


Figure 7.49 Nell, rat #5: Breath Isoprene over ARF Trial

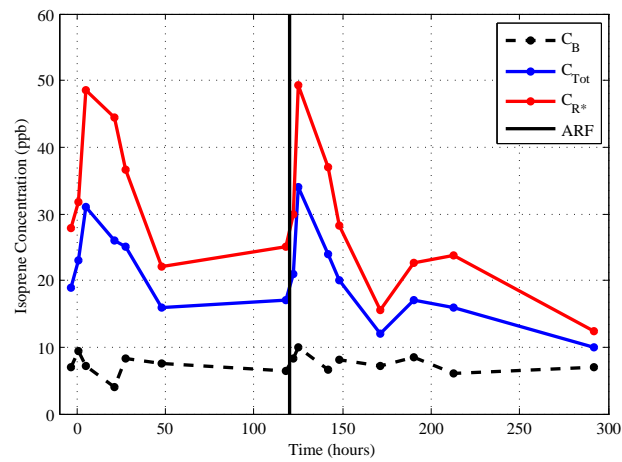


Figure 7.50 Olive, rat #6: Breath Isoprene over ARF Trial

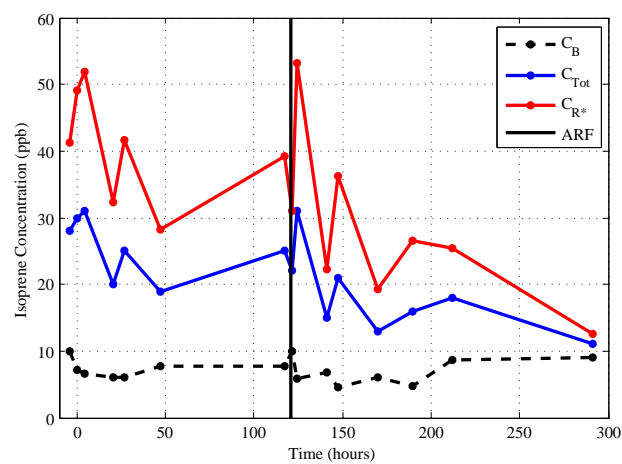


Figure 7.51 Paige, rat #7: Breath Isoprene over ARF Trial

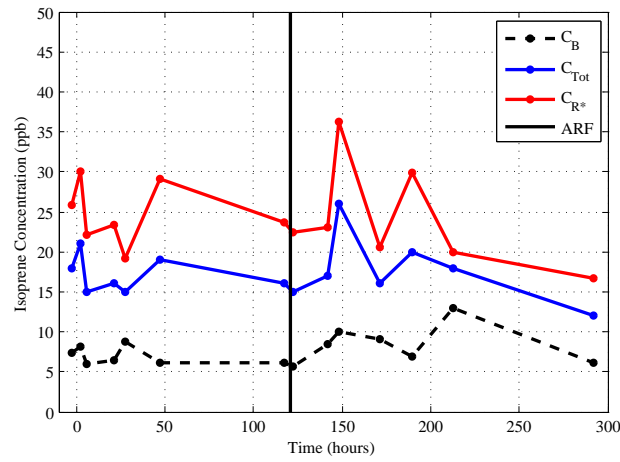


Figure 7.52 Quin, rat #8: Breath Isoprene over ARF Trial

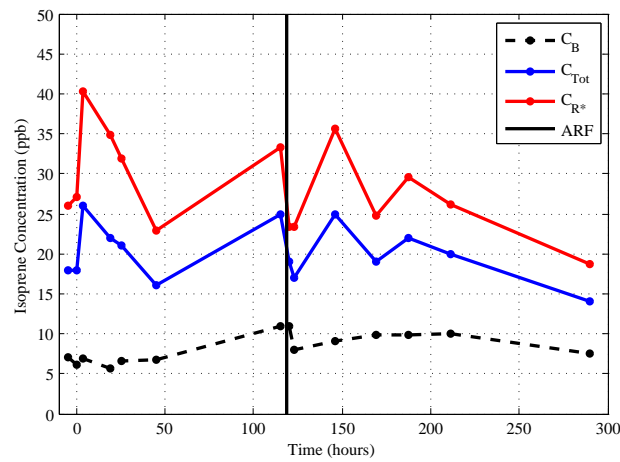


Figure 7.53 Sophie, rat #9: Breath Isoprene over ARF Trial

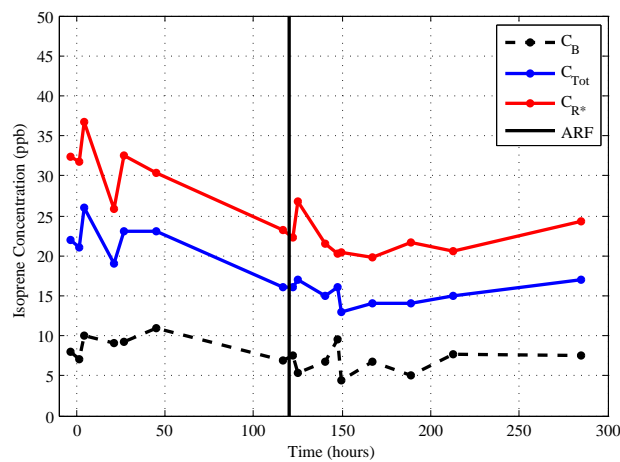


Figure 7.54 Tosca, rat #10: Breath Isoprene over ARF Trial

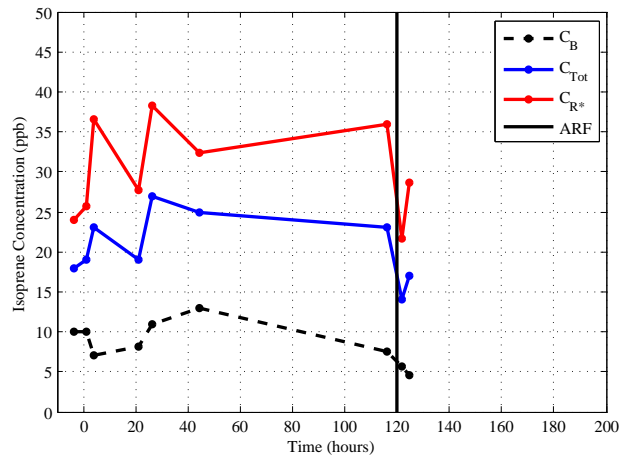


Figure 7.55 Ula, rat #11: Breath Isoprene over ARF Trial

Isoprene concentration in 5 of the rats appeared to increase towards the end of the trial. Despite the apparent short-term *recovery* of these rats from ARF, there is a strong likelihood that they would develop some degree of chronic renal failure following this trial. Isoprene has been reported to be increased in patients with end-stage renal failure, [Davies et al., 2001]. Hence, the increase in isoprene observed in this trial may be an indication of the onset of chronic renal failure.

7.3 Renal Histology

Preparations of normal renal pathology were shown in Chapter 5.1.4. The following types of abnormalities are commonly encountered in the renal tubules with ARF [Danciu and Mihailovici, 2004]:

- Brush border changes
- Cell Swelling/dilatation
- Apoptosis
- Basement membrane detachment
- Blocked lumen
- Casts

The most commonly seen abnormality in the experimental ARF studies was a blocked lumen, which results from necrotic epithelial cells falling into the tubule lumen and obliterating it, as seen in Figure 7.56. If the basement membrane remains intact, the tubular epithelium can regenerate, [Danciu and Mihailovici, 2004]. Note that all slides shown here were prepared from the excised kidneys of Nell and Maya.

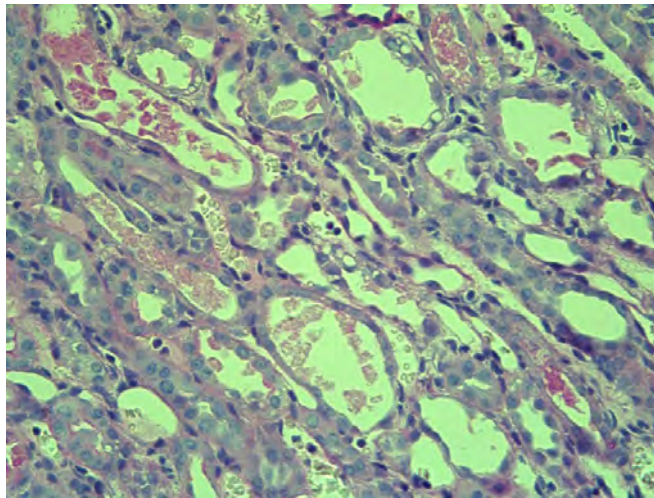


Figure 7.56 Rat kidney (Nell) 7 days after a 60 minute ischaemia-reperfusion injury. The dilated collecting ducts contain cell debris, sloughed apoptotic and necrotic cells.

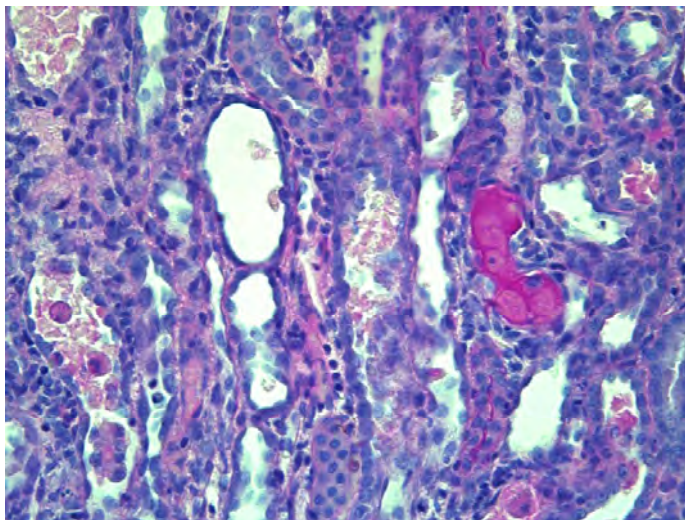


Figure 7.57 Rat kidney (Nell) 7 days after a 60 minute ischaemia-reperfusion injury. Dilated collecting ducts show both necrotic and viable epithelial cells. A dense pink stained tubular cast is seen.

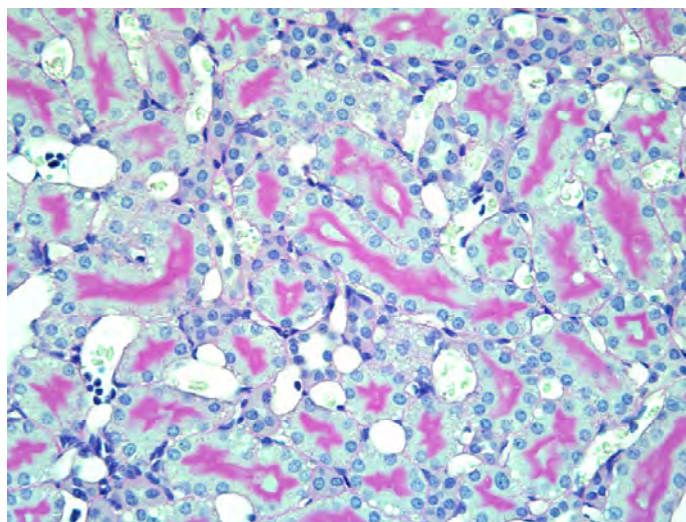


Figure 7.58 Rat kidney (Maya) 7 days after a 60 minute ischaemia-reperfusion injury. Cortical proximal tubules with largely intact brush borders (pink stain).

Abnormalities commonly observed with acute renal failure, such as the presence of casts, brush border changes, and necrotic cells in the tubular lumen, were identified in the excised kidneys of selected rats in this study. These slides provide histological evidence of significant renal injury, but also of viable or recovering proximal tubules. They highlight that injury and recovery are ongoing processes, even when GFR has apparently returned to normal. The combination of structural with physiological methods, are critical in determining the role of breath analytes in this model.

7.4 Identification of Biomarkers of ARF

The biomarker identification methods described in Chapter 3 and used in Chapters 4 and 5, were used to identify biomarkers of renal function in this rat ARF trial. Classifications were performed comparing the normal breath analyte concentrations against the analyte concentrations after induction of ARF. For validation, analyte concentrations after cannulation surgery were also compared with those after ARF induction. Classifications were performed using the H_3O^+ and O_2^+ precursors only, since these are the most useful precursors for identifying the expected biomarkers found in the dialysis studies.

7.4.1 H_3O^+ Precursor

7.4.1.1 Normal verses ARF

Mass scan results shown here compare the concentrations between the *normal* state, obtained from the average of samples 1, 6, 7, 14, and 15 of the trial, with the *ARF* state, obtained from the maximum concentration in samples 8, 9, 10, and 11 of the trial (Refer Table 5.1). These 2 states are thus the j and k states, respectively, from Section 3.1. Mass scans results are shown using classification the method on the normalised data, (Equation (3.1)), and the relative change biomarker identification method (Equation (3.3)), for comparison. Note that the background air was removed from the sample, using a mass-specific Equation (6.20) prior to classification, such that classification was performed on C_{R*} .

Using the H_3O^+ precursor, Figure 7.59 was obtained from classification of normal and ARF data. A 0.61% classification error and a ROC area of 0.999 was observed with a bootstrap sample size of 200. Note this figure covers all masses scanned and shows good separation between groups. Using the biomarker identification method, which displays the density profiles of the means of 200 bootstrap samples, (Equation (3.3)), Figure 7.60 was obtained. A summary of the top biomarkers identified using each method is shown in Table 7.12, with their respective scores. Using the classification method, top biomarkers have minimal overlap between log-odds density profiles and thus a *low* score. Using the biomarker identification method, top biomarkers have a high mean to standard deviation ratio, and thus a *high* score.

Table 7.12 Top Biomarkers of ARF with the H_3O^+ precursor.

Classification Method		Biomarker ID Method	
Mass	Score	Mass	Score
63	0.0377	79	13.18
38	0.0481	77	12.61
79	0.0530	59	11.49
77	0.0570	38	9.16
59	0.1050	78	8.82
78	0.1694	63	8.01
60	0.1942	60	6.19

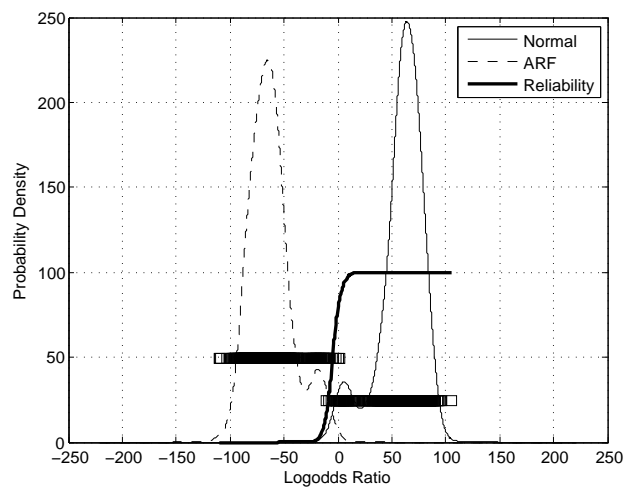


Figure 7.59 Classification between *normal* and *ARF* over all masses using the H_3O^+ precursor

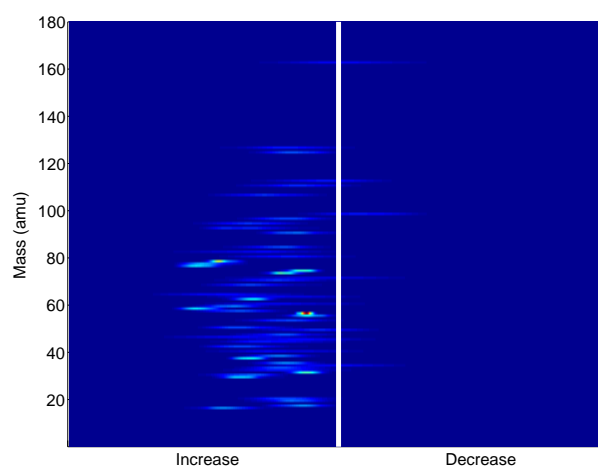


Figure 7.60 Biomarker identification in the *normal* and *ARF* states using the H_3O^+ precursor

Figures 7.61-7.67 show the density profiles of the top biomarkers of Table 7.12. The *left* plot shows the density profile of the normalised data. The *right* plot shows the density profile of the log-odds ratio of the normalised data. Again, good separation is the hallmark of a good potential biomarker.

It was observed that similar to the dialysis studies, TMA, acetone, and acetic acid emerged as the top biomarkers between the *normal* and *ARF* states. This result was expected since both studies investigate renal function.

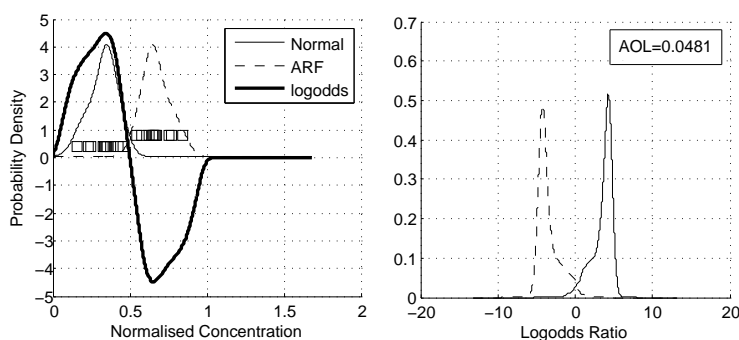


Figure 7.61 *Left:* Probability density profile for Mass 38 obtained via normal and ARF datasets with the H_3O^+ precursor. *Right:* Log-odds probability density profile for identification of biomarkers is shown, right.

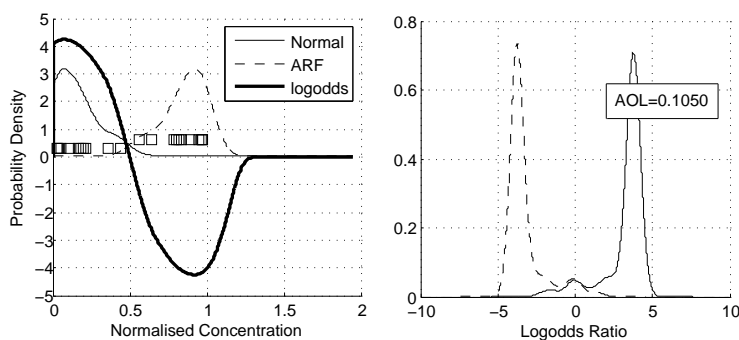


Figure 7.62 *Left:* Probability density profile for Mass 59 obtained via normal and ARF datasets with the H_3O^+ precursor. *Right:* Log-odds probability density profile for identification of biomarkers is shown, right.

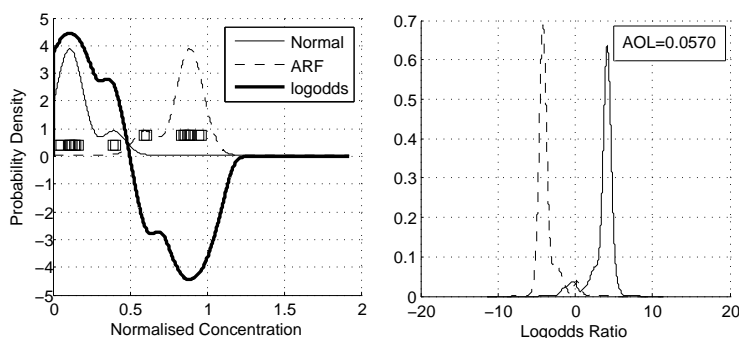


Figure 7.63 *Left:* Probability density profile for Mass 77 obtained via normal and ARF datasets with the H_3O^+ precursor. *Right:* Log-odds probability density profile for identification of biomarkers is shown, right.

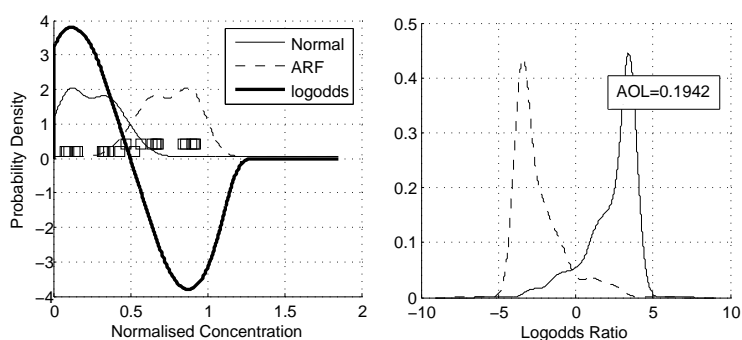


Figure 7.64 *Left:* Probability density profile for Mass 60 obtained via normal and ARF datasets with the H_3O^+ precursor. *Right:* Log-odds probability density profile for identification of biomarkers is shown, right.

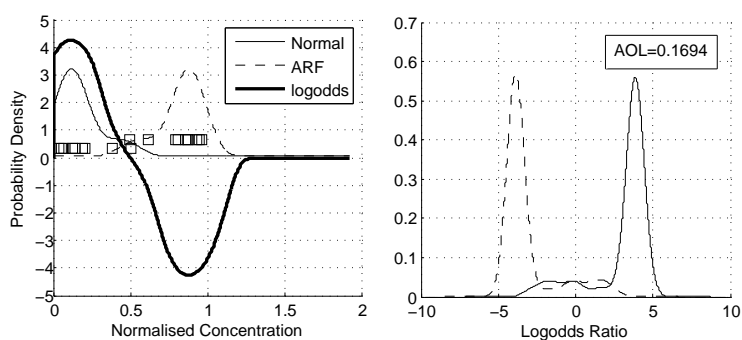


Figure 7.65 *Left:* Probability density profile for Mass 78 obtained via normal and ARF datasets with the H_3O^+ precursor. *Right:* Log-odds probability density profile for identification of biomarkers is shown, right.

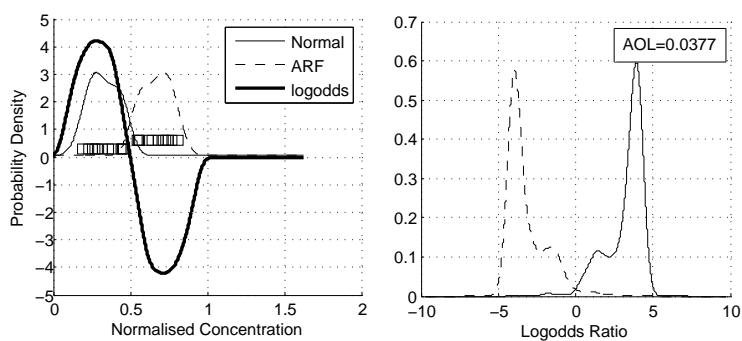


Figure 7.66 *Left:* Probability density profile for Mass 63 obtained via normal and ARF datasets with the H_3O^+ precursor. *Right:* Log-odds probability density profile for identification of biomarkers is shown, right.

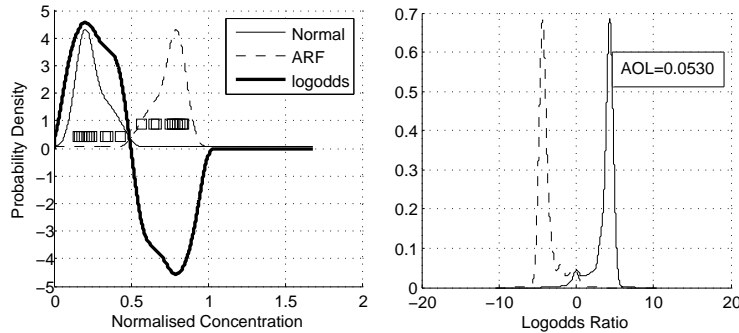


Figure 7.67 *Left:* Probability density profile for Mass 79 obtained via normal and ARF datasets with the H_3O^+ precursor. *Right:* Log-odds probability density profile for identification of biomarkers is shown, right.

7.4.1.2 Cannulation Surgery versus ARF Surgery

Mass scan results shown here compare the concentrations between the *post-cannulation* state, obtained from the maximum of samples 2, 3, 4, and 5 of the trial, with the *post-ARF* state, obtained from the maximum concentration in samples 8, 9, 10, and 11 of the trial. These 2 states are thus the j and k states, respectively, from Section 3.1. Mass scans results are shown using classification method on the normalised data, (Equation (3.1)), and the relative change biomarker identification method (Equation (3.3)), for comparison. This comparison removes the initial surgery from the analysis to provide a clear examination of just the impact of ARF.

Using the H_3O^+ precursor, Figure 7.68 was obtained from classification of post-cannulation and post-ARF datasets. A 23.14% classification error and a ROC area of 0.674 was observed with a bootstrap sample size of 200. The corresponding biomarker plot is shown in Figure 7.69.

This poor classification result, compared to Section 7.4.1.1, indicates that although several VOCs were elevated after induction of ARF, they were also, at least partially, elevated after any surgery. Hence, those biomarkers identified may not be indicative of renal function alone, but include also the impact of surgery. As a worst case, they are functions or markers of surgery or trauma. This result

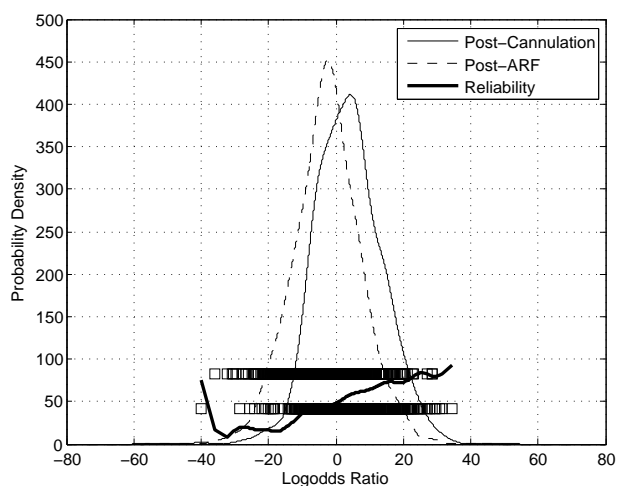


Figure 7.68 Classification between *post-cannulation* and *post-ARF* over all masses using the H_3O^+ precursor

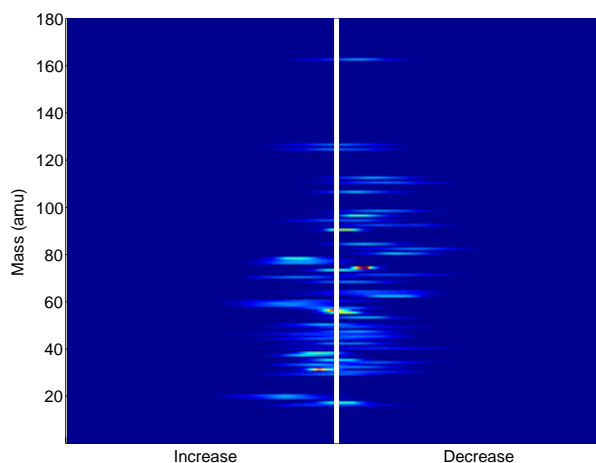


Figure 7.69 Biomarker identification in the *post-cannulation* and *post-ARF* states using the H_3O^+ precursor

could be due to low rat numbers, dilution of sample due to sampling method, or machine noise at low VOC concentration (due at least partially to sample dilution). The time course was plotted for each rat for the biomarkers identified in Section 7.4.1, as seen in Figures 7.70-7.72. Note that the results from Ula (Rat 11) are omitted since she did not survive the cannulation surgery.

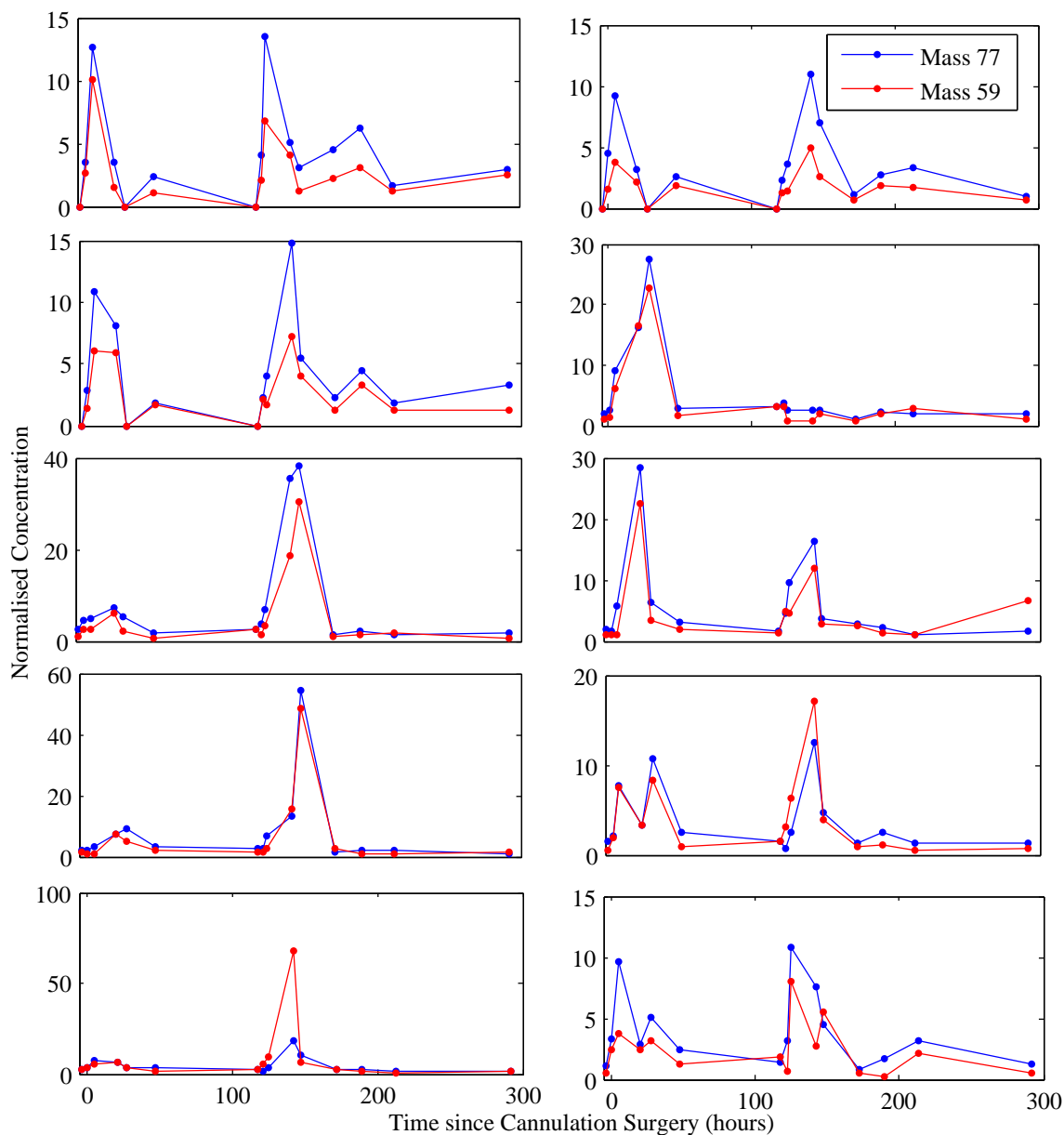


Figure 7.70 Time profiles for all rats with at 59 (acetone) and 77 (acetone with water cluster), using the H_3O^+ precursor. Odd numbered rats are in the left column, and even numbered rats are in the right column.

Masses 59 and 77 refer to acetone, and acetone with an associated water cluster, respectively. It was observed that although the concentration of these masses increases after surgery, the increase was not consistent between rats. More specifically, 7 of the rats displayed a larger peak after ARF, and 3 displayed a larger peak after cannulation surgery.

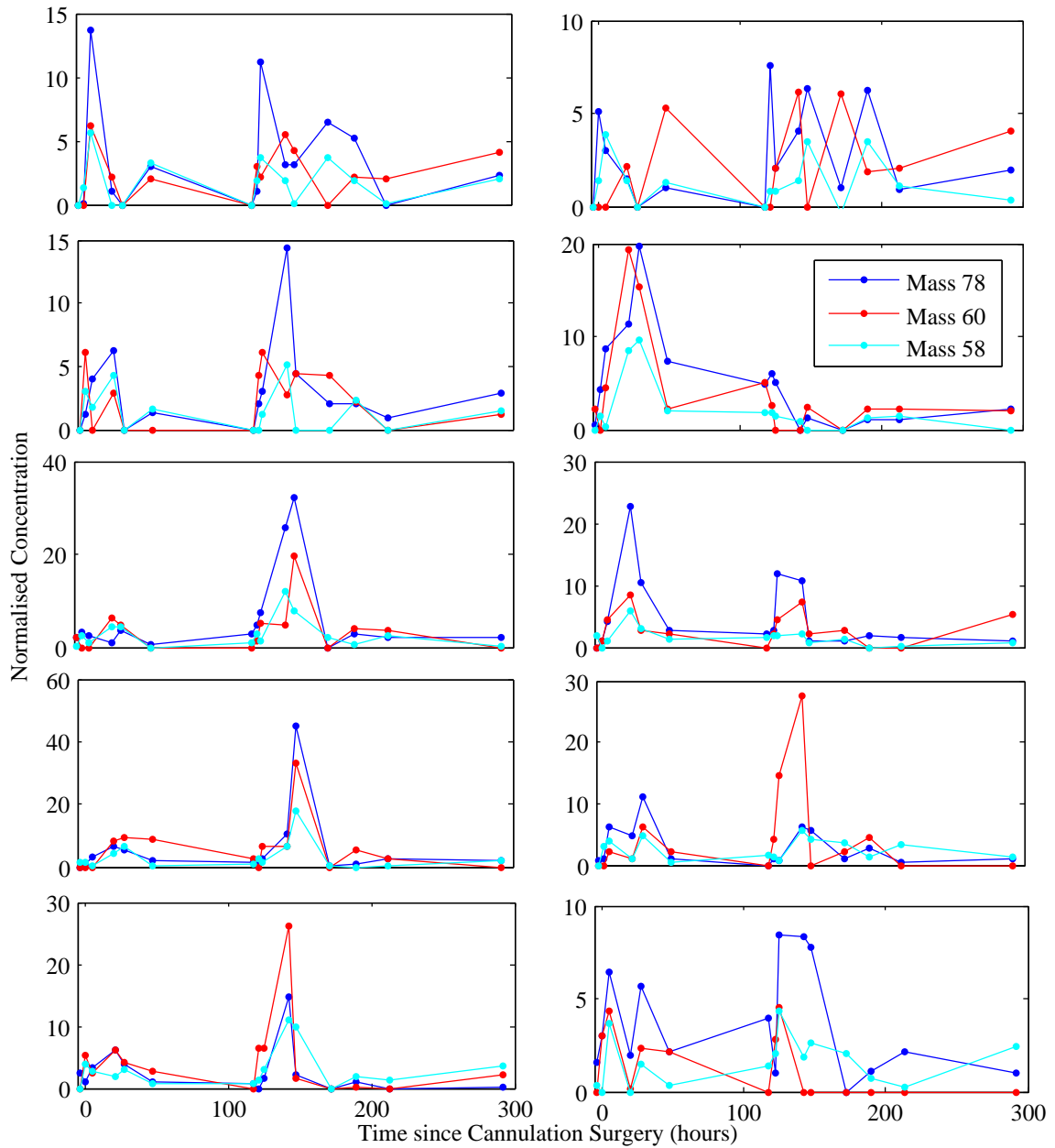


Figure 7.71 Time profiles for all rats at masses 58, 60 and 78, corresponding to TMA, using the H_3O^+ precursor. Odd numbered rats are in the left column, and even numbered rats are in the right column.

Masses 58, 60 and 78 refer to TMA. Once more, it was observed that the breath concentrations of some rats at these masses were higher after cannulation surgery than after surgery to induce ARF. Hence, the impact of surgery and ARF were intermixed.

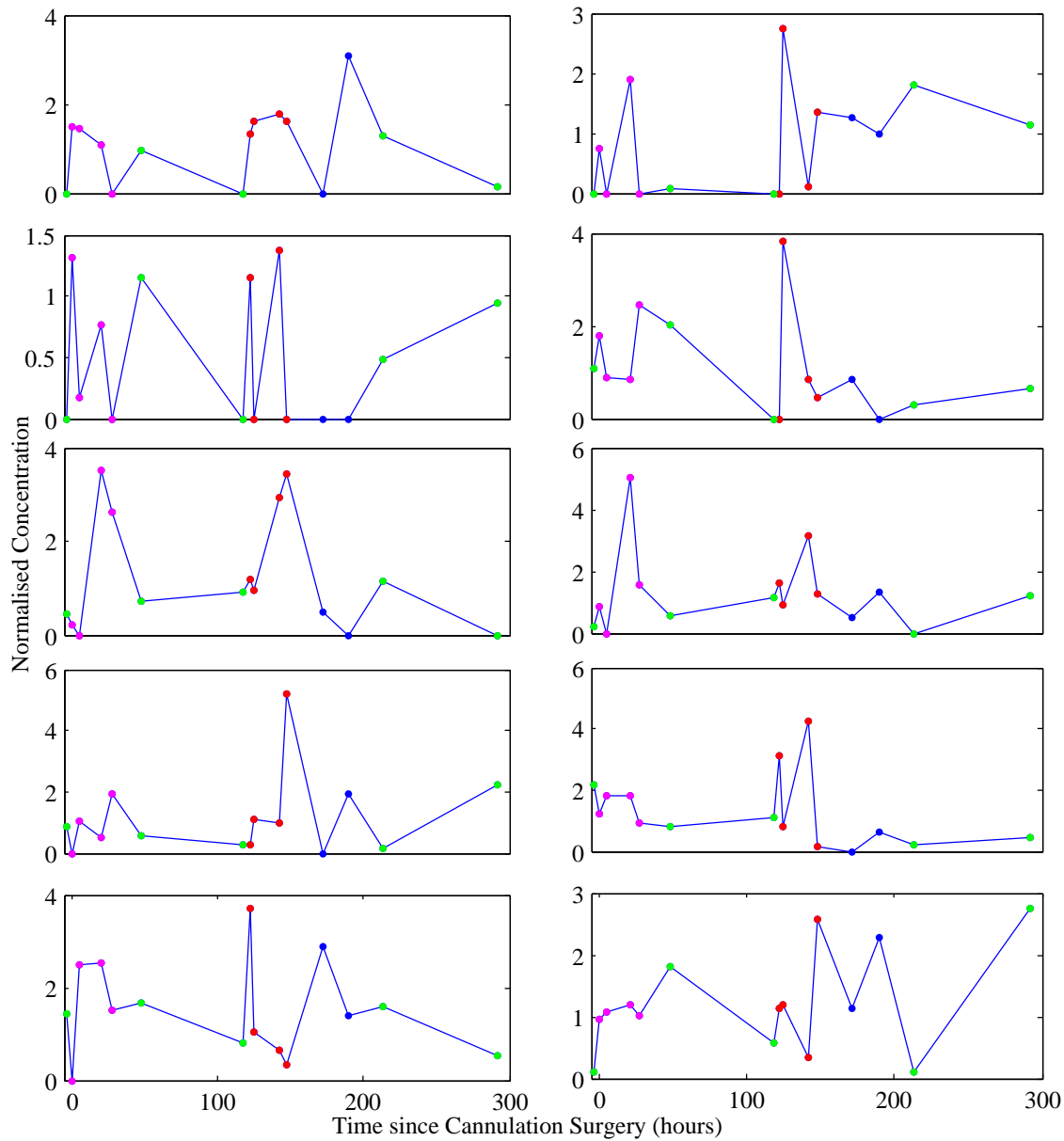


Figure 7.72 Time profiles for all rats at mass 79, using the H_3O^+ precursor. *Red*: samples used in ARF classification; *Magenta*: samples used in Cannulation classification; *Green*: samples used in Normal classification. Odd numbered rats are in the left column, and even numbered rats are in the right column.

When the criteria for classification are considered, it is easy to see how mass 79 is determined to be a top biomarker. Criteria 1 (Section 7.4.1) uses the maximum post-ARF concentration (*red*) against the average normal concentration (*green*). Criteria 2 (Section 7.4.2) uses the maximum post-ARF concentration (*red*) against the maximum post-cannulation concentration (*magenta*). It was observed that 10 and 8 rats, using criteria 1 and criteria 2, respectively, exhibited a higher post-ARF concentration. However, in the final analysis, the result at this mass was not considered consistent enough to be clinically useful.

7.4.2 O_2^+ Precursor

Using the O_2^+ precursor, Figure 7.73 was obtained from classification of *normal* and *ARF* data. A 3.3% classification error and a ROC area of 0.990 was observed with a bootstrap sample size of 200. The corresponding biomarker plot is shown in Figure 7.74. Finally, best biomarkers are identified in Table 7.13.

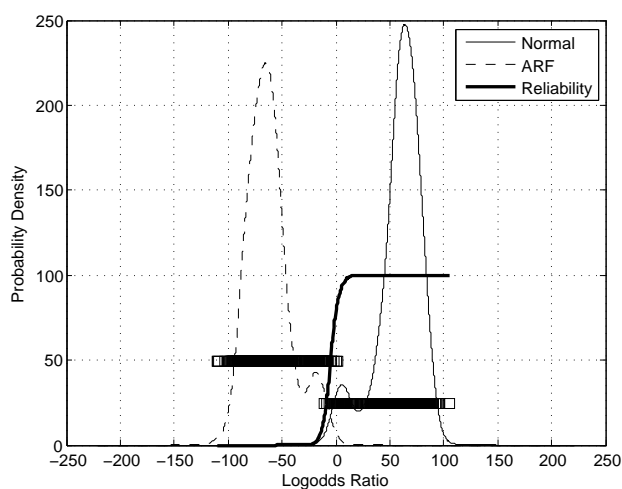


Figure 7.73 Classification between *normal* and *ARF* over all masses using the O_2^+ precursor

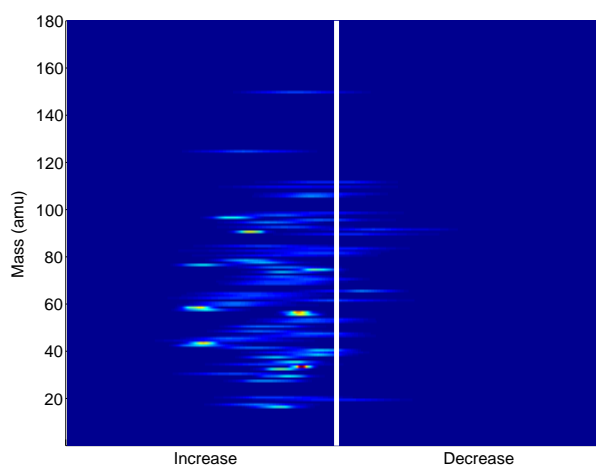
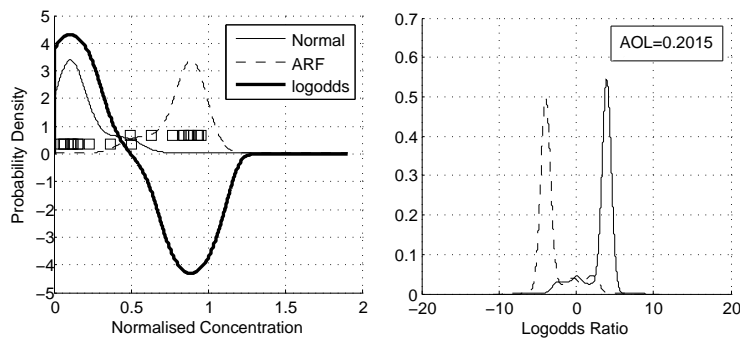
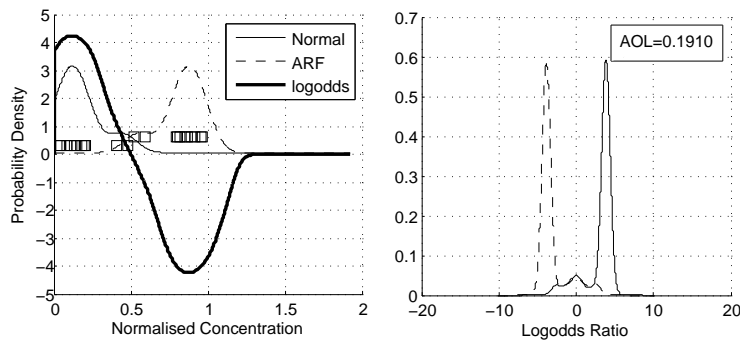


Figure 7.74 Biomarker identification in the *normal* and *ARF* states using the O_2^+ precursor

Figures 7.75-7.78 show the density profiles of the top biomarkers. The *left* plot shows the density profile of the normalised data. The *right* plot shows the density profile of the log-odds ratio of the normalised data.

Table 7.13 Top Biomarkers of ARF with the O_2^+ precursor

Classification Method		Biomarker ID Method	
Mass	Score	Mass	Score
44	0.0056	59	16.52
59	0.0066	44	15.15
97	0.0103	58	8.59
77	0.1894	77	8.49
58	0.1910	43	8.05
<hr/>			
43	0.2015	97	7.86
61	0.3234	79	5.14
17	0.3291	17	4.31
79	0.3315	61	4.21

**Figure 7.75** *Left:* Probability density profile for Mass 43 obtained via normal and ARF datasets with the O_2^+ precursor. *Right:* Log-odds probability density profile for identification of biomarkers is shown, right.**Figure 7.76** *Left:* Probability density profile for Mass 58 obtained via normal and ARF datasets with the O_2^+ precursor. *Right:* Log-odds probability density profile for identification of biomarkers is shown, right.

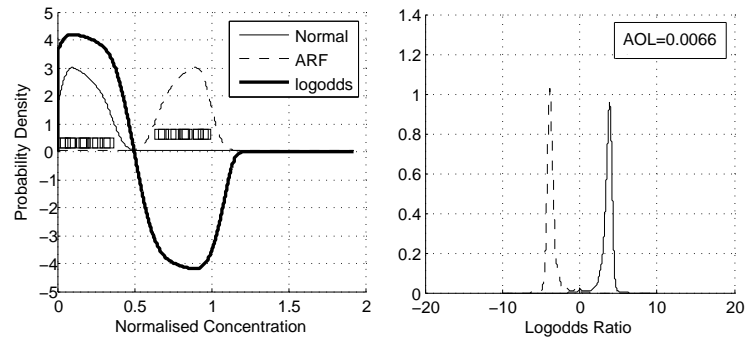


Figure 7.77 Left: Probability density profile for Mass 59 obtained via normal and ARF datasets with the O_2^+ precursor.

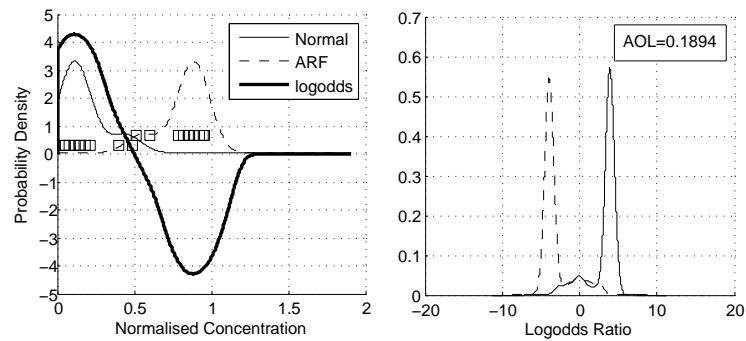


Figure 7.78 Left: Probability density profile for Mass 77 obtained via normal and ARF datasets with the O_2^+ precursor.

Classification performed using the post-cannulation and post-ARF datasets resulted in an estimated prediction error of 19.27% and a ROC error of 0.781 using a bootstrap sample size of 200, as seen in Figure 7.79.

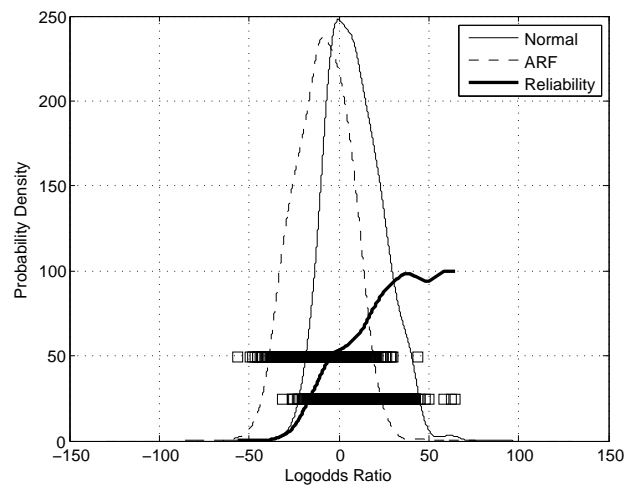


Figure 7.79 Classification between *post-cannulation* and *post-ARF* over all masses using the O_2^+ precursor

Using the biomarker identification method, Figure 7.80 was obtained, with a bootstrap sample size of 200.

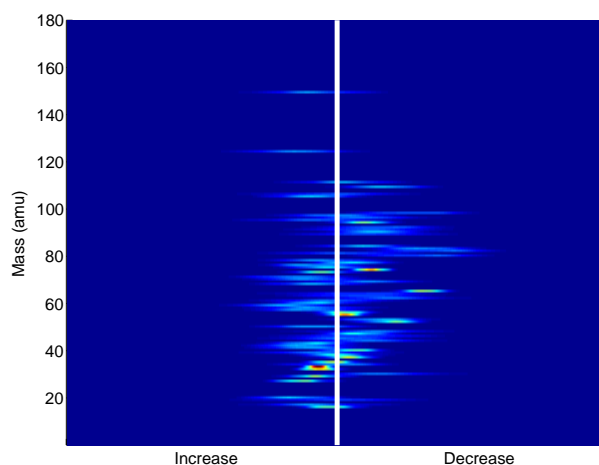


Figure 7.80 Biomarker identification between *post-cannulation* and *post-ARF* over all masses using the O_2^+ precursor

Time profiles for the top biomarkers identified during classification of the *normal* and *ARF* states, with the O_2^+ precursor, are shown in Figures 7.81-7.84. Note that the raw concentration in counts per second is displayed for the total breath (C_{Tot}), and for the background laboratory air (C_B). It was observed that the same problem occurred with the O_2^+ precursor as occurred with the H_3O^+ precursor in Section 7.4.1.2. More specifically, although some markers did appear elevated in ARF compared to normal, they were also elevated after the cannulation surgery.

It is suggested that improved results may be possible with the use of the *Voice200*[®] SIFT-MS instrument, which samples breath at a lower rate. The lower sampling rate would reduce the $\frac{V_B}{V_R}$ ratio, and result in a less dilute breath measurement, with less error, by Equation (6.18). Hence, this option should be considered in future studies.

In the mass scan mode, less time is spent counting by the channeltron particle detector. In addition, the analyte concentration result cannot be viewed directly as it is generated, compared with in SIM scan mode (see Figure 6.11). Therefore, there are less resulting datapoints from which to infer the analyte

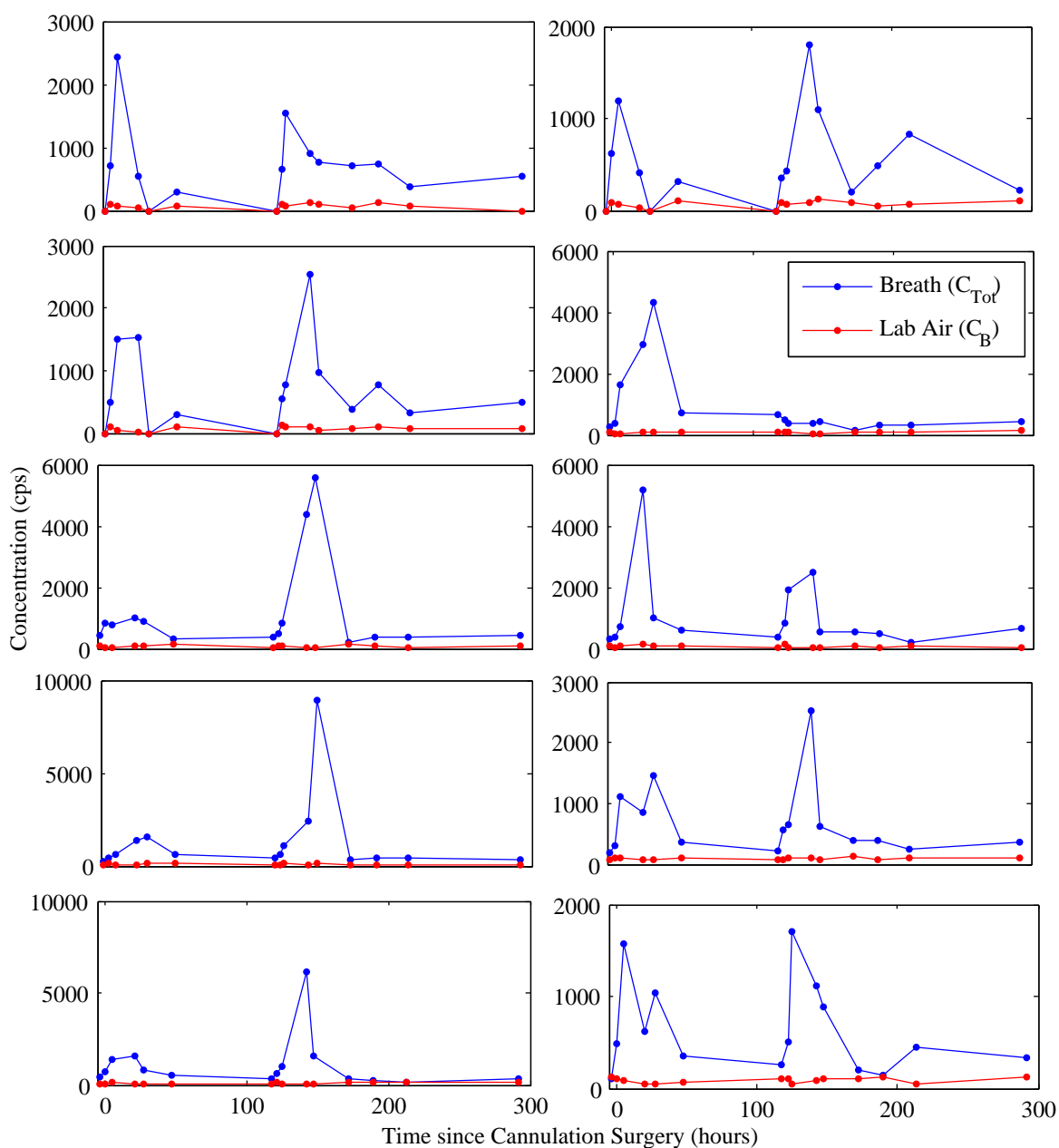


Figure 7.81 Time profiles for all rats at mass 43, using the O_2^+ precursor. Odd numbered rats are in the left column, and even numbered rats are in the right column.

concentration. Another possible source of error was the position of the rat in the bottle. In SIM scan mode, it is possible to see when equilibrium is obtained. However, in mass scan mode, if the position of the rat nose changes slightly, for example by moving closer to a breathing hole, the mixing between expired air and background air in the bottle changes. Thus, the measured breath analytes could vary significantly. Finally, the temperature in the laboratory was maintained at

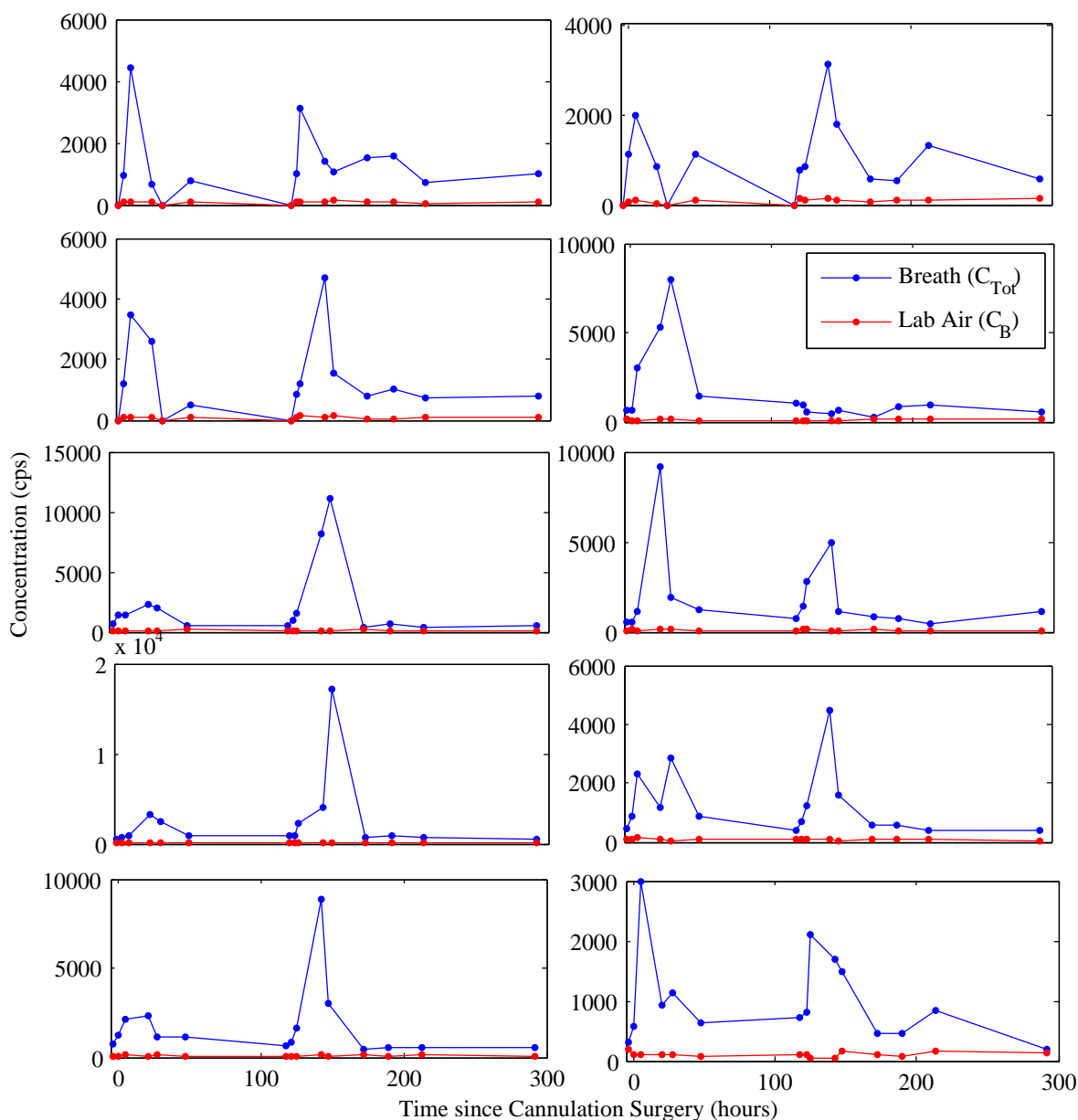


Figure 7.82 Time profiles for all rats at mass 58, using the O_2^+ precursor. Odd numbered rats are in the left column, and even numbered rats are in the right column.

approximately $25^\circ C$, and the bottles were stored in an incubator. However, it is possible that analytes could have adsorb to the bottle wall.

It was concluded that the biomarkers identified in this section of the study, in mass scan mode, were not specific to renal function across all rats at a sensitivity great enough to be measured by the *Voice100TM* SIFT-MS instrument, using the current rat breath sampling methods described in Chapter 5.6. It is suggested

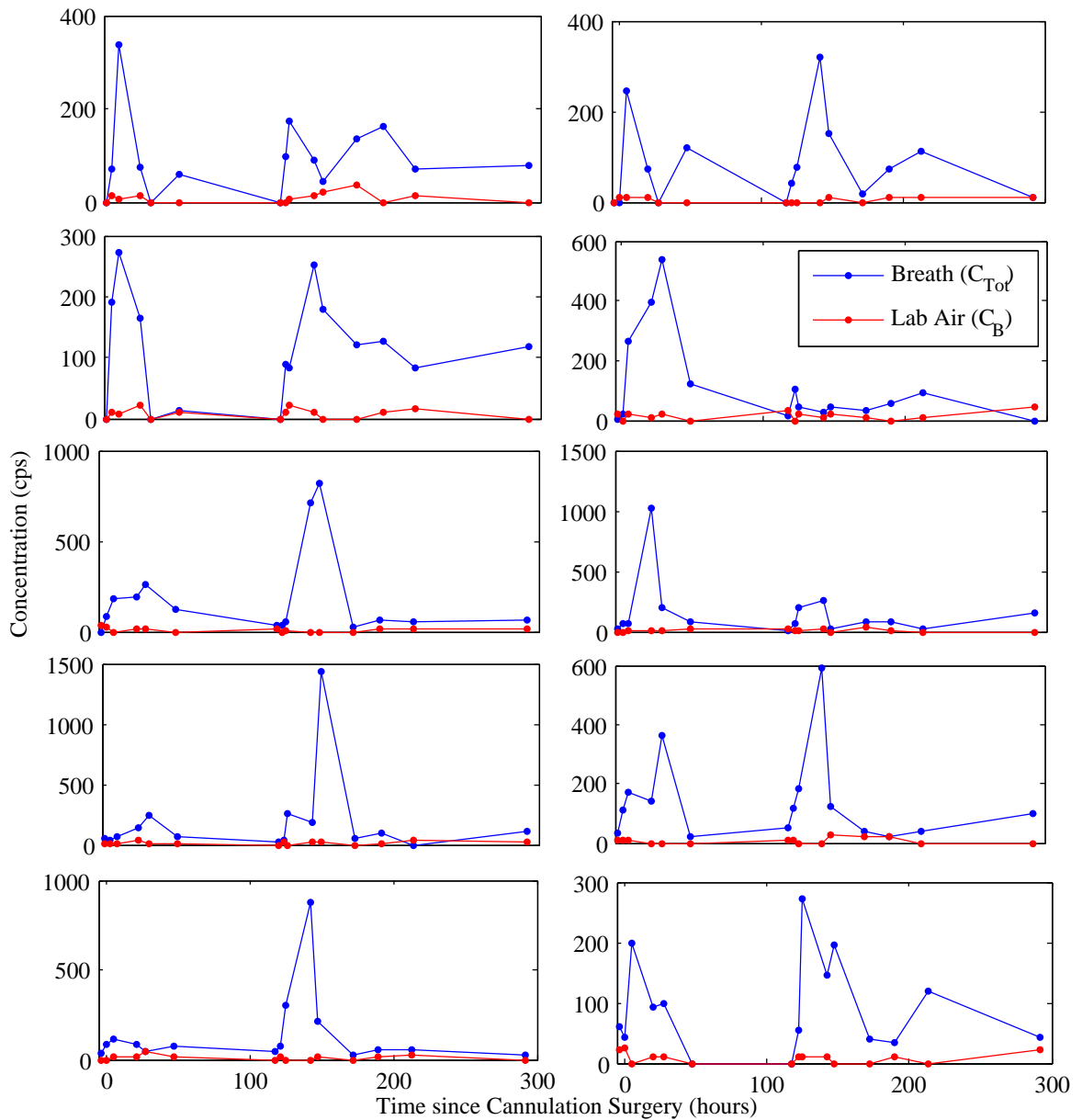


Figure 7.83 Time profiles for all rats at mass 59, using the O_2^+ precursor. Odd numbered rats are in the left column, and even numbered rats are in the right column.

that better results could be achieved using the *Voice200*[®] instrument. However, if results are not improved using this instrument, it is suggested that more efforts be focussed on obtaining a more representative alveolar breath sample from the rat.

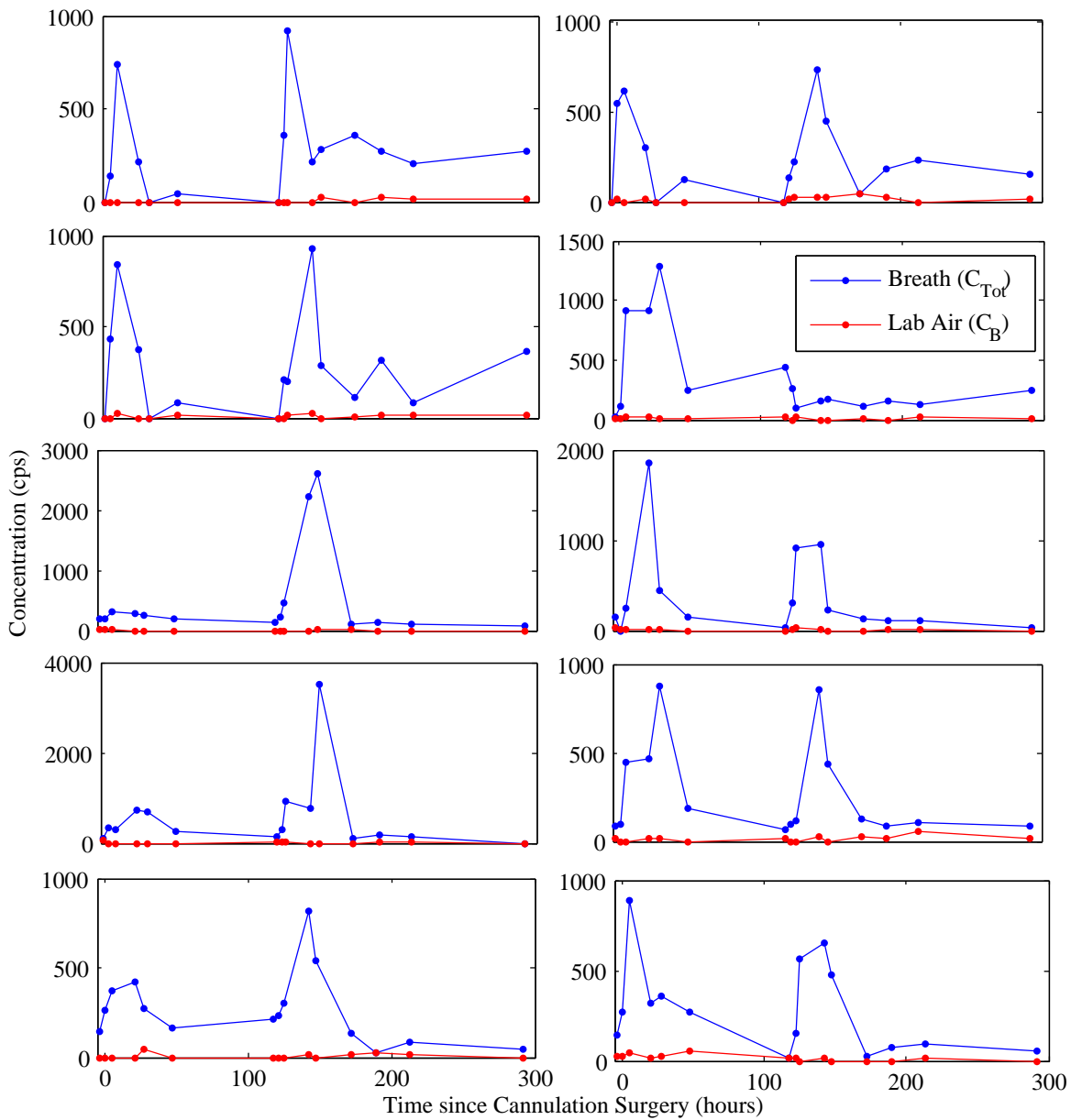


Figure 7.84 Time profiles for all rats at mass 77, using the O_2^+ precursor.

7.5 Summary

An animal trial was carried out in which ARF was induced in 11 rats. Renal function was measured following recovery from an initial surgery to insert a jugular vein cannula for serial blood sampling, as well as after induction of ARF via a 60 minute bilateral renal artery clamp. Gold standard measures of kidney function were used to successfully correlate SIM scan breath ammonia concentration

with both plasma creatinine concentration and GFR obtained via a bolus inulin clearance test. Histology slides of excised rat kidneys provided further evidence of the degree of renal damage.

Classification methods were used to identify biomarkers of renal function. Several markers were identified with the H_3O^+ and O_2^+ precursors, most likely relating to TMA, acetone and acetic acid. However, further investigation revealed that these biomarkers were not elevated to a significantly greater extent than in the cannulation surgery. Hence, it was concluded that the current breath sampling technique with the *Voice100TM* SIFT-MS instrument, in the mass scan mode, is not sufficiently sensitive to identify biomarkers of renal function in rats. However, there is scope in future work to determine if TMA, acetone and/or acetic acid might offer potential as a biomarker of acute physiological stress, since these analyte concentrations were significantly elevated after surgery.

Chapter 8

Conclusions and Future Work

8.1 Conclusions

SIFT-MS is an analytical technique for the real-time quantification of VOCs in gaseous samples. This technology has current and potential applications in a wide variety of industries, although the focus of this research is in medical science. In this field, SIFT-MS has potential as a diagnostic device, capable of determining the presence of a particular disease or condition. In addition, SIFT-MS can be used to monitor the progression of a disease state, or predict deviations from expected behaviour. All these possibilities are available non-invasively and in real-time, by measuring various analytes in breath samples.

A model was presented for the classification of cross-sectional sets of mass scan data obtained using the SIFT-MS instrument. Using this method, test datasets of known classification are used to develop probability density profiles for each of the two datasets: Groups j and k . The probability density profiles are created for each group from concentration data, using a mixed distribution made up of a kernel density and a Dirac delta function. An unknown sample is then tested against the datasets, with the result being a classification into either Group j or Group k . In a diagnostic analysis, j and k would be the non-disease and diseased states. Bootstrap methods are used to determine the estimated prediction error. Finally, by determining which masses contribute most to a successful classification, biomarkers for the disease state can be identified.

This cross-sectional classification model was validated in a simple study to determine which VOCs or their water clusters increase or diminish when nitrogen

is passed through sterile glass bottles filled with water. An additional goal was to determine which VOCs are present in tedlar bags. As expected, the estimated prediction error was 0% over all 3 precursors, and the masses most useful in classification were those corresponding to the water clusters of nitrogen and the precursor ions. Lastly, 2 biomarkers were identified that originated from the tedlar bag. As a proof-of-concept this model was also tested on the pre and post datasets from a patient undergoing dialysis. Good results were obtained, although it was recognised that the inherent paired nature of such a dataset is ignored using the cross-sectional classification model. Hence, a longitudinal classification model was developed.

A longitudinal classification model was presented that exploits the paired nature of data in a before/after setting. When monitoring the progression of a disease state, there is no baseline for intra-patient comparison, because depending on patient specific variables and degree of sickness, starting points and responses to treatment can vary dramatically. However, a single patient dataset cannot be considered on its own, because there is usually insufficient data to perform a statistically rigid classification. Hence, an appropriate normalisation method is required to allow interpatient biomarker identification.

Two clinical dialysis studies were carried out to monitor changes in the concentration of retained nitrogenous wastes over multiple dialysis sessions. Dialysis efficacy is most simply determined using the urea reduction ratio, requiring blood samples to determine changes in blood urea nitrogen. However, SIFT-MS offers potential benefits in dialysis treatment via the ability to measure dialysis efficiency non-invasively, and in real time, with a simple breath test to determine the reduction ratio of key analytes. By observing specific patient trends, one can determine the timing of the next required dialysis treatment, and thus avoid secondary complications due to delayed treatment. SIFT-MS can also be used to calculate the optimal time for each dialysis treatment, to minimise patient treatment time and maximise machine availability for others. Lastly, SIFT-MS can be used to identify key markers of renal function, as dialysis treatment effectively takes a patient from a sick to a healthy state over a few hours.

Good correlation was observed with the gold standard creatinine and BUN measures, with breath ammonia and TMA measured in SIM scan mode. Interestingly, 3 different VOC time profiles over the course of dialysis were observed.

Firstly, analyte concentrations decreased exponentially, as was the expected response, with particularly ammonia showing a small rise 2-3 hours into treatment. Secondly, analyte concentrations oscillated within an overall decreasing profile, a trend particularly observed at lower concentrations, as expected. Lastly, analyte concentrations increased for the first 30-60 minutes, before decreasing exponentially. Mass scans identified biomarkers relating to TMA, acetone and acetic acid. Estimated prediction error decreased from a maximum of 10% in the first clinical study, to a maximum of 0% in the second study, most likely due to the introduction of the *Voice200*[®] SIFT instrument, and better sampling methods.

Carrying out a trial in a human setting poses difficulties, since all patients present with a differing degree of impairment, have differing diets, and differing genetic predispositions, as well as other potential confounding factors. It was considered that running an animal trial would alleviate many of these difficulties, since in-bred animals could be used in the study. In addition, samples sizes, diet, and daily behaviour, as well as degree of renal impairment, could all be more easily controlled. Lastly, easy comparison with clinical and research gold standard measures of renal function would be possible, since several techniques in addition to creatinine and BUN blood tests would be available. Such techniques include radioactive tracer methods, which cannot be performed in a human clinical trial. Hence, an animal trial was designed for the identification of biomarkers of acute renal failure in rats.

An animal study was carried out in which acute renal failure was induced via a 60-minute bilateral renal artery clamp in 11 Sprague-Dawley rats. Renal function was monitored following recovery from a previous surgery to insert a jugular vein cannula, and for 1 week following ARF-inducing surgery. A two-compartment model was developed for estimating renal function via a bolus injection of a radio-labelled inulin tracer, and was compared with the current clinical gold standard plasma creatinine measurement, modified using the Cockcroft-Gault equation for rats. These two methods were compared with SIFT-MS monitoring of breath ammonia. Relative decreases in renal function showed very good correlation between methods, indicating good promise for fast, non-invasive determination of renal function via breath testing. In addition, it was found in a validation study, that the concentration of expired ammonia increases as a function of background ammonia concentration with a slope greater than 1. This result indicates that ammonia can be removed from the body at a concentration greater than that

possible by simple diffusion from the blood, alone, suggesting the presence of ammonia transporters in lung epithelium for actively transporting ammonia. This theory is supported in the literature by reports of ammonia transporters elsewhere in the body [Weiner and Hamm, 2007].

Identification of breath biomarkers of renal function were semi-successful. Distinction between the normal and ARF states was straight-forward, with <4% estimated prediction errors and the identification of the same VOCs identified in the dialysis clinical study. However, further investigation revealed that these biomarkers were not elevated to a significantly greater extent than after the cannulation surgery, suggesting that the biomarkers identified were for acute physiological stress as opposed to acute renal failure. It is suggested that better results could be achieved using the *Voice200*[®] instrument, which samples at a lower rate, to reduce errors incurred by dilution of the breath sample. However, if results are not improved with the the *Voice200*[®], it is suggested that more efforts be focussed on obtaining a more representative alveolar breath sample from the rat.

Finally, the concept of a mass spectrometric breath sampling technique is very new in diagnostic medicine. Therefore, the results presented here, while not ideal, provide much insight for the way forward, in terms of methods and approach. It is concluded that with better instrumentation, such as the *Voice200*[®], and better sampling techniques, the mathematical methods presented here could be applied to a wide variety of medical applications.

8.2 Future Work

Future work aims to develop a predictive model for determining the optimal time for each dialysis treatment, to minimise patient treatment time and maximise machine availability for others. Results from the second clinical dialysis study indicate that TMA would be a good analyte to monitor, since its concentration decreases rapidly regardless of initial concentration, and is maintained at a relatively constant, low concentration during dialysis. In addition, a clinical study is currently underway to collect breath samples from patients who have undergone kidney transplantation, in the weeks following their transplant. It is envisaged

that analysis of breath analytes could help predict rejection episodes by observing changes in renal function, as monitored by changes in key breath analytes.

Lastly, future work should further investigate alveolar gas exchange of analytes. The background, inspired air problem remains largely unresolved by studies reported in the literature. Some researchers ignore background air, and others have the test subject breath *pure* air prior to sampling. Some researchers *subtract* background air concentrations from the sample, and yet others remove the deadspace volume using valved devices to obtain the alveolar portion of the breath. All these techniques aim to obtain a sample representative of alveolar breath. However, even if an alveolar sample is obtained, background air still plays an important role, since most analytes travel from the blood into the alveolar breath as determined by the concentration gradient for diffusion. A model for gas exchange in the alveoli could be combined with a closed experimental setup involving an artificial respirator with reservoirs of variable, but known, analyte concentration. Analysis of the measured analyte via SIFT-MS, could then be used to study the movement of analytes in the dynamic breath scenario. Finally, this analysis could provide invaluable information about how to infer blood analyte concentration from the breath concentration measured by the SIFT-MS instrument.

References

- M.A. Bain, R. Faull, G. Fornasini, R.W. Milne, and A.M. Evans. Accumulation of trimethylamine and trimethylamine-n-oxide in end-stage renal disease patients undergoing haemodialysis. *Nephrol Dial Transplant*, 21(5):1300–1304, 2006.
- S.K. Bakar and S. Niazi. Simple reliable method for chronic cannulation of the jugular vein for pharmacokinetic studies in rats. *Journal of Pharmaceutical Sciences*, 72(9):1027–1029, 1982.
- R. Bellomo, C. Ronco, J.A. Kellum, R.L. Mehta, and P. Palevsky. Acute renal failure definition, outcome measures, animal models, fluid therapy and information technology needs: the second international consensus conference of the acute dialysis quality initiative (adqi) group. *Critical Care*, 8(4):204212, 2004.
- E.Y. Berger, S.J. Farber, and D.P. Jr. Earle. Comparison of the constant infusion and urine collection techniques for the measurement of renal function. *J. Clin. Invest.*, 27:710–719, 1948.
- B. Bubeck, R. Piepenburg, U. Grethe, B. Ehrig, and K. Hahn. A new principle to normalize plasma concentration allowing single-sample clearance determinations in both children and adults. *Eur. J. Nucl. Med.*, 19:511–516, 1992.
- L.A. Buckley, D.P. Coleman, J.P. Burgess, B.F. Thomas, L.T. Burka, and A.R. Jeffcoat. Identification of urinary metabolites of isoprene in rats and comparison with mouse urinary metabolites. *Drug Metabolism and Disposition*, 27:7: 848–854, 1999.
- J.S. Cameron. *Oxford Textbook of Clinical Nephrology*. Oxford University Press, 1992.
- E. Capodicasa, G. Trovarelli, G.E. De Medio, M.A. Pelli, G. Lippi, C. Verdura, and M. Timio. Volatile alkanes and increased concentrations of isoprene in exhaled air during hemodialysis. *Nephron*, 82:331–337, 1999.

- D.W. Cockcroft and M.H. Gault. Prediction of creatinine clearance from serum creatinine. *Nephron*, 16(1):31–41, 1976.
- A.J.L. Cooper and B.R. Freed. Metabolism of [^{13}n]ammonia in rat lung. *Neurochemistry International*, 47:103–118, 2005.
- M Danciu and M. Mihailovici. Atlas of pathology. Website, 2004.
- S. Davies, P. Spanel, and D. Smith. Quantitative analysis of ammonia on the breath of patients in end-stage renal failure. *Kidney International*, 52:223–228, 1997.
- S. Davies, P. Spanel, and D. Smith. A new ‘online’ method to measure increased exhaled isoprene in end-stage renal failure. *Nephrology Dialysis Transplantation*, 16:836–839, 2001.
- P.D. Doolan, E.L. Alpen, and I G.B. Theil. A clinical appraisal of the plasma concentration and endogenous clearance of creatinine. *Am J Med*, 32:65–72, 1962.
- Dupont. *tedlar_{TM}* polyvinyl fluoride film general properties. Technical report, USA: Dupont, 1995.
- D.P. Jr. Earle and R.W. Berliner. A simplified clinical procedure for measurement of glomerular filtration rate and renal plasma flow. *Proc. Soc. Exp. Biol. Med.*, 62:262–264, 1946.
- C.M. Erley, B.D. Bader, E.D. Berger, A. Vochazer, J.J. Jorzik, K. Dietz, and T. Risler. Plasma clearance of iodine contrast media as a measure of glomerular filtration rate in critically ill patients. *Crit Care Med*, 29:1544–1550, 2001.
- C.G. Freeman and M.J. McEwan. Rapid analysis of trace gases in complex mixtures using selected ion flow tube-mass spectrometry. *Aust. J. Chem.*, 55: 491494, 2002.
- G. Gobé, X-J. Zhang, D. Willgoss, E. Schoch, N. Hogg, and Z. Endre. Relationship between expression of bcl-2 genes and growth factors in ischaemic acute renal failure in the rat. *Journal of the American Society of Nephrology*, 11: 454–467, 2000.
- G.J. Handelman, L.M. Rosales, D. Barbato, J. Luscher, R. Adhikarla, R.J. Nicolosi, F.O. Finkelstein, C. Ronco, G.A. Kaysen, N.A. Hoenich, and N.W.

- Levin. Breath ethane in dialysis patients and control subjects. *Free Radical Biology and Medicine*, 35:1:17–23, 2003.
- C.E. Hann, J.G. Chase, J. Lin, T. Lotz, C.V. Doran, and G.M. Shaw. Integral-based parameter identification for long-term dynamic verification of a glucose-insulin system model. *Computer Methods and Programs in Biomedicine*, 77(3): 259–270, 2005.
- R. Hastie, T. Tibshirani and J.H. Friedman. *Elements of Statistical Learning: Data Mining, Inference and Prediction*. Springer, 2001.
- A.O. Hosten. *Clinical Methods: The History, Physical and Laboratory Examinations*. Butterworths, 1990.
- D King. Histology guide. Website, 2007.
- K. Lad. Breath collection equipment for clinical applications with sift-ms instruments. Master’s thesis, University of Canterbury, 2006.
- H.B. Lee and M.D. Blafox. Blood volume in the rat. *The Journal of Nuclear Medicine*, 25:72–76, 1985.
- D.G. Levitt. The pharmacokinetics of the interstitial space in humans. *BMC Clinical Pharmacology*, 3:doi:10.1186/1472–6904–3–3, 2003.
- A.S. Levy, J.P. Bosch, J.B. Lewis, T.G. Greene, N. Rogers, and D. Roth. A more accurate method to estimate glomerular filtration rate from serum creatinine: a new prediction equation. *Annals of Internal Medicine*, 130(6):461–470, 1999.
- E.K.M. Löwenborg, G. Jaremko, and U.B. Berg. Glomerular function and morphology in puromycin aminonucleoside nephropathy in rats. *Nephrol Dial Transplant*, 15:1547–1555, 2000.
- K. Martini, F. andand Welch. *Fundamentals of Anatomy and Physiology Applications Manual*. Pearson, Benjamin and Cummings, 2006.
- Merriam-Webster. Website, 2006.
- W. Miekisch, J.K. Schubert, and G.F.E. Noeldge-Schomburg. Diagnostic potential of breath analysis - focus on volatile organic compounds. *Clinica Chimica Acta*, 347:25–39, 2004.

- D.B. Milligan, G.J. Francis, B.J. Prince, and M.J. McEwan. Demonstration of selected ion flow tube ms detection in the parts per trillion range. *Anal Chem.*, 79(6):2537–2540, 2007.
- B.A. Molitoris, S.A. Falk, and R.H. Dahl. Ischemia-induced loss of epithelial polarity. role of the tight junction. *J. Clin. Invest.*, 84:1334–1339, 1989.
- K.T. Moorhead, D. Lee, J.G. Chase, A.R. Moot, K.M. Ledingham, J. Scotter, R.A. Allardyce, S. Senthilmohan, and Z. Endre. Classifying algorithms for sift-ms technology and medical diagnosis. *Computer Methods and Programs in Biomedicine*, 89:226–238, 2008.
- B.D. Myers, F. Chui, M. Hilberman, and A.S. Michaels. Transtubular leakage of glomerular filtrate in human acute renal failure. *Am. J. Physiol.*, 237:F319–F325, 1979.
- L.R. Narasimhan, W. Goodman, and C.K.N. Pate. Correlation of breath ammonia with blood urea nitrogen and creatinine during hemodialysis. *Proc. Natl. Acad. Sci.*, 98:8:4617–4621, 2001.
- J. Neilson. Integrity of storage media for clinical applications with sift-ms instruments. Master’s thesis, University of Canterbury, 2006.
- J. Oliver, D.M. Mac, and A. Tracy. The pathogenesis of acute renal failure associated with traumatic and toxic injury: renal ischemia, nephrotoxic damage and the ischemic episode. *J. Clin. Invest.*, 30:13071439, 1951.
- D.B. Parker, M.B. Rhoades, J. Koziel, and J. Spinhirne. Background odours in tedlar bags used for cafo odour sampling. In *ASAE Annual International Meeting*, 2003.
- D. Pass and G. Freeth. The rat. *ANZCCART News*, 6(4):1–4, 1993.
- A.M. Peters, B.L. Henderson, D. Lui, M. Blunkett, P.S. Cosgriff, and M.J. Myers. Appropriate corrections to glomerular filtration rate and volume of distribution based on the bolus injection and single-compartment technique. *Physiol. Meas.*, 20:313–327, 1999.
- M. Phillips. Method for the collection and assay of volatile organic compounds in breath. *Anal Biochem*, 247:272–278, 1997.

- H.L. Poulsen, H.A. Jensen, and H.H. Parving. Extracellular fluid volume determined by a single injection of inulin in men with untreated essential hypertension. *Scand J Clin Lab Invest.*, 37(8):691–696, 1977.
- L.F. Prescott, S. Freestone, and J.A.N. McAuslane. Reassessment of the single intravenous injection method with inulin for measurement of the glomerular filtration rate in man. *Clin. Sci. (Colch)*, 80:167–176, 1991.
- W.K. Purves, G.H. Orians, and H.C. Heller. *Life: The Science of Biology*. W.H. Freeman and Company, 1995.
- Z. Qi, I. Whitt, A. Mehta, J. Jin, M. Zhao, R.C. Harris, A.B. Fogo, and M.D. Breyer. Serial determination of glomerular filtration rate in conscious mice using fitc-inulin clearance. *Am J Physiol Renal Physiol*, 286:F590–F596, 2004.
- D. Randall, W. Burggren, and K. French. *Eckert Animal Physiology: Mechanisms and Adaptations*. W.H. Freeman and Company, 2002.
- T.H. Risby and S.S. Sehnert. Clinical application of breath biomarkers of oxidative stress status. *Free Radic Biol Med*, 27:1182–1192, 1999.
- C.D. Russell, A. Taylor, and D. Eshima. Estimation of technetium-99m mag₃ plasma clearance in adults from one or two blood samples. *Journal of Nuclear Medicine*, 30:1955–1959, 1989.
- L.A. Sapirstein, M.R. Herrold, M. Janakis, and E. Ogden. Validity of values for glomerular filtration rate and extracellular fluid obtained from plasma concentration-time curves after single injections of mannitol in the dog. *American Journal of Physiology*, 171:487–490, 1952.
- J. Schnermann and W. Homer. The juxtaglomerular apparatus: from anatomical peculiarity to physiological relevance. *J. Am. Soc. Nephrol.*, 14:1681–1694, 2003.
- R.W. Schrier, W. Wang, B. Poole, and A. Mitra. Acute renal failure: definitions, diagnosis, pathogenesis, and therapy. *J Clin Invest.*, 114(1):514, 2004.
- J.K. Schubert, W. Miekisch, T. Birken, K. Geiger, and G.F. Nöldge-Schomburg. Impact of inspired substance concentrations on the results of breath analysis in mechanically ventilated patients. *Biomarkers*, 10(2-3):138–152, 2005.
- O. Shemesh, H. Golbetz, J.P. Kriss, and B.D. Myers. Limitations of creatinine as a filtration marker in glomerulopathic patients. *Kidney International*, 28:830–838, 1985.

- D. Smith and P. Spanel. Application of ion chemistry and the sift technique to the quantitative analysis of trace gases in air and on breath. *Int. Rev. Phys. Chem.*, 15 (1):231271, 1996.
- D. Smith and P. Spanel. Selected ion flow tube mass spectrometry (sift-ms) for on-line trace gas analysis. *Mass Spectrometry*, 24:661700, 2005.
- R. Solomon and A. Segal. Defining acute kidney injury: what is the most appropriate metric? *Nature Clinical Practice: Nephrology*, 4(4):208–215, 2008.
- C. Sturgeon, A. D. II Sam, and W.R. Law. Rapid determination of glomerular filtration rate by single-bolus inulin: a comparison of estimation analyses. *Journal of Applied Physiology*, 84(6):2154–2162, 1998.
- K. Thurau and J.W. Boylan. Acute renal success. the unexpected logic of oliguria in arf. *American Journal of Medicine*, 61:308–315, 1976.
- S. Tjoa and P. Fennessey. The identification of trimethylamine excess in man: quantitative analysis and biochemical origins. *Anal Biochem*, 197(1):77–82, 1991.
- University of Debrecen. Anatomy topics. Website, 2009.
- B.A.C. Van Acker, G.C.M. Koomen, and L. Arisz. Drawbacks of the constant-infusion technique for measurement of renal function. *Am. J. Physiol*, 268: F543–F552, 1995.
- I.D. Weiner and L.L. Hamm. Molecular mechanisms of renal ammonia transport. *Annu. Rev. Physiol.*, 69:317340, 2007.
- J.F. Wyman, T.J. Moore, and M.S. Buring. Simple procedure for jugular vein cannulation of rats. *Toxicology Methods*, 4(1):12–18, 1994.
- C. A. Wyse, K.D. Skeldon, A.J. Cathcart, R. Sutherland, S.A. Ward, G. Gibson, L.C. McMillan, M.J. Padgett, T. Preston, P.S. Yam, and S. Love. *Breath Analysis for Clinical Diagnosis and Therapeutic Monitoring*. World Scientific Publishing Co. Pte. Ltd., 2005.
- M. Zeier, M. Schmid, R. Nowack, S. Zacharewics, C. Hasslacher, and E. Ritz. The response of gfr to amino acids differs between autosomal dominant polycystic kidney disease (adpkd) and glomerular disease. *Nephrol. Dial. Transplant*, 7: 501–506, 1992.